In-vitro Characterisation of Targeting Ligands for Enhanced Delivery Across the Blood-Brain Barrier

A thesis submitted *in accordance with the conditions governing candidates* for the degree of Philosophiae Doctor in Cardiff University

by

Jack Robert Sim

September 2017

Cardiff School of Pharmacy and Pharmaceutical Sciences
Cardiff University

Declarations

This work has not been submitted in substance for any other degree or award at this or any other university or place of learning, nor is being submitted concurrently in candidature for any degree or other award.

Signed …… (candidate) Date ……

STATEMENT 1

This thesis is being submitted in partial fulfillment of the requirements for the degree of ……(insert MCh, MD, MPhil, PhD etc, as appropriate)

Signed …… (candidate) Date ……

STATEMENT 2

This thesis is the result of my own independent work/investigation, except where otherwise stated, and the thesis has not been edited by a third party beyond what is permitted by Cardiff University's Policy on the Use of Third Party Editors by Research Degree Students. Other sources are acknowledged by explicit references. The views expressed are my own.

Signed …… (candidate) Date ……

STATEMENT 3

I hereby give consent for my thesis, if accepted, to be available online in the University's Open Access repository and for inter-library loan, and for the title and summary to be made available to outside organisations.

Signed …… (candidate) Date ……

Acknowledgements

Firstly, I would like to thank my supervisor, Prof. Mark Gumbleton for his guidance and support throughout my PhD. Without his valuable input, this work would have never been completed. I would also like to express my sincere thanks to my friends and colleagues in lab 1.38: Muthanna Albaldawi, Chiara Moriconi, Catia Neto, Robert Gutteridge, and Daniel Price. Without their support, this work would not have been possible to complete and I feel privileged to have had the opportunity to work with you and to call you my friends.

I must also thank my colleagues within the School of Pharmacy and Pharmaceutical Sciences at Cardiff University and other departments across the university. Particular thanks should go to Prof. Arwyn T. Jones for being my PhD advisor and helping with Mark to encourage and support me throughout my PhD. I would like to specifically thank Dr. David Jamieson, Dr. Edward Sayers, Dr. Jennifer Smith Wymant and the rest of Lab 1.14 for your help with all things microscopy related and the friendships we have built throughout my time with you. I'd like Dr. Kirsten Pugh for inviting me to act as an Academic Tutor to the students of my undergraduate degree course, throughout my PhD studies and giving me the opportunity to present a lecture on my work to them.

Finally, I would like to thank my family, my mum (Angelina), dad (Robert) and sister (Anna), as well as my grandparents and extended family, for all the support and encouragement you have given me throughout this process. My biggest thanks must go to my wife, Lorna, you have been by my side this entire process and put up with my temper tantrums when things haven't always been working. I could not have done this without you and I have to applaud how you have coped with me throughout this!

Lastly, I would like to thank Cardiff University School of Pharmacy and Pharmaceutical science for the financial support and for give me the chance to pursue my PhD study. I am very grateful to have had the opportunity to study for my PhD in this innovative department.

Abstract

The blood-brain barrier (BBB) is the most extensive and restrictive barrier to brain delivery for therapeutic agents. A low proportion of low molecular-weight agents can cross into the CNS. This decreases further as the molecular weight increases, meaning therapeutic antibodies, oligonucleotides and other supramolecular entities effectively cannot reach therapeutic levels within the CNS. Targeting ligands against receptors thought to undergo transcytosis across the brain microvascular endothelial cells (BMECs), can boost CNS delivery of therapeutics. Understanding these mechanisms, in an in-vitro setting, has proved challenging, due to the constraints of cell culture systems and the difficulty to replicate the in-vivo environment. With even the most extensively studied targeting receptor, transferrin receptor, not producing clear evidence to suggest the occurrence of transcytosis.

To understand in-vitro trafficking of brain targeting ligands a pulse-chase assay, in combination with sub-cellular localisation microscopy was developed and compared to the current permeability-based assay method. The characterisation was done by comparison of transferrin receptor ligands; native holo-transferrin, the 8D3 antibody and a low-affinity variant; with the non-specific uptake probe, dextran. The method could distinguish between the two endocytosis methods, with concentration-dependent efflux efficiency observed with the targeted probes. The combination of techniques was then applied to the novel targeting ligand, Rabies-Virus Glycoprotein (RVG) peptide, to assess its suitability as a brain delivery. Studies were performed to confirm the target receptor of the RVG peptide, including competitive uptake, siRNA knockdown methods. The RVG peptide demonstrated desirable delivery characteristics, and the target receptor was confirmed as the α7 nicotinic acetylcholine receptor. Finally, attempts were made to develop a total internal reflection fluorescence (TIRF) microscopy assay for the assessment of ligand arrival at the basolateral membrane of BMECs. Initial work for this was performed with the transferrin receptor and transferrin, using both labelled ligand and photoswitchable receptor constructs. In summary, the pulse-chase assay provides a complementary technique to permeability assays for the assessment of brain targeting ligand trafficking in BMEC cell-lines in-vitro.

Table of Contents

List of Figures

List of Tables

Abbreviations

8D3 – Rat anti-Mouse TfR antibody

8D3-4 – 8D3 Low Affinity Variant

AAV – Adeno-Associated Virus

ANOVA – Analysis of Variance

ABC – ATP Binding Cassette

αBGT – α-Bungarotoxin

ACM – Astrocyte Conditioned Media

AD – Alzheimer's Disease

AJ – Adherens Junction

AMT – Adsorptive Mediated Transport

AP – Adaptor Protein

AP2µ2 – Adaptor Protein 2 Variant µ2

AQP4 – aquaporin 4

ATP – Adenosine Triphosphate

BACE1 – Beta-Secretase 1

BBB – Blood-Brain Barrier

BCRP – Breast Cancer Resistance Protein

bFGF – Basic Fibroblast Growth Factor

BMEC – Brain Microvascular Endothelial Cell

BME – Brain Microvascular Endothelium

BSA – Bovine Serum Albumin

cDNA – Complementary DNA

CAM – Cell Adhesion Molecule

CME – Clathrin Mediated Endocytosis

CNS – Central Nervous System

COMPACT – Collaboration on the Optimisation of Macromolecular Pharmaceutical Access to Cellular Targets

CPP – Cell Penetrating Peptide

CRISPR – Cluster Regulated Interspaced Short Palindromic Repeats

crRNA - crisprRNA

CSF – Cerebral Spinal Fluid

DDS – Drug Delivery System

DEPC – Diethyl Pyrocarbonate

DNA – Deoxyribose Nucleic Acid

dNTPs - Deoxyribonucleotide Triphosphate

DMEM – Dulbecco's Modified Eagle Media

DTR – Diptheria Toxin Receptor

EMCCD – Electron Multiplying Charge-Coupled Detector

EPO – Erythropoietin

EtBr – Ethidium Bromide

FACS – Flow Assisted Cell Sorting

FBS – Fetal Bovine Serum

FRAP – Fluorescence Recovery After Photobleaching

GABA – Gamma-Aminobutyric Acid

GAPDH – Glyceraldehyde 3-Phosphate Dehydrogenase

GCD – Genomic Cleavage Detection

GFP – Green Fluorescent Protein

gRNA – Guide RNA

HBEGF – Herparin-Binding Epimermal Growth Factor

HEPES – (4-(2-hydroxyethyl)-1-piperazineethanesulfonic acid)

HIV – Human Immunodeficiency Virus

HRP – Horse Radish Peroxidase

IC50 – 50% inhibition concentration

ICAM – Intracellular Adhesion Molecule

IgG – Immunoglobulin G

iPSC – Induced Pluripotent Stem Cells

ID – Injected Dose

IR – Insulin Receptor

JAM – Junctional Adhesion Molecule

Kd – Association Rate Constant

Ki – Inhibitory Rate Constant

KRB – Krebs Ringer Buffer

LB – Luria Broth

LDL – Low Density Lipoprotein

LfR – Lactoferrin Receptor

mRNA – Messenger RNA

MTF – Melanotransferrin

nAchR – Nicotinic Acetylcholine Receptor

NA – Numerical Aperture

NCAM-1 – Neuronal Cell Adhesion Molecule-1

NHEJ – Non-Homologous End Joining

NVU – Neurovascular Unit

OAT – Organic Anion Transporter

OATP1A2 – Organic Anionic Transporting Polypeptide 1A2

OCT – Organic Cation Transporter

p75NTR – Low Affinity Nerve Growth Factor Receptor

PAM – Protospacer Adjacent Motif

Papp – Permeability Coefficient

PBMEC – Primary Porcine Brain Microvascular Endothelial Cell

PBS – Phosphate Buffered Saline

PFA – Paraformaldehyde

Pgp – P-glycoprotein

PLGA – Poly(Lactic-co-Glycolic Acid)

Rho – Tetramethyl Rhodamine

RMT – Receptor Mediated Transcytosis

RNA – Ribose Nucleic Acid

rtPCR – Reverse Transcription Polymerase Chain Reaction

RV – Rabies Virus

RVG – Rabies Virus Glycoprotein

SCRAM – Scrambled Sequence RVG Peptide

SEM – Scanning Electron Microscopy

siRNA – Short Interfering RNA

sgRNA – Single Guide RNA

SLNP – Solid Lipid Nanparticle

SNAP – Synaptosome-Associated Protein

SNARE - Soluble NSF Attachment Protein Receptor

Taq – Thermus aquaticus

TALEN – Transcription Activator-like Effector Nuclease

TEER – Trans-Endothelial Electrical Resistance

Tet – Tetanus Virus Derived Peptide

Tf – Transferrin

TfR – Transferrin Receptor

TIRF – Total Internal Reflection Fluorescence

TIRFM – Total Internal Reflection Fluorescence Microscopy

TJ – Tight Junction

TNFR – Tumour Necrosis Factor Receptor

tracrRNA – Trans-activating crisprRNA

UV – Ultra Violet

VAMP-2 – Vesicle-Associated Membrane Protein-2

VE-cadherin – Vascular Endothelial Cadherin

VEGF - Vascular Endothelial Growth Factor

ZFN – Zinc Finger Nuclease

ZO – Zona Occludes

Chapter 1: General Introduction

The microenvironment of the central nervous system (CNS) is tightly regulated, through the complex nature of the barriers surrounding it. While transportation mechanisms exist for the passage of essential nutrients, oxygen, glucose, proteins and immune cells into the brain. These transport processes must be closely regulated maintain the homeostatic composition of extra-cellular fluid within the brain. Regulation of the CNS microenvironment (brain parenchyma) is essential for the support of neuronal connectivity within the brain; highlighting the importance of barriers to the CNS.

The primary barrier of the CNS from the systemic circulation is the Blood-Brain Barrier (BBB). This barrier was first observed by Paul Ehrlich (1854-1915), who observed that dyes injected into the circulation were able to stain all organs, apart from the brain and spinal cord. Further experiments, by Erwin Goldmann, demonstrated that injection of trypan blue into the cerebral spinal fluid (CSF) stained the brain and spinal cord, but not the systemic organs. Max Lewandowsky first introduced the phrase Blood-Brain Barrier (BBB); after investigations with another water-soluble dye, potassium ferrocyanate was unable to reach the CNS (Hawkins and Davis 2005).

As a barrier, the BBB regulates the trafficking of molecules across the microvascular capillary beds of the brain. Due to the extensive vascularisation of the brain, an organ with high metabolic demands, the BBB makes up approximately 99% of the barrier surface area of the brain, ~ 20 m^2 in humans (Boado and Pardridge 2011). The extensive branching of the cerebral microvasculature means individual neurons receive nearly a unique blood supply, to provide the nutrients required (Schlageter *et al.* 1999). Although the brain microvascular endothelial cells (BMECs) form the restrictive barrier, that is the

BBB; they would be unable to without the close interactions and cellular signalling with multiple cell types within the CNS. Thus, it is deemed correct to view the BBB, not as a single cell type barrier, but a neurovascular unit (NVU) comprising endothelium, astrocytes, pericytes, microglial and neuronal cross-talk. These interactions facilitate the differentiation and phenotypic characteristics of all cell-types involved. The restrictive barrier created by the NVU, required for the preservation of the ionic balance of the brain microenvironment, presents a challenge in the field of drug delivery. While some small molecular weight, lipid-soluble drugs can penetrate the CNS. Large molecular weight, macromolecular therapeutic agents, such as antibodies, proteins, DNA and RNA therapies are limited in their ability to cross into the brain to elicit the desired therapeutic effect. The use of targeting ligands have been shown to interact with known putative receptors on BMECs, to increase delivery of a therapeutic across the BBB.

1.1 Biologic Macromolecules and their role in the CNS

Disorders affecting the CNS are placing an increased burden on healthcare systems around the world. Due to ageing populations across the world, the occurrence of CNS disorders has grown and is projected to be the second leading cause of death globally in 2030 (Mathers and Loncar 2006). Neurodegenerative diseases such as Parkinson's disease, Alzheimer's disease, multiple sclerosis and conditions like CNS cancers all contributing to the pressures of CNS disorders. In Europe in 2010, 38% of all Europeans were reported to have suffered from some form of CNS disorder (Olesen *et al.* 2012). A study into the leading causes of death in the UK in 2013, by the Office for National Statistics, found Dementia and Alzheimer's disease to be the leading cause of death in Women of all ages, and the third highest cause of death in men (ONS 2015).

Despite the burden of CNS disorders, the current clinical treatments are lacking in therapeutic output. Small molecule therapeutics offer a method to relieve symptoms of

the CNS disorders. However, the disease modifying effects are limited when these approaches. Substantial funding opportunities are available for CNS research; however, despite this, there is still a disconnect between *in vitro* and pre-clinical efficacy studies, with the clinical, patient setting. This may be due to the increased complexity of human brains, compared to the animal models used in pre-clinical work and the complexity of the neuronal networks of the brain.

It is widely accepted that to have a disease modifying effect in chronic conditions requires intervention with a biological therapeutic. Biological therapeutics are typically large molecules, such as peptides, proteins (antibodies), DNA or RNA, that can correct the disease phenotype and restore normal functioning of a cell/tissue. The effects may include reducing protein levels within the CNS (Aβ protein – Alzheimer's Disease), prevent interaction from taking place in a cell signalling event, induce the production of a new or correct the form of a protein to correlated to a given disease.

For the treatment of Alzheimer's Disease, several macromolecular approaches have been shown to have efficacy *in vitro*, including the anti-BACE-1 antibody of Roche, siRNA targeted therapies. These mechanisms have demonstrated *in vitro* efficiency in reducing disease causing Aβ protein. However, used alone *in vivo* are limited in their efficacy. Due to the restrictive nature of the BBB, restricting the entry of large biological therapeutics to the brain. Typically, untargeted therapeutic antibodies, only show 0.1-0.2% of injected dose reaching the CSF (Poduslo *et al.* 1994). To improve the delivery efficiency of biologics into the CNS a "shuttle" mechanism or a targeting approach is required to overcome the barriers to CNS entry.

1.2 Components of the Neurovascular Unit

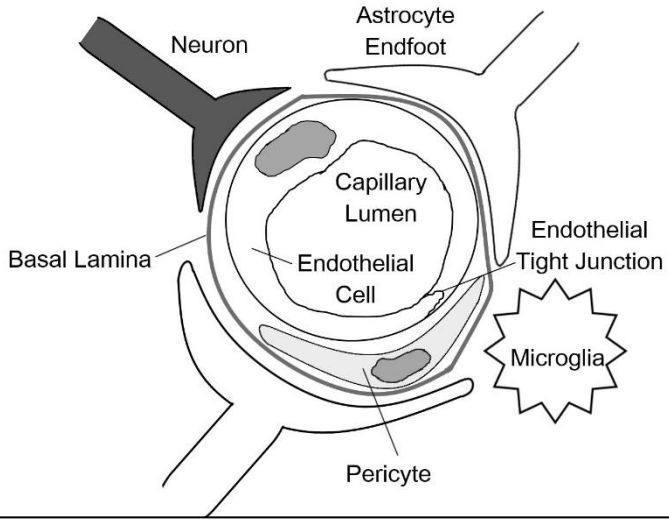

Figure 1.1: The structure and composition of the Neurovascular Unit

The neurovascular unit (NVU) is centred around the endothelial cells and the capillary lumen of the micro vessels. However, these cells are only one part of the NVU. The diagram highlights the close interaction with the multiple cell types of the NVU. Pericytes are in direct contact with the endothelial cells and the surrounding astrocyte endfoot processes are the main contributors to the BBB phenotypes. Other neuronal processes and microglial cells are also having a role in NVU formation and normal functioning. Adapted from Abbot et al (2006).

1.2.1 Brain Microvascular Endothelial Cells

The BMECs are the primary barrier cell type within the NVU, providing both a physical and chemical barrier to the passage of molecules from the blood into the brain parenchyma. Unlike the capillary networks of peripheral organs, the microvasculature of the brain displays several unique, phenotypic characteristics. These include the presence of tight and adherens junctions between adjacent BMECs, leading to the almost complete closure of paracellular pathways between cells. And a lack of fenestration in the cerebral capillaries.

Tight junctional (TJ) complexes comprise Claudins, Occludins, Junctional Adhesion Molecules (JAM) and Zona-Occludens (ZO-1, -2, -3) proteins. Claudins and occludins

are closely associated and extend into both the cytosol and the extracellular space. These molecules recognise claudins and occludins on adjacent cells to form the apical limit of the tight junction (Yaffe *et al.* 2012; Piontek *et al.* 2008). It has been shown phosphorylation of the intracellular domains of occludin molecule, by receptor-mediated processes, regulates the restriction of paracellular permeability across a tight junction (Murakami *et al.* 2009; Wong 1997). Additionally, the removal of calcium from the extracellular domains of occludin causes the loss of tight junction restriction.

The family of claudin molecules are proteins consisting of 4 transmembrane domains, which form the barrier properties of the tight junction. Within BMECs, claudin-3 and claudin-5 are mainly expressed, with claudin-12 also thought to be expressed within endothelial cell tight junctions (Morita *et al.* 1999; Soma *et al.* 2004; Schrade *et al.* 2012). Studies *in vitro* show that the addition of exogenously expressed claudin-5 to BMEC cultures, decrease paracellular permeability and increase the trans-endothelial electrical resistance (TEER) of the culture model (Coyne *et al.* 2003). Further, claudin-5 is known to contribute to early-stage angiogenesis within the CNS (Escudero-Esparza *et al.* 2012). The intracellular, C-terminal domain of claudin molecules interacts with the Zona Occludins proteins, facilitating cytoskeletal rearrangement and cell polarisation.

Basolateral to this, junctional adhesion molecule, JAM-1, is highly expressed in BMECs, whereas other members of the JAM family (JAM-2, JAM-3) are expressed throughout the cardiovascular system. JAM-1, contains an immunoglobulin like extracellular domain, within a single intracellular chain facilitating interaction with ZO-1, AF-6, cingulin and Cas kinase (Ebnet *et al.* 2004; Ozaki *et al.* 2000). The extracellular loops of JAM-1 use hydrophobic interactions to associate with molecules on adjacent cells.

Within the cells, the ZO proteins interact with the cytosolic regions of the tight junctional proteins. ZO proteins contain multiple domains for signal transduction. Within the ZO-1

protein, the PDZ-domain is vital for the interaction with the intracellular domains of claudins and JAM-1 (Ebnet *et al.* 2000), while the SH3 domain allows a connection with the cytoskeletal proteins (Balda *et al.* 1996). Dissociation or removal of the ZO-1 protein from the tight junction complex of BMECs causes a reduction in TEER and the increase in paracellular permeability across the barrier (Mark and Davis 2002; Van Itallie *et al.* 2009). Additionally, the interaction of ZO-1 with claudin is required for the claudin polymerisation seen within tight junctions. The cytoskeletal arrangement allows for the segregation of apical (blood plasma) and basolateral (brain parenchymal) membranes and cell polarisation.

Within BMECs further proteins including cingulin, AF-6 and 7H6 also interact with the tight junctional complexes to further facilitate a restriction in the paracellular permeability across BMECs (Satoh *et al.* 1996; Cordenonsi *et al.* 1999). This is done through either direct interaction with TJ proteins or increasing the presence of co-factors essential for TJ regulation. The knockdown or removal of these proteins from BMECs and other barrier cell lines has shown to reduce TEER.

To further restrict the paracellular pathway between BMECs, adherens junctions (AJs), form an unbroken link between adjacent cells. This link between the cells facilitates the formation of the tight junctions, discussed above. The main protein involved within AJs are cadherins, a transmembrane glycoprotein. Cadherins form Ca^{2+} dependent interactions with cadherin on the surface of neighbouring cells (Gumbiner and Simons 1986; Heimark *et al.* 1990). The intracellular domain of cadherin proteins interacts with several anchor proteins, belonging to the Armadillo superfamily. These include β-catenin, γ-catenin and p120 (Dejana *et al.* 2008). Between endothelial cells specifically cadherin 5 is found in AJs, this member of the cadherin family is also known as VE-cadherin (vascular endothelial). Expression of VE-cadherin is a phenotypic characteristic of

endothelial cells. The catenin molecules also contain an actin-binding domain to link the adherens junction with the cytoskeleton. β-catenin binds to several growth factor receptors. When stimulated β-catenin complexes dissociate and translocate away from the cell membrane, this causes the breakdown of the AJs between BMECs increasing paracellular permeability (Nagafuchi 2001). Without the presence of AJs between BMECs, the formation of tight junctions would not be possible, and therefore the physical barrier associated with the BBB cound not be formed (Dejana 2004).

The restrictive nature of the cell-cell junctions between BMECs at the BBB produces a physical barrier to the entry of substrates into the brain parenchyma. However, this alone is not enough to maintain the privileged microenvironment of the brain. BMECs also exhibit several other traits which aid in limiting access of substrates to the CNS. An example of this would be the low rate of endocytosis which occurs within BMECs in comparison to the peripheral vasculature. The BBB has a chemical barrier, consisting of metabolic enzymes, to break down unwanted substrates, as well as efflux transporters to remove lipophilic drugs and metabolites from the BMECs before they can reach the CNS.

The efflux transporter on BMECs and the other cells of the neurovascular unit are critical in the maintenance of the homeostatic environment of the CNS. While also preventing many potentially therapeutic agents from entering the CNS. Chief among the transporters of the CNS are the ATP-binding cassette (ABC) transporters, more specifically P-glycoprotein (Pgp). Expressed on the luminal membrane of BMECs, Pgp, has been shown to limit the uptake of antipsychotic agents to the CNS (Laduron and Leysen 1979). In addition to this, anti-viral drugs, including acyclovir and saquinavir, are prevented from entering the CNS by the Pgp protein. Knockout of the Pgp produced an increase in CNS penetration of antiviral drugs in mice, compared to wild type animals (Kim *et al.* 1998).

Other ABC transporters on the luminal membrane of BMECs include breast cancer resistance protein (BCRP) (Cooray *et al.* 2002). BCRP has been shown to have a critical role in limiting the penetration of chemotherapeutic agents, such as methotrexate, across the BBB and brain-tumour barriers in neuroblastoma, glioblastoma and brain metastases, preventing imatinib and topotecan from effectively treating tumours (de Vries *et al.* 2007).

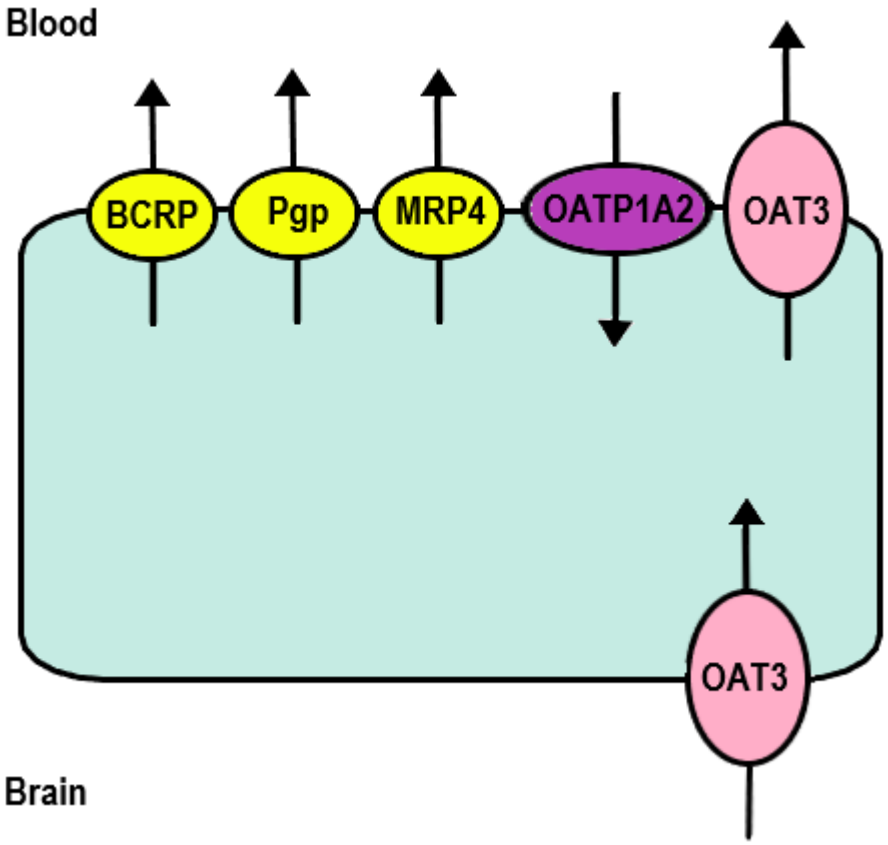

Figure 1.2: Transporter Localization at the BBB
This highlights some of the major transporter proteins present on BMECs and the direction in which they translocate their substrate. The breast cancer resistance protein (BCRP), P-glycoprotein (Pgp) and multidrug resistance protein 4 (MRP4) are ATP-Binding Cassette (ABC) proteins, shown in yellow. The organic-anion-transporting polypeptide (OATP1A2) is shown in purple as it is an influx transporter. While the OAT3 efflux transporter is shown in pink. Adapted from Dalvi et al (2006) Figure 3.

Another large family of transporters found on the cell surface of BMECs are the organic anionic transporters (OATs) and organic cationic transporters (OCTs). These are solute

carriers that can transport compounds in different directions based on the sub-type. OATs are responsible for the removal of metabolic byproducts from the CNS, which includes metabolised neurotransmitters and uric acid (Koepsell and Endou 2004). In contrast, OCTs regulate the removal of negatively charged waste products, such as those containing chloride ions. In the BBB, OAT3 has been shown to be localised to the basolateral and apical cell membranes to facilitate waste clearance from the CNS (Mori *et al.* 2003).

Not all transporters at the BBB remove drugs from the brain, the organic anionic transporting polypeptide 1A2 (OATP1A2, Figure 1.2 - purple) facilitates the transport of some drugs, including synthetic peptides, from the brain capillaries into the brain parenchyma (Urquhart and Kim 2009). However, mutations in this transporter can vary the levels of CNS exposure of certain drugs. One study showed that such a mutation could increase methotrexate delivery to the CNS by 2-fold, which caused severe damage to neurones and CNS pathology (Sioka and Kyritsis 2009).

It is the combination of physical and metabolic features that allows the BMECs of the BBB to form such a restrictive barrier to the CNS. However, for this differentiated phenotype to occur, the role of the surrounding cell types and the interaction between them is critical.

1.2.2 Astrocytes

The restrictive phenotype displayed by the BMECs of the neurovascular unit (NVU) would not be possible without the interaction with multiple cell-types within the CNS. The astrocyte endfoot processes are basolateral to the endothelial cells and surround the microvasculature of the CNS, creating a perivascular channel around the vessels of the CNS. The perivascular endfoot of astrocytes contain aquaporin 4 (AQP4) water channels and Kir4.1 K^+ channels. These are involved in the regulation of fluid volume around the

microvessels (Fukuda and Badaut 2012). And the expression of these channels is related to the production of proteoglycans in the basal lamina, for support of the BMECs. The expression of the AQP channels and differentiation of the endfoot processes requires exposure to agrin, released from BMECs.

Astrocytes release several modulation factors, including the growth factors: transforming growth factor-β, glial-derived neurotrophic factor, basic fibroblast growth factor (bFGF) and angiopoietin 1. These factors are known to act on BMECs in differentiation to induce the restrictive phenotype of the BBB. Astrocytes also release small molecule mediators of vascular tone and diameter, including nitric oxide and prostaglandins, to control localised blood flow within the CNS (Gordon *et al.* 2007; Iadecola and Nedergaard 2007). Astrocytes serve as the link between neuronal synaptic signalling and the local vasculature creating changes in blood flow to react to neuronal stimulation (Attwell *et al.* 2010). In disease states, such as stroke and epilepsy, the functioning of astrocytes may be altered. *In vitro* models of ischemic stroke demonstrated that secreted astrocytic factors, from the C6 cell line, altered the expression of tight junctional proteins in BMECs (Neuhaus *et al.* 2014). This work also showed the impact on ABC efflux pump expression in the BMECs in hypoxic vs. normoxic conditions. In epilepsy, astrocyte expression of AQP4 is decreased, and as such the presence of Kir K^+ channels at the astrocyte endfoot is also reduced (Binder *et al.* 2006). This compromises the brain parenchyma, as K^+ ions within the local parenchyma remain elevated for a prolonged time following electrical stimulation. This causes altered osmolarity of the extracellular environment of the CNS which will impact on the regulation of vascular tone.

1.2.3 Pericytes

Pericytes are present to differing levels in vasculature of multiple tissue types around the body, with the greatest coverage of the vasculature seen with the CNS. Here, pericytes

are another cell type surrounding the microvasculature of the brain, forming the neurovascular unit. As with astrocytes, pericytes have a critical role in the development, functionalization and stabilisation of the NVU. Pericytes are a smooth muscle-type cell that surrounds the endothelial cells and has a direct function in regulating the vessel diameter in response to neuronal and astrocytic stimulation. The presence of pericytes, in other tissue vasculature, is more likely to occur at vessel junctions and bifurcations. However, in the CNS coverage of the abluminal surface of the brain microvasculature can be as high as 99% in some regions of the CNS (Dalkara *et al.* 2011). Surrounding BMECs, pericytes strictly regulate the tight junctional integrity and vesicular transport rates of BMECs.

Dysregulation of pericytes and CNS disorders are closely linked. For example, in ischaemic stroke contraction of the pericytes around the BMECs restricts blood flow into regions of the brain around the damaged area. Pericytes themselves require changes in intracellular Ca^{2+} levels to regulate their contractility. Exposure to external factors, such as reactive oxygen species (ROS), can induce uncontrolled changes in Ca^{2} within the pericytes, leading to excitotoxicity and excess contractility, reducing local blood flow. This is particularly prevalent in ischemic conditions and has been demonstrated in mouse models of ischemic stroke (Yemisci *et al.* 2009). In neurodegenerative disorders, such as Alzheimer's Disease, pericytes have been observed to behave as macrophages, clearing amyloid toxin from perivascular regions (Sagare *et al.* 2013).

1.3 *In vitro* models of the BBB

1.3.1 Primary vs Immortalized vs IPSC Cell models

There is inherent difficulty in studying the *in vitro* transport of drugs across BMECs. Almost all BMEC models, even in co-culture with astrocytes and pericytes, are considered to have "leaky" paracellular pathways. This is most profound when using

immortalised cell line models of BMECs (Gumbleton and Audus 2001; Deli *et al.* 2005). Data from *in vivo* studies of rat brain capillaries revealed a trans-endothelial electrical resistance (TEER) more than 1000 $\Omega.cm^2$ (Chrone and Olesen 1982; Crone and Christensen 1981). The apparent permeability of an *in vivo* endothelial monolayer to paracellular markers, such as sucrose, in a rat, was shown to range from $0.03 – 0.1 cm.s^{-1}$ (Rapoport *et al.* 1978).

However, there are several BMEC models, used for the *in vitro* assessment of transport therapeutics across the BBB, which include both immortalised and primary cell cultures. TEER is often the key parameter described by users of such models; however, is prone to variation based on the electrode types and the measurement methodologies used. The use of paracellular markers, such as sucrose, dextrans or mannitol, allows for a more in-depth understanding of the integrity of the model barrier. And the relationship of the *in vitro* model to the *in vivo* reality. BBB models extend beyond a simple culture of the BMECs (Bowman *et al.* 1983), to co-cultures, with several additional cell lines (astrocytes and pericytes). Other studies also include the use of switch media (hydrocortisone and phosphodiesterase inhibitors) that transiently increase the paracellular resistance of the systems (Hoheisel *et al.* 1998; Cucullo *et al.* 2004). As a general trend, primary cell lines exhibit a high TEER value in comparison to immortalised cells, such as the b.End3 mouse cell line (Omidi *et al.* 2003; Smith *et al.* 2007). The co-culture systems again have been shown to increase TEER and decrease in the permeability of paracellular markers (Li *et al.* 2010).

There are various ways to create a co-culture system involving BMECs and astrocytes. The most basic of these is using astrocyte conditioned medium (ACM) which is used in the culture media of BMECs, grown on semi-permeable membrane inserts such as Transwells™. In this way, ACM can modulate the phenotypic characteristics of the

BMECs. The ACM contains growth factors and other chemical mediators released by the astrocytic cell line to regulate BBB permeability (Yamagata *et al.* 1997; Sobue *et al.* 1999); a process mimicking the *in vivo* situation. More advanced co-culture systems involve the pre-seeding of astrocytic cell lines, either onto the base of the culture plate well plate or the basal surface of the inserts themselves. The astrocytes are allowed to grow until confluence, and then the BMECs are seeded onto the apical surface of the inserts (Gaillard *et al.* 2001). All of these models have been shown that astrocytes or astrocyte-released factors enhance the expression of the phenotypic markers of brain endothelial cells such as ZO-1, claudins and Pgp (Omidi *et al.* 2003; Huber *et al.* 2001; Nitz *et al.* 2003).

The discovery and use of human induced pluripotent stem cells (iPSCs) in research have allowed for the differentiation of these cells into almost any other cell type of the body. The iPSC cells will differentiate based on the microenvironment they are grown in, including the generation of a neurovascular unit, derived from the iPSCs of an individual. In the long-term, generation of barrier models using healthy and disease state iPSCs which will allow for greater understanding of the disease phenotypes and inter-patient variability in barrier functionality. This has allowed for the development of multiple methods for the differentiation and culture of iPSC derived human brain endothelial cells.

In the simplest studies, iPSCs, in embryoid bodies, undergo spontaneous differentiation into endothelial cells. However, the efficiency of differentiation increased by the addition of growth factors, including bFGF, vascular endothelial growth factor (VEGF), and low serum media. Also, Lippmann et al. (2012), showed that culturing the iPSCs on a collagen/fibronectin extracellular matrix lead to the development of an endothelial cell phenotype (Lippmann *et al.* 2012). Other differentiation methods include the culturing of the stem cells with neuronal cell-types. The hypothesis here is that the neuronal cells act

to complete the differentiation of the endothelial cells to BMECs. Co-culture in this way has been performed through the direct mixing of cell-types and subsequent selection of the BMECs from the resultant cell pool. The development of sequential differentiation protocols such as the Lippmann protocol, and other protocols have made the formation of iPSC-derived BMECs standardised and easy to replicate (Lippmann *et al.* 2012; Lippmann *et al.* 2015).

Having established protocols for BMEC differentiation, work has begun to study the effect of neurodegenerative conditions, on the phenotype of BMECs in patients. Most recently, a study of the transcriptome of Huntington's disease cells vs "healthy" iPSC-derived BMECs revealed deficits in angiogenic and barrier properties of the cells (Lim *et al.* 2017). The loss of functionality includes a reduction in the capabilities of the BMECs to efflux foreign molecules from the CNS.

When compared to immortalised cell lines, iPSC-derived BMECs show greater paracellular restriction, reflected in increased TEER values. Monoculture of the iPSCs-derived BMECs show TEER values more than 250 $\Omega.cm^2$, which rises to over 1500 $\Omega.cm^2$ when grown in culture with astrocytes and pericytes (Lippmann *et al.* 2012). The permeability of sucrose showed a 100-fold decrease in iPSCs compared to the permeability in hCMEC/D3 cell model (Culot *et al.* 2008). With these characteristics are maintained throughout the lifetime of the iPSC cells.

Protein markers of BMECs allow for validation of a cell-based model for the study of trafficking events *in vitro*. A study comparing multiple, different iPSC-derived BMECs found that vascular endothelial markers, such as PECAM-1 and VE-cadherin generally showed increased expression compared to hCMEC/D3 cells (Patel *et al.* 2017). However, the BMECs derived from the CTR54F stem cell line showed lower expression of these markers, and lower expression of Glut-4, and the ABC transporters ABCB1, ABCC1 and

ABCG2. The CTR54F stem cell line also showed a lower TEER value than the hCMEC/D3 cells. Highlighting the heterogeneity of patient-derived samples.

Overall it seems likely that in the coming years a shift will be made towards the use if iPSC-derived BBB models over immortalised and primary cell lines. The iPSCs offer the advantage of allowing for the creation of disease-specific BBB models to examine the pathophysiology of the BBB in association with CNS disorders. Allowing for a more tailored approach to treatment strategies to restore normal CNS and BBB phenotypes. However, it must also be considered that, while the iPSC cells have been effective in recreating models of the BBB in Huntington's Disease, a mono-factorial disease. It is yet to be established if these cell models may be used to recreate the conditions of more complicated, multi-factorial diseases, such as Multiple Sclerosis, from patient stem cells.

1.3.2 Co-culture, microfluidic models of the BBB

The capillary endothelial cells of the BBB form a highly restrictive barrier to the entry of therapeutics into the CNS. Surrounding BMECs are astrocyte end-foot projections and pericyte cells. It is the crosstalk between these cell types that produce the characteristic, physical and metabolic barrier that is seen at the BBB. Mechanistically, promising therapeutics, for the treatment of CNS disorders, often fail in clinical trials due to an inability to reach efficacious levels within the CNS.

In CNS research, the long-established, preferred method of studying drug delivery to the brain has been *in vivo* studies in rodents. They offer the benefit of allowing the studies to take place in the physiological microenvironment of a live brain. However, rodents and other animals are not humans, and drug candidates that showed promise *in vivo*, often go on to lack clinical efficacy in human trials (Perel *et al.* 2007). Due to the increased ethical considerations associated with animal research, there has been a shift to establish a cell-based approach, *in vitro*, to allow for the screening of drug candidates. Drug delivery

research is continually looking to improve the *in vitro* models available, to mimic, more closely, the physiological conditions of patients and thus reducing the failure of therapeutics in clinical trials.

Traditionally, *in vitro* BBB models, have been static systems, with endothelial cells grown on either plastic, glass or semi-permeable membranes (Transwells), with probes applied to the apical surface and uptake or permeability studied. These systems looking at uptake and loss from endothelial cells only give one aspect of the puzzle, especially with regards to brain delivery. The static models have proved useful tools in research, but their departure from the physiological conditions around the endothelial cells of the neurovascular unit often leads to discrepancies between *in vitro* and *in vivo* work. To progress from the monoculture of BMECs, co- or tri-culture methodologies have been developed to culture the BMECs in "close" proximity to astrocytes and pericytes, using the Transwell system. Endothelial cells are grown on the apical side of the Transwell insert, with astrocytes and pericytes grown in the basolateral chamber or directly onto the basolateral membrane of the inserts. Studies using these multi-cellular systems have demonstrated increases in the trans-endothelial electrical resistance (TEER) across the monolayer. However, despite being demonstrated in multiple cell models, these values are still significantly outside the *in vivo* TEER ranges, reported in a review by Wolff *et al.* (2015). Other markers of physiological restriction include sucrose and mannitol permeability. These are often seen to be 10-100 times lower *in vitro* models than reported *in vivo* values.

Static BBB models inherently lack the circulation of fluids across cell surfaces. Both the luminal blood flow in the capillaries, the perivascular drainage of fluid outside the blood vessels, between the endothelium and astrocyte end-foot processes and circulation of interstitial fluid within the CNS itself. The blood-flow has significant physiological

effects on all endothelial cell types, regardless of tissue type, through mechanoreceptor-mediated differentiation mechanisms. It is known that the number of caveolae pits, at the luminal membrane of endothelial cells is influenced by the flow-rate of blood in circulation (Rizzo *et al.* 2003). As many surface receptors associate to caveolae and caveolin-mediated endocytosis is the second most common endocytic pathway, their presence on BMECs will undoubtedly influence the validity of drug delivery data from any *in vitro* models. In models of aortic endothelium, the increase in caveolae is believed to facilitate the adaptation of the endothelial cells to mechano-transduction signals (Rizzo *et al.* 2003). Other work has shown that the surface expression of adhesion molecules on the surface of HUVEC cells is influenced by the flow-rate and the turbulence across the endothelial cell surface (Khan and Sefton 2011; Morigi *et al.* 1995; Huang and Eniola-Adefeso 2012). Shear-stress across endothelial cells is also known to impact on the cytoskeletal arrangement and the expression of polarising proteins, including those of tight junctions (Cucina *et al.* 1995; Frame and Sarelius 2000; Loufrani and Henrion 2008). Without shear-stress across the surface of BMECs, they are unable to completely differentiate and produce the BBB-phenotype, and the cell-based model lacks fidelity in the results generated from it.

Flow over BMEC cultureswas first created using a rotating device, which was placed into the apical compartment of the Transwell system (Dewey *et al.* 1981). However, this model was widely refuted and short-lived, due to the variations in the shear-stress across the endothelial monolayer, affected by the distance from the centre of the dish (Wolff *et al.* 2015). The lack of control and uniformity in shear stress and the lack of co-culture data within this system led to this model's discontinuation. Other early methods to generate flow across BMECs in permeability studies also included the use of rotary plate-shakers to circulate fluid over the BMECs.

In an attempt to better mimic blood-flow *in vivo,* recent research work has focused on the creation and development of microfluidic devices. These are narrow channels, into which the BMECs can be seeded. Once cells have adhered to the growth surface, it is possible to then modulate the flow across them, recreating the shear-stress conditions the BMECs would typically experience *in vivo*. By using peristaltic or syringe pumps, it is possible to re-create physiological shear-stress across the BMECs in the capillary vessels of the brain (10-20 dynes/cm^2) (Kamiya *et al.* 1987).

In the simplest form, these microfluidic devices will be a single channel for the monoculture of BMECs, while exposed to flow over a cell surface. This system allows for direct measures on the influence of shear-stress on the physiology of BMECs. Biochemical and fluorescence microscopy assays on cells exposed to flow enables direct comparisons between the flow and static models. Comarison allows the quantification of changes to cell protein levels and the distribution of cellular proteins.

Improvements in the manufacturing methodologies, of microfluidic devices, have allowed for the creation of devices, with bifurcating channels, where the flow is split at junctions. The bifurcations in the channel create turbulence over the endothelial cells and alter their behaviour further. More complex networks can be formed with multiple junctions, both separating and re-joining. One such example of the vascular network chips have been designed by the company SynVivo and has a customisable structure that allows for up to seven bifurcations within the channel. Although these channels have been created, the direct effect on the BMECs has yet to be reported in the literature. Typically, these have been used to study leukocyte migration and endothelial interactions *in vitro,* as shown successfully by Morigi *et al.* (1998) Studies *in vivo* looking at the neurovascular unit have demonstrated the importance of the bifurcations in the regulation of capillary tone and cell distribution. Typically, pericytes are seen surrounding endothelial cells at

vessel bifurcations, its believed these regulate the flow within specific regions of the brain. Within animal models of cardiac arrest, the pericytes at "early"-generation capillary junctions show increased contractility to reduce vessel diameter (Glyn and Ward 2000).

1.3.3 Microfluidics with multiple channels for co-culture models

Having established that simulated flow, over cultured endothelial cells, causes changes in their phenotype and an enhancement of their BBB characteristics, several groups have looked to take this further and established co-culture systems for transport studies underflow. These devices have often been custom-manufactured for the purpose; however, there is a growing number that have become commercially available. In these "chips" an apical channel is separated from a basolateral channel, at the point of overlap, by a semipermeable membrane. This partitioning of channels allows for endothelial cells to be grown in the apical-most channel and form a cell monolayer over the membrane, as happens in the Transwell model. However, in this case, the endothelial cells can be exposed to a simulation of vascular flow, to mimic microvascular capillary blood flow.

The first 3-dimensional microfluidic model of the BBB was the DIV-BBB model (Cucullo *et al.* 2010). In this system, porous channels allow cells to be grown in the lumen and permeability to be measured outside of the simulated channels. The DIV-BBB model required a large density of cells for seeding (10^8 cells) to correctly fill the channels with cells. Measurements of TEER across endothelial cell monolayers, grown under flow conditions in this model was measured as 524 $\Omega.cm^2$, much higher than the static culture equivalent with the cell line (Cucullo *et al.* 2010).

In 2012 Booth and Kim fabricated a much smaller, multi-channel microfluidic BBB model, known as the µBBB model (Booth and Kim 2012). This was the first BBB model to be made on a "chip", meaning a reduction in size, without compromising the quality

of the output. The μBBB model was fabricated from PDMS polymer, using micro-etching to design and produce the channels. A semipermeable insert, between the channels, forms the barrier surface for TEER and permeability measures to be made across. The fabrication technique allows for low channel volumes (~20 μl of buffer). Co-culture systems can be easily setup to add astrocytes "below" the endothelial cells, to more accurately represent the *in vivo* setting. The fabrication techniques used in this chip device means cells in the basolateral chamber are within 400 μm of the endothelial cells in the apical channel. The ability to maintain cells underflow in the μBBB chip improves the barrier characteristics of BMECs with TEER values of 250 $\Omega.cm^2$ using the b.End3 cell line, ten-fold greater than static culture with these cells (Booth and Kim 2012). The permeability of the paracellular probe, dextran, was reduced in the μBBB system. However, the permeability values attained were still significantly higher than *in vivo*, suggesting further optimisation was required, but this could have been due to the choice of cell line. If a primary cell line was used here in the microfluidic device, these permeability values may have been closer to *in vivo*. The μBBB chip has been used to test the permeability of several CNS therapeutics, showing a decrease in permeability of all drugs compared to static culture (Booth and Kim 2014). Highlighting how flow-based culture systems may decrease the gap between *in vitro* and *in vivo* research of the BBB.

SyM-BBB model, created by Prabhakarpandian *et al.* (2013) has a different architecture to the earlier Booth and Kim μBBB model. The SyM-BBB chip has a broad central channel and a narrower outer channel separated by columns to form a semi-permeable barrier. The columns have a greater depth than the membrane used in other models but allow for cells to grow on all surfaces of the channel, to create a 3D vessel, through which flow can be simulated. RBE4 cells grown in these channels showed increased expression of tight junctional proteins (ZO-1 and claudin-1) as well as an increase in P-gp expression

compared with cells grown in Transwell (Prabhakarpandian *et al.* 2013). Additionally, the permeability of 5 kDa dextran across the SyM-BBB monolayer was 10-times less than the permeability in Transwells. The fluid capacity of this BBB chip is greater than the μBBB model. However, allows for improved coating of the device with collagen and fibronectin, to form a basement matrix and further support cell growth (Booth and Kim 2012). The SyM-BBB models have advantages over other microfluidic models in that it allows for microscopy of cells grown under flow, without destruction of the chip.

The refinement of 3D-printing technology has allowed for the creation and fabrication of more complex devices and templates for devices. Using this fabrication method has enabled the creation of microfluidic channels in a collagen hydrogel (Kim *et al.* 2015). By printing the channel structure as a series of aligned, cylindrical channels into a 3D frame, with a space between the inlet and outlet sides, for needles to be inserted which span the gap in the channel. Collagen matrix can be poured around these needles and jellified to form pores through the centre of the matrix. The needles can be removed to form a hollow lumen through the hydrogel into which endothelial cells may be seeded. The use of hydrogel matrices for modelling the BBB have several advantages over other microfluidic and static culture models. Firstly, the hydrogels support cell-growth and homeostasis for longer periods of time, meaning BMECs can be cultured in this way for weeks not days. Secondly, it is possible to introduce neuronal, astrocytic or pericytic cells into the matrix to create a neurovascular unit with all cell types in direct contact. Hydrogels have been used in this way in several over articles to create a 3-dimensional neurovascular unit within the matrix (Cho *et al.* 2015; Kohn *et al.* 2015). The combination of multiple cell types in this way allows for studies into the brain-tumour barrier and chemo-attractive drugs on cells within the matrix (Prabhakarpandian *et al.* 2015).

1.4 Cellular Trafficking

Owing to the highly restrictive nature of the BBB, it is widely accepted that for macromolecular and nanoparticulate therapeutics to be effective in treatment of CNS disorders some form of cellular trafficking must occur across BMECs. With the high density of capillaries throughout the brain, if a therapeutic can cross the BMECs it would be within almost direct contact with the target neuronal cells. Specifically, a therapeutic must undergo the process of transcytosis to gain access to the brain (see Figure 1.3). With respect to the BBB, transcytosis involves the endocytosis of the therapeutic at the luminal (blood) side of a BMEC. The sorting and transportation of the therapeutic through the endothelial cells to the basolateral membrane and its exocytosis into the brain parenchyma. Due to the high vascularization of the brain, a therapeutic released into the brain parenchyma is near the desired target site.

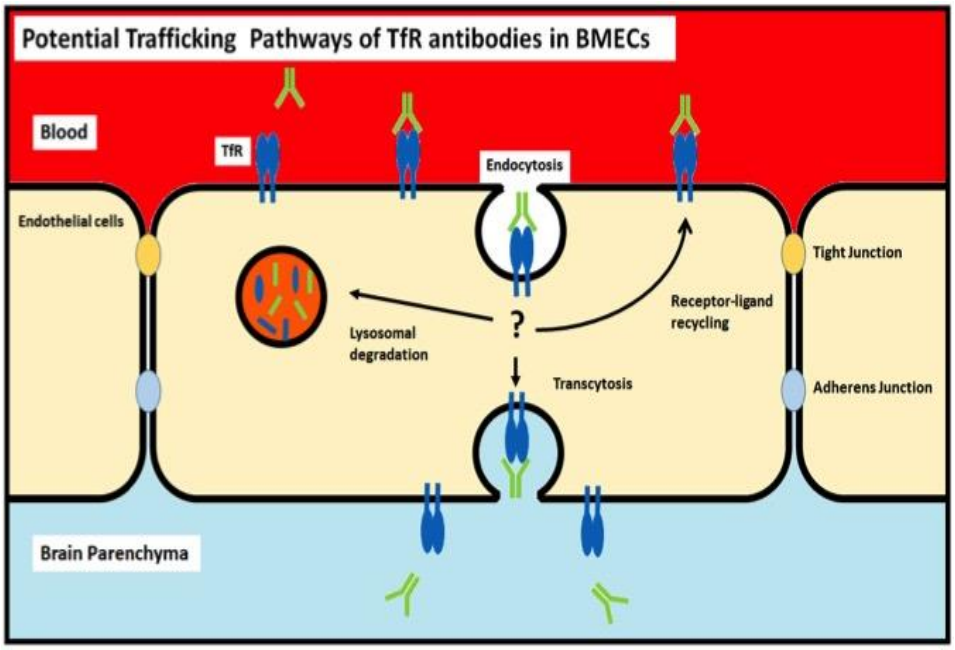

Figure 1.3: Simplification of transcytosis and cellular trafficking pathways
This is a schematic to show the potential trafficking routes of transferrin targeted antibodies. Following endocytosis at the luminal membrane, sorting within the endothelial cell can lead to: recycling back to the luminal membrane, lysosomal degradation (high affinity divalent antibodies), or transcytosis across the cells to the abluminal membrane.

1.4.1 Endocytosis

Endocytosis is the active process of uptake into a cell, involving the movement of cellular membranes and cellular components, to form structures which are capable of internalization of extracellular material. It is required for the normal homoeostasis of cells, with cargos including nutrients, plasma proteins, ligand bound to receptors. Pathogenic organisms are also able to enter cells by this process.

Endocytic events can be classified by the intracellular proteins associated with the vesicle formation. Clathrin-mediated endocytosis (CME) occurs at clathrin-coated pits. Here the clathrin triskelion assembles around adaptor proteins (AP) which link the cell surface receptors with the clathrin proteins. Briefly, the process involves: 1) initial invagination of the vesicle at the cell membrane (Henne *et al.* 2010). 2) Adaptor protein association with the intracellular domains of cell surface receptors (Stimpson *et al.* 2009). 3) Assembly of clathrin proteins onto the APs and the formation of the clathrin-coated pit (Saffarian *et al.* 2009). 4) Dynamin-mediated cleavage of the vesicle from the plasma membrane, to bring the vesicle entirely within the cell (van der Bliek *et al.* 1993). 5) Clathrin proteins dissociate from the vesicle surface to allow for interaction with intracellular compartments (Taylor *et al.* 2011). The vesicles formed by CME are typically between 100-200nm in size; due to the limitations of the clathrin network coating the vesicle. The process of CME is believed to occur in the majority of eukaryotic cell types as the predominant endocytic mechanism. The archetypal receptor that undergoes CME is the transferrin receptor, used by cells for the internalisation and recycling of the transferrin protein and the delivery of iron into the cells.

Partitioning of plasma membrane lipids, through non-enzymatic and non-protein-based processes, allows for the formation of "lipid rafts" which contain specific lipids. The main classification of these lipid rafts are those which contain the caveolin family of proteins

(Caveolin-1, -2 and -3). Numerous proteins associate with caveolin in these lipid rafts, including src, protein kinase C and actin. Caveolin-mediated endocytosis occurs at pits formed in lipid rafts of the plasma membrane (Figure 1.4). The formation of caveolin pits in endothelial cells is directly related to the uniformity and strength of flow across the luminal membrane of the cells (Rizzo *et al.* 2003). Caveolin-1 forms multimeric complexes at the cell membrane (14 – 16 monomers/complex) and in association with cavin form the curvature of the caveolae pits (Nabi 2009). Scission of the vesicle from the cell membrane is done by the dynamin protein, and once within the cytosol, fusion to other cellular trafficking compartments is through vesicle-associated membrane protein-2 (VAMP-2) and synaptosome-association protein (SNAP). Perhaps, the most advantageous feature of caveolin-mediated endocytosis is its ability to bypass the lysosomal compartment of cells. Caveolin-mediated endocytosis is therefore associated with several pathogenic organisms and toxins that need to avoid lysosomal degradation to elicit a cellular response, including cholera toxin B and Shiga toxin. However, both toxins also utilise other endocytic mechanisms to enter cells.

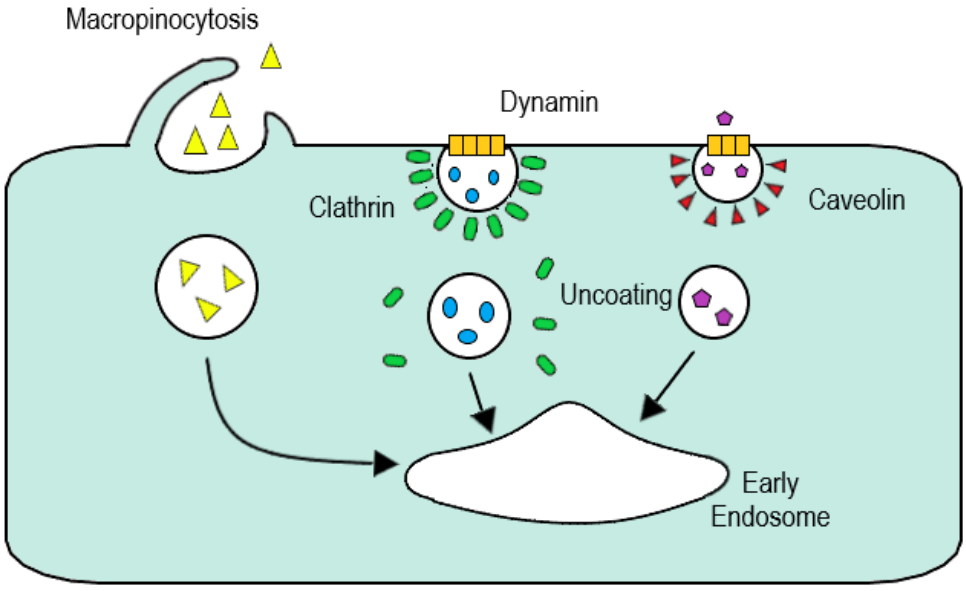

Figure 1.4: Endocytosis mechanisms
The above is a simplification of the endocytic mechanisms within eukaryotic cells. While other endocytic processes exist, these three: Macropinocytosis (yellow triangles), clathrin-mediated endocytosis (blue circles) and caveolin-mediated endocytosis (purple pentagons) are the main focus of this work. Adapted from Figure 1. Mayor and Pagano 2007.

In the nanoparticle delivery across biological barriers field, the ability of a trafficking pathway to avoid lysosomal degradation is an advantageous feature of a delivery system. If more of the cargo can cross the barrier, without being degraded, then the therapeutic effect will be higher at the target site (Oh *et al.* 2007).

Of the remaining endocytic pathways in eukaryotic cell biology, the most relevant to consider for BBB delivery would be macropinocytosis (fluid phase endocytosis). Macropinocytosis, involves the rearrangement of the actin cytoskeleton of cells, at the plasma membrane, to cause membrane ruffling (Lim and Gleeson 2011). In this process, molecules do not require contact with the cell membrane or surface receptors to be internalised. Instead, the ruffling of the plasma membrane traps extracellular fluid with the molecules in and internalised it into the cell. This method is believed to be the main route of entry into the CNS, for the plasma protein albumin, which has no known receptors on BMECs (Smith and Gumbleton 2006). The process of macropinocytosis can

be triggered by activation of the EGF receptor to induce increased membrane ruffling and formation of lamellipodia, some of which fold back on themselves and close (Kerr *et al.* 2006). This creates a vesicle with a non-uniform shape, typically larger than 200 nm in diameter that can be internalised (Racoonsin and Swanson 1993; Lim and Gleeson 2011). However, constitutive membrane turnover can also allow for macropinocytosis to take place.

Due to the non-specificity of macropinocytosis, it is a commonly exploited route of entry of pathogens (bacteria and viruses) (Mercer and Helenius 2008). With some bacteria able to induce membrane ruffling and gain access to host cells for survival and replication (Alpuche-Aranda *et al.* 1994). The endocytosis of the complex sugar molecule dextran is another example of macropinocytosis. Once within cells, as dextran does not have a molecular target, it initially distributes itself across all endocytic compartments (within 2 hours of uptake). However, if left for longer it will accumulate in lysosomal compartments, for degradation, as dextran cannot direct its distribution in the cell. As fluid is "turned-over" and sent for degradation, so dextran accumulates in the lysosomes (Lencer *et al.* 1990). This property of dextran makes it a highly useful tool in the analysis of cellular trafficking and compartment localisation of potential transcytosis-mediating ligands.

1.4.2 Exocytosis

For drug delivery to occur across the BMECs cargos that have been internalised into the endothelial cells at the lumen surface must undergo exocytosis at the basolateral membrane of cells. Exocytosis has been extensively characterised in neuronal cell models, looking at the release of neurotransmitters at synaptic junctions. The proteins involved in exocytosis are seen to be derived from a common ancestral predecessor, which evolve to the gain specificity for the required role. Proteins are required for docking

of a vesicle with the cell membrane, vesicle priming (preparation for release), a signal to trigger release and finally the fusion of vesicle and cell membrane.

The SNARE recognitition protein complex forms at the cell membrane for the docking of vesicles. Membrane-bound, syntaxin-1, associates with Munc18. Munc18 is necessary for the SNARE interactions, and if knocked out, causes complete attenuation of exocytosis from cells (Sudhof and Rothman 2009; Furgason *et al.* 2009). Ex-vivo studies of liposome fusion revealed how Munc18 selects the optimal structure of the R-SNARE complex for the zippering process (Shen *et al.* 2007; Xu *et al.* 2010). Recruitment of Munc18 by syntaxin-1 allows the complex to bind SNAP-25 (Fassshauer and Margittai 2004). SNAP-25 can associate with the N-terminal region of the forming complex and has the capability of recognising up to two complexes at a given time (Fassshauer and Margittai 2004). Fusion to two syntaxin-1 complexes prevents the activation of further membrane fusion processes. To complete the recognition complex for vesicular binding, the Munc13 protein associates to the complex. Through interaction with vesicular Rab proteins, (rab3 and rab27) the Munc13 facilitates vesicular priming at the membrane.

On a vesicle surface are the proteins synaptotagmin and synaptobrevin. When localised in the recognition zone of the SNARE complex, helical domains of synaptobrevin associated to syntaxin-1, forming a “groove” on the surface of the complex. Into this space, complexins can associate, to mediate the unzipping of the complex at the point of membrane fusion. However, this unzippering is dependent on completion of the complex with vesicular synaptotagmin. The synaptotagmin protein is modulated by calcium, with the ability to bind two molecules of ionic calcium. Calcium binding induces a conformational change in synaptotagmin and triggers the release of complexins and the unzipping of the complex (Vrljic *et al.* 2010). With the conformation of the proteins

before unzipping, the process of unzipping causes membrane fusion and exocytosis of vesicular content from the cell.

The process of cargo exocytosis is required for transcytosis to take place. Without an ability to under exocytosis from the barrier cell type, a drug delivery system would be trapped at the barrier, unable to reach the target site.

1.5 Nanoparticle Targeting Strategies for CNS delivery

Due to the restrictive nature of the BBB and the efflux transporters present, a small proportion of all low molecule drugs are able to reach the CNS to have a therapeutic effect. The ability of large molecules, such as proteins and DNA therapeutics to cross BMECs is further restricted, due to their size, unless targeted in some way. Several methods have been developed, which fall into two categories: disruptive (non-specific) and targeted. An invasive approach would involve direct injection of the therapeutic into the brain, either into the ventricular system of the brain or intracerebral injection (Bobo *et al.* 1994; Haley and McCormick 1957). Other disruptive methods would involve temporary disruption of the BBB, using osmotic modulators (bradykinin, mannitol) (Siegal *et al.* 2000), or ultrasound disruption (Sheikov *et al.* 2006). Although these methods allow for doses of drugs to be delivered directly into the CNS, invasive methods can involve complex surgical and are non-targeted methods, potentially causing adverse effects. To prevent this from occurring and reduce the risk, brain targeting of therapeutics, either in macromolecule complexes or on nanoparticles aims to improve safety and efficacy of brain delivery.

The targeted, selective approach to delivery across the BBB can be through adsorptive mediated transport (AMT) or receptor-mediated transcytosis (RMT). Both of these will involve trafficking within the vesicle pathway of cells. In AMT, the surface charge of a nanoparticle allows it to interact with the cell membrane of the BMECs, positively

charged (cationic) particles can associate with anionic domains of the luminal membrane of cells (Hervé *et al.* 2008). Once internalised within the endothelial cells the vesicular trafficking will allow a small fraction of the internalised particles to reach the abluminal membrane and the CNS. Due to the non-targeted nature of this delivery mechanism, accumulation in the CNS by intravenous dosing is limited. However, AMT delivery has been demonstrated to be effective through intranasal delivery (Thorne *et al.* 2004).

Receptor-mediated trafficking processes work on the principle that a targeting ligand on the surface of the particle can dock onto its receptor on the luminal side of the BMECs. The receptor binding will trigger the process of endocytosis, to form a vesicle within the endothelial cell containing the receptor-ligand-nanoparticle complex. Internalised particles are then able to undergo trafficking across the BMECs to the abluminal cell membrane. Here, vesicles containing the nanoparticles can fuse with the membrane and exocytose the contents into the CNS (Tuma and Hubbard 2003).

Target receptors for RMT for CNS delivery include: transferrin receptor, insulin receptor, low-density lipoprotein (LDL) receptor, nicotinic acetylcholine receptor (nAchR), lamin receptor, leptin receptor, tetanus receptor (Fang *et al.* 2017). This is not an exhaustive list, however, it represents the most commonly targeted receptors for CNS delivery. A summary of the receptors and targeting ligands can be seen in Table 1.1. Targeting ligands themselves may be native ligands for the receptors (i.e. transferrin for the transferrin receptor) or antibodies and peptides, designed to bind to an allosteric domain of the receptor that will not be competed by native ligands, present in the blood plasma.

Table 1.1: Summary of receptor targeted BBB delivery strategies				
Receptor	**Ligand**	**Delivery System**	**Model System**	**Reference**
Transferrin Receptor	Transferrin	Albumin nanoparticles, dendrimers	Albino rats, b.End3, BALB/c mice, ICR (CD-1) mice	(Mishra *et al.* 2006; Somani *et al.* 2014; Ulbrich *et al.* 2009)
	OX26	Albumin nanoparticles, pegylated liposomes, radiolabelled OX26, chitosan-peg particles	ICR (CD-1) mice, BMVECs/C6, mice	(Ulbrich *et al.* 2009; H. W. A. J. Lee *et al.* 2000; Yue *et al.* 2014; Aktaş *et al.* 2005)
	8D3	Gold Nanoparticles, fusion protein	Mice	(Paris-Robidas *et al.* 2011; Zhou *et al.* 2010)
Insulin Receptor	mAb83-14	Radiolabelled, SLNPs	Rhesus Monkey, hCMEC/D3	(Pardridge *et al.* 1995; Kuo and Ko 2013)
	HIRMAb	Fusion proteins,	Rhesus Monkey	(Boado, Hui, Lu and Pardridge 2010; Boado, Hui, Lu, Zhou, *et al.* 2010; Boado *et al.* 2008)
	29B4	Albumin Nanoparticles	ICR (CD-1) mice	(Ulbrich *et al.* 2011)
Lactoferrin Receptor		Polyersomes, DNA loaded nanoparticles	b.End3, BCECs	(Gao *et al.* 2010; Huang *et al.* 2009)
LDL Receptor	Melanotransferrin	Fusion protein, SLNP	C6 mice; ZR-75-1 mammary tumour mice	(Karkan *et al.* 2008; Kuo and Wang 2015)
	Angiopep-2	Polymeric micelle,	Immunosuppressed mice, glioma model mice, U87 Glioma cells	(Shao *et al.* 2012; Xin *et al.* 2011)
Ganglioside GT1b	Tet peptide	Phage display	HEK293, PC12	(Liu *et al.* 2005)

Diphtheria Toxin Receptor	CRM197	Polybutylcyanoacrylate nanoparticles, liposomes,	hCMEC/D3, HBMEC, HA, SK-N-MC cells	(Yung Chih Kuo and Chung 2012; Kuo and Liu 2014; Wang *et al.* 2010)
Laminin Receptor	AAV9	Protein cargo	C57Bl/6 mice	(Xue *et al.* 2010)
Acetylcholine Receptor	RVG peptide	Dendrimers, Exosomes, DNA complexes	Neuro 2A cells, mice	(Kumar *et al.* 2007; Alvarez-Erviti *et al.* 2011; Liu *et al.* 2009)
Opioid Receptors	G7 peptide	PLGA nanoparticles	C57BL/6 mice, rat model	(Salvalaio *et al.* 2016; Tosi *et al.* 2011)

1.5.1 Transferrin Receptor

Possibly the most studied receptor for RMT across BMECs, the transferrin receptor (TfR) is known to be expressed at high levels in BMEC, to facilitate the delivery of iron, bound to transferrin (the endogenous ligand) from the blood plasma into the brain parenchyma. The TfR itself is a dimeric transmembrane protein, with two sub-units being joined by covalent, disulphide bonds between the chains. Each sub-unit of the TfR is capable of binding one molecule of the transferrin protein (Moos and Morgan 1998). Transferrin is a globular protein, with two high affinity, iron-binding domains. The binding of iron to transferrin changes the structure of the transferrin protein and increases its affinity for the TfR (Dautry-Varsat *et al.* 1983). This change in affinity with addition or loss of iron from transferrin is vital for the intracellular delivery of iron once within the endosomal sorting system of cells.

Despite the quantity of research on the TfR as a candidate to undergo RMT, questions still exist about the ability of a TfR ligand to undergo transcytosis. Research has shown that while the iron is shuttled across BMECs from the vasculature, the amount of transferrin within the CNS is lower than would be expected. Regardless of these concerns,

several studies have used transferrin as a targeting ligand for nanoparticles (Mishra *et al.* 2006) and antibodies (Shin *et al.* 1995) and shown to strongly increase delivery of the nanoparticles. The delivery of the antiviral agent, azidothymidine, into rat brains using Tf-targeted albumin nanoparticles produced a 2.26-fold increase in CNS accumulation with targeting versus untargeted control particles (Mishra *et al.* 2006).

It should be noted, that as with other endogenous ligands that circulate within the plasma, the use of transferrin as a targeting ligand is limited. The homeostatic concentration of transferrin in circulation is thought to be 25 μM, so any targeting ligand must compete with this transferrin for the receptor (Qian *et al.* 2002). More successful tools for targeting the TfR include antibodies, raised against an allosteric binding site on the extracellular domain of the TfR. In this approach the antibody binding is unaffected by circulating ligand and so competition of the therapeutic is avoided. Several anti-TfR antibodies have been developed for use in pre-clinical models; these include the OX26 (anti-rat), 8D3 (anti-mouse), 128.1 Mab (anti-human/monkey). Of these antibodies, the characterisation of OX26 is the most complete. Radio-labelled forms of the OX26 antibody have been shown to accumulate in the CNS and cargo targeted with OX26 has demonstrated enhanced CNS delivery (H. J. Lee *et al.* 2000). Coupling of the OX26 to NGF improved the prognosis of Huntington's Disease model rats. Reducing neurodegeneration and stabilising the condition in the treated animals. OX26 has successfully delivered plasmid DNA to the CNS, in pegylated, targeted liposomes (Yue *et al.* 2014). Liposome targeting with OX26 also allowed delivery of small oligonucleotides, peptides and low molecular weight therapeutics, all of which demonstrated increased efficacy with targeting compared to untargeted.

In mice, the 8D3 antibody has been used for over a decade as a targeted delivery strategy against the murine TfR (Kissel *et al.* 1998). As with the OX26 antibody, a radiolabelled

8D3 antibody was seen to accumulate in the CNS. However, examination of electron micrographs, of gold-targeted nanoparticles have shown this appears to be localised to the cerebral vascular endothelial cells, and parenchyma accumulation of these particles was limited (Paris-Robidas *et al.* 2011; Niewoehner *et al.* 2014). More successfully, however, 8D3 was used to deliver plasmid DNA to the CNS, confirmed by gene expression in neuronal cells. Although the same study also found the delivery of the plasmid to other TfR-rich tissue, including the liver and spleen. These antibodies have not only been used for a therapeutic application. Conjugation of radiolabelled Aβ-peptide to the 8D3 antibody has provided an imaging tool for the visualisation of amyloid plaques within Alzheimer's Disease model mice (Lee *et al.* 2002).

Despite the time invested into these antibodies and the measurable improvements in therapeutic outcome, or genetic alteration within neuronal cells, these antibodies have failed to reach clinical trials. This is mainly due to the lack of selectivity for the CNS, owing to the global expression of the transferrin receptor in nearly every tissue type of the body. Toxicity of the drug delivery systems at peripheral sites has limited their progression into the clinic. Additionally, neither the 8D3 antibody or OX26 have been demonstrated to recognise the same epitope on the human form of the TfR and the use of non-human-derived immunoglobulins, in the clinic has been shown to trigger severe immune reactions to the antibodies. Attempts to overcome this have been made with insulin receptor antibody and this will be discussed in the coming section.

1.5.2 Insulin Receptor

In vivo, the insulin receptor (IR) is a four domain, glycosylated receptor, which in BMECs, is able to transport insulin across the BBB into the brain parenchyma from the blood (Pardridge *et al.* 1985). However, insulin itself is not used as a targeting ligand, due to its short plasma half-life and competition with native insulin in circulation (Matthews

et al. 1985). Instead several antibodies have been synthesised, against different epitopes of the murine and human insulin receptor (mAb83-14, mAB83-7 and mAB29B4) (Ulbrich *et al.* 2011). The mAB83-14 has shown high delivery into the brain with 3.8% injected dose (ID) per 100g brain (Pardridge *et al.* 1995). Control IgG showed no brain association. mAB83-14 has been shown to be able to enhance delivery of anti-nociceptive drugs in solid-lipid nanoparticles (SLNP) and polymeric nanoparticles in Rhesus monkeys and across hCMEC/D3 cell monolayers (Kuo and Ko 2013). Attempts to use mAB83-14 in humans, however resulted in immune responses to the antibody. To overcome this, a humanized form of the antibody was developed, by attachment of the variable domain to the human IgG Fc region to form the HIRMAb antibody (Boado *et al.* 2007). The HIRMAb has been used in fusion constructs with therapeutics for genetic or metabolic conditions, such as mucopolysaccharidosis type I (Boado *et al.* 2008), or as a vector to deliver enzymes to compensate for lack of expression in patients. These fusion constructs have shown an ability to deliver to the CNS in Rhesus monkeys and to restore normal functioning in cell line models of the conditions. The success of the fusion protein method for delivery across the BBB has led to its application with other biopharmaceutical macromolecules, including erythropoietin (EPO), tumour necrosis factor receptor (TNFR) and glial-derived neurotrophic factor (Boado, Hui, Lu, Zhou, *et al.* 2010; Boado, Hui, Lu and Pardridge 2010).

1.5.3 Lactoferrin Receptor

Lactoferrin is a glycoprotein with similar properties to transferrin; it is able to bind two molecules of iron in plasma for transport into multiple cell types, including BMECs. Lactoferrin itself can recognise and bind to both the lactoferrin receptor (LfR) and LRP protein. Studies have shown that lactoferrin targeting of nanoparticles increases the CNS accumulation to a greater extent than TfR ligands (transferrin and OX26 antibody) (Ji *et*

al. 2006). However, other studies have shown the opposite effect on particle delivery with Tf and OX26 targeted polymeric particles and liposomes showing increased delivery potential compared to lactoferrin-targeted equivalents (Gao *et al.* 2010). Dendrimers and solid lipid nanoparticles (SLNPs) showed increased delivery with lactoferrin targeting (Huang *et al.* 2009). These results would suggest that both thetargeting ligand and the nature of the nanoparticle are critical for efficient brain delivery.

1.5.4 LDL Receptor

The most extensively utilised ligands of the LDL receptor and its related proteins (LRP1 and LRP2) are the angiopep-2 and melanotransferrin. Radiolabelled melanotransferrin, injected into mice showed an almost 6-fold increase in volume of distribution (V_D) to the brain compared with radiolabelled transferrin (Demeule *et al.* 2002). Melanotransferrin (MTF) has such been considered and used as a targeting ligand for CNS delivery. Fusion with adriamycin (ADR) increased the uptake into the CNS of the drug, compared to albumin and lactoferrin fusion constructs (Karkan *et al.* 2008). MTF-ADR constructs have successfully been used to treat mouse glioma models. The use of MTF as a targeting ligand for particle delivery to the CNS has also been demonstrated with SLNP for tumour therapy and the delivery of the adenovirus gene therapy vector into the CNS (Kuo and Wang 2015).

The angiopep-2 peptide recognises and binds to the LRP1 receptor on BMECs and has demonstrated an ability to cause transcytosis of cargo into the CNS. Modifications have been made to the angiopep-2 peptide including the synthesis of the peptide with “unnatural” D-amino acids (Xin *et al.* 2011). This has improved the serum stability while maintaining the capability of delivery to the brain. Angiopep-2 has been used to functionalise multiple types of nanoparticles, including: polymeric particles, gold nanoparticles and carbon nanotubes. Polymeric nanoparticles, decorated with the

angiopep-2 peptide and containing amphotericin (antibiotic for the treatment of meningitis), have been able to deliver the therapeutic into the CNS with greater efficacy than the antibiotic alone or untargeted control particles (Shao *et al.* 2012). Other therapeutics which showed increased CNS delivery when incorporated into angiopep-2 targeted nanoparticles include the doxorubicin, paclitaxel and its derivative ANG1005 (Thomas *et al.* 2009).

1.5.5 Tetanus Receptor

Tetanus virus-derived peptide (Tet) is thought to undergo retrograde axonal transport along neurones to access the CNS. When expressed by viruses the Tet peptide is formed of two sub-chains: a light (neurotoxic) and heavy (non-toxic) chains. The non-toxic form is known to bind to ganglioside GT1b with high affinity on neurones (Shapiro *et al.* 1997). This target has been used in phage display to generate a small peptide targeting ligand (tet1) to be identified, which has similar binding kinetics to the heavy chain of the Tet peptide to ganglioside GT1b (Shapiro *et al.* 1997; Liu *et al.* 2005). The tetanus toxin-derived vectors offer an alternative delivery route to the CNS. Rather than transport across the BBB, these vectors allow transport through neurones to the brain parenchyma. This route of brain delivery is one utilised by other viruses that infect the CNS and so may offer an enhanced delivery over "traditional" BBB targeting methods (Fang *et al.* 2017).

1.5.6 Diphtheria Toxin Receptor

The diphtheria toxin receptor (DTR) or the heparin-binding epidermal growth factor (HBEGF) is known to be expressed on the cell surface of BBB endothelial cells (Gaillard *et al.* 2005). HBEGF itself has no native ligands, as it is a precursor to the final receptor. However, it can bind to the non-toxic mutant of the diphtheria toxin CRM197. *In vivo* experiments on PLGA targeted with CRM197 demonstrate accumulation into CNS cells with time (Wang *et al.* 2010; Kuo and Liu 2014). Low diameter particles decorated with

CRM197 and containing zidovudine increase the permeability of zidovudine across *in vitro* BBB models (Y.C. Kuo and Chung 2012).

1.5.7 Laminin Receptor

Extra-cellular domains of the Adeno-Associated Viruses (AAVs) have multiple forms, each of which can bind to a different receptor subtype. AAV-9 can interact with the laminin receptor present in BMECs (Akache *et al.* 2006). This targeting method has been used to deliver erythropoietin gene into a Parkinson disease mouse model. These studies confirmed the gene was expressed within the CNS and the EPO had a therapeutic effect within the mouse model (Xue *et al.* 2010).

1.5.8 Acetylcholine Receptors - RVG

Virus protein-derived peptides have shown some success as potential targeting ligands for CNS delivery. One such peptide is derived from the rabies virus glycoprotein (RVG) and is believed to interact with the alpha 7 nicotinic acetylcholine receptor (α7nAchR). The RVG peptide itself is a 29-amino acid peptide, with a region that of highly conserved sequence with loop neurotoxins, including α-bungarotoxin. Indeed, early work with RVG peptide was to test its ability to compete the binding of neurotoxins for the α7nAchR (Lentz *et al.* 1987; Lentz 1982; Lentz TL 1990; Lentz *et al.* 1986). The abundance of α7nAchR within the CNS and their potential expression in the microvasculature of the brain leading to the increase in brain delivery of the cargo (Abbruscato *et al.* 2002). Some evidence has also arisen to suggest a potential alternate receptor for the RVG peptide. There is some thought that the GABA receptors may also provide a binding site for the RVG peptide as the co-incubation of RVG-targeted dendrimers with GABA decreased uptake into neuronal SH-SY5Y cell (Liu *et al.* 2009). This evidence is supported by work which showed the α-bungarotoxin is able to act on GABA-A receptor (Hannan *et al.* 2015). Further study of the interaction of the whole glycoprotein and the whole virus

reveals two further receptors, NCAM-1 and p75NTR (Thoulouze *et al.* 1998; Gluska *et al.* 2014). The RVG peptide was first shown to have potential for BBB targeting when Kumar et al showed it was able to enhance brain accumulation of siRNA polyplexes (Kumar *et al.* 2007). Silencing of GFP expression in transgenic mice was observed in the brain, with limited silencing effects observed in the liver and spleen. Further work with RVG targeted exosomes again showed the peptide increased brain accumulation of the exosomes and siRNA encapsulated within them had a silencing effect on BACE-1 within the brains of mice (Alvarez-Erviti *et al.* 2011). Overall, the evidence for the use of the RVG peptide as a brain targeting ligand appears to show potential. However, the uncertainty over the target receptor would present a concern.

1.5.9 TAT Peptide

A second, viral-derived peptide, derived from the Human Immunodeficiency Virus (HIV), the TAT-peptide is a cell-penetrating peptide (CPP), that will globally increase cell uptake and tissue distribution. Thus, allowing for an increase in tissue penetration of a drug delivery system into the brain. The TAT peptide has a cationic charge to facilitate cell membrane interactions and internalization. The functionalization of quantum dots, and biologically active proteins with the TAT peptide all showed increases in the accumulation within the CNS (Santra *et al.* 2005; Schwarze *et al.* 1999). However, *in vitro* work to support these findings has been less conclusive, with the TAT peptide failing to enhance the permeability of GFP-TAT conjugates across endothelial monolayers (Georgieva *et al.* 2011).

1.5.10 G7 peptide

The g7 peptide is modified from the MMP-2200 opioid, an agonist of the δ- and μ-opioid receptors. The modifications when forming the g7 peptide reduce the nociceptive effects on opioid receptors (Tosi *et al.* 2011). The g7 peptide has been shown to increase the

delivery of PLGA nanoparticles and encapsulated fluorescent dyes to the brain parenchyma (Tosi *et al.* 2011; Tosi *et al.* 2013), with a study using rhodamine-123 finding 15% of total animal fluorescence located in the brains of injected animals (Vilella *et al.* 2014). G7-targeted particles have also been shown as a potential vector for the delivery of treatments for lysosomal storage disorders of the CNS. Particles loaded with corrective enzymes were able to restore lysosomal functionality in *in vivo* models of disease (Salvalaio *et al.* 2016).

1.6 Thesis Goals

Having looked at the literature of cellular trafficking methodologies concerning BMECs, there is a lack of clarity as to whether a probe can undergo both endocytosis into the endothelial cell and subsequent efflux from the cell. In permeability assays, BMEC models are subject to paracellular leakage, contributing to higher permeability levels of probes. The main goals of this thesis were to around the investigate the capability of the targeting ligands to undergo the process of transcytosis in an *in vitro* BMEC model. The development of a transcytosis index was pursued. This combined permeability assays with sub-cellular microscopy and pulse-chase flow cytometry, to allow for a multifaceted evaluation ligand trafficking in BMECs. Looking at, barrier permeability of the ligand, alongside the ability of it to undergo some form of uptake and efflux process. This was initially developed using a receptor-targeted ligand (transferrin) and a fluid-phase uptake marker (dextran) to test the ability of the methods to distinguish between the two trafficking routes.

Using the transcytosis index, the particularly the pulse-chase assay as the primary method, further trafficking ligands were tested in this manner to evaluate their ability to bind to BMECs and undergo cellular trafficking. This was done with antibodies against the transferrin receptor of high affinity (8D3) and a low-affinity variant, supplied by Abbvie

(8D3-4). This was with the aim to assess the impact of ligand affinity on the efflux potential of the targeting ligand from cells. With consideration being given to the work of Roche and Genentech with decreased affinity targeting ligands enhancing brain delivery of therapeutic cargos.

Following the work with transferrin receptor ligands, the viral derived rabies virus glycoprotein peptide (RVG) was examined as a candidate brain targeting ligand. Due to concerns over receptor specificity and the ability of the peptide to be taken up by the COMPACT consortium work was done to characterise RVG uptake in BMECs. The RVG peptide was also tested in the pulse-chase assay to confirm it is a probe that can undergo active efflux from BMECs and assess the subcellular distribution of the peptide following the assay.

In the final section of this thesis, work was undertaken to explore the use of complex microscopy techniques in the understanding of cellular trafficking at the basolateral cell membrane. This included the use of total internal reflection fluorescence microscopy (TIRF) to image targeting ligands at the basolateral membrane of BMECs. The associated analysis of the collected microscopy videos, to classify trafficking events into putative exocytic events and other trafficking events taking place within the cells. To explore the trafficking of receptors within BMECs further, the photoswitchable protein PSmOrange was conjugated to the transferrin receptor. In this work, a formula to calculate the distribution of the fluorescent states of a photoswitchable protein was derived. And initial studies into the distribution of the receptor at the basolateral cell membrane were attempted. With the overall goal to develop a technique which could be used examine the dynamics of receptor localisation in the basolateral region of barrier cell types.

1.7 Thesis Aims

1. Establish an *in vitro* model for cellular trafficking that can be used to differentiate between brain targeting ligands.
2. Characterise the uptake and intracellular trafficking of transferrin receptor antibodies, with differing affinities in brain microvascular endothelial cells in vitro.
3. Characterise the uptake and intracellular trafficking of the RVG peptide in brain microvascular endothelial cells *in vitro*.
4. Identify the target receptor, mediating endocytosis of the RVG peptide into BMECs using multiple methodologies.
5. Use TIRF microscopy to examine basolateral membrane trafficking of the transferrin receptor and its ligands.

Chapter 2: The Role of the Transferrin Receptor in Brain Microvascular Endothelial Cells and its use as a drug delivery target

2.1 Introduction

It is well established that transferrin is the molecular shuttle to aid in the uptake and transport of iron across highly restrictive biological barriers, as well as into cells for physiological functioning. Transferrin itself is an 80kDa, globular protein which can bind ferric iron (Fe^{3+}) with an affinity of 10^{-24}M and fully saturated can bind two molecules of Fe^{3+}, one to each lobe of the protein. In the di-ferric (holo) conformation transferrin binds more strongly to the transferrin receptor (TfR), at plasma pH, than mono-ferric or iron-free (apo) transferrin. This difference in affinity between holo- and apo-transferrin is essential in the trafficking and recycling dynamics of transferrin and the TfR (Dautry-Varsat *et al.* 1983). Despite the main trafficking route pathway of transferrin being recycling, there is some evidence of alternative trafficking of transferrin through cells.

The transferrin receptor is membrane spanning, dimeric glycoprotein, each subunit is 90kDa and capable of binding one molecule of transferrin. Uptake of the TfR is constitutive and controlled by clathrin-mediated endocytosis (CME). Briefly, adaptor proteins associate with the intracellular domain of the receptor and recruit clathrin heavy and light chains to the receptor, allowing the formation of the clathrin triskelia and clathrin-coated pits (CCP). There are several adaptor protein (AP) complexes that are utilised in CME, AP1-3, with the main complex being AP2. The AP2 complex is formed of four subunits, α-, β-, μ- and σ-units, each with its role in the CME process. To form fully internalised vesicles from the CCPs, dynamin, a helical GTPase, associates with the neck of the CCP and cleaves the vesicle from the membrane. The removal of clathrin,

from the vesicles, once internalised, is an ATP-dependent process, using heat shock protein 70 and auxilin. The uncoating allows trafficking of the vesicles through association to various proteins within the cell.

When in the late endosome, the pH surrounding the TfR-Tf complex is approximately 5.5, resulting in the loss of Fe^{3+} from the transferrin molecule (Dautry-Varsat *et al.* 1983). This low pH environment allows the now apo-transferrin to remain bound to the TfR while trafficked back to the luminal membrane of the cells (Dautry-Varsat *et al.* 1983).

The TfR is highly expressed in brain microvascular endothelial cells (BMECs) relative to most other organs' microvasculature, with an exception being the hepatic vasculature. Studies into the number of TfRs present in primary bovine BMECs estimated 100,000 receptors per cell (Raub and Newton 1991). In the immortalised rat cell-line, RBE-4, TfR expression was approximated at 70,000 receptors per cell (Huwyler *et al.* 1999). In normal physiological states, approximately 10-20% of TfRs are localised at the cell membrane; the remaining are localised in intracellular vesicles due to constitutive recycling of the receptor. The levels of TfR expression in cell culture appear to depend on the metabolic demand of the culture, and expression decreases when cells are grown beyond the point of confluence (Tripothi *et al.* 1992). This increase in TfR expression relative to metabolic demand can be seen in tumour cells where the continual cell division in tumour growth places a high metabolic demand on the cells and increases their iron demand (Huebers and Finch 1987).

In BMECs transferrin and the transferrin receptor are believed to be required for the iron trafficking into the brain parenchyma for neuronal and glial metabolism. However, it is unclear as to the precise mechanism by which iron transcytosis occurs in BMECs. Experiments using perfused rat brains to assess uptake and loss of radiolabelled transferrin revealed retention of transferrin by the microvascular endothelium (Fishman

et al. 1987). Of the transferrin lost from the cells in, this study, it appears 20% is recycled back into the perfusate, while 80% of the radiation is detected in the brain supernatant, suggesting a transcytosis process has occurred. Roberts et al. (1993) performed morphological studies with transferrin conjugated to horse-radish peroxidase (Tf-hrp) and used electron microscopy to assess the localisation within the BMECs. There was no apparent evidence of transferrin at the abluminal membrane at any stage; however, the presence of Tf-hrp in recycling vesicles was seen in the final time point of the experiment (Roberts *et al.* 1993).

The examinations of rat brain sections, after perfusion with anti-TfR conjugated colloid gold, confirmed the localisation of the TfR to all areas of the brain vasculature (Bickel *et al.* 1994). Immunofluorescence microscopy of brain capillaries shows TfR expressed on both the apical and basolateral endothelial cell membranes (Huwyler and Pardridge 1998). More recently, studies looking at the co-localisation of anti-TfR antibodies with markers for the apical and basolateral membranes revealed high localisation with the apical marker (Paris-Robidas *et al.* 2011; Niewoehner *et al.* 2014). These studies also saw slight co-localisation of the antibody with type IV collagen also confirmed trafficking to the basolateral membrane, across the brain microvascular endothelium.

2.1.1 Antibody targeting of the TfR

Several antibodies against the transferrin receptor have been generated to examine the trafficking of the TfR and the ability to enhance the uptake of therapeutics into the brain. The OX-26 and 8D3 antibodies are both monoclonal antibodies that bind to rat and mouse TfR respectively. These antibodies bind with high affinity to allosteric sites on the TfR and do not disrupt transferrin binding. The 8D3 has a Kd of 2.3nM (Boado *et al.* 2009). Both antibodies have been shown to associate to BMEC cells *in vivo* and *in vitro* and have shown to gain entry to the brain parenchyma (H. W. A. J. Lee *et al.* 2000; Bickel *et al.*

1994). A chimeric form of the 8D3 antibody has been generated by introducing the mouse IgG1 heavy chain and kappa regions into the antibody to improve fusion protein constructs for studies in mice (Boado *et al.* 2009). The chimeric antibody was shown to have the same binding and bio-distribution properties as the wild-type 8D3 antibody. Further modification of the chimeric 8D3 antibody has been performed by Sanofi, as part of the COMPACT consortium, to reduce the formation of cross-linking between antibodies when labelling nanoparticles (unpublished work).

The RI7 antibody is another high-affinity antibody, which has been used to target the TfR in mice. However, the 8D3 antibody has superseded RI7 for targeting mouse TfR. For assessment in human cell lines and monkey animal models, the monoclonal antibody 128.1 has been used (Walus *et al.* 1996). Although this antibody was primarily designed for use in tumour targeting therapies (Ng *et al.* 2002), it has also been assessed with relation to BBB targeting (Sade *et al.* 2014; Walus *et al.* 1996).

Antibodies against the transferrin receptor have been shown to increase the brain association of a targeted drug delivery systems (DDS) compared to control particles. However, electron microscopy studies have shown that while TfR-targeted gold nanoparticles accumulate within BMECs, relatively fewer nanoparticles are actually observed within the brain parenchyma (Cabezon *et al.* 2015; Wiley *et al.* 2013). This was exemplified by electron microscopy of brain slices, at post-dosing time points, to assay the distribution of the antibody targeted particles within the BMECs (Cabezon *et al.* 2015). Using techniques in this manner confirms that the TfR-targeted particles have limited penetration to the brain parenchyma.

2.1.2 Genentech and Roche anti-transferrin receptor antibody studies

Recent studies in Genentech using a bi-specific antibody, with both anti-TfR and anti-BACE targeted variable regions (see Figure 2.1 and 2.2 below) showed increased brain

penetration than a previous high specific anti-TfR antibodies (Yu *et al.* 2011; Couch *et al.* 2013). The bispecific construct has a lower affinity for the TfR than a standard anti-TfR IgG (Yu *et al.* 2011). The constructs created by Genentech have been tested both *in vitro* and *in vivo* and revealed that high-affinity anti-TfR antibodies appear to become "trapped" within lysosomes of cells as the exposure time increases, while the lower affinity antibody does not remain in the cells for longer than necessary. This accumulation is thought to result from the inability of the high-affinity antibody to dissociate from the transferrin receptor once bound, and therefore continual association with the receptor. Time point analysis of the TfR expression following exposure to both constructs sees a decrease in TfR protein with the high-affinity antibody variants, while the lower affinity antibodies do not alter the levels of TfR protein within the cells (Couch *et al.* 2013). Further studies, changing the affinity of the bi-specific construct to TfR revealed that there appears to be an optimal affinity range for the receptor where delivery is enhanced. If the antibody affinity is too low, then maximal binding and uptake into the brain cannot occur at therapeutic doses, and the clearance of the antibody from plasma is sub-optimal for safe dosing strategies (Yu *et al.* 2014).

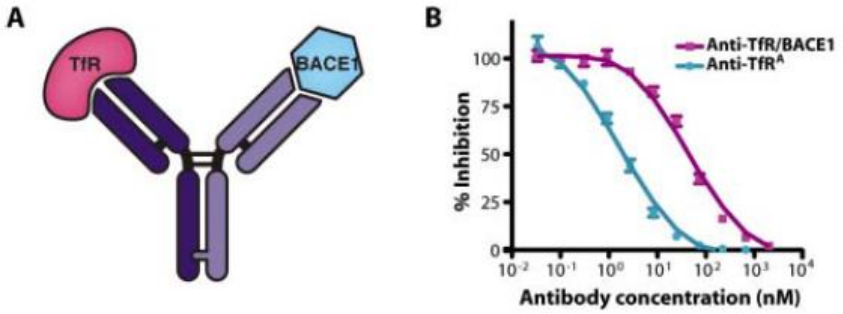

Figure 2.1: Genentech Bispecific, TfR targeted antibody construct
Taken from Figure 5. Yu et al (2011), it shows the structure of the bispecific antibody created by Genentech, with the dark purple arm targeting the TfR and the light purple arm targeting BACE-1 protein for therapeutic effect. Graph B shows the effect on affinity for the TfR with the bispecific antibody (purple) compared to a high affinity monospecific anti-TfR antibody.

These studies have been performed in several test animal species, including rodents and monkeys. Thus far in all species the moderate affinity, bi-specific antibody appears to be the most effective and safest construct for brain delivery.

Roche is also studying the effect of lower affinity constructs on enhancing brain delivery. This has been done using a payload of the anti-BACE-1 antibody mAb31, conjugated to Fab fragments specific to the TfR (Niewoehner *et al.* 2014). These constructs are formed of either one or two Fab fragments and showed that the valency altered the TfR affinity as well as the trafficking that was observed *in vitro* and *in vivo*. The lower affinity mono-valent construct had enhanced brain delivery of the payload, did not alter TfR expression within BMECs in culture and had a lower retention time in the BMECs *in vivo* while the di-valent construct appeared within the endothelium throughout their studies (Niewoehner *et al.* 2014). The effect of the avidity of a targeted construct to TfRs on the BBB has also been reported with relation to transferrin-targeted liposomes, the number of transferrin molecules associated to the surface of the liposomes appeared to alter the penetration into the brain (Wiley *et al.* 2013).

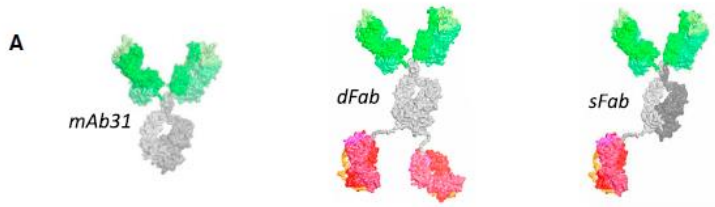

Figure 2.2: Roche mono- and divalent, TfR targeted antibody construct
Taken from Figure 1. Niewoehner et al (2014), The above figure shows the structure of the antibody constructs used in the Roche research. The therapeutic antibody (green and grey) is coupled to either one (sFab) or two (dFab) transferrin receptor targeting domains.

Overall, these studies from Roche and Genentech have shed some light on the mystery of transferrin receptor trafficking at the BBB and factors that alter it. The studies suggest

three potential pathways for receptor trafficking that are dependent on both the affinity for the receptor and the avidity of the targeting.

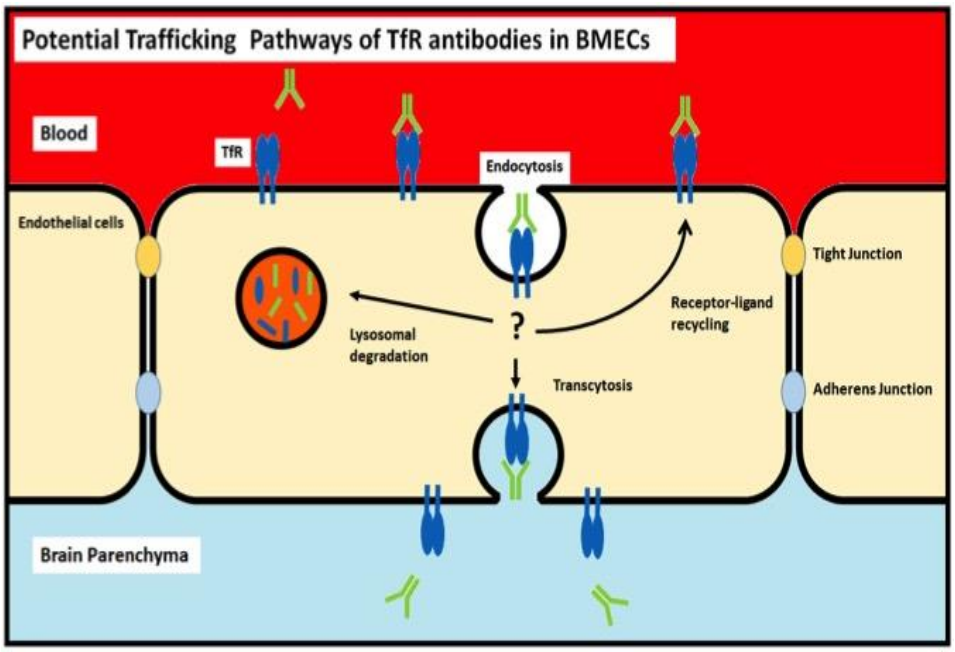

Figure 2.3: Potential cellular trafficking routes of TfR targeted antibodies and the BBB
This is a schematic to show the potential trafficking routes of transferrin targeted antibodies. Following endocytosis at the luminal membrane, sorting within the endothelial cell can lead to: recycling back to the luminal membrane, lysosomal degradation (high affinity divalent antibodies), or transcytosis across the cells to the abluminal membrane.

2.1.3 Chapter Aims

The primary aim of this chapter was to develop an assay for assessing the potential of nanoparticle and supramolecular delivery systems to undergo transcytosis at the BBB. This work was done for the COMPACT Consortium as a deliverable for the Brain Delivery work package. The focus of the development was around the transferrin receptor, and initial work was done to characterise the uptake of TfR ligands into the b.End3 cell line.

The objectives of this study were as follows:

1) To design and test the assay that used multiple components to assess the potential for an endogenous ligand to undergo transcytosis across the BBB. To characterise the methodology with respect to the transferrin receptor. As a non-specific mark, dextran was used to give a reference for the behaviour of a fluid-phase endocytic probe. Having established an assay, it was then tested with further transferrin receptor ligands, 8D3 antibodies.
2) As part of the development of the assay, the effect of ligand concentration on the ability of the cells to efflux a ligand was also examined with transferrin, and two different affinity 8D3 antibodies.
3) To demonstrate that the uptake of the TfR ligands used is through a receptor-mediated process, regulated by clathrin-mediated endocytosis.

2.2 Methods

2.2.1 Materials

Dulbecco's modified eagle medium (DMEM) + Glutamax, Medium 199 (M199), Sensicell MEM, Opti-MEM, fetal calf serum (FCS), horse serum, trypsin-EDTA dissociation solution, Penicillin and Streptomycin (10,000U/mL), Dextran 10kDa conjugated to Alexa 488 and Alexa 647, Dextran 70kDa conjugated to tetra-methyl Rhodamine, Holo-transferrin conjugated to Alexa 488 and Alexa 568 and the AlexaFluor® 488 protein labelling kits (1mg of IgG/ labelling procedure) were obtained from Invitrogen, UK. EBM-2 media was purchased from Lonza, Germany.

Transwell inserts for 24-well plate (0.33 cm^2) with pore sizes 0.4 µm and 3.0 µm, and Hoechst was obtained from Sigma Aldridge, UK. All other plastics for cell culture were purchased from Fisher Scientific,UK, as well as paraformaldehyde (PFA), sodium chloride, potassium chloride, magnesium chloride, calcium chloride, disodium hydrogen phosphate, potassium dihydrogen phosphate, sodium dihydrogen phosphate, sodium bicarbonate, D-glucose, bovine serum albumin (BSA). Cell imaging dishes were purchased from MatTek, UK

The anti-mouse transferrin receptor antibody 8D3 was kindly provided from Sanofi through COMPACT. The low-affinity variant 8D3-4 was kindly supplied from Abbvie through the COMPACT consortium.

Type 1 Rat Tail Collagen was purchased from Millipore-Merck.

2.2.2 Cell Culture

The b.End3 cell-line was supplied by COMPACT from the GSK source and grown in accordance with their SOP and replenished from stocks when the cells had undergone 20 passages or 60 days after defrosting the vial. b.End3 cells are cultured in 90% DMEM + Glutamax (Invitrogen) with 10% FCS (Invitrogen) (summarised in Table 2.1below).

Table 2.1: Summary of growth conditions for cell-lines and media supplements					
Cell Line (Source)	**Medium**	**Serum**	**Antibiotics**	**Dissociation Media**	**Seeding Density**
b.End3 (COMPACT)	DMEM + Glutamax (90%)	Fetal Bovine Serum (10%)	NO	Trypsin-EDTA (0.05%)	1 x 10^4 cells/cm^2

2.2.3 Fluorescent labelling of 8D3 and Isotype control antibodies

The antibodies were kindly supplied by Sanofi, through the COMPACT consortium, and labelled with either Alexa Fluor 488 or Alexa Fluor 647 using the Life Technologies antibody labelling kit. Briefly, 500μL of 2mg/mL antibody solution was added to the dye, in powder form, and vortexed to dissolve. The mixture is stirred for 90 minutes at room temperature to allow the reaction of the dye with the antibody. Purification of the labelled antibody from free dye was performed by size exclusion chromatography, using the columns provided within the kit, with samples of fluid collected every 1mL. The absorbance of these samples was analysed using the Cary 60 UV-spectrophotometer to scan from 250nm to 800nm. The relationship between the fluorophore absorbance peak (488nm or 647nm, depending on dye) and the absorbance of tryptophan residues in the antibodies (280nm) allows the calculation of the concentration of antibody (Eqn 2.1. + 2.2.) and the labelling efficiency of the dye (Eqn 2.3 + 2.4). Within the equations 203,000 $cm^{-1}M^{-1}$ is the molar extinction coefficient of a typical IgG molecule, 71,000 $cm^{-1}M^{-1}$ is the extinction coefficient of the Alexa Fluor 488 dye and 239,000 $cm^{-1}M^{-1}$ the extinction coefficient of Alexa Fluor 647. Labelling integrity was checked five months post-

labelling by re-purification of the antibody through the size exclusion column to ensure only labelled antibody remained present in the sample.

Equation 2.1.

$$IgG\ Molar\ concentration = \frac{A_{280} - (A_{494} \times 0.11) \times dilution\ factor}{203{,}000}$$

Equation 2.2.

$$IgG\ Molar\ concentration = \frac{(A_{280} - (A_{647} \times 0.03)) \times dilution\ factor}{203{,}000}$$

Equation 2.3.

$$Moles\ of\ Dye\ per\ Mole\ of\ IgG = \frac{A_{494} \times dilution\ factor}{71{,}000\ \times IgG\ concentration\ (M)}$$

Equation 2.4.

$$Moles\ of\ Dye\ per\ Mole\ of\ IgG = \frac{A_{647} \times dilution\ factor}{239{,}000\ \times IgG\ concentration\ (M)}$$

2.2.3 siRNA Transfection

To modulate the expression of the clathrin adaptor protein AP2µ2, in b.End3 cells, siRNA against the murine AP2µ2 was used (sequence – GUGGAUGCCUUUCGGGUCAdTdT) (Al Soraj et al., 2012). As well as a control siRNA against luciferase (sequence – CGUACGCGGAAUACUUCGAdTdT). b.End3 cells were seeded, at a density of 10,000 cells/cm^2 into individual wells of a 6-well plate for both lysis and uptake assays and allowed to grow for five days before transfection. For transfection siRNA stock solutions

(20 µM) are added to Opti-MEM® at a ratio of 10 µL:160 µL and mixed gently. In parallel to this, 6 µL of the Oligofectamine reagent is diluted in 30 µL Opti-MEM®. The two mixtures (siRNA and Oligofectamine) are combined and mixed gently, before incubating them at room temperature for 20 minutes to allow for complex formation. After the incubation, the cells to be transfected are washed with PBS twice before the addition of the siRNA complexes (200 µL per well). Additionally, 800 µL of Opti-MEM® was added to each well. The cells are incubated with this mixture for 4-6 hours, before the addition of 500 µL growth media, containing 30% FBS. Cells are then left for 48 hours before performing the uptake assay or cell lysis for Western blot.

2.2.4 Western Blot

Following the incubation with siRNA sequences for 48 hours, the cells to be lysed were dissociated from the 6-well plates and pelleted by centrifugation at 500 x g for 5 minutes at 4 ^{o}C. The media was then aspirated, and the pellets washed with PBS, using the same centrifuge configurations. The pellets were stored at -20 ^{o}C until lysis or proceeded straight to lysis.

The initial Cell Lysis buffer was prepared by the combination of 0.875g NaCl (150 mM), 0.6g Tris (50 mM), 0.19g EDTA (5 mM) and 1 mL Triton (1%) to a final volume of 100 mL, pH 7.5. To prepare this buffer for lysis, 10 mL of Cell Lysis Buffer is aliquoted and to it the following is added: 200µl $NaVO_4$ (100mM), 50µl NaF (10M), 100µl PMSF (100mM), 10µl Phenylarsine oxide (20mM), 100µl Sodium Molybdate (1M), 20µl Leupeptin (5mg/ml), 40µl Aprotinin (2µg/ml). This buffer is stored on ice until lysis was performed. To each cell pellet, 40-50 µL of lysis buffer was added and incubated with the cells for 30 minutes at 4 ^{o}C, with regular agitation of the cells throughout the incubation. After the lysis, cells are centrifuged at 10,000 x g for 30 minutes at 4 ^{o}C.

Protein quantification was performed using the Bicinchoninic Acid (BCA) assay, using the BCA assay kit (Thermo Fisher, Paisley, UK). Briefly, the reagents within the kit Reagent A and Reagent B, are combined in a 50:1 ratio, to produce 200 µL of reagents per sample. The combination of reagents was added to 25 µL of lysate (diluted 1:2) or a protein standard (BSA – range 2 mg/mL – 25 µg/mL). The samples are incubated at 37ºC for 30 minutes, before the absorbance at 562 nm is measured, using an LT5000MS ELISA reader (Labtech International Ltd, Uckfield UK). From the protein standards, the concentration of the cell lysates may be calculated.

For gel electrophoresis, a running buffer is prepared, containing 25mM Tris Base, 192 mM Glycine at a pH of 8.3. Pre-cast, 10% Mini-PROTEAN® TGX™ gels (BIORAD, Hertfordshire, UK) were loaded into the Mini-PROTEAN apparatus. 10 µg of cell lysate was loaded per well, plus the protein ladder, Precision Plus Protein™ Dual Colour Standards (BIORAD, Hertfordshire, UK). The gels were exposed to a 100V for 2 hours.

At the conclusion of the electrophoresis stage, the proteins are transferred, via semi-dry blotting, to a nitrocellulose membrane. For this, filter paper and the nitrocellulose membrane are pre-incubated in a blotting buffer, containing: 25 mM Tris Base, 192 mM Glycine, 20% Methanol. The components were assembled in the BIORAD Transblotting system, so the electrophoresis gel is in contact with the nitrocellulose membrane. The gel was exposed to 25V for 30 minutes to allow blotting to take place.

The membrane was then removed and washed in Washing Buffer (0.1 M Tris, 0.1 M NaCl, 0.1% Tween 20), to remove residual methanol, before blocking, by incubation with Washing Buffer containing 5% milk. This is done with continual agitation for 1 hour at room temperature. The membrane was cut in two at 42 kDa, and the high molecular weight section incubated with mouse anti-AP50 antibody (BD Bioscience, UK), diluted 1 in 200 with the blocking buffer overnight. The low molecular weight section of the

membrane was incubated with a rabbit anti-GAPDH antibody (Cell Signalling, UK), diluted 1 in 1000 in blocking buffer.

After, the primary antibody incubation, membranes are washed 6 times for 5 minutes with Washing Buffer, before incubation with a secondary, HRP-linked antibody, against the respective species of the primary. Anti-rabbit IgG secondary antibody (Cell Signalling, UK) or anti-mouse IgG secondary antibody (Cell Signalling, UK), in both cases the antibody is diluted 1 in 10,000 with blocking buffer. Following the secondary incubation, membranes are washed a further 6 times for 5 minutes with Washing Buffer. Antibodies are detected using SuperSignal^{TM} West Dura Substrate (Thermo Fisher, UK) and imaged using the BIORAD ChemiDoc XRS system.

2.2.5 Pulse-Chase Flow Cytometry in b.End3 cells.

Cells are seeded onto either 12-well or 24 well plates for growth at a seeding density of 10,000 cells/cm^2 and allowed to grow until a confluent monolayer could be observed by light microscopy (typically day 6-7 post seeding). When a confluent monolayer was observed, the growth media is replaced by Krebs-Ringer buffer containing 0.1% bovine serum albumin (KRB+BSA) for 30 minutes to remove serum proteins from the cells. The cells are then pulsed with one of the formulations shown in Table 2.2, for 45 minutes at either 37^{o}C or 4^{o}C, to confirm active uptake into the cells. Following the pulse, cells are washed with PBS three times to remove non-internalised probes from the cells and then incubated in blank KRB-BSA for the duration of the chase (0, 10, 30, 60 minutes). The chase steps are performed at both 37^{o}C and 4^{o}C to confirm an active efflux process has occurred. After the conclusion of the chase phase, the cells are placed at 4^{o}C and washed three times in PBS to remove effluxed probes from the solution. A pH 2.5 acid wash is then applied to remove and surface-bound probes before dissociation of the cells, using EDTA solution (2.5mM). The dissociation is performed at 4^{o}C for approximately one

hour and completed by repeated pipetting of cells to ensure maximum collection from a well. The dissociated cells were added to tubes containing PBS + 5% fetal bovine serum, and centrifuge at 300 x g for 10 minutes at 4ºC three times to remove EDTA from the cells. Following the final centrifuge, the cells are re-suspended in serum-free PBS for analysis using the FACS Verse (BD Biosciences). From 24-well plates a minimum of 10,000 events are collected per tube, and from 6-well plates, 50,000 events were collected. Further analysis of the data collected is performed using FlowJo software, and non-linear regression of fluorescence loss from cells is performed using GraphPad Prism 5.

Table 2.2: Concentration of Macromolecules used in Pulse-Chase Flow Cytometry

Macromolecule	Concentration (nM)	Source
Transferrin-Alexa fluor 488	588, 50 or 5	Life Technologies
Dextran 10kDa Alexa fluor 647	10,000	Life Technologies
8D3 anti-TfR Alexa fluor 647	170, 30, 10 or 1	Sanofi, Labelled in Lab
Isotype control Alexa fluor 647	30	Sanofi, Labelled in Lab

2.2.6 Transferrin Receptor Competition Flow Cytometry Studies

Competition studies to confirm receptor-mediated uptake were performed in b.End3 cells using fluorescently-labelled transferrin receptor targeting strategies, transferrin Alexa fluor 647, 8D3 Alexa fluor 647 and an isotype control antibody labelled with Alexa Fluor 647. B.End3 cells were seeded, as before, onto 24- or 6-well plates at a density of 10,000 cells/cm^2 and grown until a confluent monolayer could be observed. When confluent, cell growth media was replaced with KRB-BSA for 30 minutes at 37^oC to remove serum proteins from cells. Fixed concentrations of the labelled proteins were applied to the cells with various concentrations of unlabelled protein, to compete for the receptor, and the probes allowed to internalise for 45 minutes at 37 ^oC. To assess the specificity of the 8D3 antibody, supplied by Sanofi, for the transferrin receptor a further competition study using a fixed concentration of labelled 8D3 with varying concentrations of isotype control antibody.

Following the conclusion of the uptake, cells were washed three times in PBS and incubated with a pH 2.5 acid wash buffer for 30 seconds. The cells were washed a further three times in PBS containing EDTA (2.5mM) and allowed to dissociate in PBS-EDTA solution for approximately 1 hour on ice. After dissociation, cells were collected into centrifuge tubes containing PBS + 5% FBS and washed three times by centrifugation at 300 x g, for 10 minutes, at 4^oC. Following the final wash, cells were re-suspended in serum-free PBS for analysis using the FACS Verse.

Table 2.3: Transferrin competition study setup	
Concentration of unlabelled Transferrin (nM)	**Concentration of Transferrin Alexa fluor 488 (nM)**
0	10
0.5	10
1	10
5	10
10	10
50	10
100	10
500	10

Table 2.4: 8D3 competition study setup	
Concentration of unlabelled 8D3 (nM)	**Concentration of 8D3 Alexa fluor 647 (nM)**
0	30
5	30
10	30
50	30
100	30
500	30
1000	30

Table 2.5: Isotype control competition study setup	
Concentration of unlabelled Isotype Control (nM)	**Concentration of Isotype control fluor 647 (nM)**
0	30
5	30
10	30
50	30
100	30
500	30
1000	30

Table 2.6: 8D3 vs Isotype control competition study setup	
Concentration of unlabelled Isotype control (nM)	**Concentration of 8D3 Alexa fluor 647 (nM)**
0	30
5	30
10	30
50	30
100	30
500	30
1000	30

2.2.7 Macromolecule Permeability Assays and confocal microscopy, using B.End3 cells

The b.End3 cells were seeded onto the apical side of Transwell inserts for 24-well plates (0.4 μm pore diameter, polycarbonate membrane), at a seeding density of 10,000

cells/cm^2. During cell growth measurements of trans-endothelial electrical resistance (TEER) are taken daily to gauge the confluence of the cells on the inserts. TEER values are taken using Endohm chambers connected to the EVOM2 ohmmeter (World Precision Instruments). Briefly, the Endohm chamber is washed with ethanol to sterilise and filled with 1mL, b.End3 growth media. A blank insert, with no cells grown on it, is placed into the chamber, containing culture media and the resistance recorded. The resistance of the membrane will contribute to the total resistance when cells are grown on the inserts and must be subtracted to reveal the resistance of the monolayer. In parallel to TEER assessment, cells seeded at the same density on plastic, well-plates can be examined to assess monolayer formation.

In the permeability studies, cells are incubated with KRB-BSA for 30 minutes at 37^{o}C to remove serum proteins from cells. The media is aspirated from the apical chamber and replaces with KRB-BSA containing fluorescent macromolecules (Transferrin Alexa fluor 488, 588nM; Dextran Alexa fluor 488nm 10kDa, 10μM; Dextran rhodamine 70kDa, 2.85 μM; 8D3 Alexa Fluor 488 anti-TfR, 170nM). The plates are placed at 37^{o}C for 90 minutes, with samples taken from the basal well at 10, 30, 60 and 90 minutes, and replaced with an equal volume of blank KRB-BSA. The fluorescence of the collected samples was measured using FluoStar Optima plate-reader (BMG Labtech). The permeability coefficients (P_{app}) can be calculated according to Equation 2.5 below. This accounts for differing concentrations of a probe and differing surface areas of the inserts. P_{app} has the units, cm/s.

Equation 2.5:

$$P_{app} = \frac{\Delta mass}{\Delta time. Area. C_0}$$

Following the conclusion of the permeability study, the inserts are washed three times with PBS, to remove free probes from the cells. Fixation of cells is performed using 3% paraformaldehyde incubated with the cells for 15 minutes at room temperature. Following the fixation, cells are washed a further three times with PBS before the application of the nuclear stain Hoechst (0.1μg/mL) for 15 minutes at room temperature. The inserts are then washed three times with PBS, and the membrane cut away from the insert and placed onto a microscope slide in Daco Mounting Media for confocal fluorescence microscopy.

The imaging of the inserts removed from the Transwell studies was done on a Leica TCS SP5 confocal microscope, using a series of three sequential scans to compensate for the different fluorophores used. The main fluorophores analysed were Hoechst (excitation laser = 405nm, emission detection = 420-440nm), Alexa fluor 488 (excitation laser = 488nm, emission detection = 510-540nm), Tetramethyl Rhodamine (excitation laser = 544nm, emission detection = 560-600nm) and Alexa fluor 647 (excitation laser = 633nm, emission detection = 650-680nm).

2.2.8 Statistical Analysis

2.2.8.1 Flow Cytometry

For analysis of all flow cytometry fluorescence data, the geometric mean of the fluorescence intensity of the gated the single cell population was used as a single technical replicate for these experiments (see figure for gating example). In all studies, blank cells are initially tested to measure cellular autofluorescence and this value is subtracted from the fluorescence intensities of the assayed cells in that experiment. To normalize data from for each fluorescence probe, the mean fluorescence intensities of the technical replicates, of 37 ^{o}C pulsed cells (minus blank cell fluorescence) is taken as 100% and the intensities of the other cell treatments are expressed as a percentage of this value.

In the pulse-chase assays, to confirm there has been a significant change in cell associated fluorescence over the duration of the chase. The fluorescence associated to chase cell time points were compared to the fluorescence associated to the cell that have only undergone the pulse at 37 ^{o}C, through a one-way ANOVA with Dunnett's post-test. In this the pulse only cells were used as the reference for the multiple comparison analysis. Significance is defined as a p-value < 0.05. In addition, to confirm that any efflux from cells was due to an active process, the chase time points at 37 ^{o}C were compared to the same time point at 4 ^{o}C. This was done using a one-way ANOVA with Tukey post-test, significance was defined as a p-value < 0.05.

Competitive uptake assays, using TfR ligands, were analysed by comparison of cells that were only pulsed with the fluorescent ligand only, at a fixed concentration. With cells that were pulsed with the same concentration of fluorescent ligand and variable concentrations of unlabelled ligand. The comparison was made with a one-way ANOVA with a Dunnett's post-test, using the non-competed cells as the control group for the post-test. Significance was defined as an output p-value < 0.05.

For graphical representation of the data, presented in this chapter, unless stated otherwise in the figure legends, the data within a graph will be expressed as the mean ± standard deviation. Flow cytometry gating and extraction of the geometric means of the data was performed using the FlowJo software package. Initial normalization of the data was performed in Microsoft Excel, with statistical analysis and graph production done using GraphPad Prism 5 (CA, USA).

2.2.8.2 Microscopy Co-localization:

Following collection of z-stack image files, these were imported into the Fiji image analysis software for processing and co-localization analysis. Here each stack is split into

individual slices for analysis using JACoP (Just Another Colocalization Plugin) in Fiji. In this analysis the Mander's Colocalization method was selected, to observe the proportion of thresholded ligand fluorescence which was co-localized with thresholded dextran fluorescence, at the conclusion of the chase phase (Manders *et al.* 1993). Thresholding in this way of the images allows for the removal of background fluorescence from the analysis. The colocalization fractions for each slice in the z-stack were averaged to produce an output for value for that replicate, and for final analysis the combination of multiple microscopy stacks were used to produce the output colocalization fractions for the ligands with dextran labelled lysosomes. These were expressed as mean ± standard deviation.

2.2.8.3 Permeability Assays:

TEER values of bEnd3 cells alone were calculated by subtracting the resistance across a blank insert from the resistance of the inserts with cells grown on them. The resistance value of the cells alone was then multiplied by the area of the inserts (0.33 cm^2) to calculate the TEER value. The TEER value of the inserts used in all permeability studies was expressed as mean ± standard deviation.

The permeability co-efficient of each probe, across the endothelial cells, was calculated using the equation below. This is done by considering the permeability of the probe across the filter alone, before it reached saturation if applicable.

Equation 2.6:

$$\frac{1}{Papp_{Total}} = \frac{1}{Papp_{Endo}} + \frac{1}{Papp_{Filter}}$$

Comparison of the apparent permeability coefficient of all probes across the b.End3 cells was performed using a one-way ANOVA and Tukey post-test, to compare all possible combinations of the probes. Significance was defined as a p-value < 0.05 from the post-test. Graphical representation of the data was done using the mean ± standard deviation for all data points and were produced using GraphPad Prism 5 software.

2.3 Results and Discussion

2.3.1 Fluorescent Labelling of 8D3 and Isotype Control IgGs

The Life Technologies IgG labelling kits provided sufficient labelling and purification of both IgGs. The 8D3 antibody had a calculated 4.19 moles of Alexa Fluor 647 dye per mole of IgG, while the isotype control had 4.8 moles of the dye per mole of IgG. Re-purification of both 8D3 and isotype control antibodies at 5 and 4 months respectively showed that the isotype control labelling remained intact. However, of the labelled 8D3, only 80% of Alexa Fluor 647 absorbance remained associated with the 8D3 antibody, with 20% appearing as free-dye, unbound to the antibody. The presence of free dye altered the calculation of the concentration of antibody and the dye binding, showing a lower than expected IgG concentration, but an increase in the number of molecules of dye per molecule of antibody. The decrease in antibody concentration is likely due to a loss of protein within the column, which may be present in other elution volumes from the column.

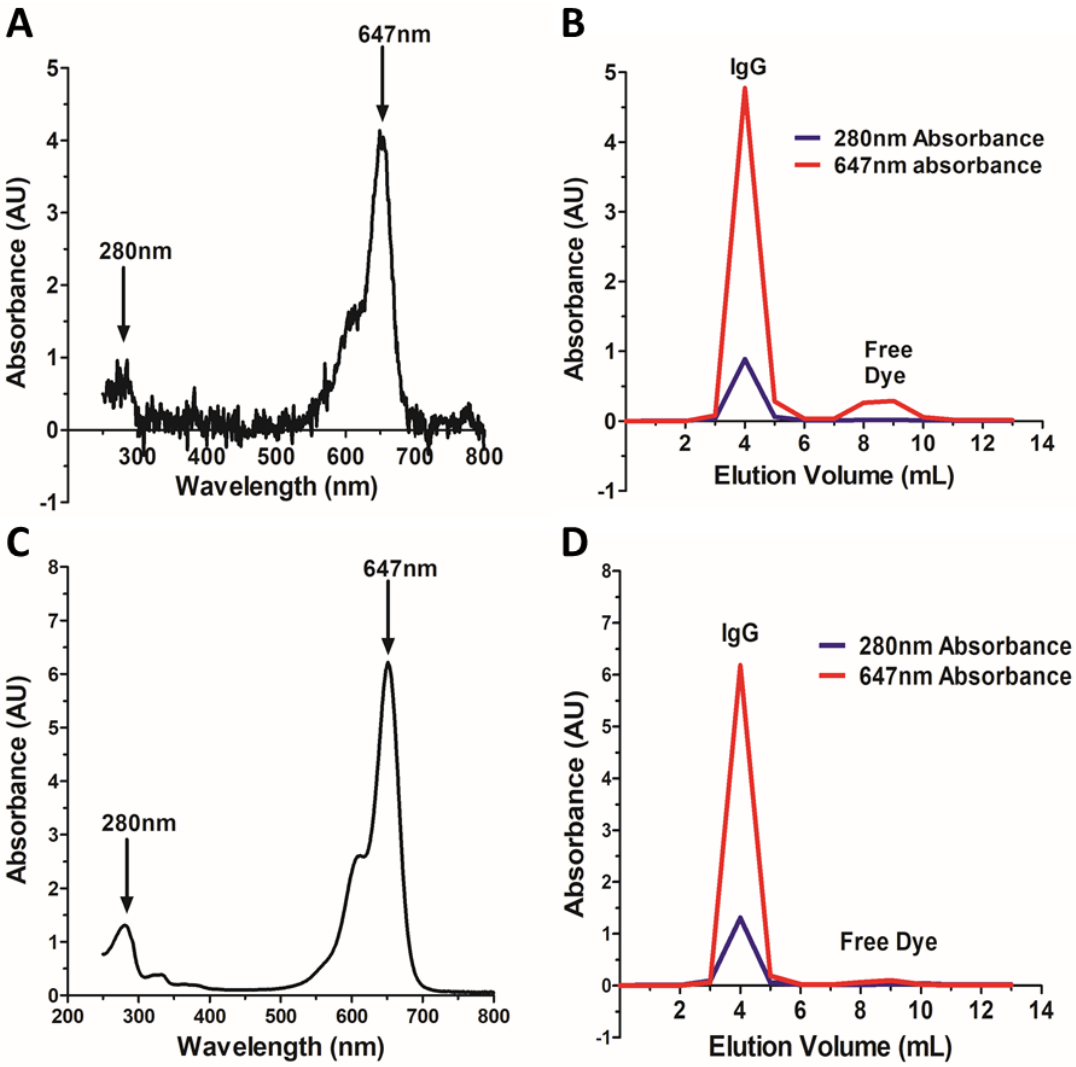

Figure 2.4. Labelling of 8D3 and Isotype Control IgGs with Alexa Fluor 647

Graphs A and B refer to 8D3 labelling, A shows a absorbance of the labelled antibody from 250nm-800nm, with the peaks at 280nm (tryptophan residues) and 647nm (fluorophore) highlighted. B shows the integrity of the labelling, and the presence of free dye in the sample, 5 months after labelling. Graphs C and D refer to Isotype Control IgG labelling and it can be seen that all dye is associated with the antibody and no free dye is seen in the re-purification (D).

2.3.2 Retention of fluid-phase endocytic probe dextran by b.End3 cells

The uptake of 10kDa dextran by the cells was confirmed to be an active process, with a significant increase in the uptake at 37^{o}C compared to 4^{o}C ($P<0.0001$). Active efflux of the 10kDa dextran was not observed during the chase steps, with no significant difference ($P>0.05$) at all pairs of chase time-points (4^{o}C and 37^{o}C). Retention of the 10kDa dextran

is highly likely, due to the known, fluid-phase uptake and trafficking to lysosomes of dextrans. Some loss may occur with longer chase durations. This was confirmed by the data in these studies, with only 10-20 % of pulsed fluorescence lost from cells over the one hour chase.

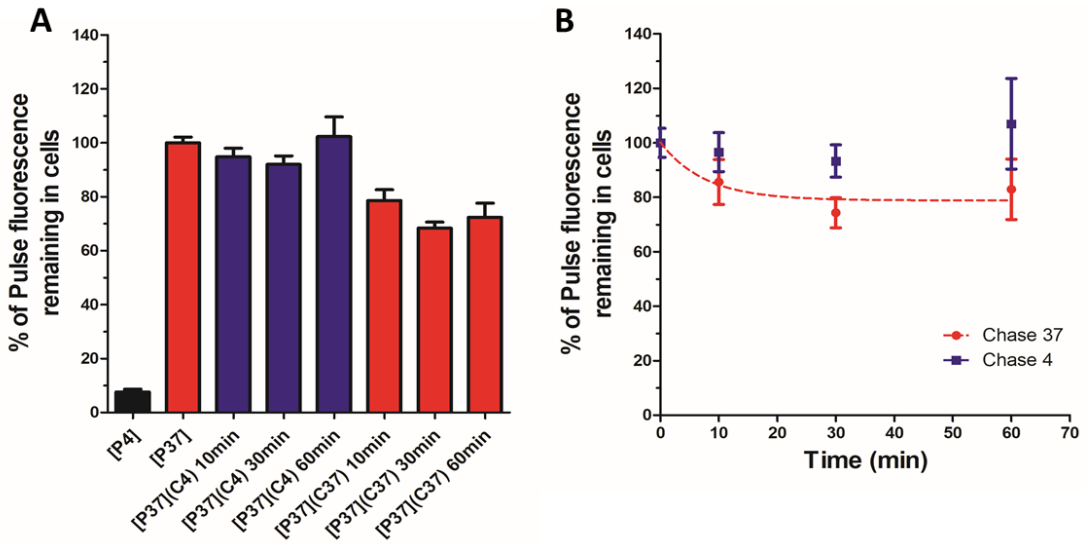

Figure 2.5. Dextran 10kDa Alexa Fluor 647 Pulse-Chase studies in b.End3 cells
Graph A and B show the proportion of dextran 10kDa remaining in cells, following a 45 minute pulse and chase at either 4ºC (blue) or 37ºC (red). The fluorescence associated with cells at 4ºC is also shown in black on graph A. n=3 in triplicate for all time points and background auto-fluorescence of cells has been subtracted from all data points, mean ± std.

2.3.3 Modulation of transferrin endocytosis into b.End3 cells.

Three strategies were examined to modulate the uptake of transferrin by b.End3 cells, 4 ºC vs 37 ºC uptake, the direct competition of holo-transferrin Alexa Fluor 488 uptake using unlabelled holo-transferrin and siRNA against the clathrin assembly protein AP2µ2.

The b.End3 cells pulsed at 4ºC show a similar fluorescence intensity to that seen with the blank cell population, with the flow cytometry, intensity profiles overlapping. This confirms endocytosis was unable to take place at 4 ºC in b.End3 cells. In contrast to blank cells and 4ºC pulse cells, those pulsed at 37ºC, produce a significantly increased cell-associated fluorescence at the conclusion of the pulse. This would indicate that the

internalisation of transferrin into b.End3 cells is an active process, requiring cellular metabolic activity to induce (Figure 2.8). The transferrin receptor is known to be internalised by clathrin-mediated endocytosis, which involves several GTPase proteins. Therefore, for optimal endocytic activity 37^{o}C is likely to be required for the metabolic demands of the process.

The competitive uptake studies demonstrate that the process of transferrin endocytosis is a self-competitive process. Maximum fluorescence intensity was obtained in the case of the 10nM labelled holo transferrin incubated with 0nM unlabelled holo transferrin. Increasing the concentration of unlabelled transferrin reduced the cell-associated fluorescence from transferrin Alex Fluor 488. This allows the inference that uptake of holo transferrin is saturable. The data in Figure 2.6, also confirms that the transferrin protein has a defined ligand-binding site on the transferrin receptor and that its internalisation is due to a receptor-mediated process within the cells.

By using the existing data in the literature on the affinity of transferrin for the TfR, it is possible to calculate an experimental Ki for the efficiency of the competition with unlabelled transferrin in this experiment. Modelling of the curve in Figure 2.6.B. allowed for the calculation of the Ki, which was found to be 7.5 nM. This value for the Ki is representative of the Kd of transferrin for the receptor. Reported values in the literature for holo transferrin's affinity for the TfR range from 2-8 nM, confirming that this methodology enables accurate and comparable measures of ligand-receptor interactions.

Additionally, the experimental IC50 was calculated to confirm that the labelling of the transferrin protein had not altered its ability to bind to the TfR. The IC50 was calculated as 33.2 nM, within acceptable tolerance accepted for these studies. As the labelled and unlabeled compounds are the same, the IC50 (50% displacement of fluorescence) should occur at the when the concentration of both probes is approximately equal.

The demonstration of the self-competitive nature of transferrin uptake confirms why the transferrin protein itself has limited use *in vivo* as a targeting ligand. The high plasma concentrations of the transferrin protein were represented by the increasing concentrations of the unlabelled ligand in these studies. Transferrin targeted DDS's are seen to be competed *in vivo* by transferrin in circulation, and overall, they lack effective brain penetration ability.

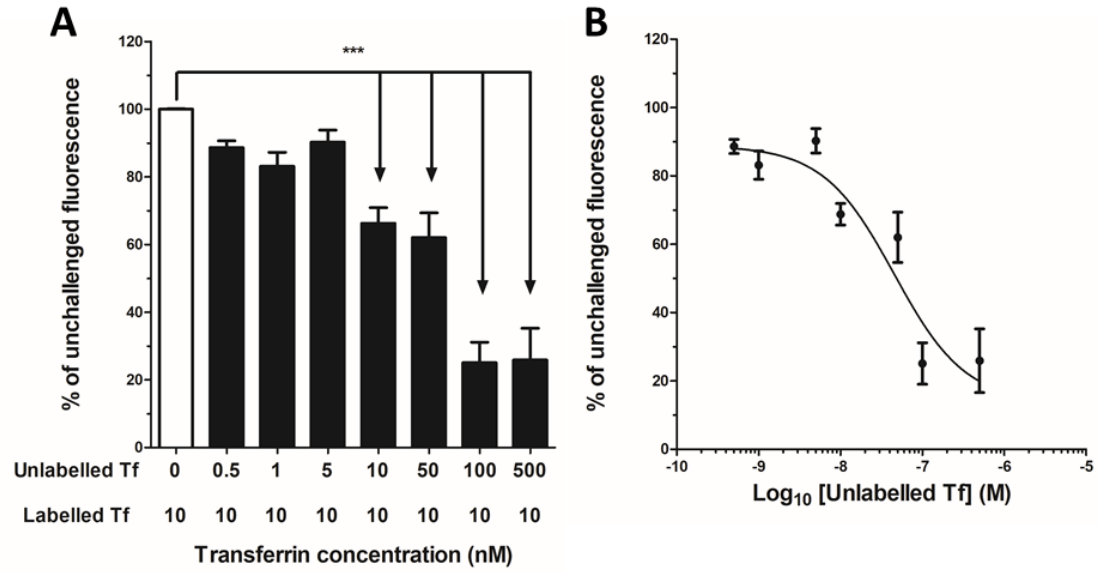

Figure 2.6. Competition of holo-transferrin Alexa Fluor 488 uptake by unlabelled
Both graphs show the effect of increasing concentrations of unlabelled transferrin on the uptake of. Transferrin Alexa Fluor 488 concentration – 10nM, all values expressed as a percentage of unchallenged cellular fluorescence. *** denotes P<0.001 when compared to unchallenged fluorescence, n = 3 in triplicate, mean ± std.

Finally, the uptake of transferrin was reduced through siRNA knockdown of the AP2µ2 adaptor protein of CME. Knockdown of this protein prevents the assembly and formation of the clathrin-coated pits at the plasma membrane of cells. Flow cytometry demonstrated that the knockdown AP2µ2 reduced transferrin uptake to 55% of the uptake of untransfected or control transfection cells (Figure 2.7.B). Due to the heterogeneity of

siRNA uptake into b.End3 cells, it is always unlikely that siRNA transfection would reduce transferrin uptake to the levels of blank cells or 4 ^{o}C treated cells. However, the fact the reduction of transferrin uptake is significant, using the AP2µ2 siRNA, confirms the involvement of clathrin-mediated endocytosis in the internalisation of the transferrin receptor in b.End 3 cells. The knockdown of the AP2µ2 was confirmed by Western Blot analysis of cell lysates. This confirmed the effects seen by flow cytometry were due to direct modulation of the AP2µ2 protein and not the results of the transfection protocol.

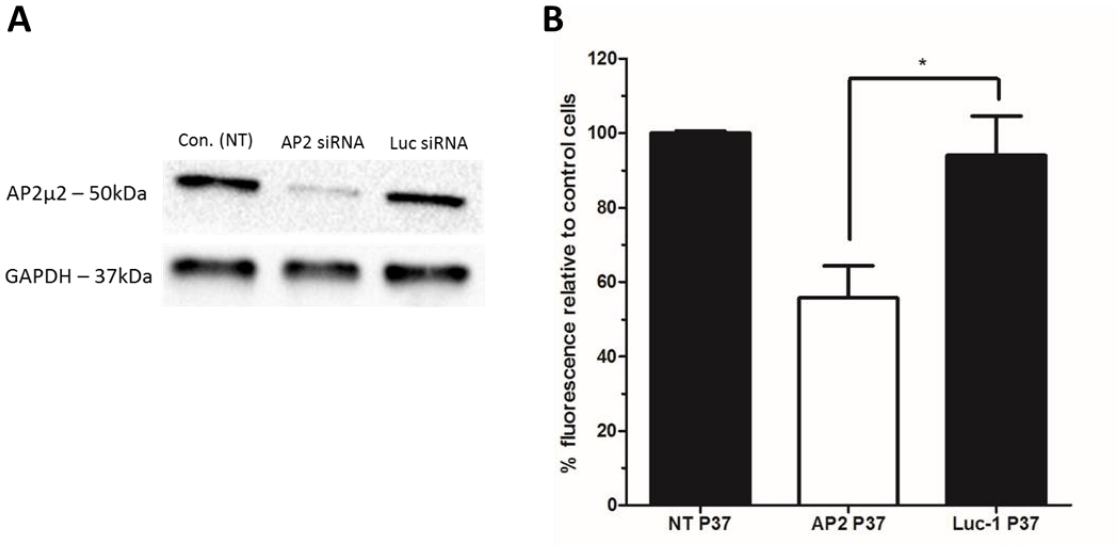

Figure 2.7. siRNA Modulation of Transferrin uptake in b.End3 cells
A. shows the Western Blot images confirming siRNA knockdown of AP2µ2 protein levels. B. shows AP2µ2 knockdown to reduces transferrin uptake in b.End3 cells, n=3 in triplicate, * = P<0.05.

2.3.4 Effect of ligand concentration of transferrin efflux from b.End3 cells

Transferrin is known to undergo receptor-mediated endocytosis in BMEC cells. However, by increasing the concentration of the ligand to beyond saturation of the receptor, it appears possible to drive uptake through both receptor-mediated and fluid phase pathways. Transferrin-AlexaFluor 488 again showed significantly increased uptake at 37^{o}C compared to 4^{o}C in all studies (P<0.001, Figure 2.8.). The efflux of transferrin was

confirmed as an active process by the comparison of fluorescence remaining within cells at matched 4 ^{o}C and 37 ^{o}C time points.

In the pulse-chase experiments, it was demonstrated that receptor saturation, with transferrin-AlexaFluor 488, altered the proportion of transferrin lost from cells during the chase phase. Unlike the 10kDa dextran, transferrin can enter the cell via receptor-mediated endocytosis, as shown in Figure 2.6. Uptake of transferrin-AlexaFluor 488 was competed by the addition of increasing concentrations of unlabelled transferrin. When 10nM of fluorescent transferrin was added to the cells Ki for unlabelled transferrin competing for the receptor was found to be 33.2 nM (range 19-46nM, n=3). When low concentrations of transferrin were applied to cells (5nM), the proportion remaining associated to the cells after a 60-minute chase was 12% of the pulse fluorescence. Pulse concentrations above the Kd of transferrin for the TfR, 50nM and 588nM, resulted in an increased proportion of pulse fluorescence retained by cells, 25% and 52% respectively.

The half-life of transferrin loss from cells does not appear to be altered by varying pulse concentrations of transferrin, ranging from 6-10 minutes across all concentrations. Comparisons to dextran pulse-chase data show the fluid phase marker is retained by cells with only 10-20 % of pulsed dextran fluorescence lost from cells over the 60-minute chase phase at 37 ^{o}C.

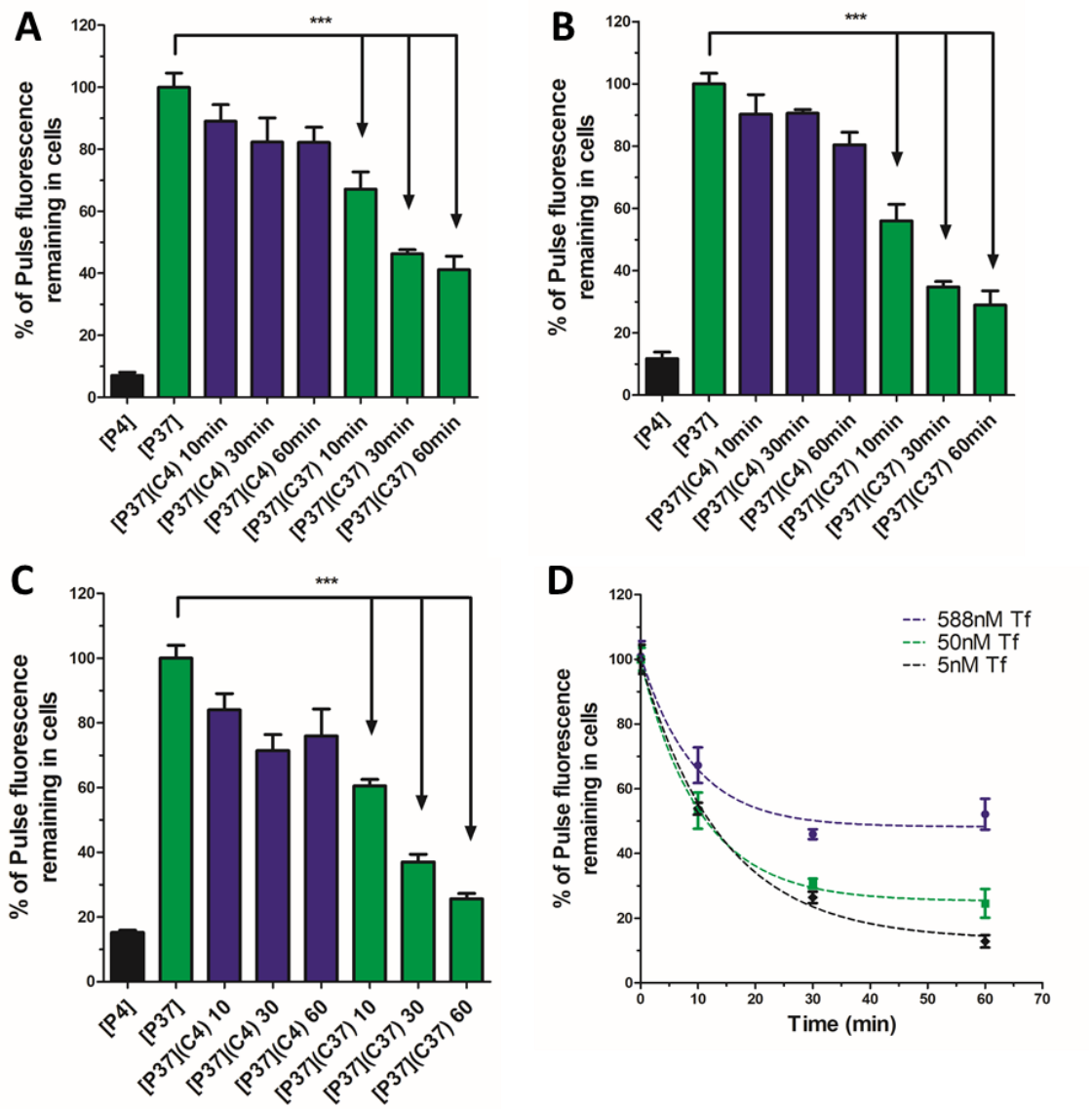

Figure 2.8: Transferrin Pulse-Chase Studies: the effect of Pulse concentration on transferrin retention

Figures .A-C show varying concentrations of fluorescently-labelled transferrin applied to the cells in a single 45 min pulse, and the proportional retention of the ligand remaining cell associated during a 60 min 'chase' performed at 4°C (BLUE) and the 37°C (GREEN). The concentrations shown in each graph are as follows: A = 588 nM, B = 50 nM, C = 5 nM. Figure D shows a summary graphic of the 37°C chase from Figures A-C. n = 3, in triplicate, *** denotes P<0.001 compared to [P37].

2.3.5 Characterisation of 8D3 Antibody

As with the transferrin protein, initial characterisation of the 8D3 antibody was made by studying the endocytic process of the antibody. This was done by comparing the uptake of 8D3 at 4 ^{o}C and 37 ^{o}C, as well as confirming the antibody's affinity for the transferrin receptor. Throughout these studies, comparisons were made between the 8D3 antibody and an isotype control antibody.

When cells were pulsed at 4 ^{o}C, there was limited fluorescence associated with cells for both antibodies. The fluorescence was only slightly increased over that of cellular auto-fluorescence. Both the 8D3 antibody and the isotype control antibody required 37 ^{o}C conditions to increase uptake into the b.End3 cells. This confirmed the uptake of both antibodies was an active cellular process. Confocal microscopy of the 4 ^{o}C and 37 ^{o}C conditions for the 8D3 and isotype control antibodies also confirmed the uptake of both as an active process. This was to be expected with the 8D3 antibody, as it targets the TfR to be internalised within the cell. In contrast, it was unexpected that the isotype control be taken up as it has no target receptor. However, some of the uptake of the isotype control antibody may be due to interactions with the Fc Receptor, more specifically the neonatal Fc Receptor (FcRn) on the surface of the b.End3 cells. The localisation of these receptors with BMECs is unclear and evidence in the literature suggest expression of FcRn is varied throughout the CNS, limiting its use as a target receptor for brain delivery (Schlachetzki *et al.* 2002). There may also be the possibility for the isotype control IgG to be internalised through non-specific, fluid phase mechanisms, in a similar manner to dextran in the previous study (Figure 2.5).

To confirm the specificity of the uptake mechanism, competitive uptake studies were performed using both antibodies. To look at the self-competitive uptake of both

antibodies as well as confirming the specificity of the 8D3 antibody by attempting to compete its uptake using the isotype control antibody.

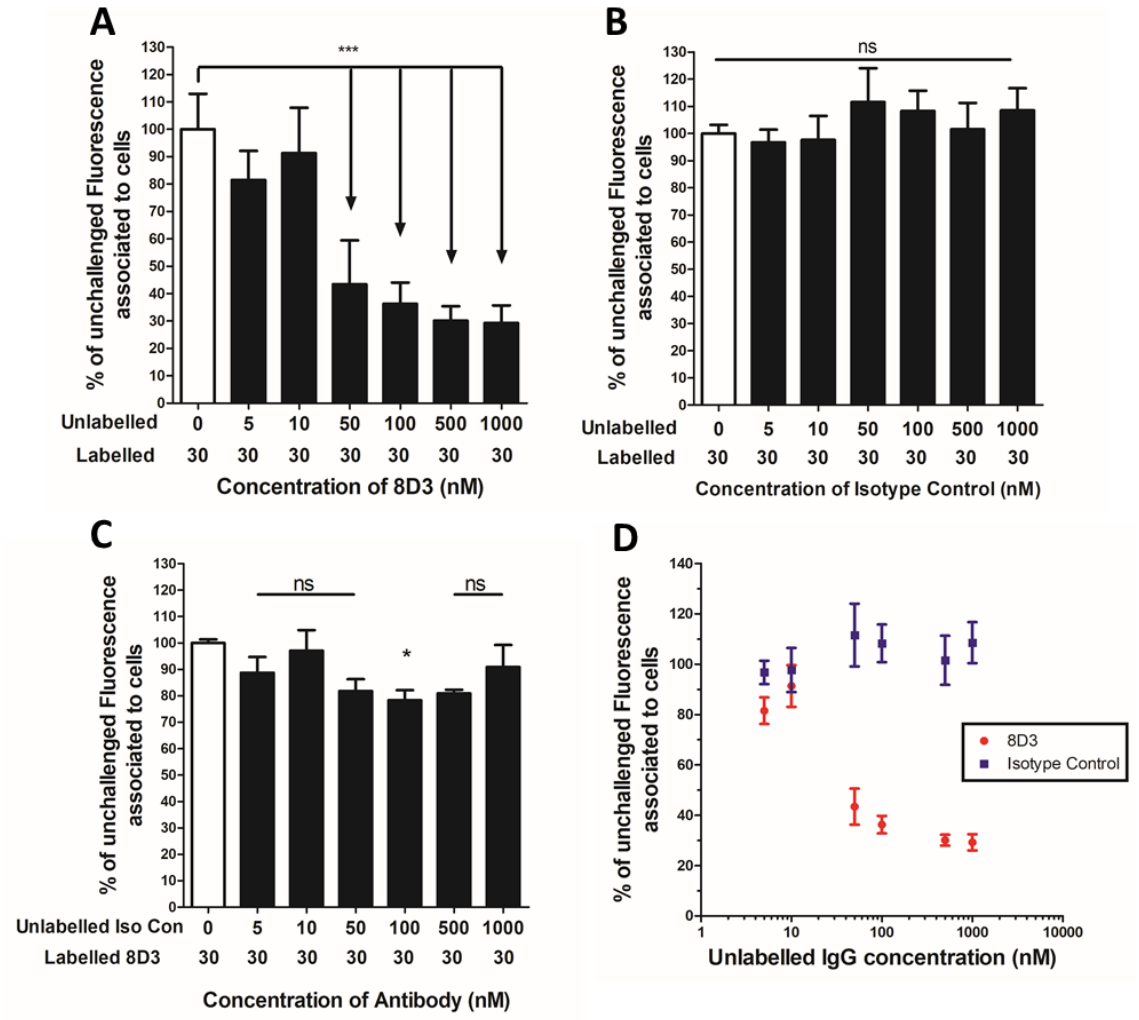

Figure 2.9: Comparison of the Competitive Uptake of Chimeric 8D3 and Isotype Control IgG

Figures 3.A-C show the competition of labelled antibody (either 8D3 or isotype control) uptake by varying concentrations of unlabelled antibody (either 8D3 or isotype control). A = 8D3-647 competed by unlabelled 8D3, B = Labelled Isotype control competed by unlabelled isotype control and C = 8D3-647 competed by unlabelled isotype control antibody. The data indicates 8D3 uptake to be specific and saturable. Figure D shows the competitive uptake curves for the labelled 8D3 and labelled isotype control (competed by respective unlabelled species) predicting an apparent affinity constant Ki =1.6nM. n = 3, in triplicate, *** = $p < 0.001$ compared to unchallenged cells (white bar), * = $p < 0.05$ compared to unchallenged cells (white bar), ns = $p > 0.05$.

The uptake of labelled 8D3 antibody was competed using an unlabelled 8D3 antibody, confirming receptor-mediated uptake, a process which appears saturable. The apparent affinity constant of 8D3 for the receptor was calculated as a Ki of 1.6 nM, confirming

8D3 as a high-affinity antibody. The calculated Ki, from Figure 2.9, validates published work with the 8D3 antibody which has a measured the affinity of the antibody as between 2-3 nM in mouse brain microvascular endothelial cells (Lee *et al.* 2000).

The specificity of 8D3 uptake was confirmed by competition with unlabelled isotype control antibody, which did not affect labelled 8D3 uptake by b.End3 cells (Figure 2.9. C). This confirms that the 8D3 antibody has a specific receptor binding site, that is not shared with an untargeted control antibody.

Finally, the uptake of the isotype control antibody into BMECs was confirmed as a non-specific, endocytic process. Attempted competition of the control antibody with unlabelled control antibody failed to decrease the fluorescence associated with the b.End3 cells. Thus, confirming a non-saturable, non-specific uptake pathway for the isotype control antibody (Figure 2.9.B).

The 8D3 anti-TfR antibody shows active efflux from cells at all concentrations and all time points (Figure 2.10). This was confirmed by significant differences between the pulse fluorescence and the 37ºC chase time points. Additionally, significant differences were seen between 4ºC and 37ºC chase time points. As with transferrin a similar concentration-dependent efflux potential from b.End3 cells were observed with the 8D3 antibody in the pulse-chase studies. At low concentrations (1nM) of labelled 8D3, only 22% of the pulse fluorescence remains associated with cells after a 60-minute chase at 37ºC (Figure 2.10.C). Whereas, at the high pulse concentrations (10 nM and 170 nM) the fluorescence was retained by the cells at 60 minutes was 40 and 45 % of the pulse fluorescence, respectively.

Following the conclusion of the chase phase, cells imaged by confocal microscopy exhibited high levels of co-localization between the 8D3 antibody and dextran labelled

lysosomes when pulsed with the highest concentration of 8D3 antibody (170 nM). Using the Manders co-localization test, ~87% of 8D3 fluorescence, remain in cells, was seen to be associated with lysosomal compartments, Figure 2.11. Indicating trapping of the antibody and an inability for it to undergo further transcellular trafficking. When looking at the data from the pulse-chase flow cytometry study (Figure 2.10.A.), in parallel to microscopy, it would indicate that at the conclusion of the chase, 39.15% of the pulsed antibody is unable to undergo further cellular trafficking. That is to say, it will remain trapped within the endothelial cells and be unable to undergo an efflux process at either the apical or basolateral cell membrane, as the ligand is within the lysosomes and therefore degraded. In the Roche and Genentech studies with high and low affinity antibodies against the TfR, they demonstrated high affinity antibodies becoming trapped within lysosomes and downregulation cell surface TfR expression (Niewoehner *et al.* 2014; Bien-Ly *et al.* 2014). This would be supported by the high localisation of 8D3 with dextran-loaded lysosomes in this study. These findings could suggest that high concentrations of 8D3 antibody leads to surface crosslinking of the TfR, by antibodies, prior to endocytosis. If crosslinking does take place, Moody *et al* (2015) demonstrated that this can lead to increased lysosomal trafficking of the crosslinked receptor, as observed by colocalization with dextran labelled lysosomes (Moody *et al.* 2015; Humphries *et al.* 2011).

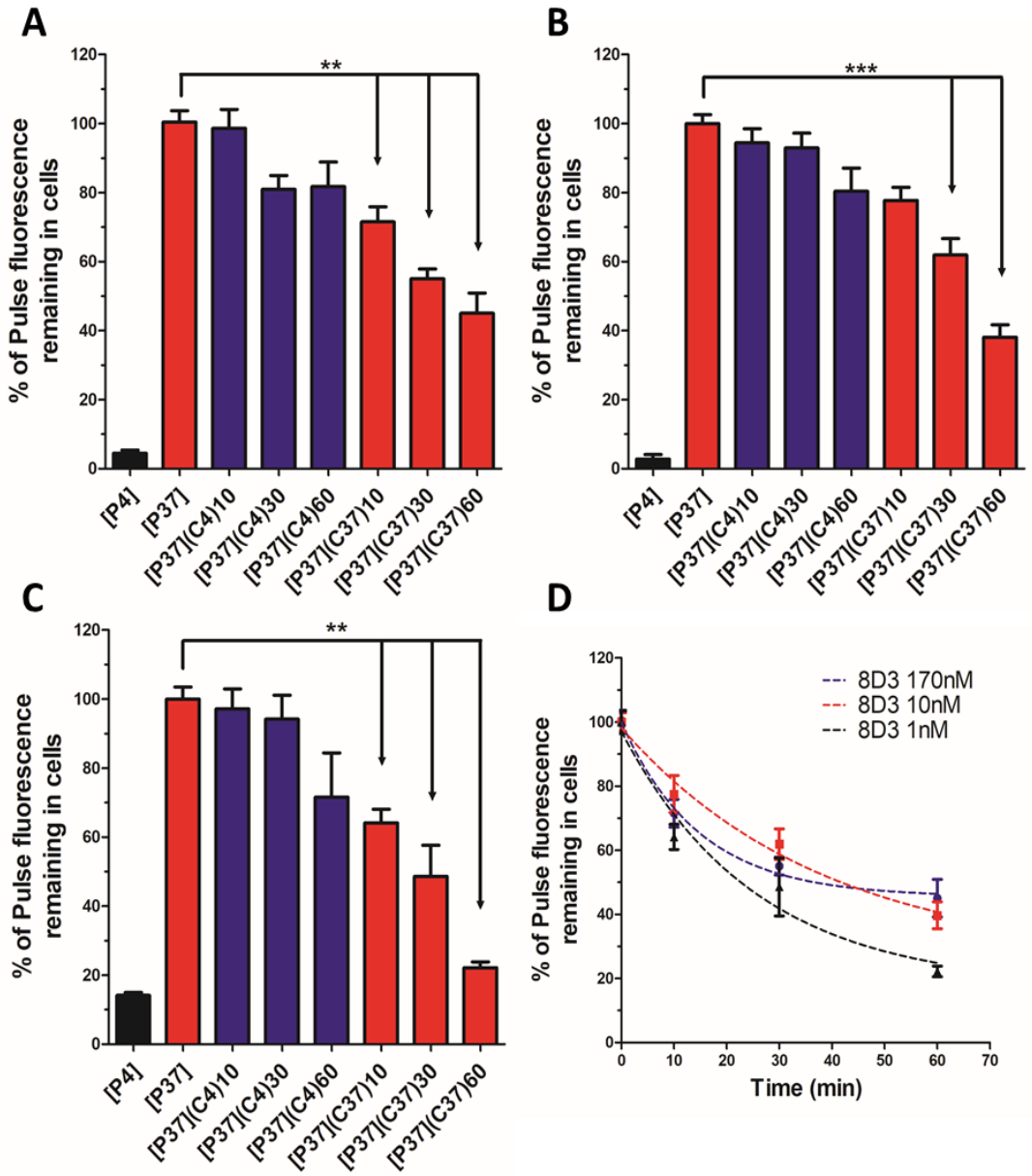

Figure 2.10: 8D3 Pulse-Chase Studies: the effect of Pulse concentration on 8D3 retention

Figures A-C show varying concentrations of fluorescently-labelled 8D3 applied to the cells in a single 45 min pulse, and the proportional retention of the ligand remaining cell associated during a 60 min 'chase' performed at 4oC (BLUE) and the 37oC (RED). The concentrations applied to cells are as follows: A = 170 nM, B = 10 nM, C = 1 nM. Figure D shows a combined graphic of the 37oC chase from Figures A-C. n = 3 in triplicate, mean ± std, ** = $p < 0.01$, *** = $p < 0.001$, this is when compared to the [P37] cells.

At the lowest 8D3 pulse concentration (1 nM), less co-localization was observed between the antibody and lysosomes, with more distinct separation between the fluorescence channels. Quantification of the co-localization with low 8D3 concentrations showed 23%

of the fluorescence remaining in cells was associated to lysosomal compartments of the cell. This would equate to 5.06% of the pulsed fluorescence which is unable to undergo further cellular trafficking at the conclusion of the chase phase. This proportion is based on the Mander's colocalization coefficient for 8D3 1 nM multiplied by the percentage of pulse fluorescence associated to cells from Figure 2.10.C.

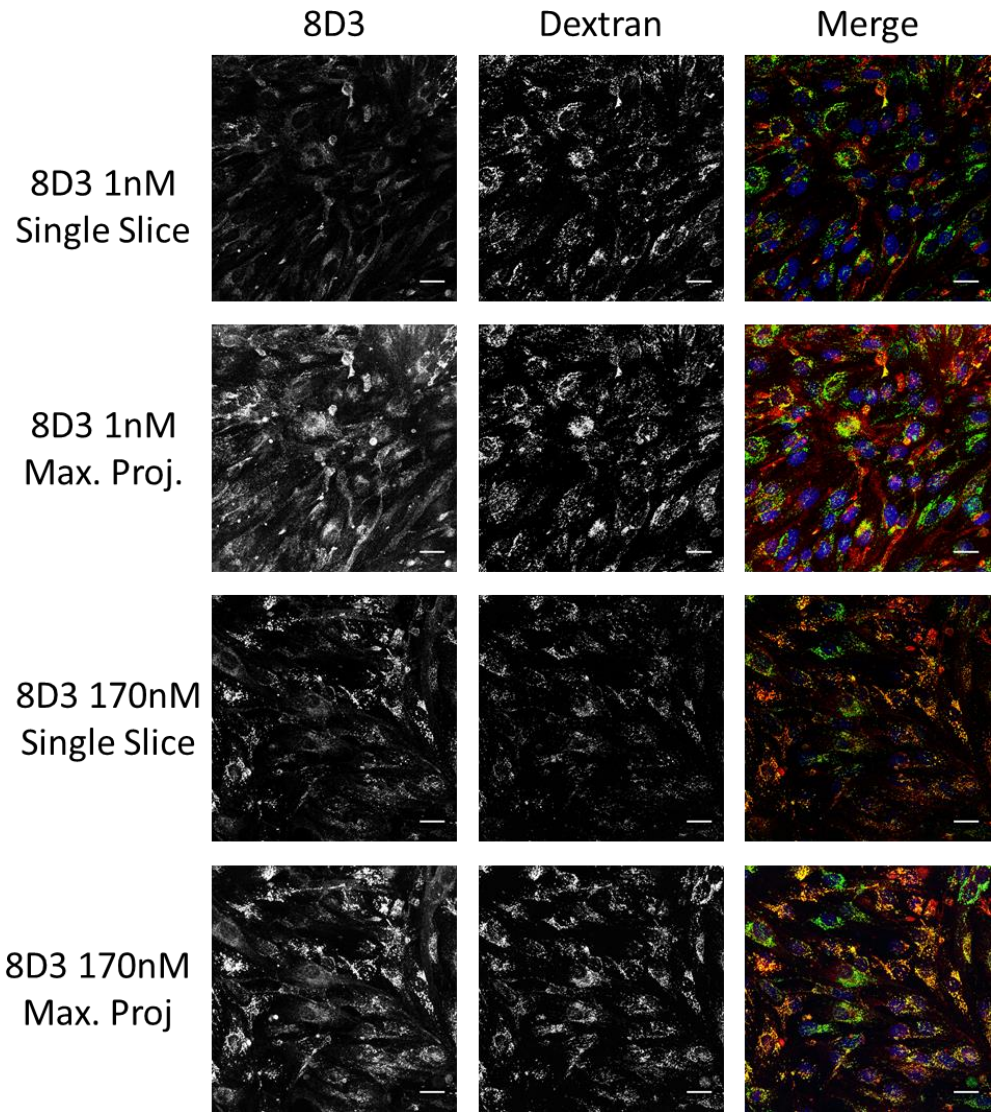

Figure 2.11: Sub-cellular localization of 8D3 following the chase
The above shows the distribution of the 8D3 antibody from Sanofi, at the conclusion of the 1 hour chase at the highest and lowest applied concentrations. The figure shows both a single slice and a max projection for each concentration. In the merged images, red = 8D3, green = dextran, blue = Hoechst, Scale Bar = 25 µm.

The saturation of the TfR, with an excess 8D3 antibody, as with the Tf ligand, will lead to a proportion of the antibody being taken up by fluid-phase, non-specific uptake mechanisms. This proportion is unable to undergo the same cellular trafficking as the antibody bound to the receptor, and as exemplified by other fluid-phase markers like dextran. In a clinical/*in vivo* setting, this over-saturation would represent "wasted" formulation, that although reaching the vasculature of the brain (i.e. the barrier to entry) is unable to reach the brain parenchyma and target site. Degradation of a formulation within lysosomes the brain endothelial cells would be a costly outcome, due to the wastage of expensive materials. By optimizing the concentration used in studies *in vitro* and *in vivo*, there will be minimal wastage of the dose, with the maximal proportion of the compound available to undergo further cellular trafficking in the BMECs and potentially undergo transcytosis. However, when considering the total amount/mass of compound available to undergo potential transcytosis, high, receptor saturating concentrations may result in a greater mass compound reaching the target site. Even though at high concentrations this may represent a lower proportion of the internalized compound.

The isotype control antibody, although taken up by b.End3 cells were not seen to be effluxed from the cells during the chase phase of the study. No significant difference was observed between the pulse fluorescence and the fluorescence associated with the cells at the 37^{o}C chase time points. Additionally, there was no difference between the 4^{o}C chase and 37^{o}C chase matched time points. This confirms the lack of a specific uptake pathway for the isotype control IgG.

2.3.6 Characterisation of the 8D3-4 antibody

The recent work of Roche and Genentech, studying the effect of affinity and valency on the ability of TfR targeting ligands to highlights the importance of these factors in

delivery across the BBB. The 8D3 antibody, provided by Sanofi and previously characterised is a high-affinity antibody, with low nanomolar (2-3 nM) affinity for the TfR. However, this high-affinity causes decreased TfR levels on the cell surface of endothelial cells and show limited delivery capacity across the barrier.

To test the effects of antibody affinity on the cellular trafficking and uptake of anti-TfR antibodies, the 8D3-4 antibody was obtained from Abbvie. This is a mutated form of the 8D3 antibody with an estimated 10-fold lower affinity for the TfR compared to the native 8D3 antibody. The 8D3-4 antibody was fluorescently labelled with the same method as previously described. However, with the 8D3-4 antibody, this lead to over-labelling of the antibody, with 11.95 moles dye/mole of antibody. The degree of antibody labelling was reduced by decreasing the labelling time and the fluorophore concentration. Firstly, the labelling time was reduced to 40 minutes, with the same quantity of fluorophore, this produced a labelling efficiency of 7.51 moles dye/mole of antibody. This would still be considered over-labelling of the protein. To further reduce the labelling efficiency the quantity of fluorophore used was reduced to 1/4 of the sample provided. The labelling reaction time was also reduced to 20 minutes. This enabled the labelling efficiency to be decreased to 1.38 moles dye/mole antibody.

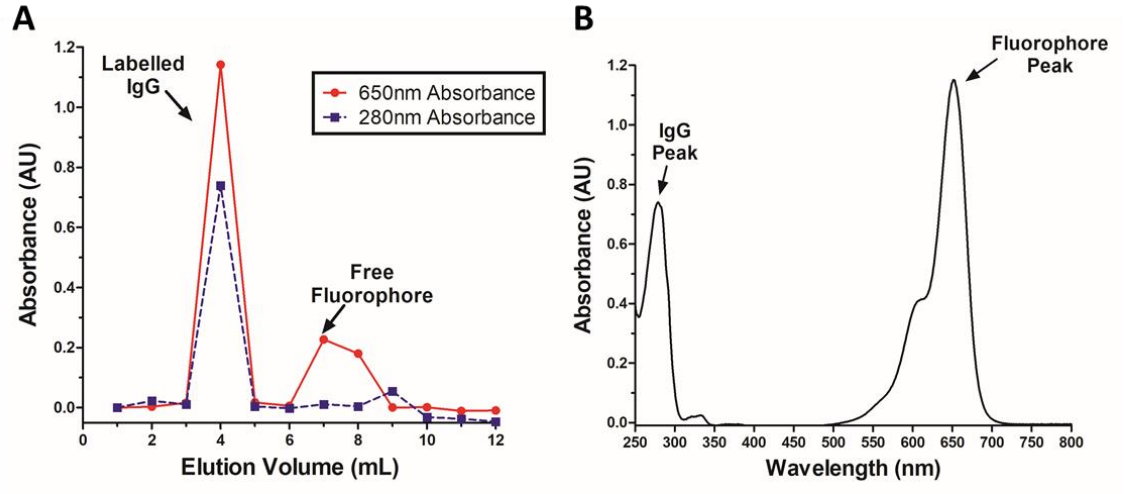

Figure 2.12: The elution profile and UV-vis spectra for the labelling of 8D3-4

Figure A shows the elution of the profile of the 8D3-4 antibody through a Sephadex-g70 column. The red line represents the absorbance of the fluorophore at 650 nm at a given elution volume, while the blue line represents tryptophan absorbance at 280 nm. The full absorbance spectra, from 250 – 800 nm is shown in Figure B. The labelling efficiency in this case was equivalent to 1.38 moles dye/ mole IgG.

To confirm that over-labelling of the 8D3-4 antibody would alter the kinetics of receptor interaction and uptake all three labelling efficiencies were tested in competitive binding and uptake studies in b.End3 cells. Self-competition of 8D3-4 binding to b.End3 cells at 4 ^{o}C produced three different profiles for the fluorescence associated with cells.

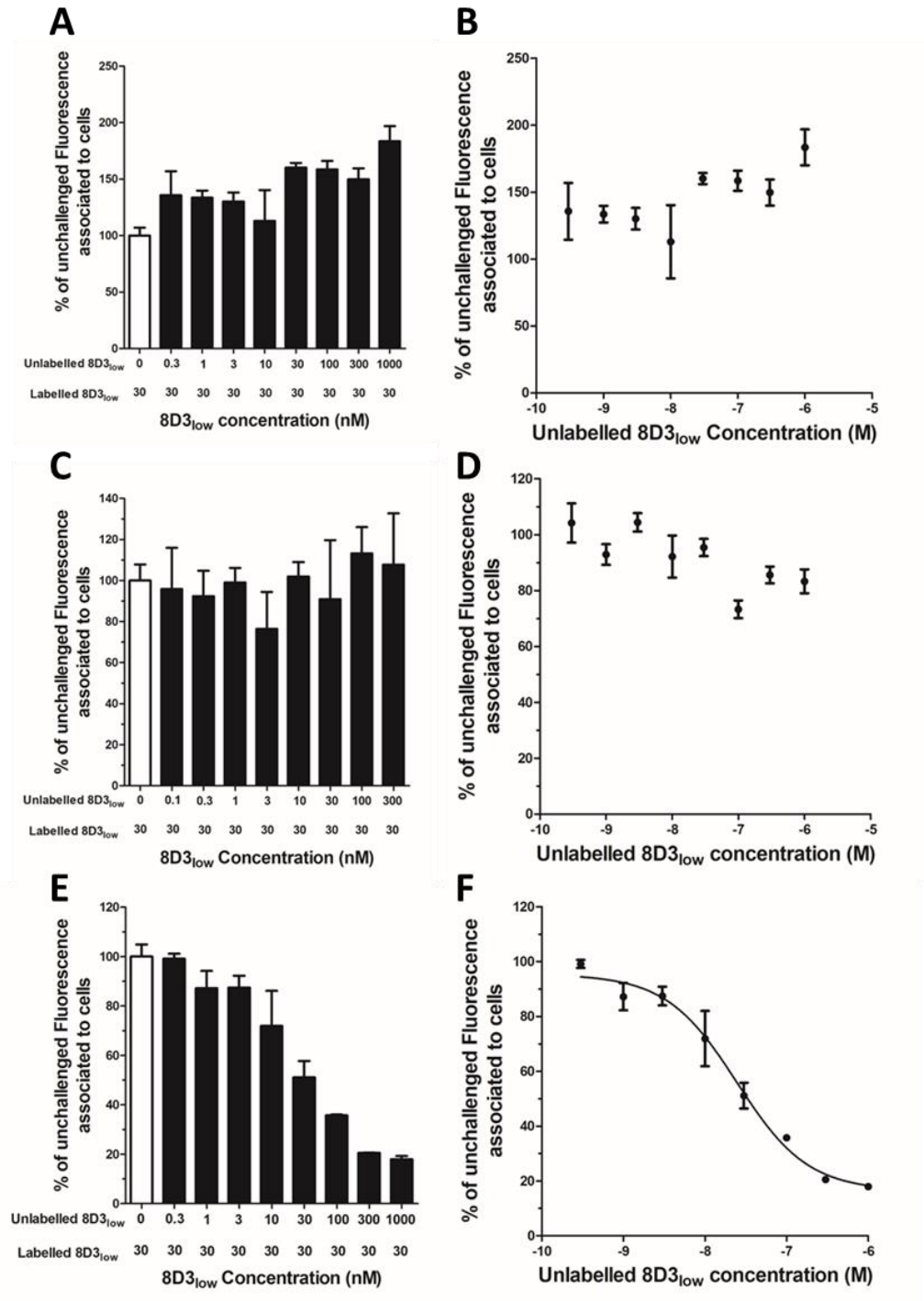

Figure 2.13: The effect of fluorophore labelling efficiency on $8D3_{low}$ ability to bind to the TfR

The figure summarizes the effects of over labelling of an antibody on its ability to interact correctly with the target receptor. Challenge of an over-labelled IgG, as occurs in graphs A-D, with unlabelled antibody fails to decrease fluorescence. In A and B the antibody is labelled with 11.95 moles dye/mole IgG, while in C and D 7.51 moles dye/mole IgG. Figures E and F show appropriately labelled antibody (1.38 moles dye/mole IgG) and self-competition was observed and the binding curve model can be applied. For all labelling efficiencies n = 3, mean +/- std., background of unlabelled cells subtracted from all values prior to analysis.

With the highest over-labelled antibody, the addition of increasing concentrations of unlabelled 8D3-4 caused the cell-associated fluorescence to increase. This may be due to a self-quenching effect of high fluorophore concentrations, in close proximity, at regions of high levels of TfR on the surface of the cells. When unlabelled antibody was added, this would cause a spacing out of the labelled antibodies on the cell surface. The increased space between labelled antibodies is then likely to reduce the effect of self-quenching and so caused an increase in cell-associated fluorescence, as seen in Figure 2.13. The intermediately labelled antibody (7.51 moles dye/mole antibody) showed non-significant, the competition of binding to the b.End3 cell surface. While there was no visible competition of uptake at this labelling efficiency, it is also likely that the over-labelling is still having a self-quenching effect, as seen with the higher labelling efficiencies. However, as the degree of labelling is lower, the self-quenching effects are likely to be less. Therefore, the increased spacing of labelled 8D3-4, on the b.End3 cell surface, with increased unlabelled 8D3-4 concentrations, produces a less observable effect on the fluorescence (See Figure below).

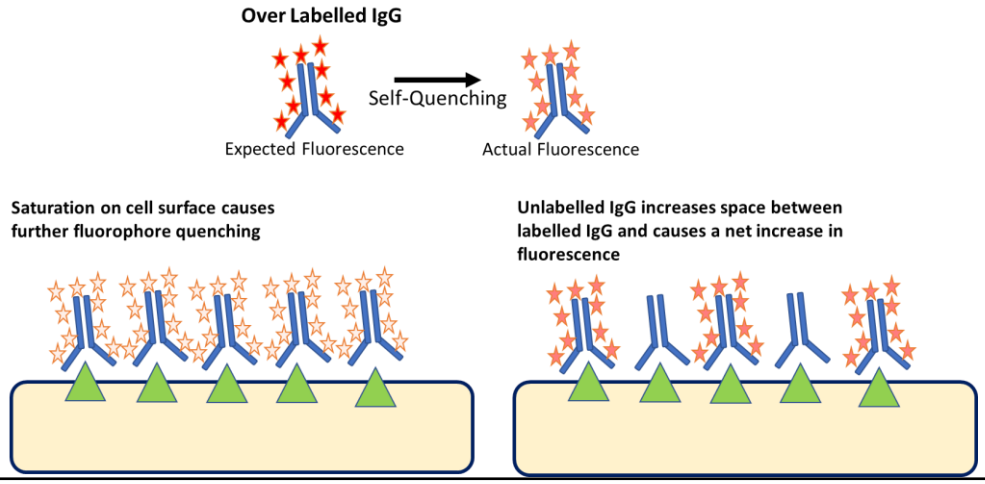

Figure 2.14: The effect of over labelling on antibody fluorescence intensity
The above is a schematic as the potential effect of over labelling an antibody with fluorophore. The schematic at the top of the figure shows how over labelling can cause self-quenching of fluorophores and diminished fluorescence from the labelled antibody. When these over-labelled antibodies are applied to the cell surface, in the case of receptor saturation (lower left), the fluorophore is further quenched by the close proximity of neighbouring antibodies. When unlabelled IgG is applied to cells (lower right) competition occurs, and the space between labelled IgGs increases. This causes the fluorescent intensity from the labelled IgG to increase, resulting in a net increase in cell associated fluorescence.

With the lowest labelling efficiency of 8D3-4 (1.38 mole dye/mole antibody) the binding to b.End3 cells was decreased in the presence of unlabelled 8D3-4. This confirms the binding of 8D3-4 to b.End3 cells as a self-competitive process. Modelling of the binding curve using standard kinetic models calculates the experimental IC50 of the antibody to be 24.6 nM (Figure 2.13.F). As the labelled concentration of 8D3-4 was 30 nM for these studies, this would also provide evidence of the self-competitive nature of 8D3-4 binding. This competition data also serves as proof that the over-labelling of the antibody in the previous studies was contributing to the lack of competition seen in the analysis. The self-quenching of the fluorophore and the potential for a reduction of antibody specificity with over-labelling of the antibody were confirmed by these binding studies with the different affinities.

Pulse-chase analysis of the low-affinity 8D3-4 antibody's uptake and efflux from b.End3 cells confirmed that the uptake into cells is an active process. This was seen by comparison of 37 ^{o}C to 4 ^{o}C pulse phases, with a 10-fold increase in fluorescence associated to cells in the 37 ^{o}C pulse. As with the other transferrin receptor probes, this was to be expected, as previously stated, the turn-over of the TfR from the cell membrane is an active endocytic process. Involving, rac GTPase proteins in the assembly and cleavage of vesicles from the cell membrane, to form the clathrin-mediated endosome.

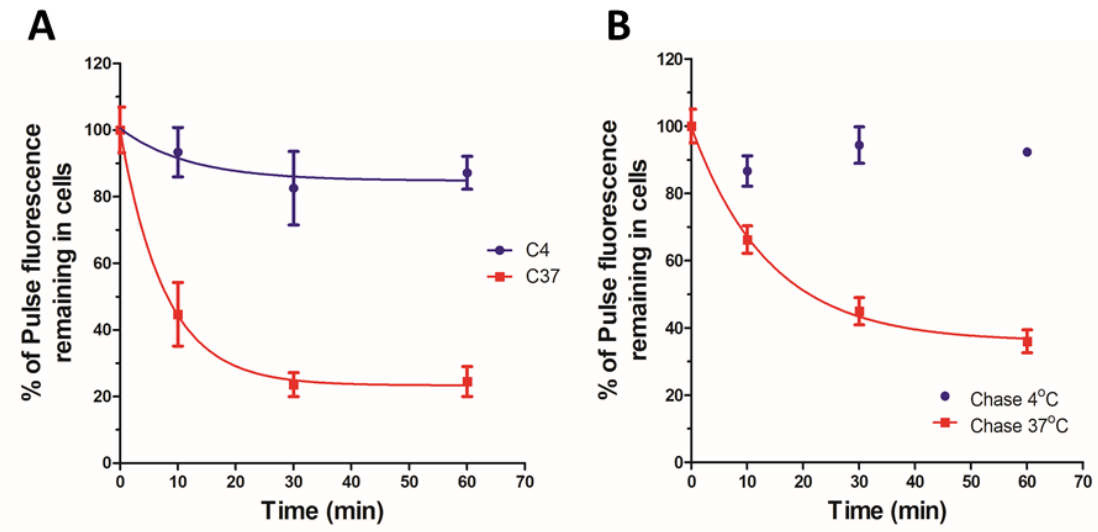

Figure 2.15: The effect of pulse concentration of retention of 8D3$_{low}$ antibody in b.End3 cells
The figure above shows how increasing the concentration of the low affinity antibody decreases the proportional release of fluorescence over the chase. Figure A shows the pulse concentration of 10nM (lower than Kd) while figure B a higher concentration, 100 nM. Blue signifies the chase at 4 ^{o}C, while red indicates the active chase at 37 ^{o}C. Data shown as mean ± std, n = 3 in duplicate, all data points have the auto-fluorescence of blank cells subtracted prior to further analysis.

The 8D3-4 antibody exhibits active efflux from b.End3 cells using the pulse-chase assay (Figure 2.15). All 37 ^{o}C chase time-points show a significant decrease when compared to the 37 ^{o}C pulse associated fluorescence. At all chase time-points, a significant difference was observed between the 37 ^{o}C and 4 ^{o}C chase fluorescence values. Varying the pulse concentration of 8D3-4 again demonstrated how receptor saturation has an impact on the proportion of internalised ligand that can be effluxed from cells. As the labelled 8D3-4 concentration was increased, from 10 nM and then to 100nM, the fraction of pulsed fluorescence remaining cell-associated after a 60 minutes chase at 37 ^{o}C also increased from 24.4% to 36%. However, when comparing these values to those of the 8D3 (high-affinity antibody), the 8D3-4 antibody has a greater efflux potential at these concentrations than that of the 8D3. Due to the lower affinity for the receptor with the 8D3-4 antibody, TfR saturation will not occur until a significantly higher concentration

than the 8D3 antibody. As such, at high concentrations, more of the 8D3-4 antibody will be internalized when bound to the TfR versus the fluid-phase uptake that could occur when the receptors are fully saturated. Therefore the 8D3-4 antibody that is within b.End3 cells still retain the ability to be trafficked throughout the cell.

In Roche and Genentech studies, the high affinity and bivalent forms of the targeting strategy caused down-regulation of the TfR within BMECs *in vitro*. This was believed to be due to both receptors cross-linking, with the bivalent forms, triggering lysosomal delivery signals for the bound TfR (Bien-Ly *et al.* 2014; Yu *et al.* 2014). Additionally, it has been theorised that the high-affinity forms of the anti-TfR antibodies are unable to release from the receptor when they reach the basolateral membrane of BMECs. Whereas, low-affinity antibodies against the TfR, can be taken up into BMECs from the luminal cell surface, undergo a transcellular trafficking process, and release from the receptor at the basolateral membrane.

2.3.7 Permeability Assay

The data presented here relates to the b.End3 cell line and transport studies using different molecular weight dextrans (10kDa and 70kDa), recombinant human holo-transferrin and the chimeric anti- TfR antibody 8D3 (a rat anti-mouse IgG_1 isotype). Figure 2.16.A shows the percentage mass transported of dextran 10kDa across a Transwell insert. Across the blank inserts there was nearly 40 % mass transport, a permeability coefficient of 1539 x 10^{-6} $cm.s^{-1}$. The presence of cells reduced the mass transport over the 90-minute experiment to approximately 13 % of loaded dose, and did not reach an equilibrium over the duration of the study. Dextran 10 kDa had a permeability coefficient of 12.5 ± 6.3 $cm.s^{-1}$ across the b.End3 monolayer. Dextran 70 kDa (Figure 2.16.B) showed a lower permeability coefficient than dextran 10 kDa, with a Papp across the b.End3 monolayer of 9.2 ± 5.1 x 10^{-6} $cm.s^{-1}$. This was expected, as dextran is used in permeability assays as a marker of paracellular permeability and barrier integrity. It is widely believed that any observed dextran in the basolateral chamber is due to paracellular leakage in the system. As the molecular weight of dextran increases, the permeability is expected to decrease, which was seen in this study. The permeability of dextrans across the across the b.End3 monolayer does appear to be slightly high, when compared to the permeability of sucrose across b.End3s in the literature. Omidi et al. (2003) measured sucrose permeability as 19.6±2.6 x 10^{-6} $cm.s^{-1}$ in b.End3 cells. Further studies of b.End3 permeability found lower permeability coefficients for both 10 and 70 kDa dextrans (Li *et al.* 2010), approximately 10-fold lower than the Papp calculated in this chapter. Again demonstrating the limitations of a purely permeability assay based approach to evaluating targeting ligands and delivery systems.

Transferrin permeability studies showed the a permeability coefficient of 4.6±1.8 x 10^{-6} $cm.s^{-1}$ across the monolayer (Figure 2.16.C). This was lower than the permeability of all

other probes used in the study. As transferrin is a targeted ligand it may be possible that the uptake or cell association was greater than that of dextran, and so was internalised rather than exploiting paracellular transport mechanisms. When considering the hydrodynamic radius of transferrin, it is greater that both dextran 10 and 70 kDa, and so this may be a factor influencing the permeability of transferrin. Studies of transferrin permeability across primary BMECs *in vitro* have shown permeability coefficients of approximately 1×10^{-7} $cm.s^{-1}$ (Hersom *et al.* 2017). This is a far lower than the transferrin permeability seen in this study and indicates how limiting permeability assays across immortalised BMECs can be.

The final ligand studied in this chapter was the 8D3 anti-TfR antibody. Across the b.End3 cell monolayer this antibody was found to have a higher apparent permeability than the endogenous ligand transferrin, as shown in Figure 2.16. Indeed, 8D3 had a higher permeability coefficient than dextran 70 kDa, suggesting there may be some form of trafficking enhancement to the delivery of 8D3 across the monolayer. This is to be expected as 8D3 is a targeting ligand and as such has been shown to gain access to the CNS and enhance delivery of a cargo to the CNS.

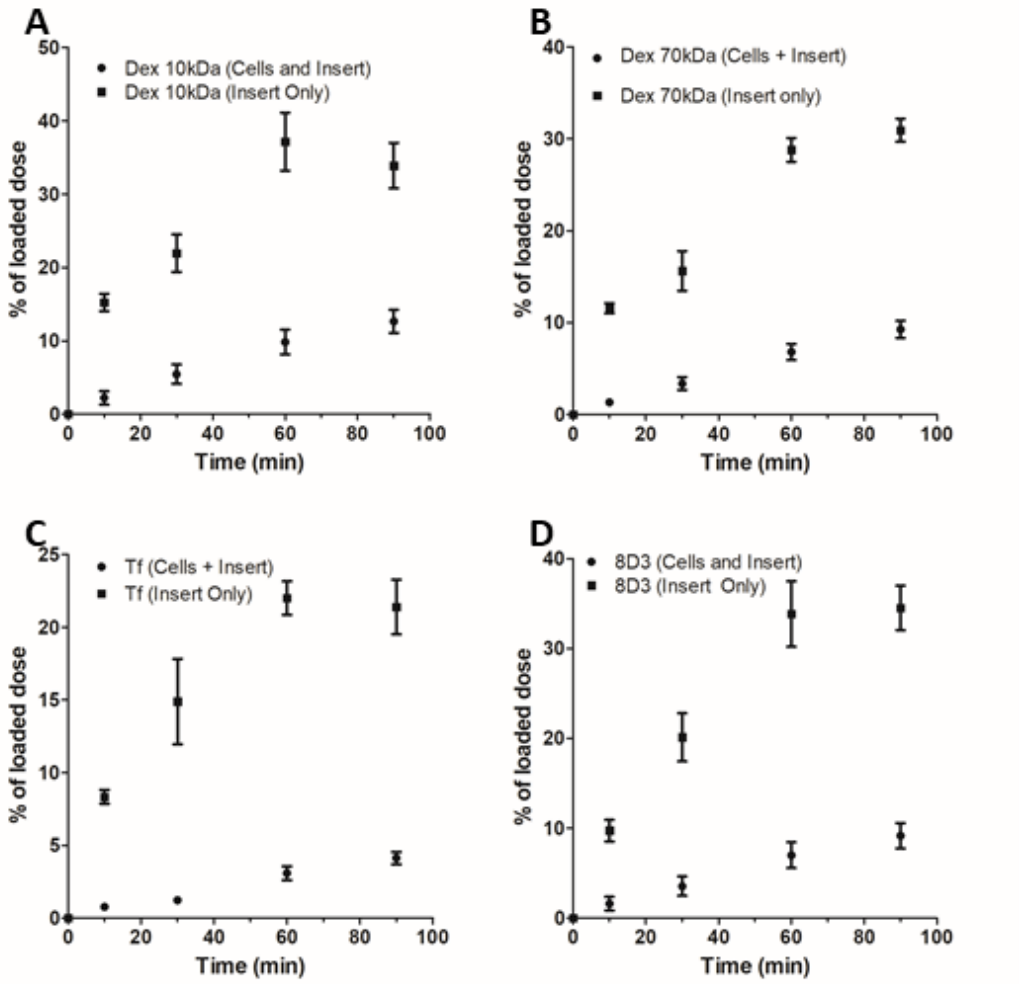

	Permeability Coefficient (x 10^{-6} cm.s^{-1})		
Probe	**Insert Only**	**Cells + Insert**	**Cells Only**
Dextran 10 kDa	1539 ± 263	12.4 ± 6.2	12.5 ± 6.3
Dextran 70 kDa	1169 ± 125	9.2 ± 5.0	9.2 ± 5.1
Transferrin	841 ± 108	4.6 ± 1.8	4.65 ± 1.8
8D3 (anti-TfR IgG)	983 ± 270	15.1 ± 5.4	15.3 ± 5.5

Figure 2.16 Permeability Assay Data, b.End3 cells

The above figure shows the permeability assay data for the following probes: Dextran 10 kDa (A), Dextran 70 kDa (B), Transferrin (C) and 8D3 anti-TfR IgG (D). The studies were performed on Transwell inserts with 0.4 µm pores, 0.33 cm^2 area. Each graph shows the delivery across blank inserts (squares) and inserts with b.End3 cells grown on (circles). Prior to conducting the permeability assay all inserts with cells grown on had a mean TEER value of 12.2 ± 1.6 Ω.cm^2 (n = 40 inserts). The data in graphs A-D is expressed as mean ± std with the following number of replicates. Dextran 10 kDa: insert only n = 4, cells and insert n = 6. Dextran 70 kDa: insert only n = 6, cells and insert n = 13. Transferrin: insert only n = 6, cells and insert n = 15. 8D3: insert only n = 4, cells and insert n = 8.

The table in E summarises the permeability coefficients for the probes used in this study. Looking at the permeability across insert only, the combined cells and insert and the permeability of the b.End3 monolayer only. The data in the table is shown as mean ± std.

From an initial comparison of the permeability coefficients, it would appear to suggest a size-dependent restriction of transport across the barrier, based on the data for dextran 10kDa, dextran 70kDa and transferrin. However, the antibody against the transferrin receptor appears to behave against this trend, showing the highest Papp of all macromolecules used. Both the lower percentage mass transported and the lower Papp for transferrin could serve to demonstrate the recycling process from cells, which is the dominant trafficking pathway of transferrin within cells. The other macromolecules used do not exhibit as defined a process as transferrin and so this data could suggest that transferrin taken in by the cells is then re-released into the apical compartment, thus lowering the rate permeability across the monolayer and insert.

A consideration that must be considered in the permeability assay is the numerous possible routes a molecule could take to cross the barrier system, not only transcellular pathways but also paracellular routes. These will contribute significantly to the observed permeation of the macromolecules. The b.End3 barrier integrity can be questioned based on the low electrical resistance values recorded, $12\Omega.cm^2$, which in comparison to rodent *in vivo* cerebrovascular capillaries resistances, which typically exhibit greater than $1000\Omega.cm^2$ TEER (Crone and Christensen 1981; Crone and Olesen 1982). *In vitro* studies with BBB models of increasing resistance have shown that the permeability of molecules such as dextran is reduced in a manner reflecting the increase in resistance of the system (Gaillard and de Boer 2000). The *in vivo* permeability coefficient of the paracellular marker, sucrose, to the brain is has been observed to be typically less than $0.1x10^{-6}$ $cm.s^{-1}$ (Ohno et al. 1978; Rapoport et al. 1978). The *in vitro* permeability of these macromolecules is greatly above this known *in vivo* marker and therefore raises further questions as to the integrity of the b.End3 monolayer used in these experiments.

2.3.8 Confocal Microscopy of Inserts

	Dextran 10kDa (green)	Dextran 70kDa (red)	Merge
Apical	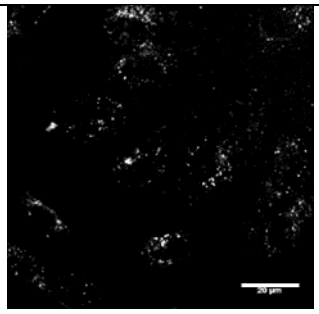	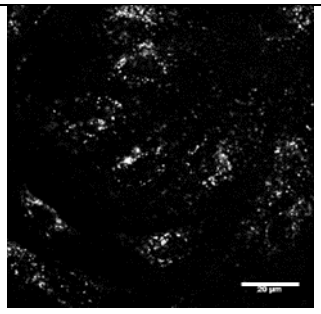	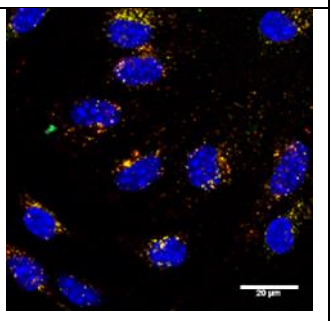
Basal	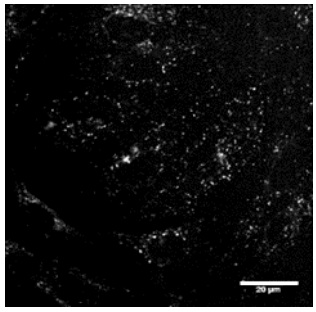	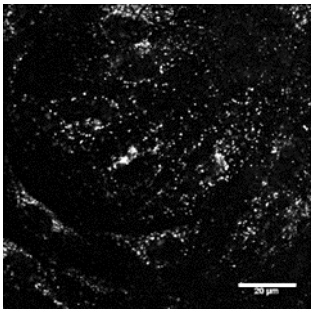	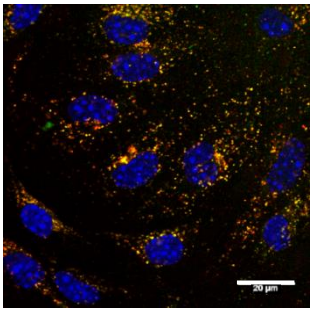

Figure 2.17 – Dextran 10kDa and Dextran 70kDa co-incubation

Cells grown on apical surface of 0.33cm^2 Transwell membrane, pore size = 0.4µm, mean TEER value = 12.2 ± 1.6 Ω.cm^2. Cells are incubated with 200µL of Dextran 10kDa (10µM) and Dextran 70kDa (2.9µM) in the apical well for 90 minutes at 37°C. Frame depth varies by 2.0µm from a z-stack image. Red = Dextran 70kDa, Green = Dextran 10kDa, Blue = nuclear dye Hoechst, scale bar = 20 µm, n =3 in triplicate.

As shown in the Figure 2.17 above, both the 10kDa and the 70kDa dextran can enter into the cell and are present across the entire depth of the cell. The punctate nature of the internalised structures in both greyscale images as well the merge confirms the vesicular localisation of both dextrans in the cells. Within all cells in the field of view there was evidence of both probes, showing uptake across the monolayer as a whole, not just localised regions of cells. There is almost complete co-localisation of the probes within the cells suggesting they are trafficked through common pathways following endocytosis,

as expected for dextran 10kDa and 70kDa combinations. This is due to dextrans non-specific fluid phase entry and therefore localisation many aspects of all endocytic pathways.

	Transferrin 80kDa (green)	**Dextran 70kDa (red)**	**Merge**
Apical	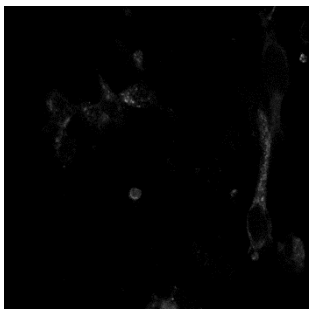	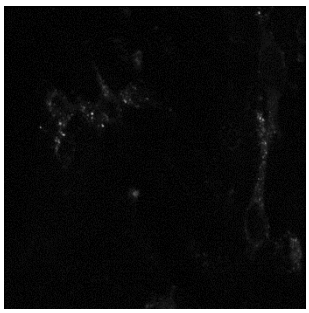	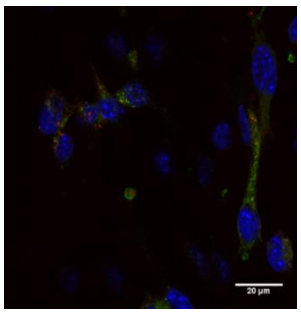
Basal	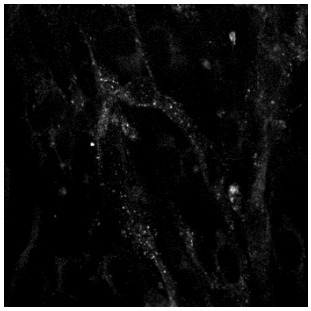	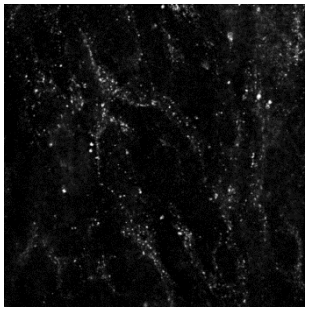	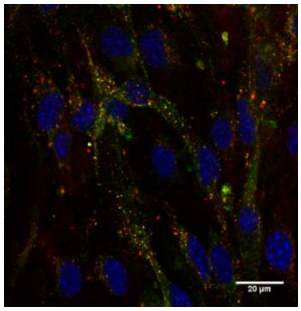

Figure 2.18 – Dextran 70kDa and Transferrin co-incubation in b.End3 cells
Cells grown on apical surface of 0.33cm^2 Transwell membrane, pore size = 0.4 µm, mean TEER value = 12.2 ± 1.6 Ω.cm^2. Cells are incubated with 200µL of Dextran 70kDa (2.9µM) and Transferrin (625nM) in the apical well for 90 minutes at 37°C. Frame depth varies by 2.0µm from a z-stack image. Red = Dextran 70kDa, Green = Transferrin, Blue = nuclear dye Hoechst, scale bar = 20 µm, n = 3 in triplicate.

In these images (Figure 2.18), as in the previous set, there are clear, punctate structures visible throughout all planes of the cells, indicative of vesicular structures and confirming cell entry of the macromolecules. The presence of both transferrin and dextran 70kDa can be seen throughout all cells within the image, confirming a distribution throughout all cells within the monolayer. Colocalisation between the two macromolecules appears to be to a lesser extent than observed in Figure 2.18, dextran 10kDa – dextran 70kDa co-incubation. The regions of co-localisation may be due to a fluid phase encapsulation of

dextran 70kDa molecules within regions of TfR mediated internalisation. There is also the potential for co-trafficking following sorting to regions such as the lysosomes of both transferrin and dextran that are applied to the cells (Baravalle et al. 2005).

Overall the use of confocal microscopy of Transwell inserts to confirm cellular uptake of the probes used was beneficial, as it allowed confirmation of uptake into cells during the permeability assay. However, quantitative comparison of this uptake, with different probes is not possible, due to differences in factors such as laser power variation and fluorescent intensity of different probes. As all probes showed uptake into cells during the permeability assay it would suggest that this methodology is ineffective as a differentiator between ligands. More detailed information on the uptake and loss of probes from the cells was gained in the pule-chase assays performed earlier in the chapter.

2.4 Conclusion

In other studies looking at anti-TfR antibody uptake and transport, in either perfused brains or cell monolayers, the isotype control antibody used also shows uptake into the brain microvascular endothelial cells (Bickel *et al.* 1994). The control IgG used in these studies is raised against tri-nitrophenol and so has no expected activity on BMEC cells. Although uptake of the control is unexpected, it is likely due to fluid phase uptake through non-specific cell processes in a similar manner to the behaviour of dextran.

It should be noted, that in these studies there is no way to determine whether efflux is from the apical or basal membranes. However, the ability to measure the uptake and subsequent loss from the cells is a key tool in the characterisation of potential targeting ligands. Permeability assays, as used here and in other research work are limited by the poor paracellular restriction seen with *in vitro* brain microvascular endothelial cells. Even the “best” *in vitro* models, using primary cells, still show paracellular permeability values that are one or two orders of magnitude worse than the *in vivo* systems (Smith *et al.* 2007;

Gumbleton and Audus 2001). By focusing on endocytosis and efflux trafficking in single cell-type culture, the actual trafficking kinetics can be examined directly.

As seen with the data presented here, non-specific, fluid-phase markers, like dextran are seen to have high permeability across the b.End3 cell model used. However, when looking at the kinetics of uptake and loss of dextran in b.End3 cells, it was observed that the dextran is “trapped” within the endothelial cells. This contradictory evidence was observed with transferrin, where the permeability assay showed lower permeability than the non-targeted dextran. However, in the pulse-chase assay, transferrin was shown to have the desirable characteristic of being able to be effluxed from cells. Also, this assay has shown it could distinguish between probes that have undergone fluid-phase uptake and trafficking versus receptor-mediated endocytic probes, with a defined trafficking pathway. The pulse-chase methodology therefore, provides a more robust and useable measure of a ligands potential to undergo transcellular trafficking.

The pulse-chase technique, in combination with sub-cellular colocalization microscopy, will be used in other work within this thesis to validate the potential of other BBB targeting ligands. In this chapter, we have validated the findings of other transferrin antibody papers, which have shown lowering the affinity for the TfR, improves the capabilities of the delivery system. Exemplified by comparison of the pulse-chase low affinity and high-affinity antibody data. This methodology will be used throughout the remainder of this thesis to characterise the RVG peptide. Further work will also be done to expand on this assay, by combining it with total internal reflection fluorescence (TIRF) microscopy, to view exocytosis events taking place at the basolateral cell membrane.

Chapter 3: Rabies Virus Glycoprotein trafficking through brain microvascular endothelial cells

3.1 Introduction

The Rabies Virus is a negative-strand RNA virus that belongs to the Rhabdoviridae family of viruses in the Lyssavirus genus. Infection of rabies virus is usually following a bite to the skin from an infected animal (Warrell and Warrell 2004). The virus can undergo a retrograde transport process from the site of infection, along the axons of neurons to enter the CNS at the spinal cord and ascend into the brain (Schnell *et al.* 2010). Ingestion of infected meat has also been shown to be a potential route of entry for rabies virus into the body (Lejeune and Hancock 2001), in this situation the virus is absorbed across the mucosal lining of the gut. Studies in mice have shown that there is no observed viral replication in the site of infection. Instead, the viruses migrate along unmyelinated neurones to cell bodies in the spinal cord and transmit between neurones across synapses (Shankar *et al.* 1991). The virus particles must reach neurones of the brain for replication to occur. This ability to pass through a cell without causing infection, it to reach a replication target is also observed in human immunodeficiency virus (HIV) entry across the mucosal epithelial cells of the gut (Amerongen *et al.* 1991). Here the virus crosses the epithelial cells by transcytosis. However, no replication occurred within these cells (Bomsel 1997).

Several studies looking at the uptake mechanism of rabies virus by cells suggested that clathrin-mediated endocytosis is the dominant uptake pathway of the rabies virus. Piccinotti et al. (2013) showed co-localisation of labelled virus particles with GFP conjugated AP2 protein, as a marker of clathrin-mediated endocytosis. It was observed in

these studies that 76% of virus particles appeared in the same region as the AP2-GFP construct and 24% appeared to enter into the cells through an alternate pathway (Piccinotti *et al.* 2013). Earlier studies into rabies infection of cells gave evidence that acidification of the endosome alters the rabies virus glycoprotein (RVG) to facilitate viral aggregation and membrane fusion (Gaudin *et al.* 1993; Finke *et al.* 2004).

Retrograde transport of rabies virus along axons is believed to occur through the interaction of the external surface glycoprotein, RVG, with the microtubule cytoskeleton of the neurone. Transport in this manner occurs at varying rates, but generally between 3-10mm/hr depending on the virus (Sodeik 2000). To facilitate transport viruses will interact with the microtubules, through the dynactin, dynein cytoskeletal proteins within neurones. This movement along neuronal axons can occur in multiple states, through direct interaction of the viral coat protein with cytoskeletal motors. Alternatively, viruses within an endosome may also undergo trafficking along an axon through the interaction of endosomal membrane proteins with neuronal cytoskeletal proteins. The virus can move across neuronal synapses to facilitate its trafficking to the brain and the subsequent transport to other peripheral infection and replication sites.

The complexity of RVG has meant a single receptor has not been identified to mediate rabies virus internalisation. The RVG protein is seen on the surface of the virus particles arranged in a trimer, as confirmed by SEM imaging of rabies virus particles (Gaudin Y *et al.* 1992; Sissoëff *et al.* 2005). Additional studies with other Lyssavirus surface glycoproteins have shown glycoprotein trimers can extend or contract into the virus depending on the local environment (Gaudin *et al.* 1993; Ferlin *et al.* 2014; Albertini *et al.* 2012). However, this has not been performed on the crystalline structure of RVG.

Although initially rabies virus was thought to enter cells through the nicotinic acetylcholine receptor, more recent studies have highlighted multiple potential targets for endocytosis of the virus (Gluska et al. 2014). In this chapter the potential receptor targets for RVG and the evidence supporting them in the literature was examined. Furthermore, the expression of these receptors on cerebral vascular endothelium and therefore their potential use as a target for ligands for brain-specific delivery of nanoparticle and macromolecular entities was examined.

3.1.1 Evidence for Nicotinic Acetylcholine Receptor Binding of Rabies Virus

There have been links shown between the administration of α-bungarotoxin and a reduction in the effects of rabies virus infection *in vivo* (Lentz 1982; Lewis *et al.* 2000). The amino acid sequence of RVG has been shown to have regions of homology with known neurotoxins that can target the nicotinic acetylcholine receptor (nAchR) (Neri *et al.* 1990; Lentz 1985). This evidence has led to the belief that this is a binding site and route of entry of the rabies virus into neuronal cells in muscle tissue. However, in the same article by Lentz (1985), there was a reference to studies which looked at switching the Arg333 residue, of the glycoprotein, for other amino acids and showed this mutation dramatically changed the ability of the virus to infect the host cells (Dietzschold *et al.* 1985). This alteration in uptake would be suggestive of either an alternate receptor for RVG with the host cells or show the structural importance of this residue in the confirmation of the protein as a whole. The binding of rabies virus to isolated *Torpedo* nAchR was shown to be competed by cholinergic receptor antagonists, such as α-bungarotoxin and tubocurarine (Lewis *et al.* 2000; Lentz *et al.* 1986).

This evidence presented above, as well as the accumulation of rabies virus in muscular tissue at the neuromuscular junction, is why the nAchR is believed to have a key role in rabies virus uptake and infection.

The RVG peptide (DYTIWMPENP RPGTPCDIFT NSRGKRASNG) itself is derived from the region 194-222 a.a. of the parent glycoprotein. Within this region is the homologous sequence, shared between RVG and several neurotoxins targeting nAchR, as shown in Table 3.1. Additionally, this peptide has been shown to reduce the binding of loop neurotoxins, such as α-bungarotoxin to isolated subunits of the acetylcholine receptor (Lentz TL 1990).

Table 3.1: Analysis of homology between the Rabies Virus Glycoprotein sequence and the nAchR binding domains of long-chain neurotoxins

1.	**C**	**D**	**I**	**F**	**T**	**N**	**S**	**R**	**G**	**K**	**R**	**Rabies Virus Glycoprotein**
2.	**C**	**D**	**A**	**F**	**C**	**S**	**S**	**R**	**G**	**K**	**V**	**α-Bungarotoxin (*Bungarus multicinctus*)**
3.	**C**	**D**	**K**	**F**	**C**	**S**	**I**	**R**	**G**	**P**	**V**	**κ-Bungarotoxin (*Bungarus multicinctus*)**
4.	**C**	**D**	**A**	**F**	**C**	**S**	**I**	**R**	**G**	**K**	**R**	**α-Cobratoxin (*Naja naja*)**
5.	**C**	**D**	**G**	**F**	**C**	**S**	**S**	**R**	**G**	**K**	**R**	**Long Neurotoxin 2 (*Ophiophagus hannah*)**
6.	**C**	**D**	**N**	**F**	**C**	**A**	**S**	**R**	**G**	**K**	**R**	**Long Neurotoxin 2 (*Naja melanoleuca*)**
7.	**C**	**S**	**P**	**G**	**E**	**S**	**S**	**C**	**Y**	**N**	**K**	**Erabutoxin A (*Laticauda semifasciata*)**

Studies in bovine brain microvasculature have shown the presence of nAchR subunits in the endothelial cells and have linked these to modulation of BBB permeability following activity of nicotine and other nAchR agonists on these receptors (Abbruscato *et al.* 2002).

Further to this, expression of nAchR has been observed in non-cerebral endothelial cells from the human aorta (Macklin *et al.* 1998) which gave evidence of vascular expression of these receptors at other sites within the body. Questioning the selectivity of nAchR as a target for brain-specific delivery. A study using the RVG peptide to look at binding to Neuro-2a and HeLa cells showed a decrease in 4 ^{o}C binding of the peptide in the presence of increasing concentrations α-bungarotoxin (Kumar *et al.* 2007). The same study also showed that siRNA conjugated to and RVG peptide-R9 constructs was able to deliver the siRNA and mediate gene silencing in neurones both *in vitro* and *in vivo*.

The precise internalisation mechanism for the nAchR is not fully understood. Several papers show the involvement of CME, while others implicate caveolin-mediated endocytosis and further suggest lipid raft partitioning as the mechanism for nAchR endocytosis. The receptor regulation of nAchR expression occurs without changes in mRNA levels, indicative of a conservation pathway by which these receptors may be stored within intracellular pools until required (Fenster *et al.* 1999). The data relating to nAchR trafficking has so far been collected using neuronal cell models, and any potential trafficking pathways within BMECs are unknown. Concerning rabies virus infections, while the nAchRs location on post-synaptic cell membranes is understood, evidence of their presence on the pre-synaptic membrane is not clear. As such the role of the nAchR in rabies virus infections is thought to be involved in the initial amplification of the virus in muscle tissue before retrograde transport to the CNS (Lafon 2005).

3.1.2 Evidence for GABA receptor binding

Recent studies looking at nanoparticles decorated with RVG29 showed co-administration with GABA reduced the uptake of these particles. However, the administration of nAchR agonists and antagonists appeared to not affect the uptake of these particles (Liu *et al.* 2009). There is some kinetic data which suggests the loop neurotoxins have a lower

affinity for variants of the $GABA_{A/B}$ receptors than the nAchR, with an affinity in the range of 50-90nM for the GABA receptors (McCann *et al.* 2006; Hannan *et al.* 2015). However, there are currently no crystal or NMR models for this interaction, drawing questions as to these GABA receptors being putative receptors for the RVG29-peptide.

GABA receptors are known to be endocytosed via clathrin-mediated pathways associated with this receptor (Kittler *et al.* 2000; Sato *et al.* 2009), which could contribute to the observed clathrin-mediated endocytosis of rabies virus as a whole (Piccinotti *et al.* 2013). However, as their ability to bind and internalise the RVG-29 peptide is currently unknown. And a binding site for the loop neurotoxins has not been identified and characterised on the GABA receptors, GABA receptors were not investigated as the major target receptor for the RVG peptide.

While the previously discussed receptors appear to be able to bind both the RVG peptide or the whole virus, the next receptors discussed have only been studied with intact rabies virus or rabies virus glycoprotein internalisation. And have not been studied with loop neurotoxins or the RVG peptide.

3.1.3 Evidence for p75NTR binding

The low affinity nerve growth factor receptor, p75NTR, is considered a rabies virus receptor after studies using chimeric IgG Fc domain bound to the p75 protein was shown to reduce rabies infections and viral count *in vivo* (Langevin and Tuffereau 2002). Additionally, co-localisation between fluorescently labelled rabies virus and fluorescent anti-p75NTR IgG has been shown in endosomes of dorsal root ganglion cells of mice (Gluska *et al.* 2014). This co-localisation could be observed throughout the length of neuronal axons, suggesting virons remain bound to the receptor throughout trafficking by this pathway. Studies into the co-localisation of rabies virus with putative receptors also show high percentages of the internalised virus, which did not co-localise with the

receptor of interest in their respective studies, highlighting the heterogeneity of rabies virus entry into cells. Indeed, a study by Jackson and Park (1999) demonstrated that mice deficient in p75NTR were not protected from developing viral encephalitis following rabies infection.

The p75NTR receptor itself has been observed, in neuronal cell types, to alter endocytosis pathways from clathrin-independent to clathrin-dependent for axonal transport of the receptor (Deinhardt *et al.* 2007). This shift appears enhanced by the presence of bound rabies virus at the receptor, further indicating the heterogeneity of cellular infection mechanisms.

3.1.4 Evidence for NCAM-1 binding

An extensive study by Thoulouze et al (1998) showed that in both an *in vitro* and *in vivo* setting the expression of neuronal cell adhesion molecule-1 (NCAM-1) has a role in cellular uptake of rabies virus and transmission of infection. However, they also conclude that there are likely to be other receptor-mediated pathways that can affect viral entry as infections were observed to a lesser extent in knockdown models *in vitro* and *in vivo* (Thoulouze *et al.* 1998). NCAM-1 has several extracellular IgG-like domains that can interact with other NCAM molecules on adjacent cells (Sandi 2004). These molecules maintain the spacing between neurones, glial and other cell types *in vivo*. They also serve a protective role to limit overstimulation of cells by neurotransmitters and can cause cell migration and controlled neuronal plasticity. The NCAM L1 isoform of the receptor has been shown to associate with adapter protein 2 (AP2) in endocytosis, thus considered to undergo clathrin-mediated endocytosis when internalised by cells (Kamiguchi et al. 1998). Other studies have shown that rabies infection and progression can be reduced or delayed by the co-administration of decoy, soluble NCAM-1 receptors or by competition with antibodies against the NCAM-1 receptors (Thoulouze et al. 1998).

In parallel to this, a recent study by Hsu et al (2014) showed that nanocarriers targeted to ICAM-1 appear to undergo transcytosis across the BBB endothelial cells in culture and other component cells of the neurovascular unit. ICAM is another example of a cell adhesion molecule (CAM) family of proteins. In this article, they postulate an endocytic route of transport that is independent of clathrin and caveolin, CAM-mediated endocytosis (Hsu et al. 2014). This idea is one that has been postulated for cell adhesion molecules previously, where anti-ICAM receptor antibodies were shown not to co-localize with markers of clathrin- or caveolin-mediated endocytosis (Muro et al. 2003). As NCAM molecules also belong to the CAM family of proteins, it may be possible that this is an alternate route of entry for the receptor endocytosis into the cell and trafficking through the cytosol in transcytosis.

3.1.5 Modulation of Protein Expression

There are several techniques which can be utilised to downregulate or completely ablate expression of a protein within cells. These techniques can result in the transient knockdown of a protein (siRNA), the generation of a stable cell line with reduced protein expression (RNAi or Ribozyme) or the complete knockout of a protein (CRISPR/Cas9, Transcription Activator-Like Effector Nucleases - TALENs, Zinc Finger Nucleases - ZFNs). All these techniques utilise known biological mechanisms, within eukaryotic or prokaryotic cells as well as viral mechanisms to facilitate genome or transcriptome manipulation. More precisely, CRISPR/Cas9, TALENs and ZFNs, all cause double-strand breaks at targeted sequences within genomic DNA. The latter two methods use a system of endonucleases, bound to DNA-recognition proteins to mediate the cleavage at the target location. However, the complexity of the endonuclease used in the TALEN and ZFN methods means redesigning the enzyme for each target site. Whereas CRISPR/Cas9

uses the same endonuclease, guided to the target by guide RNA (gRNA) and so can screen multiple sequences with ease.

3.1.5.1 CRISPR/Cas9 Genomic Editing

This system of genetic knockout utilises the Cas9 endonucleases from bacteria, such as *Streptococcus pyogenes, S. themophilius* and *Neisseria meningiditis*. These endonucleases are part of an adaptive immune system for bacteria to protect from bacteriophage infection by cleavage of targeted DNA regions, selected for by clustered regulated interspaced short palindromic repeats (CRISPR) RNA (crRNA). This crRNA, typically 20 nucleotides in length – the guide RNA (gRNA), with proximity to a protospacer adjacent motif (PAM), is specific to regions of the infecting organism. Additionally, these gRNAs require trans-activating crRNA (tracrRNA) to recruit the Cas9 enzymes to the site of cleavage. In bacteria, the cleavage of the infecting, viral DNA results in its degradation and preventing the spread of infection. Within the field of genomic editing in eukaryotic cells the cleavage of genomic, double-stranded DNA requires endogenous repair mechanisms to correct the break. In the case of a "clean" double-stranded break, there are no overlapping sequences of DNA present, and so no template to facilitate the repair process. To overcome this and ensure the maintenance of chromosomal DNA the cellular process call non-homologous end joining (NHEJ) will take place to attempt to cleaved DNA (see Figure 3.1 below). The process of NHEJ is error prone and so is likely to result in either the insertion or deletion of regions of DNA around the cleavage site. This error-prone repair mechanism is exploited in the CRISPR/Cas9 technique to result in the expression of a non-functional mRNA and proteins within the cell. Leading to complete knockout of a target gene.

With the CRISPR/cas9 technique, it is possible to remove entire sections of the genomic DNA, using multiple targeted gRNA sequences in the same cell. This approach is known

as a double nickase approach. Into the "gap" in the DNA created it is possible to insert sequences of DNA, rather than allowing the NHEJ approach to take place. In this way, the CRISPR/cas9 technique has been used as a way to produce stable cell lines co-expressing a receptor with a fluorescent protein attached to it. Highlighting the versatility and functionality of the CRISPR/cas9 method in cell biology.

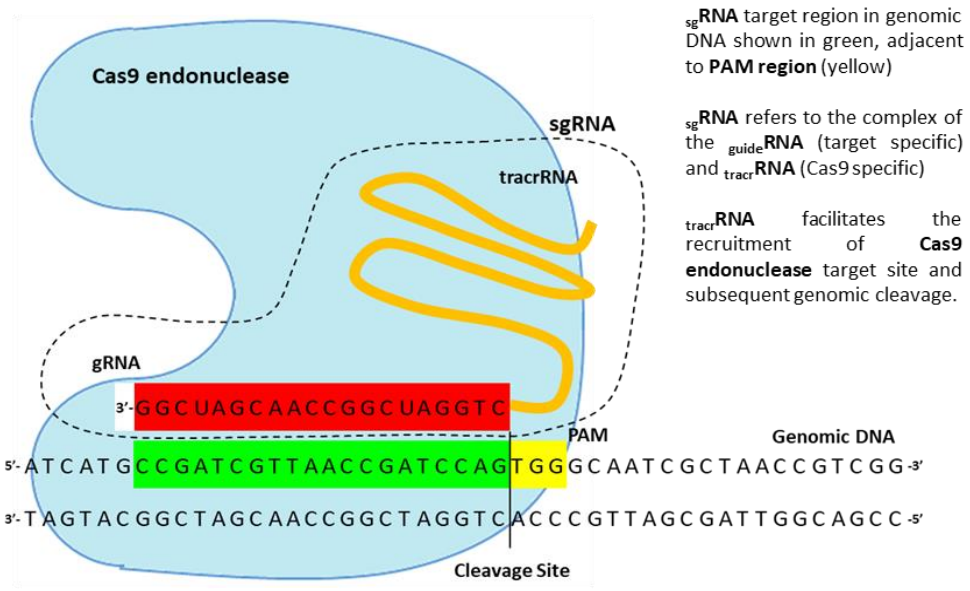

Figure 3.1: CRISPR/Cas9 system for genomic editing
The above figure shows a schematic overview of crispr/Cas9 mediated genomic editing. In this example, the guide RNA (red) sequence recognises the region immediately adjacent to the PAM (yellow). The tracrRNA (orange) is then recognised by the Cas9 enzyme (blue), which is recruited to the site to mediate genomic cleaveage. Adapted from Figure 1 Ran et al. (2013)

Going beyond the field of cell biology and into complex organisms, the CRISPR/cas9 genomic editing tool has been used *in vivo*. Embryonic modification has been used to create disease models for experimental use. While, also allowing for inducible genetic modulation, to trigger a disease causing mutations in adult species and study the effects.

Overall, the CRISPR/cas9 approach in its simplest form offers a rapid and reproducible technique to create stable cell lines with genetic modifications. For the work clarifying the RVG peptide target receptor, this technique will be used as a method to create a permanent knockout of the α7-nAchR. Allowing testing of the target receptor with the brain targeting ligand and clarification of the reports in the literature about the putative receptors for the RVG peptide.

3.1.6 Chapter Aims

To assess the expression of putative receptors for the RVG peptide in BMECs, reverse transcription polymerase chain reaction (rtPCR) were performed in the immortalised, mouse b.End3 cell-line (ATCC) and primary porcine brain microvascular endothelial cells (isolated in the laboratory). Following this, the uptake of the RVG peptide and scrambled sequence control peptide were assessed in BMECs, to confirm the viability of the peptide as a potential targeting ligand for brain delivery, through the pulse-chase assay used in the previous chapter. The final aim of this chapter was to assess the involvement of the α7-nAchR in the uptake of the RVG peptide. The objectives for this chapter were as follows:

1. To confirm the uptake at labelled RVG peptide into BMECs as an active, sequence-dependent and self-competitive process.
2. To assess the uptake and efflux of the RVG peptide within BMEC models.
3. To confirm the expression of putative target receptors within BMECs.
4. To confirm the uptake mechanism of RVG into cells, through competitive uptake approaches and protein expression modulation (siRNA and CRISPR/cas9) .

3.2 Methods

3.2.1 Materials

Dulbecco's modified eagle medium (DMEM) + Glutamax, Medium 199 (M199), Sensicell MEM, fetal calf serum (FCS), horse serum, trypsin-EDTA (0.5%) dissociation solution, Penicillin -Streptomycin (10,000U/mL), dispase, α-Bungarotoxin, α-Bungarotoxin AlexaFluor® 647, Cell Mask AlexaFluor® 647, BODIPY-LACER, Dextran 10kDa Alexa Fluor® 647, gRNA Synthesis Kit, Genomic Cleavage Detection Assay and all custom synthesized DNA oligomers for PCR and RNA oligomers for CRISPR/Cas9 were purchased from Life Technologies, UK. Hoechst, Percoll solution and ethidium bromide were obtained from Sigma Aldridge. All plastics for cell culture were purchased from Fisher Scientific as well as sodium chloride, potassium chloride, magnesium chloride, calcium chloride, disodium hydrogen phosphate, potassium dihydrogen phosphate, sodium dihydrogen phosphate, sodium bicarbonate, D-glucose, bovine serum albumin (BSA) and sodium hydroxide. Type 1 Rat Tail Collagen solution and collagenase-dispase were purchased from Millipore-Merck. See Appendix 1 and 2 for the formulation of the buffers. The RVG derived peptides were synthesised by EZ Bio Labs, the fluorescent label used was tetramethyl rhodamine (Rho).

3.2.2 Overview of brain microvascular cell lines used in these studies

The b.End3 (mouse brain microvascular endothelial cells) cell line was supplied by COMPACT from the GSK source and grown according to their SOPs and replenished from stocks when the cells had undergone 20 passages or 60 days after defrosting the vial. Briefly, the b.End3 cell line is the most commonly used mouse model of the BMECs *in vitro*, these were immortalised by use of a middle T antigen (Williams *et al.* 1989). The characterisation of b.End3 cells showed the expression of key transport proteins and efflux pumps as well as expression of tight junctional proteins (Omidi *et al.* 2003). When these cells are grown on insert membranes the electrical resistance across a confluent barrier, have been observed to be approximately 12.2 ± 1.6 $\Omega.cm^2$, much lower than known *in vivo* values for brain microvascular endothelial cells (Omidi *et al.* 2003).

Table 3.2: Summary of growth conditions for cell-lines and media supplements

Cell Line (Source)	Medium	Serum	Antibiotics	Dissociation Media	Seeding Density
b.End3 (COMPACT)	DMEM + Glutamax (90%)	Fetal Bovine Serum (10%)	NO	Trypsin-EDTA (0.05%)	1 x 10^4 cells/cm^2
PBMEC (Gumbleton Laboratory)	M199 (90%)	Heat Inactivated Horse Serum (10%)	YES	Single passage only	12 x 10^4 cells/cm^2
hCMEC/D3 (VH Bio)	EBM-2 (95%)	Heat Inactivated Fetal Bovine Serum (5%) +bFGF (1ng/mL)	YES	Trypsin-EDTA (0.05%)	2 x 10^4 cells/cm^2
SH-SY5Y (ATCC)	EMEM (45%) + DMEM/F12 (45%)	Heat Inactivated Fetal Bovine Serum (5%) + HEPES (20 mM)	YES	Trypsin-EDTA (0.05%)	2 x 10^4 cells/cm^2

Further, 1st/ 2nd passage porcine BMECs were used that had been isolated by other researchers in the Cardiff Laboratory. These porcine cells are grown on collagen-coated surfaces to promote closer cell-cell contacts in culture (5µg/cm^2, see Appendix 3 for details on the mass and volumes required for coating various cell culture surfaces). Following seeding of frozen cells onto plastic, the PBMECs are washed with PBS 2 days post-seeding to remove debris, and the media was changed every third day until a confluent monolayer was observed. There are many well established primary cell lines used in research, for the modelling of the BBB, including porcine, rat and bovine models. These tend to exhibit phenotypes, at lower passages *in vitro* that are more similar to the *in vivo* vessel endothelium. The establishment of a porcine cell model was first reported and evaluated by Franke et al (1999) and subsequent studies have proven its integrity as an *in vitro* model for the BBB (Franke *et al.* 1999; Smith *et al.* 2007; Patabendige *et al.* 2013). Studies have shown it is possible to produce high trans-cellular resistance values, in excess of 800 Ω.cm^2, in cultures where "switch" media is used to promote tight junctional formation through the removal of serum 3-4 days post seeding (Hoheisel et al. 1998; Franke et al. 1999; Nitz et al. 2003). As well as sucrose permeability ranging between to $1x10^{-6}$ cm.s^{-1} to approximately $3x10^{-6}$ (Smith et al. 2007; Patabendige et al. 2013a), that is comparable to known *in vivo* data for sucrose permeability (Rapoport *et al.* 1978).

The hCMEC/D3 cell line was purchased from Cedarlane and are immortalised human BMEC. These cells are cultured according to the manufacturer's guidelines, between passages 26-35 for use in studies to maintain the BMEC phenotype. hCMEC/D3 cells are grown on collagen-coated surfaces. hCMEC/D3 was established by Weksler et al (2005) through the transformation of isolated frontal cortex endothelial cells with hTERT and SV40 T antigen to immortalise them for use. hCMEC/D3 cells are well characterised for

junctional proteins as well as use in transport studies. They typically show higher trans-cellular resistance values than rodent models as well as an ability to undergo in excess 35 passages while maintaining a non-transformed phenotype (Weksler *et al.* 2005; Dauchy *et al.* 2009). Studies have shown an electrical resistance vary greatly between 40Ω.cm^2 to in excess of 100Ω.cm^2 (Hatherell *et al.* 2011; Daniels *et al.* 2013) and a high sucrose permeability of 26.6x10^{-6} cm.s^{-1}. These TEER values are seen to be close to those of isolated primary cells (Daniels *et al.* 2013), however are still much lower than *in vivo* levels and the inherent "leaky" nature is confirmed by the sucrose permeability.

In routine culture the b.End3 and hCMEC/D3 cell lines are passaged at 80-90 % confluency. Briefly, cells are washed 3 times with calcium- and magnesium-free PBS to remove any cellular debris. Trypsin-EDTA solution (0.05 %) is then applied to cells for 5 minutes to dissociate cells from plastic. Finally, cells are re-suspended in the appropriate culture medium and counted for seeding. Primary porcine cells are typically only used for a single passage and so are seeded from frozen stocks for the desired assay.

3.2.3 RNA Isolation

Cells are grown in T25 flasks until a confluent monolayer can be observed by light microscopy. Trypsin-EDTA (Life Technologies) was used to dissociate cells from plastic and these are pelleted by centrifugation. The media was removed and cells are lysed by the addition of 1 mL TriReagent (Sigma Aldridge) and vigorous pipetting to homogenise the mixture. To this, 0.2 mL of chloroform (Sigma Aldridge) was added and the tube was vortexed then allowed to settle, on ice, for five minutes. The chloroform-TriReagent mix was then centrifuged at 12,000 x g for 15 minutes at 4 ^{o}C to allow phase separation of protein, genomic DNA and RNA. The upper, aqueous phase, containing RNA carefully collected and added to 0.5 mL of isopropanol (Sigma Aldridge) to allow pelleting of RNA by centrifuging at 12,000 x g for 10 minutes at 4 ^{o}C. The RNA pellet was then washed

twice with 70% ethanol and finally re-suspended in between 40-60 µL of DEPC water. The RNA extracts were quantified using Genequant machine and ensuring 260nm:280nm absorbance ratio of ~1.8.

3.2.4 Reverse Transcription Reaction

To an RNase free tube was added oligo (dT), dNTPs (200 µM of each), 500ng of isolated RNA and DEPC water (volumes shown in Table 3.4) and this mixture was heated to 65 ^{o}C for 5 minutes. Following this heating the tube was placed on ice and 5x First Strand Buffer, DTT and RNasin were added to it. The tube was heated to 37 ^{o}C for 2 minutes. M-MLV was added and the tube is placed in the thermocycler with the following protocol in Table 3.3.

Table 3.3: Reverse transcription reaction program

	Temperature (^{o}C)	**Time (min)**
Step 1	25	10
Step 2	37	50
Step 3	72	15
Step 4	4	∞

Following the reaction, the cDNA was diluted one in three with molecular biology grade water and kept at -20 ^{o}C until use.

Table 3.4: Reverse Transcription reaction volumes

Component	**Volume (µL)**
Oligo (dT)	1
dNTPs (10mM)	1
5x First Strand Buffer	4
DTT (0.1M)	2
RNasin (40 units/µL)	1
M-MLV reverse transcriptase (200 units/µL)	1
500ng RNA	Variable
DEPC water	To give 20µL total

3.2.5 Polymerase Chain Reaction

PCR reactions were performed using HotStart Taq Polymerase kit (Qiagen,UK) and the protocol provided. In summary, cDNA from the previous step was added a microfuge tube containing PCR buffer ($MgCl_2$ included), HotStart Taq polymerase, dNTPs, molecular biology grade water and the forward and reverse primers for the gene of interest (Table 3.5). In case of negative controls excess molecular biology grade water was added, equal to the cDNA volume.

Table 3.5: PCR reaction components

Component	**Volume (μL)**
10x PCR Buffer	2
dNTPs (10 mM)	0.4
HotStart Taq Pol (2.5 units/reaction)	0.1
F-Primer (10 μM)	1
R-Primer (10 μM)	1
cDNA	1
Molecular Biology Grade Water	14.5
Total Volume	20

The reactions are run in thermocycler using the protocol in Table 3.6, steps 2-4 to amplify the desired gene products are cycled through 34 times in total. Due to the HotStart Taq polymerase an initial period of 15 minutes at 95 ^{o}C is used to activate the enzyme prior to the amplification process.

Table 3.6: PCR reaction program

		Temperature (^{o}C)	**Time**	
Step 1	**Enzyme Activation**	95	15 minutes	
Step 2	**DNA Denaturing**	94	30 seconds	**34 Cycles**
Step 3	**Primer Annealing**	54	45 seconds	
Step 4	**Amplification**	72	60 seconds	
Step 5	**Final Amplification**	72	10 minutes	
Step 6	**Until Analysis**	4		

3.2.6 Gel Electrophoresis

Amplification products are analysed on a 2% agarose gel. The agarose was dissolved in TBE buffer by rapid heating and stirring. As the agarose solution cools 30 µL of ethidium bromide (EtBr) solution was added and mixture is shaken to ensure an even distribution. Once the agarose solution has cooled to approximately 55-60 ^{o}C it can be poured into the gel cast and allowed to set for ~30 minutes. When set the gel was placed in the electrophoresis tank and TBE buffer was added to submerge the gel and ensure all wells are filled with buffer. PCR products were mixed with an appropriate volume of 5x Gel Loading Buffer (New England Biolabs). From this mixture 7.5 µL was added into a well of the electrophoresis gel and 5 µL of DNA ladder loaded into the first lane of the gel. The gel was run at 90V for 40 minutes to allow separation of the DNA bands. Immediately following the electrophoresis, the gels are imaged using the ChemiDoc (BioRad) with and EtBr filter and minimising saturation of control bands.

3.2.7 Primer Design

Gene accession numbers for mRNA of mouse and porcine genes were found using the Nucleotide search function of NCBI. Primers were designed using the Primer Blast (http://www.ncbi.nlm.nih.gov/tools/primer-blast/) with the melting temperature range between 57-63 ^{o}C, the GC content between 45-60%, primer length between 18-25 bases and a maximum product size of 1000 base pairs. The human primer pairs were predesigned from Life Technologies (Refer to table 3.9).

Table 3.7: Mouse PCR primers

Gene Name	F/R	Sequence 5-3	Amplification Length (bp)
CHRNA3	F	GAA GGT GAC GCT CTG CAT CT	416
	R	CCC TAC GGT GGT GGC AAT AG	
CHRNA4	F	CGT CTA GAG CCC GTT CTG TG	191
	R	GGC CGA GAC CAC TTG TTG TA	
CHRNA5	F	AGC ATG GCC TAC TCT GGA AG	876
	R	TCA GAA ACG AGA GCC CGA TG	
CHRNA7	F	ACA TGT CTG AGT ACC CCG GA	264
	R	AGG ACC ACC CTC CAT AGG AC	
CHRNB2	F	ACT CCT CCC CTA GTA GTT CCA C	777
	R	CAG GTC AAT CTC AGT GCG GT	
CHRNB3	F	CGA GGC TCT GAA CCA CTT GT	356
	R	TGG TCT GTC CAT TCC ACA TCT	
CHRNB4	F	CCG GCC ATG AGG GGT ACG	271
	R	GGC GGT AGT CAG TCC ATT CC	
NCAM-1	F	CCA TCA TGG GCC TGA AAC CT	167
	R	GAG CGC TCT GTA CTT GAC CA	
p75 NTR	F	GGC TAC TAC CAG GAC GAG GA	580
	R	TGT CGC TGT GCA GTT TCT CT	
GAPDH	F	TGT TCC TAC CCC CAA TGT GT	382
	R	TGT GAG GGA GAT GCT CAG TG	

Table 3.8: Porcine PCR primers

Gene Name	F/R	Sequence 5-3	Amplification Length (bp)
CHRNA3	F	TCA CTG GTG ATC CCC CTG AT	272
	R	GAC TCG GTA CGG TTG AAG CA	
CHRNA5	F	GAA CCC GGA TGA CTA CGG TG	340
	R	CGC GCT CAC AAT TTC CCA TT	
CHRNA7	F	TGA TGT GCA GCA GTG CAA AC	847
	R	CCG CAC CTC CTC CAA AAT CT	
CHRNB2	F	CTC CCA CCA CTT TAG GCG AG	185
	R	TGG GCG GAT AAG CTT GTT GT	
CHRNB3	F	AAC GTT CAC CAC CGA TCC TC	573
	R	CCC TGA GAC CAA CAC AGG AC	
CHRNB4	F	GGA ACA GCT CCC GCT ATG AG	276
	R	ACC ATG TCG ATC TCC GTG TG	
NCAM-1	F	TCC ATA GCC CTC CTC CAC AA	483
	R	CGG CTT TTC CAC ACA GGT TG	
p75NTR	F	GGA CTC CAC TGG AAG CCG AG	157
	R	GTG TAC ATG CCT GTG GGA CA	
B-actin	F	ACT ATC GGC AAT GAG CGG TTC	288
	R	AGA GCC ACC AAT CCA CAC AGA	

Table 3.9: Human Primers

Gene Name	F/R	Sequence 5-3	Amplification Length (bp)
CHRNA1	F	TCC CTG TTA CCC ATA TTG ATT TCC T	503
	R	TCT GTT AGA AGG AAC TGA GGC TTA T	
CHRNA3	F	TTT AAG CAC AGT GGG CCA AAA AC	248
	R	GGG AAG TAA AAC CAG GCT GAT TCT	
CHRNA4	F	ATG CTG CAG GAG CTC TTG TAA ATG G	505
	R	GTG TGT CAG GCA CTC GTA GGT	
CHRNA5	F	CTT AAG GAG CTC AGC ATA TTC CAA T	506
	R	ATA TGC ACA CCT ACC ACA TCC A	
CHRNA7	F	GGG CCA GGT TTG GGA TCT C	266
	R	GAG TGG TTG CGA GTC ATT GG	
CHRNB2	F	CCT CAT GTT CAC CAT GGT GCT	270
	R	AAG CAC GTG CAG GAG TCG	
CHRNB3	F	GTG GTT GGG ACA TTA GAT GCA TTT	546
	R	GAG CTC AAG CCT GGA CCT ATG ATC	
CHRNB4	F	TTG ATG GCC AAT GCT CAC ATA TTT ACT TA	258
	R	AGT ACG TGG CTA TGG TGG TG	
NCAM-1	F	AAT GGC AGT AAA AAG AAT TTG AGA GC	503
	R	AAG CTG ACA CTT GTT GGC ACA T	
p75 NTR	F	GAC GGA GGC CTC TAC AGC	260
	R	CAC AGA CTC TCC ACG AGG TC	
GAPDH	F	CCA ACG TGT CAG TGG TGG A	268
	R	CCT GCA CTT TTT AAG AGC CAG TC	

3.2.8 Confocal Microscopy of RVG Uptake

All imaging studies were performed on live cells using the Leica TCS SP5 inverted, confocal microscope. In these studies b.End3 cells were seeded in MatTek imaging dishes at a density of 10,000 cells/cm^2 and allowed to grow until a confluent monolayer was observed. The culture media was then aspirated from cells and the cells were incubated with DMEM, HEPES with 0.1% bovine serum albumin (BSA) for 30 minutes at 37 ^{o}C to remove serum proteins from cells. DMEM + 0.1% BSA was then removed and cells incubated with RVG-rhodamine (5-100 μM) for 60 minutes at 37 ^{o}C or 4^{o}C. Cells were

then stained with Hoechst (0.1µg/mL) for 5 minutes, washing three times with PBS before imaging. When comparing the uptake of RVG-rhodamine with the scrambled sequence peptide, a concentration of 5 µM was used for comparison for a 1 hour pulse duration at 37 ºC. Cells were then stained with Hoechst (0.1µg/mL) and Cell Mask Alexa Fluor® 647 (diluted 1 in 1000 from stock) for 5 minutes. The cells were then washed 3 times in PBS prior to imaging. Cells were imaged live, in MatTek glass bottomed dishes, this allowed Z-stack images were taken through the cells at 0.75 µm intervals. These single slices were then combined to for a maximum projection image post acquisition using Fiji software. With the fluorophores used the lasers and corresponding emission settings were as follows: Hoechst - Excitation 405nm, Emission 420-440nm; Rhodamine - Excitation 544nm, Emission 560-600nm; Alexa Fluor® 647 - Excitation 633nm, Emission 650-680nm.

Table 3.10: RVG peptide sequences

Peptide Name	**Peptide Sequence**
RVG-[Rhodamine]	Rho-DYTIWMPENPRPGTPCDIFTNSRGKRASNG
RVG Unlabelled	DYTIWMPENPRPGTPCDIFTNSRGKRASNG
Scrambled Peptide-[Rhodamine]	Rho-DSRGTMPYANTWFTPGSRNECKPIDPRGNI
RVG δC-[Rhodamine]	Rho-DYTIWMPENPRPGTPADIFTNSRGKRASNG
α-Bungarotoxin	YTIVCHTTATSPISAVTCPPGENLCYRKMWCDAFCSSRGKVVELGCAA TC PSKKPYEEVTCCSTDKCNPHPKQRPG

3.2.9 Fluorescence Plate Reader and Flow Cytometry Assays of RVG and α-Bungarotoxin binding and uptake

To quantify the binding and uptake of rhodamine-labelled RVG derived peptides into cells a fluorescence plate reader assay has been developed. For these studies b.End3 or hCMEC/D3 cells were seeded into 12-well plates at a density of 10,000 cells/cm^2 or 25,000 cells/cm^2 respectively and allowed to grow until confluency. The culture media was aspirated from cells and the cells are then incubated with Krebs-Ringer buffer with 0.1% bovine serum albumin (BSA) for 30 minutes at 37 ^{o}C to remove serum proteins from cells prior to assessing uptake or binding. When comparing the uptake of the RVG-rhodamine, scrambled sequence-rhodamine (SCRAM) and the delta C peptides (sequences in Table 3.10) 10 µM of the peptide was applied to the cells for 1 hour at 37 ^{o}C. Following this, cells were washed with PBS and rapidly dissociated using high concentration Trypsin-EDTA (0.125%) solution at room temperature. Cells were then pelleted by centrifugation at 1000 xg for 10 minutes at 4 ^{o}C and lysed using 0.1M sodium hydroxide solution for 1 hour on ice. Lysates were centrifuged at 10,000 xg before quantification of rhodamine fluorescence within the lysates.

In binding assays cells were dissociated from plastic and concentrated to 10^6 cells per mL in Krebs-Ringer buffer. A concentration range of α-Bungarotoxin-Alexa 647 used was 0 – 1000 nM, which was applied to cells for 1 hour at 4 ^{o}C. Cells were then washed by centrifugation at 300 xg for 10 minutes and re-suspended in PBS for analysis of cellular associated fluorescence using flow cytometry. Non-linear regression to estimate B_{max} and the Kd were performed in Graphpad Prism 5. B_{max} is the maximal binding that can occur within the system, when there is 100 % occupancy of the receptor with the ligand.

3.2.10 Pulse-Chase Fluorescent Plate Reader Assay

As in the previous chapter, with transferrin receptor ligands, the pulse-chase assay was used to assess the ability of the RVG peptide to be endocytosed and released from the BMECs *in vitro*.

3.2.11 siRNA Knockdown of α7nAchR

The protocol for siRNA transfection and Western Blots are given in the previous chapter in sections 2.2.3 and 2.2.4 respectively. The siRNA sequences against the α7nAchR are shown in the Table 3.11 below and the primary antibody, rabbit anti-human-α7nAchR was obtained from Sigma Aldridge, UK, and used at a dilution of 1 in 250. The secondary antibody was an HRP-linked anti-rabbit IgG (Cell Signalling, UK) diluted to 1 in 10,000 of the stock.

Table 3.11: siRNA sequences used in α7nAchR knockdown studies

siRNA Name	siRNA Sequence
CHRNA1	GUACCUGCCUCCAGGCAUA(dTdT)
CHRNA2	CCACGCCUGGUUCUGUACA(dTdT)
CHRNA3	AGCCAGCAAUUCUGAGUUC(dTdT)
Luc-1	CGUACGCGGAAUACUUCGA(dTdT)

3.2.11 CRISPR/Cas9 Genomic Editing

3.2.11.1 gRNA Design

The guide RNA sequences were designed in accordance with the requirements for recognition by both the Cas9 enzyme and the DNA. The guide sequences were designed to be between 18-20 base pairs in length, to reduce the chance of cross-reactivity with

other sequences of DNA. Secondly, the target sequence must be immediately downstream of a protospacer adjacent motif (PAM). This three-base sequence, 5'-NGG-3' must be present for the Cas-9 enzyme, from *Streptococcus pyogenes*, to recognise and cleave the DNA at the target site. Cas9 enzymes from other species of bacteria have different PAM requirements, for example 5'-NNAGAA-3' (*Streptococcus thermophilius*) and 5'-NNNNGATT-3' (*Neisseria meningiditis*). Due to the requirement of the Cas9 enzyme to recognise a PAM, the Crispr/Cas9 can be targeted to any PAM site within the target species genome. The PAM sequences must immediately follow the 20-nucleotide, guide sequence, but are not included in the 20 bases.

The off-target activity of the selected guide sequences was assessed within the design tools. For these studies, the guide sequences were designed using Thermo Fishers own GeneArt CRISPR Search and Design Tool. For designing guide sequences against *Homo sapien,* α7-nAchR, the gene ID (CHRNA7) and species were input into the application. The search identifies the gRNA sequences from a database of over 600,000 potential sequences and ranks them based on cross-reactivity with other genomic sites. The design tool also provides the PAM motif adjacent to the target site. From this information, it was possible to confirm the locations within the genomic sequence of the α7-nAchR. This allows for the design of primers, around the cleavage site for the detection of genomic cleavage at a later stage of the Crispr/Cas9 process.

3.2.11.2 gRNA Synthesis

This was done using the gRNA Synthesis Kit supplied by Thermo Fisher. Briefly, this process comprised three main steps: assemble the gRNA DNA template, *in vitro* transcription of the DNA template to form the gRNA, purification of the gRNA products.

To assemble the gRNA template, the pre-designed targeting oligonucleotides mixture was combined with the tracrRNA Fragment and T7 primer mix. The custom oligonucleotides are designed to anneal to the tracrRNA fragments and this product can be amplified by Taq polymerase and the T7 primers to produce the final template for transcription. Following the PCR amplification of the template sequences, agarose gel electrophoresis was performed to ensure the products were the correct size before proceeding to the second step. The expected product size at this stage was 120bp.

The gRNA template, from stage 1, was then incubated with TranscripAid Enzyme Mix and NTPs (ATP, CTP, GTP, UTP) at 37^{o}C for 3 hours. This was longer than the recommended 2 hours, however it led to an increased yield of the gRNA product. Any template DNA remaining after the *in vitro* transcription (IVT) stage was removed by incubation with DNase I for 15 minutes at 37^{o}C. Following this, the purity of the gRNA was assessed by agarose gel electrophoresis. For this, 0.5 μL of the IVT product was diluted in 10 μL DEPC water and then with 2x RNA loading buffer (10 μL). This mixture was heated to 70^{o}C and then chilled rapidly prior to gel loading. The predicted product size for this step is 100 bases, 20 from the guide sequence and 80 from the TracrRNA.

Having created the gRNA and degraded the DNA template, the gRNA was purified using the gRNA Clean Up Kit. This was done using micro-centrifuge, RNA purification columns, in combination with buffers to remove all unnecessary dNTPs, enzymes and salts from previous reactions. Briefly, gRNA products from the previous steps are diluted in water to give a final volume of 200 uL. To this, 100 uL of Binding Buffer and 300 uL of ethanol was also added and the mixed by pipetting. The mixture was added to the GeneJET purification column and centrifuged for 30 seconds at 14,000 xg. Flow through was discarded and 700 uL of Wash Buffer 1 is added, this was recentrifuged using the same settings as the previous step. The flow through was discarded and Wash Buffer 2 is

added to the upper chamber and centrifuged as before. Prior to elution of the RNA a final centrifuge was carried out of the empty GeneJet column to remove any excess residues from the tube. To elute the RNA 10 uL of nuclease free water was added to the column, and placed in a fresh Eppendorf tube. This was centrifuged for 60 seconds at 14,000 xg to elute the gRNA from the column. The concentration of the gRNA was then quantified by UV/VIS spectrophotometer and stored at -80 ^{o}C until required.

3.2.11.3 Cas9-GFP plasmid preparation

The Cas9-2A-GFP plasmid was purchased from Addgene, USA (Addgene ID: 48138) as an E.coli stab culture in agar. All bacteria work was performed in proximity to a Bunsen burner flame to ensure a sterile working field and to avoid contamination of the samples, waste was collected separately and autoclaved prior to disposal. To isolate the plasmid for transfection into mammalian cells, E.coli from the stab culture was plated onto LB Agar plates containing 100ug/mL kanamycin. The E.coli streaked onto the agar plate was left overnight at 37^{o}C to allow the growth of single colonies.

3.2.11.4 Bacterial Expansion

Single colonies of bacteria are then “picked” from the LB Agar plate and incubated in 5 mL of LB Broth, containing 100 ug/mL kanamycin, in a 15 mL Eppendorf centrifuge, for 8 hours at 37 ^{o}C under agitation. This allowed the bacteria to enter the log-phase of growth. At this stage, the media appears cloudy when viewed. To allow further expansion of the E.coli for plasmid isolation, 1 mL of the bacteria solution was taken and incubated in 100 mL LB Broth containing kanamycin. The bacteria are incubated overnight for ~16 hours to allow for maximal growth prior to plasmid isolation. After this step, the solution was opaque due to the presence of high bacterial numbers present. This was taken forward into the plasmid isolation stage.

To prepare bacterial stocks for future use, after the single colony had been expanded in 5 mL of LB Broth, the remaining solution was diluted 1:1 with 80% sterile glycerol solution. From this, 1mL aliquots were taken for storage at -130 ^{o}C in cryovials.

3.2.11.5 Plasmid Isolation

Plasmid isolation from bacterial cells was done using the Qiagen Plasmid MidiPrep Kit, using the protocol provided. Briefly, the solution of expanded bacteria from the previous stage was first centrifuged at 5000 xg for 30 minutes at 4 ^{o}C to pellet and isolate the bacterial cells from the culture media. The pellet was then resuspended in the buffer provided (P1) and incubated with alkaline lysis buffer (P2) for 10 minutes at room temperature. The lysis reaction was stopped by the addition of neutralising solution (P3) and inversion of the reaction tube to ensure all cells are covered.

Cellular debris was removed by filtration, through the provided filter cartridge, this initial stage removes cell membranes, leaving a solution containing the bacterial DNA and cytosolic proteins. The extruded supernatant was placed into a DNA binding column, that specifically allows for the binding of plasmid DNA, while all other components of the solution will pass through the gel matrix. The bound plasmid was washed three-times with the provided wash buffer (QC buffer) to ensure non-essential components of the bacteria have been eluted from the column. To elute the plasmid DNA itself, 8 mL of elution buffer (QBT buffer) warmed to 60 ^{o}C was added to the column. The eluted solution kept for further preparation steps.

To concentrate the plasmid DNA to a useable concentration, isopropanol was added to the eluted solution to precipitate the DNA. The solution was centrifuged at 13,000 xg for 30 minutes at 4 ^{o}C to pellet the DNA. The remaining solution was discarded and replaced with 75% ethanol to wash the DNA pellet. The pellet in 75% ethanol was centrifuged a

further three times, at 13,000 xg for 30 minutes at 4 ^{o}C, replenishing the solution after each centrifuge step. Following the final centrifuge step in the ethanol solution, the solution was aspirated from the plasmid DNA pellet and the pellet itself air-dried for ~15 minutes. The plasmid DNA pellet was then resuspended in 50 uL of Tris-Buffer (pH 7.4) and stored at -20 ^{o}C until use. The DNA concentration was quantified by UV-spectrophotometry. Typically, from this protocol yields were close to 1 ug/uL.

3.2.11.6 Mammalian Cell Transfection

The Cas9-GFP plasmid and the gRNA sequences were co-transfected into cells using Lipofectamine 3000 (Life Technologies). Optimization was performed on confluent monolayers of cells in 96 well plates to confirm the optimal DNA concentration for the final transfection for analysis. This optimization found that for transfection in 6-well plates 2.5 ug of DNA per well was optimal for maximum transfection efficiency. This was added to the cells in Optimem containing 2.5 uL of Lipofectamine 3000 and 5 uL of P3000 reagent. The gRNA was added into this complexation mixture to give a final mass per well of 200 ng. These masses of DNA and gRNA ensure an almost 1:1 molar ratio of the oligonucleotides for transfection. To transfect the cells the volumes and masses of transfection reagent and oligonucleotides, summarized in the table below, were added to Optimem (750uL per well) for 10 minutes to allow lipid complexation with the DNA and RNA. Following the complexation, the normal culture media was aspirated from cells and replaced with the Optimem-DNA-RNA-Lipofectamine 3000 solution. Cells were incubated with this for four hours without the presence of serum, to allow maximal uptake of the complexes into cells. After four hours 750 uL of media containing 20% serum was added into the transfection wells, to give a final serum concentration of 10% in the wells. The cells are cultured for a further 48 hours before analysis of transfection efficiency by genomic cleavage detection assay or cell sorting and clonal cell line generation.

3.2.11.7 Genomic Cleavage Detection Assay

To confirm that the gRNA and Cas9 enzymes had been taken up into cells and had mediated genomic cleavage within the population, the genomic cleavage detection assay (GCD) was used. The GCD assay used here for these studies was from Thermo Fisher. For this protocol, transfected cells in 6-well plates were dissociated from plastic using trypsin-EDTA solution (as per standard cell culture protocols) and pelleted to removed serum proteins from the cells. The cell pellets could then either be stored at -20 ºC or directly lysed to isolate the genomic DNA for analysis. For lysis, the cell pellets were resuspended in 50uL lysis buffer provided in the kit, containing protein degrader solution (25:1 ratio lysis buffer: protein degrader). The cell-lysis solution was then incubated in the thermocycler for 15 minutes at 68 ºC, 95 ºC for 10 minutes, then 4 ºC to end the reaction.

Table 3.12: PCR Reaction Mixture for GCD Assay

Component	DNA Sample	Control Reaction
Cell Lysate	2 µL	-
10µM F/R primer mix	1 µL	-
Control Template & Primers	-	1 µL
AmpliTaq Gold® 360 Master Mix	12.5 µL	12.5 µL
Water	9.5 µL	11.5 µL
Total Volume	25 µL	25 µL

After cell lysis, the genomic DNA adjacent to the potential genomic editing site was amplified by PCR reaction. For this, primers are designed to produce products of ~600 bp, that uneven spacing around the genomic cleavage site, i.e. the forward primer is 200 bp from the gRNA site, the reverse was 400 bp from the gRNA site. This was important for the final detection step of the GCD process. Other primer criteria are as standard for primer design: 20 bases in length, 45 – 55 % GC content, melting temperature of 55 – 58 ^{o}C.

The lysates undergoing PCR are added to the reaction mixture as shown in the Table 3.11 below. Samples are prepared on ice and transferred to the thermocycler for amplification, using the protocol shown in Table 3.13.

Table 3.13: PCR reaction GCD Assay

Stage	Temperature	
Enzyme Activation	95 ^{o}C	
Denaturing	94 ^{o}C	**40 cycles**
Annealing	55 ^{o}C	
Amplification	72 ^{o}C	
Final Amplification	72 ^{o}C	
Finish	4 ^{o}C	

Following amplification of the genomic DNA regions the integrity of the reaction was confirmed by agarose gel electrophoresis. Briefly, 1.8% agarose gels were cast by boiling agarose in TBE buffer to dissolve and pouring into the gel mould, while in the liquid form 30 uL ethidium bromide was added to the gel for DNA staining. Once the agarose gel has been cast and was set, 5 uL of PCR product was mixed with loading buffer (5:1 ratio) and

added into a well in the gel. In addition, a 100bp DNA ladder was added to the first row of the gel to allow measurement of DNA product length. The gel was run at 80 V for 45 minutes to allow product separation. After this, the gel was imaged on the ChemiDoc imager, using the ethidium bromide settings.

Having confirmed the product of the PCR was the correct size and only a single product band was present, the sample can then be taken into the genomic cleavage assay stage. To set this up, 3 µL of DNA product was added to 1 µL of 10x Reaction Buffer and 5 µL of water. This now undergoes a re-annealing reaction, where the tube was heated to 95 ^{o}C for 5 minutes to break apart double-stranded DNA, the reaction was then cooled slowly (0.1 ^{o}C/s) to 25 ^{o}C. This allows the formation of hetero-duplexes of DNA with mis-matched DNA sequences. Adding the Detection Enzyme now allows for the detection of the % occurrence of DNA mis-matches within the sample. To control this process, every sample has a negative control, where water (1 uL) was added in place of the Detection Enzyme (1 uL) at this stage. For the reaction to take place the samples were kept at 37 ^{o}C for 1 hour and then placed at 4 ^{o}C to finish the reaction.

Samples were immediately analysed by gel electrophoresis to confirm that genomic cleavage has taken place. The protocol for this was the same as described above to verify the PCR reaction product, with the only modification being that the entire 10 uL of the GCD product was added at this stage. Once the gel has been run and imaged the fraction cleaved can be calculated by measuring the sum of the intensities of the cleaved bands in a lane compared to the total DNA intensity of all bands in a sample (Equation. 3.1.). From this the % cleavage efficiency of the products was be calculated using Equation 3.2.

Equation 3.1:

$$Fraction\ Cleaved = \frac{Sum\ of\ Cleaved\ Bands}{Sum\ of\ Cleaved\ Bands\ and\ Parental\ Bands}$$

Equation 3.2:

$$Cleavage\ Efficiency = 100 \times \left(1 - \sqrt{1 - Fraction\ Cleaved}\right)$$

3.2.11.8 Cell Sorting and Cell Line Generation

Having detected that genomic cleavage has occurred, using the gRNA sequences prepared against the α7nAchR, in the co-transfection cells, the next stage was to produce a clonally isolated cell line that has undergone genomic editing. To do this, SH-SY5Y cells were seeded into 6-well plates at a density of 100,000 cells/cm^2, to produce a confluent monolayer 24 hours post-seeding. Cell were then co-transfected (as described above) with the gRNA and Cas9-GFP plasmid and allowed to grow for a further 48 hours post-transfection. Where in the previous section cells were then dissociated and lysed, cells were dissociated from the 6-well plate, but prepared for flow assisted cell sorting (FACS). Briefly, grown in the 6-well plates were washed three times with PBS to remove serum proteins and Ca^{2+} ions from the cells and incubated with trypsin-EDTA (0.05%) for 5 minutes until dissociated. The dissociated cells were then resuspended in PBS containing 5% serum and pelleted by centrifugation at 500 xg for 5 minutes. The centrifugation steps were repeated three further times to remove the dissociation solution from cells and any cellular debris. Cell pellets were then resuspended in PBS at 4 ^oC for analysis by FACS.

Cell sorting was performed using a BD Biosciences FACS Aria, with gating for GFP positive cell defined as the upper 0.5% of the un-transfected cell population. Each gRNA sample was sorted to fill two 96-well plates with a single cell per well for clonal expansion, this was visually confirmed by light microscopy as colony expansion occurred. In addition to the 4 gRNA sequences + Cas9-GFP plasmid samples, the negative control of the Cas9-GFP plasmid only was also sorted to control for the effects

of the enzyme alone, without the presence of targeting gRNA sequence. The sorted GFP positive single cells were maintained in standard culture media and monitored regularly for cell growth. The cells which grew were expanded into 48-well plates, when confluent in the 96-well plate. From here cells were further expanded into 6-well plates and subsequently T25 flasks as their growth continued. For each gRNA sequence, that was sorted, approximately 5% of wells grew to produce clonally different cell lines for further testing. Once cell-lines reached the stage of confluency in T25 flasks they were frozen-down for storage before characterisation with the RVG peptide.

3.2.12 Statistical Analysis

3.2.12.1 Uptake assays

In all uptake studies, data was analysed by initially subtracting the autofluorescence of blank cell lysates from the measured intensities of the cells in the assays. These fluorescence values are then normalized to the intensity of cells pulsed with RVG-Rho at 37 ^{o}C, without any treatment applied to them. In the RVG uptake studies the unchallenged, active uptake of RVG peptide (RVG-Rho) into BMECs was compared to the uptake at 4 ^{o}C, uptake in the presence of unlabelled RVG peptide, the uptake of the scrambled sequence peptide (SCRAM-Rho) at 37 ^{o}C and the uptake of the δC peptide at 37 ^{o}C. These comparisons were made using a one-way ANOVA with the Dunnett's post-test, with RVG-Rho pulse 37 ^{o}C used as the control for comparisons.

In the competitive uptake assay, where labelled RVG-Rho peptide was competed with increasing concentrations of unlabelled RVG peptide or unlabelled α-BGT. The unchallenged uptake of RVG was used as the control for comparison by one-way ANOVA with Dunnett's post-test. Significance was defined as a p-value < 0.05.

When comparing the uptake of RVG into cells SH-SY5Y that have been transfected with different sequences of siRNA against the α7-nAchR. The raw fluorescence was first

normalized to the intensity of the uptake of RVG peptide into untransfected cells and then the effect of the siRNA transfection was assessed using a one-way ANOVA with Dunnett's post-test.

3.2.12.2 Pulse-Chase Assay

As in the previous chapter the analysis of the pulse-chase assay first involves the subtraction of blank cell autofluorescence from the assayed cells fluorescence intensity. These values were then normalized as a percentage to the mean intensity of cells that have been pulsed with the RVG-Rho peptide at 37 ^{o}C. To assess the efflux of the peptide from the cells over the duration of the chase, the fluorescence at each chase time point was compared to the pulse only fluorescence through a one-way ANOVA with Dunnett's post-test. To confirm that efflux was active, at each chase time point the fluorescence at the 37 ^{o}C chase was compared to the equivalent time point, chased at 4 ^{o}C, through a one-way ANOVA with a Tukey multiple comparison post-test.

3.2.12.3 Microscopy Studies:

Following collection of z-stack image files, these were imported into the Fiji image analysis software for processing and co-localization analysis. Here each stack was split into individual slices for analysis using JACoP (Just Another Colocalization Plugin) in Fiji. In this analysis the Mander's Colocalization method was selected, to observe the proportion of thresholded RVG-Rho fluorescence which was co-localized with thresholded dextran fluorescence or BODIPY-LaCer fluorescence, at the conclusion of the chase phase (Manders *et al.* 1993). The colocalization fractions for each slice in the z-stack were averaged to produce an output for value for that replicate, and for final analysis the combination of multiple microscopy stacks were used to produce the output

colocalization fractions for the ligands with dextran labelled lysosomes. These were expressed as mean ± standard deviation.

3.3 Results and Discussion

3.3.1 Expression of Putative RVG receptors in BME cells

In the mouse cell line repeated PCRs, performed in multiple passages confirmed expression of several potential RVG peptide receptors. Of these, NCAM-1 appears to have the strong expression in b.End3 cells. Other receptors expressed include the nicotinic receptor alpha 3 and alpha 7 subunits and p75NTR as seen in Figure 3.2.

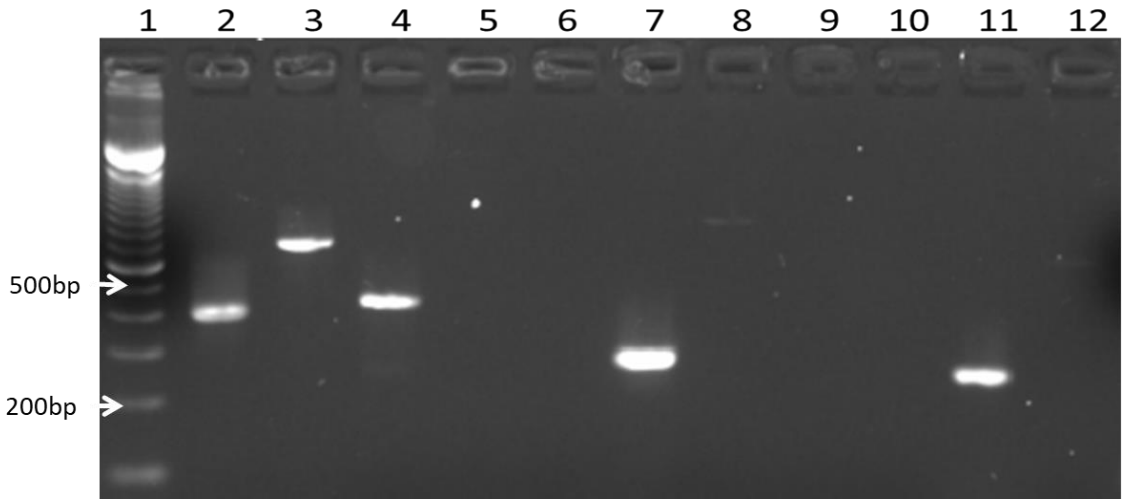

Figure 3.2: Putative RVG receptor expression in b.End 3 cell-line
The above plot shows the output of a PCR in b.End3 cells to examine the expression of putative receptors for the RVG peptide. The lane numbers correspond to the following: Lane 1 - DNA ladder, 2 – GAPDH, 3 – α1 nAchR, 4- α3 nAchR, 5 – α4 nAchR, 6 – α5 nAchR, 7 – α7 nAchR, 8 – β2 nAchR, 9 – β3 nAchR, 10 – β4 nAchR, 11- NCAM-1, 12 – p75NTR. In this blot there was observed strong expression of α1, α3 and α7 nAchR and NCAM-1

Of the receptors expressed in b.End3 cells the most probable for RVG peptide interaction is the alpha 7 subunit of the nAchR. This is due to the evidence of α-bungarotoxin competing the binding of the RVG-R8 construct (Kumar *et al.* 2007). As well as the high homology between the bungarotoxin binding region for nAchR-α7 and the RVG peptide sequences.

The b.End3 cells are an immortalised cell-line and as such the expression of these receptors may be altered from the *in vivo* setting. It has been shown in several primary

cell-lines that taking the cells through only two or three passages can changes some of the key phenotypic characteristics of BBB endothelium. Further studies, performed in the primary porcine BMEC cells show similar receptor expression to the b.End 3 cell line. Primary porcine BMECs show expression of the alpha 3 and 5 subunits of the nAchR as well as weak expression of the beta 4 subunit and p75NTR (Figure 3.4). Expression of the alpha 7 subunit of the nAchR or NCAM-1 was not seen in these cells across 4 independent isolations of the PBMECs. In the human hCMEC/D3 cell line the receptors observed were the alpha 3 and 4 and beta 3 and 4 subunits of the nAchR in addition to both NCAM-1 and p75NTR (Figure 3.3). In hCMEC/D3 there was inconsistent expression of the alpha 7 subunit of the nAchR between independent replicates.

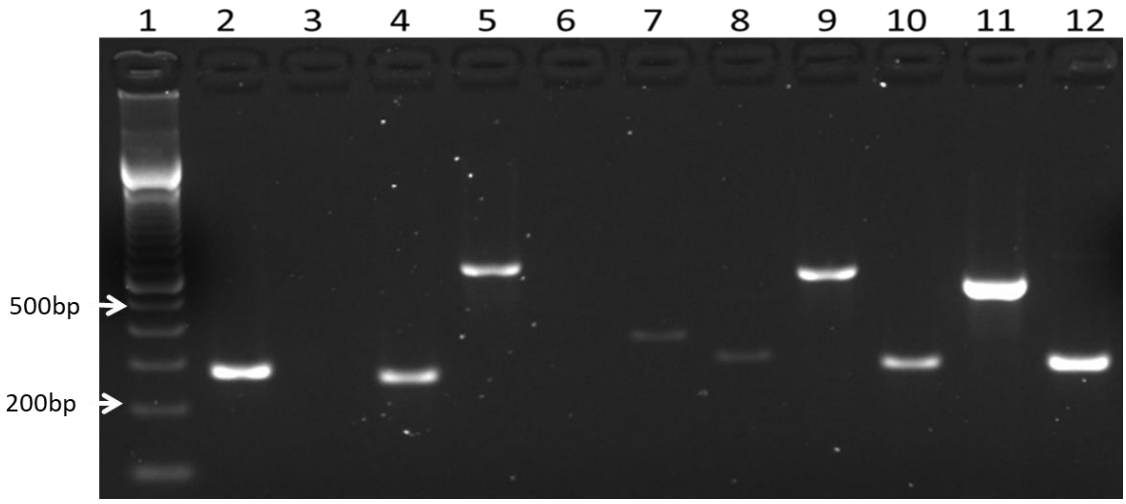

Figure 3.3: Putative RVG receptor expression in hCMEC/D3 cell line
The above plot shows the output of a PCR in hCMEC/D3 cells to examine the expression of putative receptors for the RVG peptide. The lane numbers correspond to the following: Lane 1 - DNA ladder, 2 – GAPDH, 3 – α1 nAchR, 4- α3 nAchR, 5 – α4 nAchR, 6 – α5 nAchR, 7 – α7 nAchR, 8 – β2 nAchR, 9 – β3 nAchR, 10 – β4 nAchR, 11- NCAM-1, 12 – p75NTR. In hCMEC/D3 there was observed strong expression of α3, α4, β3 and β4 nAchR, NCAM-1 and p75NTR. There was also observed weak expression of α7 nAchR

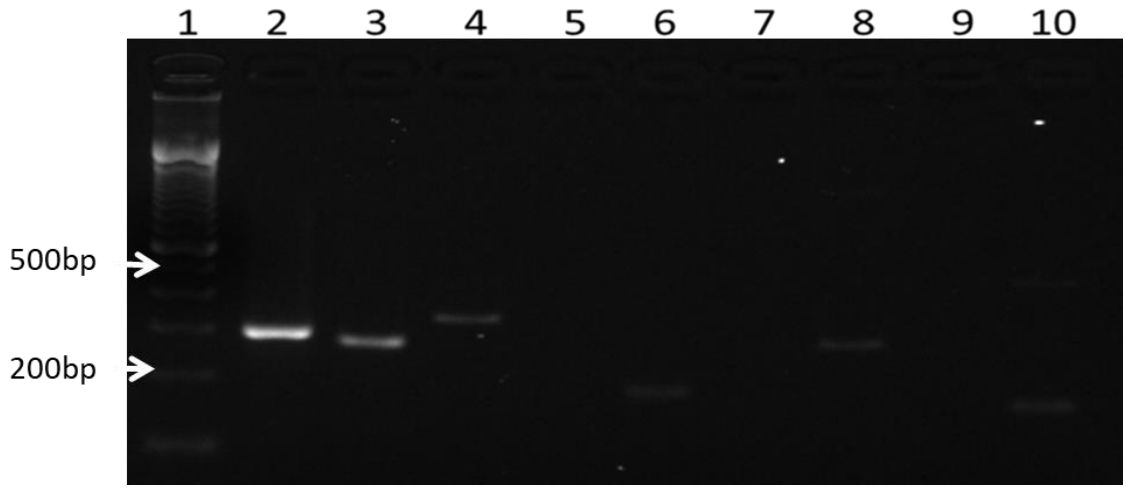

Figure 3.4: Putative RVG receptor expression in Primary Porcine Brain Microvascular Endothelial Cells

Lane 1 - DNA ladder, 2 – β-actin, 3 – α3 nAchR, 4 – α5 nAchR, 5 – α7 nAchR, 6 – β2 nAchR, 7 – β3 nAchR, 8 – β4 nAchR, 9 – NCAM-1, 10 – p75NTR.

3.3.2 Uptake of RVG peptide by brain microvascular endothelial cells

RVG-Rho peptide uptake at 37 ºC was observed in b.End3 cells at concentrations from 5 – 100 µM by confocal microscopy (Figure 3.5.A-C). However, binding to the cell membrane was not seen in studies performed at 4 ºC (Figure 3.5.D). This may be due to low receptor numbers on the surface of the cells and the strength of signal from the rhodamine fluorophore.

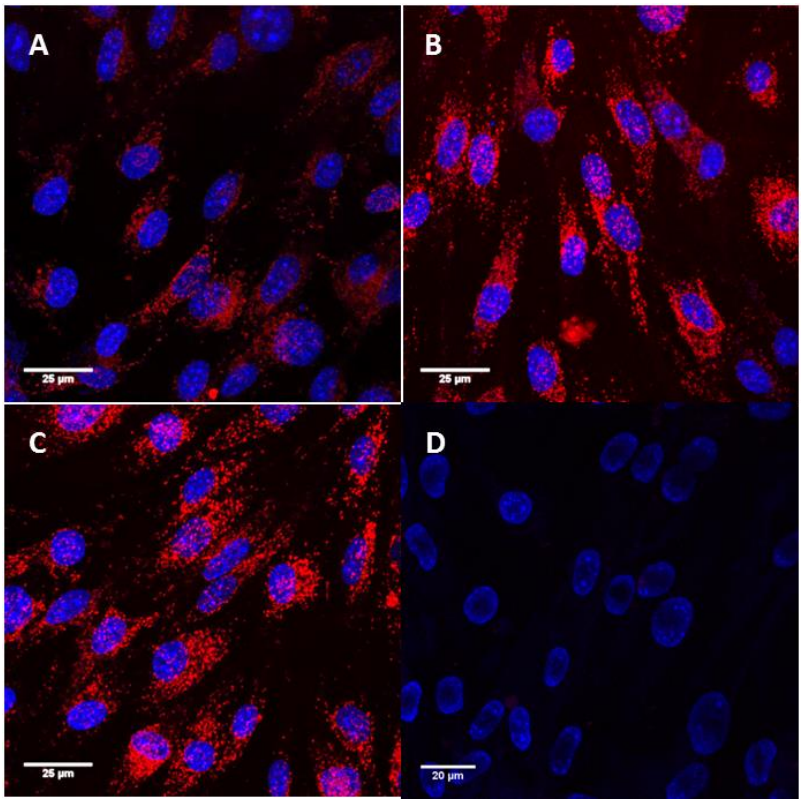

Figure 3.5: RVG peptide uptake in b.End 3 cells

The images in the panel to the left are maximum projections from a minimum of 12 slices, taken at 0.75µm spacing through the cells. A-C have received a 1 hour pulse at 37 ºC of 5, 20 and 100 µM RVG-Rho peptide respectively. D are cells pulsed for 1 hour at 4 ºC with 5 µM of RVG peptide. The scale bars in A-C is 25 µm, in D is 20 µm, n = 3 in triplicate

The RVG-Rho peptide and the scrambled sequence peptide have the similar mass, charge and amino acid chain length characteristics. Nevertheless, the RVG-rhodamine peptide shows significantly higher uptake into cells that the scrambled sequence peptide. Shown by both confocal microscopy and a fluorescence plate reader assay (Figures 3.6 + 3.7). The use of the scrambled sequence peptide demonstrates the importance of amino acid sequence on the uptake capability of a targeting strategy. It has previously been shown that the presence a cysteine residue in short cell penetrating peptides causes entry through the formation of disulphide bonds with membrane proteins. In order to, test if the cysteine in the RVG sequence the cysteine residue was replaced with an alanine. Figure 3.6 shows that in the removal of the cysteine residue from the RVG sequence significantly reduces the uptake of the peptide into the b.End 3 cell line. The uptake of the δC sequence peptide was at similar levels to the scrambled sequence peptide, two orders of magnitude lower than the native RVG peptide sequence in b.End 3 cells. While in the human cell line, hCMEC/D3 the uptake of both scrambled sequence and delta C peptides was approximately five times lower than that of the standard RVG peptide (Figure 3.6.B). The differences in uptake between RVG and the scrambled sequence peptide were also visible in confocal microscopy studies (Figure 3.7)

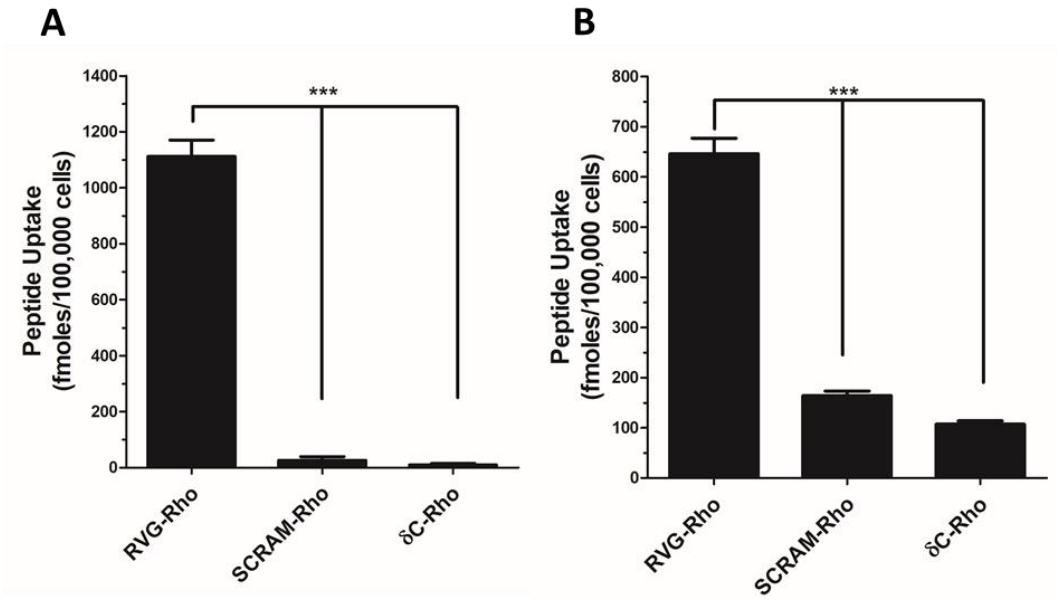

Figure 3.6: Comparison of RVG peptide derivatives uptake in brain microvascular endothelial cells

The graphs show the uptake of the RVG derived peptides in two *in vitro* BMEC cell lines, A is the uptake in b.End3 cells, while B is the uptake in the hCMEC/D3 cell line. All comparisons are made between the standard sequence (RVG-Rho) uptake and the scrambled sequence peptide (SCRAM-

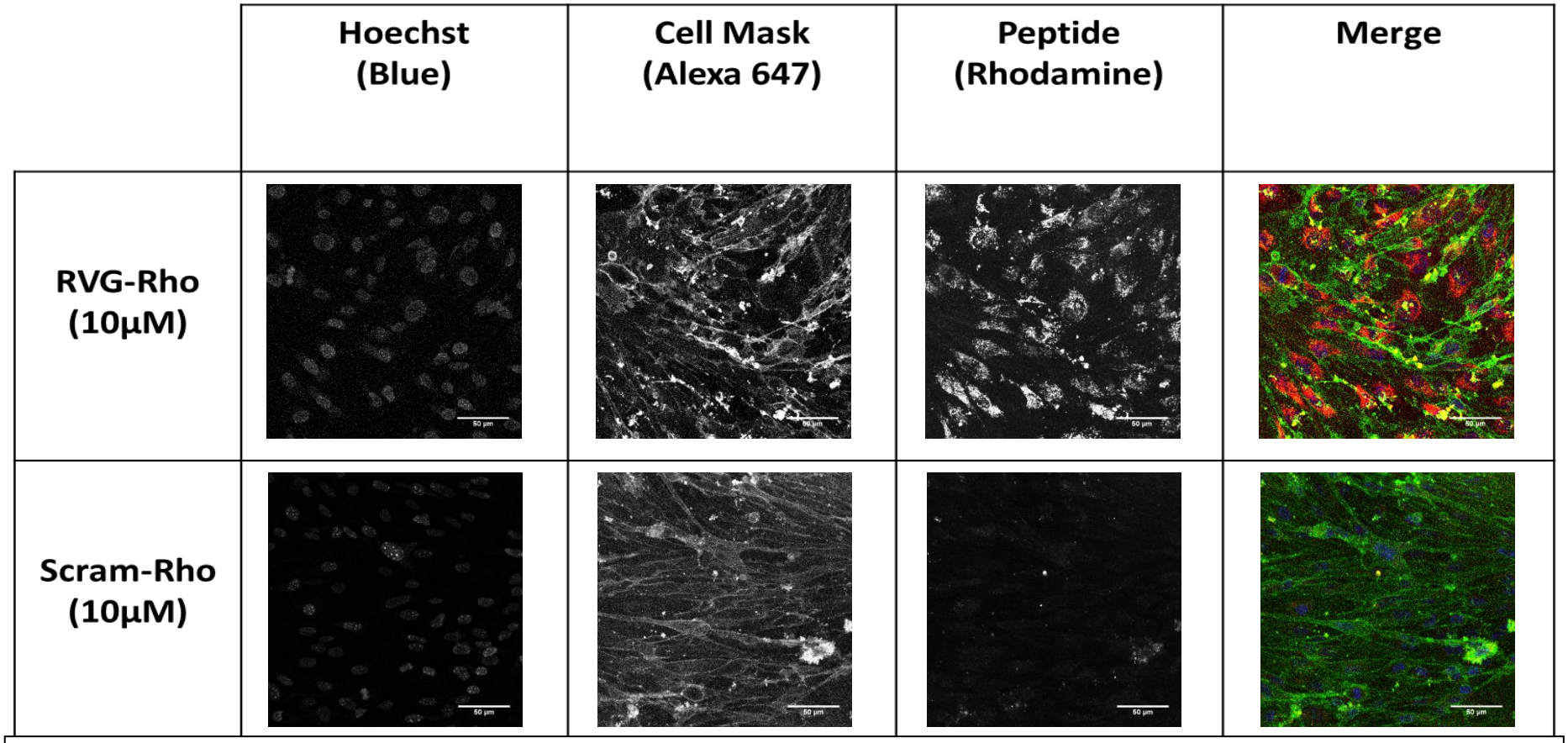

Figure 3.7: Comparison of RVG peptide and Scrambled sequence peptide uptake in b.End 3 cells

The images above are maximum projections from a minimum of 12 slices, taken at 0.75µm spacing through the cells. Cells have received a 1 hour pulse at 37 ºC with 10 µM of either RVG-rhodamine or Scrambled sequence-rhodamine peptides. Cells are additionally stained with the nuclear stain Hoechst (blue) and Cell Mask Alexa 647 (green), a cell membrane stain. The rhodamine labelled peptides are shown in red in the merged image. Scale bar = 50 µm.

3.3.3 RVG uptake is a self-competitive process

The uptake of labelled peptide RVG into BMECs was shown to be a self-competitive process through direct competition with unlabelled RVG peptide. The addition of increasing concentrations of the unlabelled peptide decreased the uptake of RVG-[Rho] to ~40% of the unchallenged fluorescence. An experimental IC50 was calculated as 10.5 µM, again an indicator that the RVG peptide has a specific binding site (Figure 3.8). This suggests the uptake of RVG peptide is through a receptor mediated process, with a defined binding site for the peptide. This initial decrease in fluorescence seen in Figure 3.8.A, with low concentrations of unlabelled RVG appears strange. In later studies with unlabelled α-bungarotoxin a similar effect was observed, where an initial decrease in cell associated fluorescence with low concentrations of unlabelled α-BGT was followed by an increase, before returning to the expected trend (Figure 3.13). It is unclear as to what may be affecting the behaviour of the peptide in this way but could highlight the potential complexity and multifactorial nature of ligand uptake.

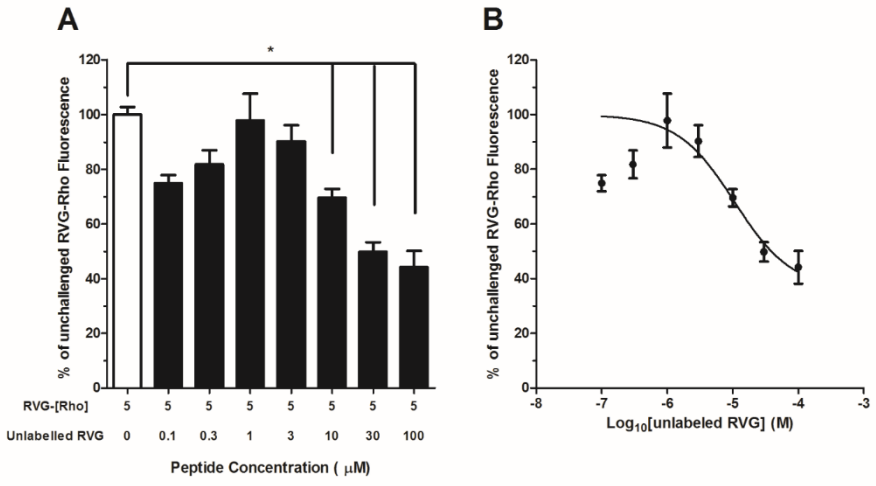

Figure 3.8: Self-Competition of RVG-[Rho] uptake with unlabelled RVG

The above figure shows the ability of the RVG peptide to demonstrate self-competitive uptake in hCMEC/d3 cells. Figure A demonstrates the decrease in labelled fluorescence in the prescence of unlabelled RVG. While Figure B shows the competition curve from this assay. * = $p < 0.05$ compared to RVG-[Rho] only cells (white bar), n = 3 in triplicate, mean ± std.

3.3.4 Pulse-Chase RVG Studies

As with the studies in the previous chapter, these pulse-chase studies are designed to assess the ability of a targeting ligand to "escape" from the endothelial cells and potentially reach the CNS. In both b.End3 cells (mouse) and hCMEC/d3 cells (human), the RVG peptide demonstrated an ability to undergo active efflux from cells, over the course of the chase. At the conclusion of the 37 ^{o}C chase the proportion of pulsed RVG peptide fluorescence, remaining cell associated was 25% in b.End3 cells and 44% in hCMEC/d3 cells (Figure 3.9). In both cell lines, the proportion remaining cell associated at 37 ^{o}C and 4 ^{o}C were significantly different at all time-points. Indicating that the RVG peptide can be actively effluxed from BMECs. A desirable characteristic for a brain targeting ligand, as it means the peptide that is cell associated can undergo further trafficking and potentially reach the basolateral cell membrane and the CNS if this was *in vivo*.

This proportion of RVG peptide remaining in b.End3 cells was comparable to the proportion of transferrin and 8D3 retained by b.end3 cells, in the previous chapter. While the proportion retained was higher in the hCMEC/d3 cells, the efflux profile was still different to the fluid phase marker, dextran in b.End3 cells from the from the previous chapter (Figure 2.5). Comparison of the respective 37 ^{o}C and 4 ^{o}C time-points confirms the active loss from the cells. To understand where the remaining RVG peptide was located within the endothelial cells, following the conclusion of the chase, colocalization microscopy was performed on the cells after the assay.

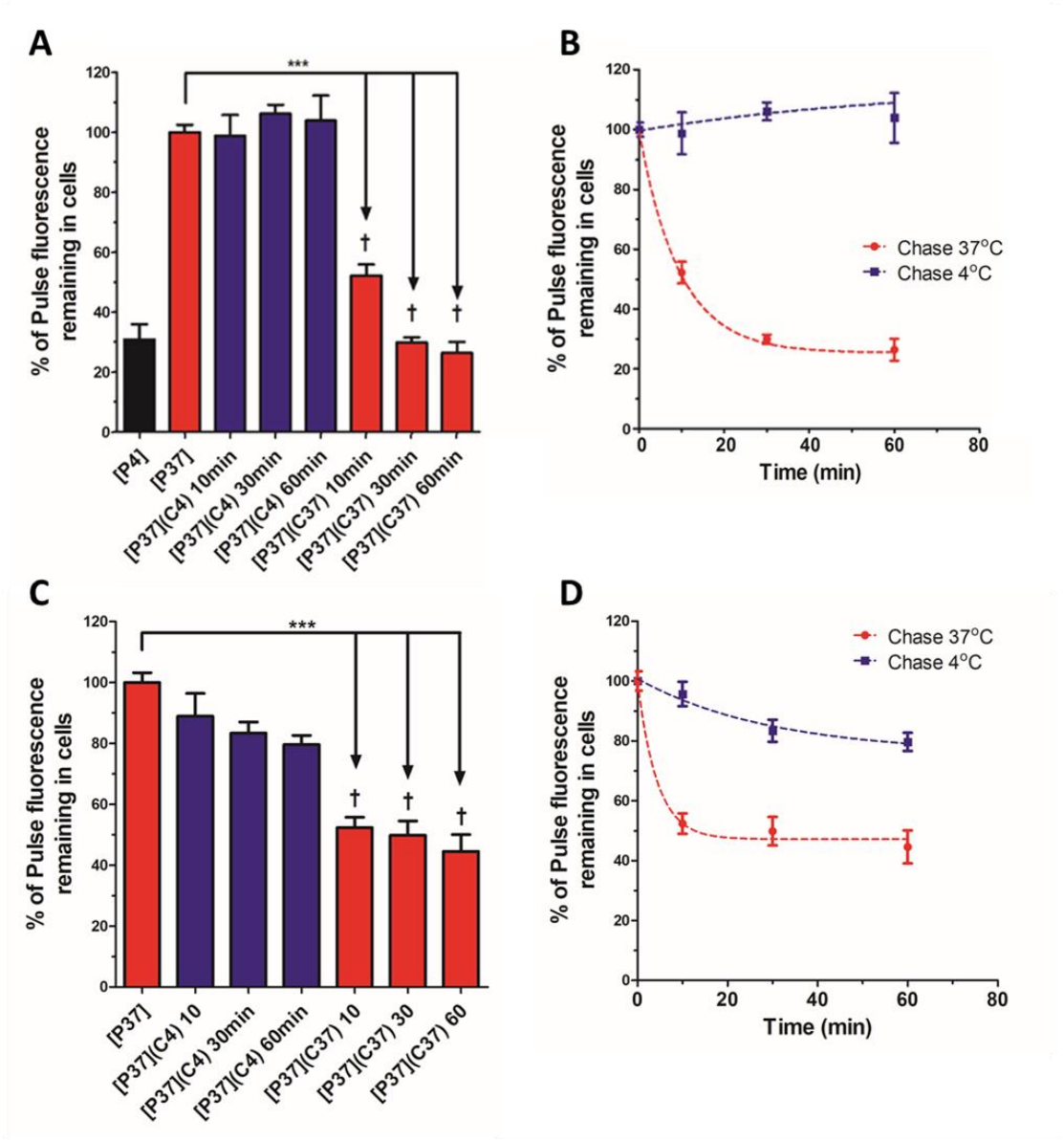

Figure 3.9: RVG peptide Pulse-Chase BMECs *in vitro*

The above graphs show the pulse-chase results for the RVG peptide in two BMEC cell-lines. A + B show the pulse-chase in b.End3 cells (mouse), while C + D the pulse-chase in hCMEC/d3 (human). In both cell lines the RVG concentration as 5 µM In the bar graphs the bars in the red represent the 37 ^{o}C chase and the blue bars the 4 ^{o}C chase. *** = $P < 0.001$ when comparing the column to the fluorescence within cells after the pulse at 37 ^{o}C. † = $P < 0.05$, when compared a time-point at 37 ^{o}C

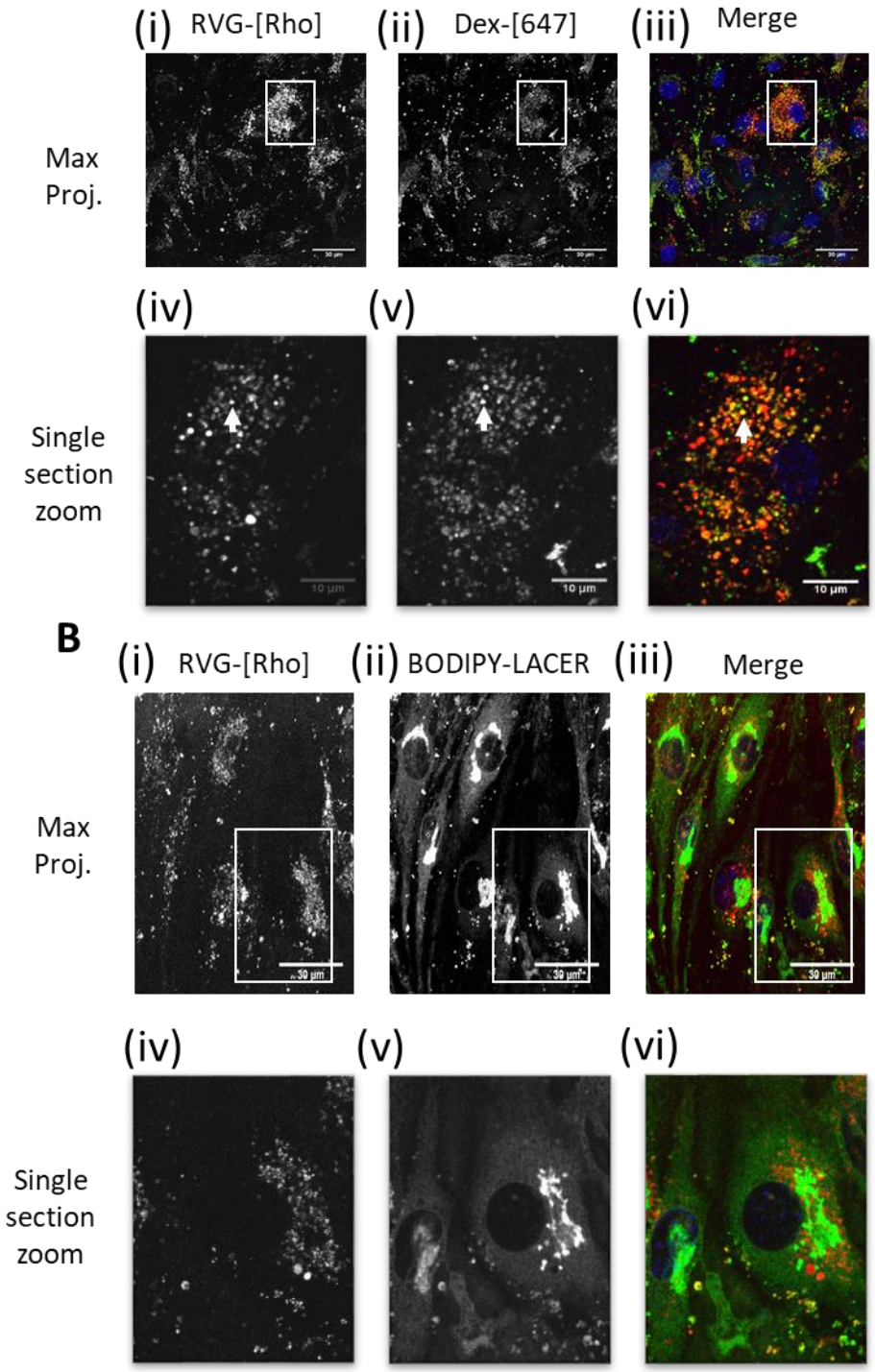

Figure 3.10: Distribution of the RVG peptide following the conclusion of the Pulse-Chase assays in hCMEC/D3 cells

The above microscopy images show the colocalization of the RVG peptide (5µM, pulse-chase) with both dextran labelled lysosomes (A) and BODIPY-LACER labelled golgi-apparatus (B). In the false colour merged images of A.(iii) and A.(vi), red = RVG-[Rho], green = dextran-[647] and blue = Hoechst. In the false colour, merged images of B.(iii) and B.(vi), red = RVG-[Rho], green = BODIPY-LACER, intense green = golgi appartus and blue = Hoechst. Co-localization analysis of RVG-[Rho] with dextran gives a Mander's Co-efficient of 0.582 ± 0.012, while co-localization between RVG-[Rho] and the Golgi was a Mander's Co-efficient of 0.213 ± 0.034. n = 3 in triplicate. Scale Bar in A and B i-iii = 30µm

This revealed that ~21% of the RVG peptide fluorescence remaining in the cell was associated with the golgi apparatus (Figure 3.10.B). Suggesting that this can undergo further cellular trafficking and transport processes. However, the majority of the remaining RVG fluorescence is associated to the lysosomal compartment, as confirmed by co-localization with dextran. This lysosomal associated peptide accounted for 58% of the remaining cell associated RVG fluorescence (Figure 3.10.A). Due to the sensitivity of the fluorescence detection in the pulse-chase assay and the microscopy the pulse concentration of the RVG peptide was 5 μM, which is likely to be greater than the Kd for the receptor. As shown in the previous chapter, if the concentration of the ligand is significantly greater than the Kd of the receptor (50% receptor occupancy) there is an element of non-specific endocytosis. This non-specific uptake leads to an increase in lysosomal association of the ligand and may account for the high lysosomal association of the remaining RVG peptide following the chase.

3.3.5 Competition of α-bungarotoxin by RVG peptide

Due to the homology of the RVG peptide sequence with the loop 2 region of α-bungarotoxin, the region known to bind nAchR, flow cytometry studies were performed to assess the binding α-bungarotoxin-Alexa 647 to b.End3 cells at 4 oC and thus the presence of a putative RVG receptor. This was shown to be a saturable process with the Kd of α-bungarotoxin in b.End3 cells calculated to be 191 nM (Figure 3.11).

Competition of RVG-Rho uptake was performed using unlabelled α-bungarotoxin. Imaging of the cells reveals that the uptake of RVG-Rho can be decreased by the addition of increasing concentrations of unlabelled α-bungarotoxin. To further these findings competitive uptake studies were performed by flow cytometry, studies using α-bungarotoxin labelled with Alexa 647. The labelled α-bungarotoxin was competed using both unlabelled RVG and unlabelled α-bungarotoxin to confirm a receptor specific uptake

process. Both unlabelled probes could reduce the uptake of the labelled α-bungarotoxin Alexa 647. The decrease in uptake appeared to be dependent on the concentration of the unlabelled probe (RVG or α-bungarotoxin). From this data, an estimation of the IC50 values for both α-bungarotoxin and RVG for competing 250 nM α-bungarotoxin 647 have been found as 98 nM and 23 nM respectively (Figure 3.12). These findings support that RVG and α-bungarotoxin share a binding site for uptake in b.End3 cells.

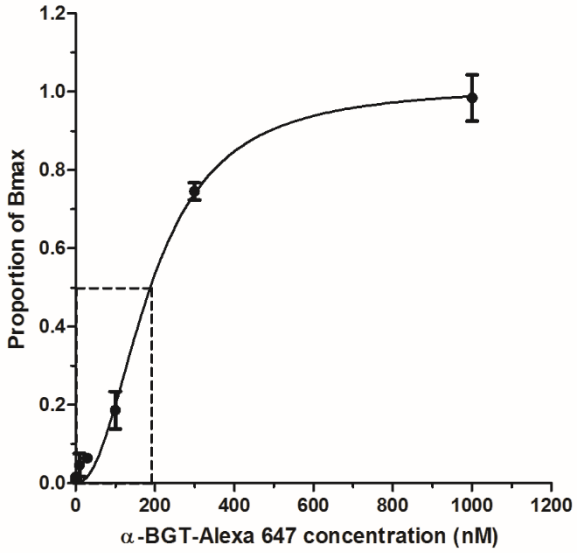

Figure 3.11: α-Bungarotoxin Binding Curve in b.End 3 cells

The figure shows the flow cytometry data on the binding of α-Bungarotoxin-Alexa 647 to receptors on the surface of b.End 3 cells. Concentrations range from 0-1000 nM of α-Bungarotoxin-Alexa 647. The data has been normalised to the estimated B_{max} and the dashed line represents the Kd. n=3

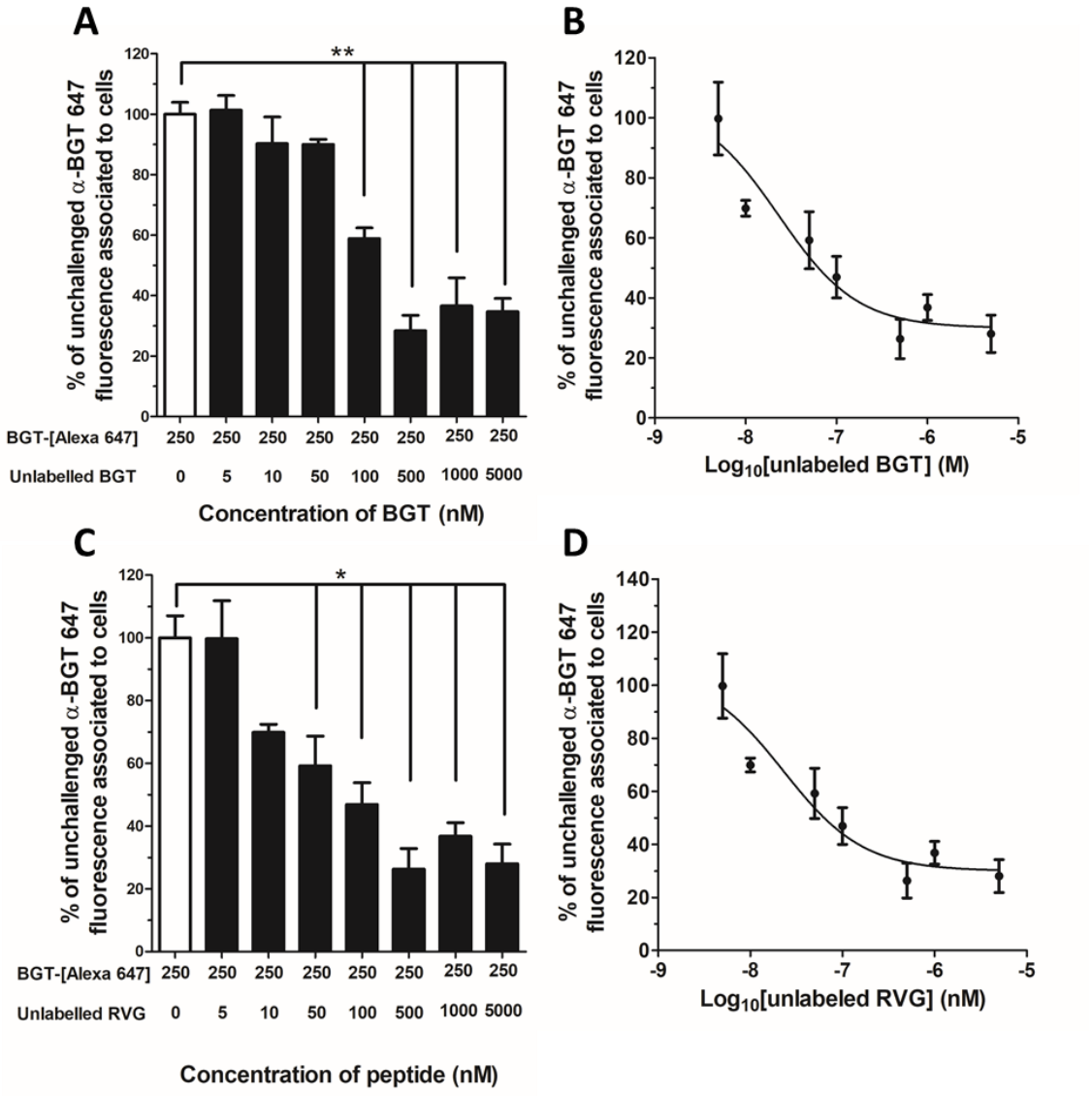

Figure 3.12: The competition of α-Bungarotoxin-Alexa 647 uptake by unlabelled RVG and α-Bungarotoxin in b.End3 cells

Figure A shows the competition of 250nM α-Bungarotoxin-Alexa 647 with varying concentrations of unlabelled RVG peptide. C the direct competition of α-Bungarotoxin-Alexa 647 (250nM) with varying concentrations unlabelled α-Bungarotoxin. Figures B+D shows the competitive uptake curves for the labelled α-Bungarotoxin when competed with unlabelled RVG and α-Bungarotoxin respectively. * = $P<0.05$, **= $P<0.01$ compared to unchallenged cells (white bar), n=3 in triplicate, mean ± std.

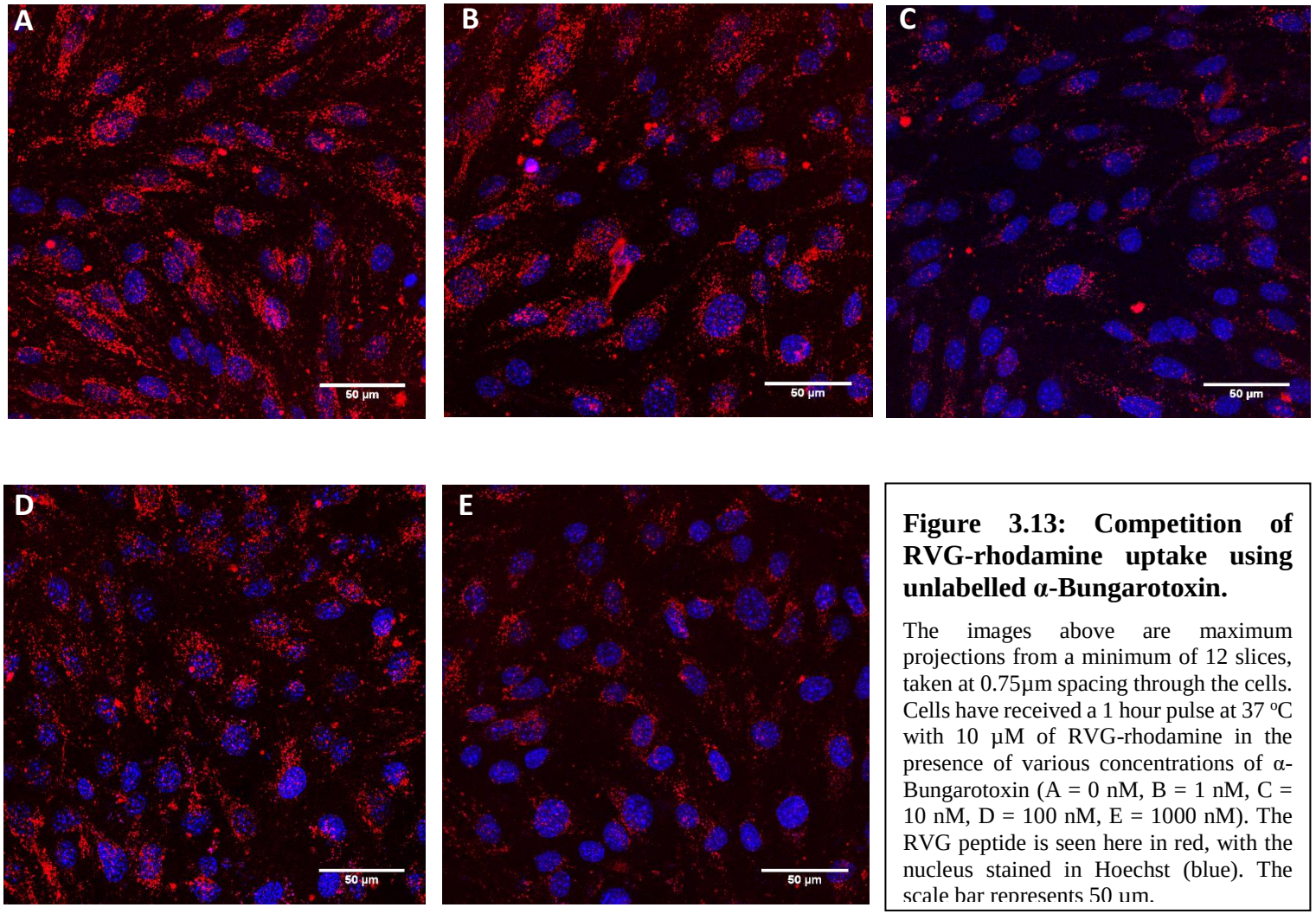

Figure 3.13: Competition of RVG-rhodamine uptake using unlabelled α-Bungarotoxin.

The images above are maximum projections from a minimum of 12 slices, taken at 0.75µm spacing through the cells. Cells have received a 1 hour pulse at 37 ºC with 10 µM of RVG-rhodamine in the presence of various concentrations of α-Bungarotoxin (A = 0 nM, B = 1 nM, C = 10 nM, D = 100 nM, E = 1000 nM). The RVG peptide is seen here in red, with the nucleus stained in Hoechst (blue). The scale bar represents 50 µm.

The competition of labelled RVG uptake into b.End3 cells was further analysed using the fluorescent plate reader assay (Figure 3.14). Here it was shown the unlabelled α-bungarotoxin was able to significantly decrease the uptake of the RVG peptide into cells. With a calculated experiment IC50 of 8.3 nM for bungarotoxin's competition of RVG uptake. The findings from the studies in this section are consistent with the findings of a study from Kasheverov et al. (2009), who examined the ability of synthetic peptides to the nAchR to compete bungarotoxin binding. The findings also align with those of Lentz, who, in multiple studies has demonstrated the ability of RVG and α-bungarotoxin to interact at the α7-nAchR (Lentz *et al.* 1987; Lentz TL 1990; Lewis *et al.* 2000). These findings will contribute to the evidence built within this chapter that the RVG peptide is internalized into cells through the α7-nAchR.

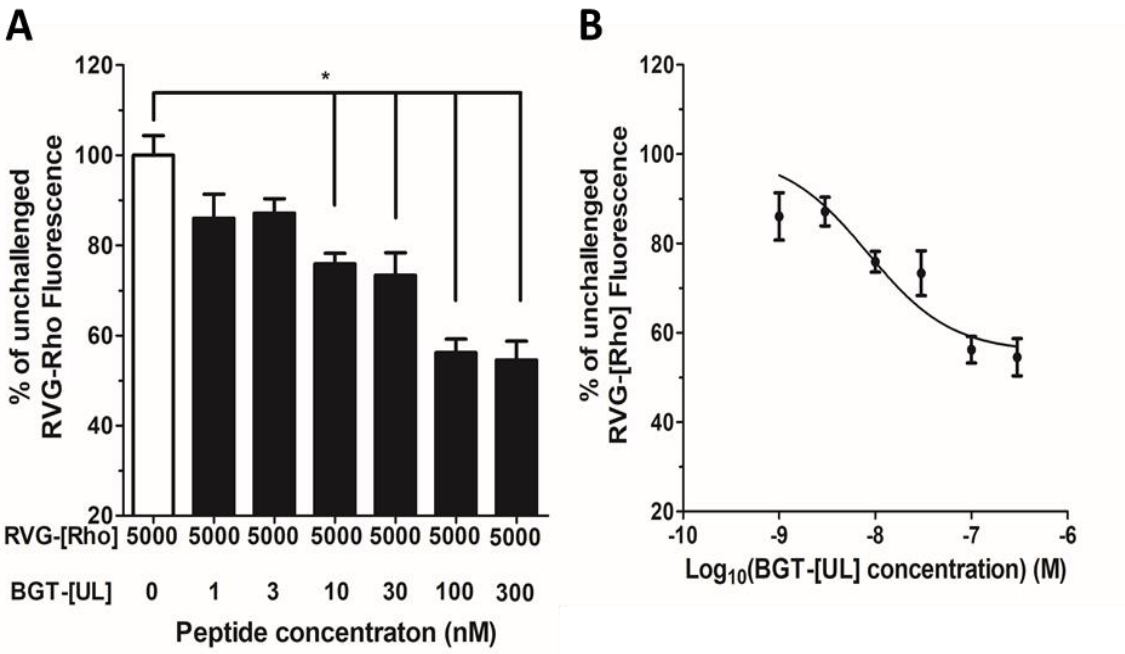

Figure 3.14 Competition of labelled RVG peptide uptake into b.End3 cells by unlabelled α-bungarotoxin

The above figure confirms the uptake of RVG-[Rho] peptide into b.End3 cells is competed by the presence of increasing concentrations of unlabelled α-bungarotoxin. Figure A confirms that significant inhibition RVG-[Rho] uptake was seen at higher concentrations of α-bungarotoxin (BGT-[UL]). While Figure B shows the competitive uptake curve for this study. From Figure B an experimental IC50 was estimated as 8.3 nM. * = $p < 0.05$ when compared to unchallenged cells (white bar), n = 3 in triplicate, mean ± std.

3.3.6 siRNA Knockdown

To further confirm the role of α7-nAchR in the uptake of the RVG peptide into cells, transient knockdown of the CHRNA7 gene attempted using multiple siRNA sequences against the gene. Due to the low expression levels of the α7-nAchR in hCMEC/d3 cells and their inherent resistance to transfection, siRNA studies were not performed on this cell line. Instead the SH-SY5Y cells are known to express α7-nAchR at high levels on their cell surface, so making them the ideal candidate cell line to test the effect of knockdown on the uptake of the RVG peptide. Transfection of all three siRNA sequences produces a significant reduction in the uptake of the RVG-[rho] peptide into SH-SY5Y cells. The effect of the transfection was visible in the uptake assay, when comparing the targeted siRNA to the control sequence and untransfected cells (Figure 3.15.A). Of the three sequences used, siRNA seq1 produced the greatest reduction in the RVG uptake, but all sequences produced significant reductions in uptake. Confirmation of the knockdown of α7-nAchR was done by Western blot, and confirmed the siRNA was acting on the desired target. However, due to difficulties with the antibody, a clear effect on the expression levels of α7-nAchR and the levels appeared reduced in the control sample compared to untransfected cells. This was confirmed by band quantification, in untransfected cells the expression of α7-nAchR relative to GAPDH intensity was 0.96 ± 0.14, while the expression in luc-1transfected cells was decreased to 0.84 ± 0.11. In cells transfected with α7-nAchR siRNA had a mean relative expression of 0.69, 0.53 and 0.55 respectively. These relative expression levels would suggest that the siRNA against the receptor is contributing to the decrease in RVG uptake.

The combination of the bungarotoxin competition of RVG and the siRNA knockdown of RVG uptake both add significant evidence to the critical role α7-nAchR plays in the uptake of the RVG peptide. The use of multiple techniques is key in the confirmation of

the RVG receptor to ensure consistency in the findings. In the literature, thus far there has been confusion over the target receptor. But, by using this multi-technique approach a clear result can be found with regards to which receptor is the main target of the RVG peptide.

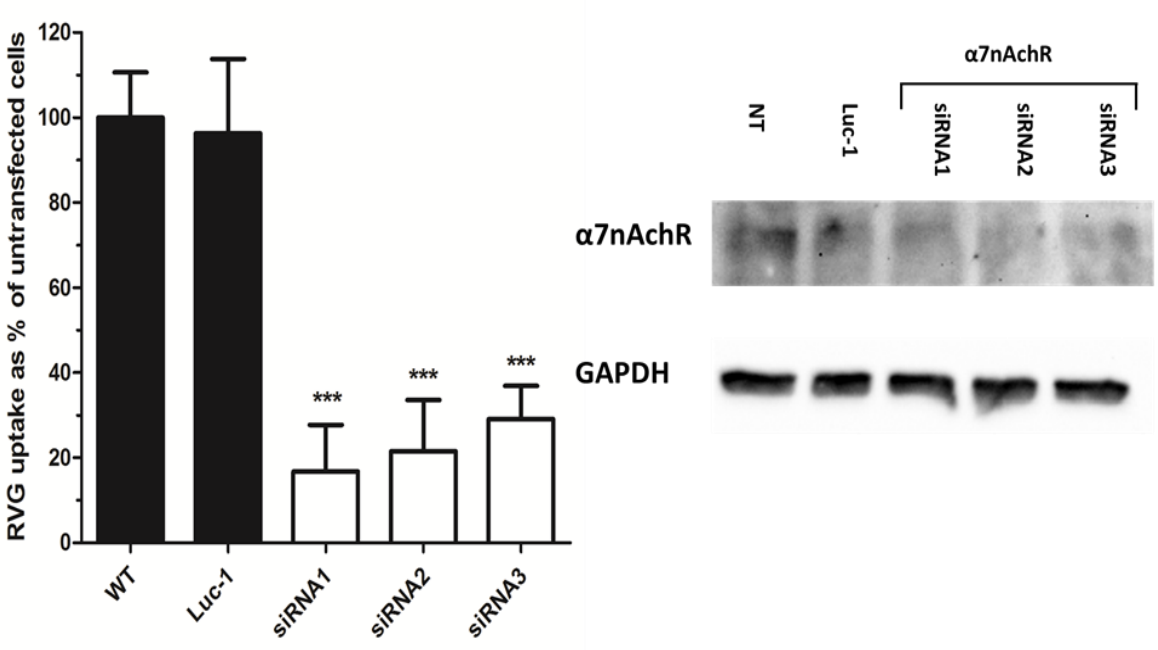

Figure 3.15: siRNA modulation of RVG uptake into SH-SY5Y Cells
The above figure shows the effect of siRNA knockdown of the α7-nAchR decreased the uptake of the RVG peptide in the neuronal SH-SY5Y cell-line. Graph A is the quantification of the RVG uptake, normalized to the uptake in un-transfected cells. The images in B are the Western blots to show the effect of the three siRNA sequences on α7-nAchR protein expression. *** = $p < 0.001$, n = 3 in triplicate, mean ± std.

3.3.7 Modulation of RVG uptake by crispr/Cas9 genomic editing

Transfection of the plasmid into cells was confirmed by fluorescence imaging of the cells 48 hours post transfection to ensure stable expression of the Cas9-GFP plasmid. This was seen to have greater expression in the control cells, where only the plasmid was transfected and no crRNA was present. However, all transfection conditions showed expression of GFP and were continued to the cell sorting by FACS.

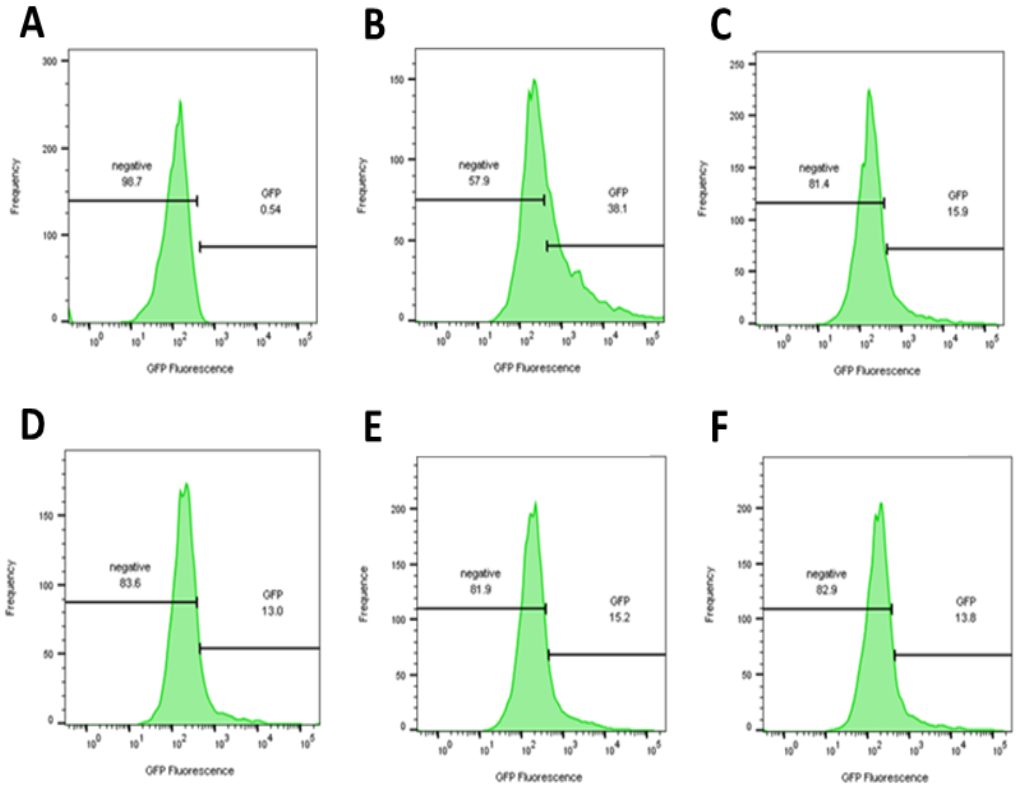

Figure 3.16: FACS sorting histograms for GFP positive transfected cells
The graphs above show the FACS sorting and gating for the transfected cells for use in the CRISPR/cas9 studies. Graph A shows the auto-fluorescence associated to un-transfected cells and the gating for GFP positive cells was based on the upper 0.5% of this population. Graph B shows Cas9-GFP plasmid only transfected into cells. Graphs C-F Cas9-GFP co-transfected with the four gRNA sequences.

FACS sorting for GFP positive cells showed the transfected cells represented between 13 – 15.9 % of the total cell population in the co-transfected cells and 38.1% of the Cas9 plasmid only cells (Figure 3.16). This is based on a gating for GFP positive cells set such that 0.5% of the un-transfected cell population fall within it. GFP positive cells were sorted into one cell per well in 96-well plates and clonally expanded from this point. When sorting individual cells were directed into a single well that contained 100 µL of cell culture media in preparation.

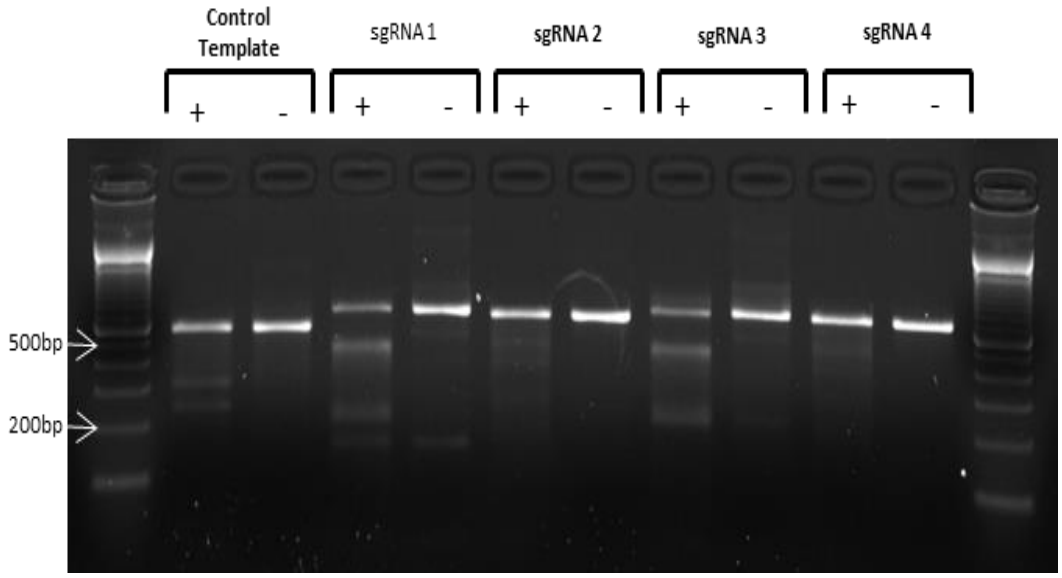

Figure 3.17: Genomic Cleavage Detection of transfected and sorted cells
The above blot shows the results of a genomic cleavage detection assay performed on an expanded population of sorted cell (10,000 cells per treatment). It confirms that genomic cleavage events have occurred with all gRNA sequences, with sequence 1 and 3 showing greatest cleavage.

Additionally, 10,000 GFP positive cells from each treatment group were seeded into a well of a 24-well plate and allowed to grow to confluency. These cells were used to test the efficiency of genomic cleavage within the GFP positive cells, i.e. the efficiency of both sgRNA and the Cas9 plasmid being transfected into the same cell. Cleavage was observed with all sequences of sgRNA in the GFP enriched population, with sgRNA1 and sgRNA3 showing the highest genetic modification efficacy, with 24.1% and 24.9% respectively. sgRNA2 and sgRNA4 showed lower modification efficacy, 10.3% and 13.4% respectively (Figure 3.17). These values were calculated using Equations 3.1 and 3.2 from the methods section of this chapter. The results confirmed that genomic editing had taken place within the sorted cell populations, that had been selected for clonal expansion.

Of the 192 cells per population sorted for clonal selection (1 cell per well in two 96-well plates), between 7 to 16 colonies grew from the cells seeded for expansion. Each

expanded population was grown to a stage where it was confluent in a T-25 flask, before stocks were made.

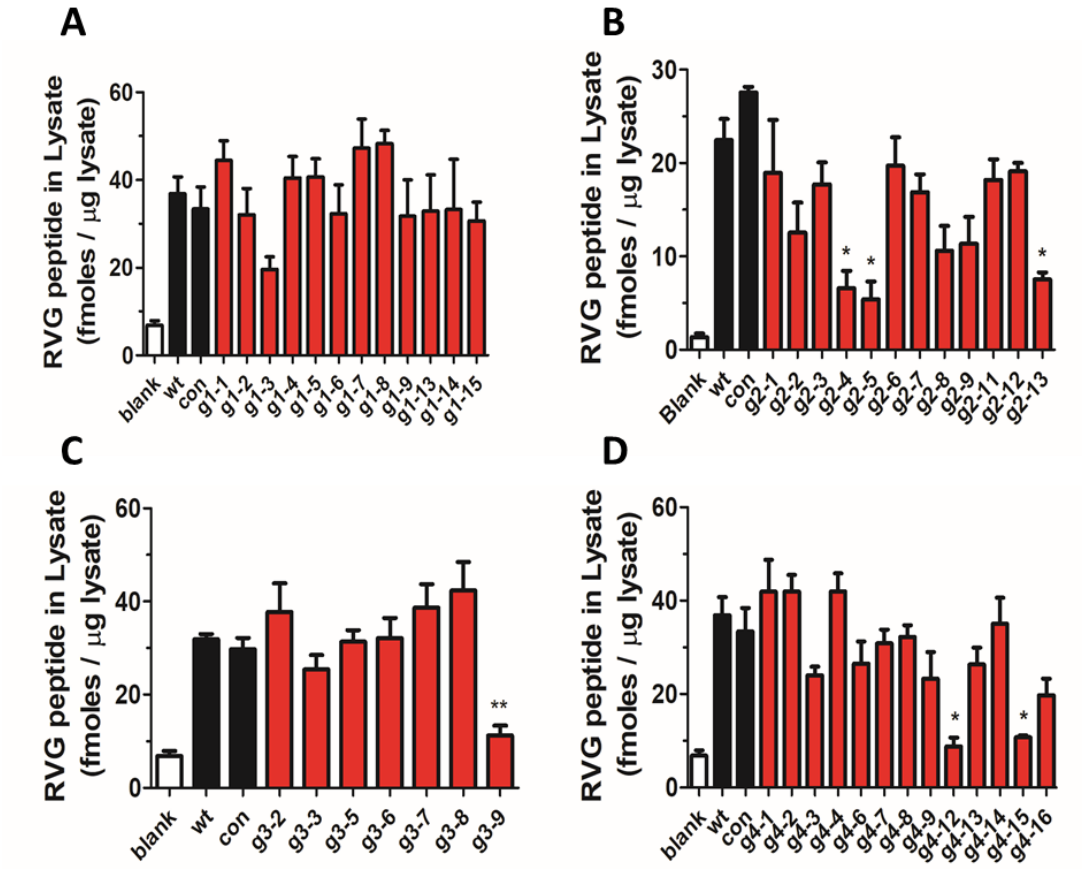

Figure 3.18: The uptake of the RVG peptide into CRISPR/Cas9 modified cell-lines

The above graphs show the uptake of RVG-[Rho] peptide into genomically edited cell lines. Each graph represents the cell-lines generated from a one gRNA sequence (A – gRNA1, B – gRNA2, C – gRNA3, D – gRNA4). The empty bars on the graph represents the auto-fluorescence of cells not exposed to the RVG peptide for the 1-hour uptake study. The black bars are the controls: wt – wild-type and con – Cas9-GFP plasmid only without a gRNA targeting agent. * = $p < 0.05$ and ** = $p < 0.01$, when compared to the wt fluorescence. n = 4 replicates from two independent experiments, mean ± std.

At this stage, all clonal cell-lines were tested with the RVG peptide to assay the uptake into the cells. It was predicted, that due to the co-transfection of sgRNA and cas9-plasmid that not all cell-lines would be co-transfected and therefore showing a reduction in the uptake of the RVG peptide. Uptake assays found that seven cell lines showed a significant reduction in the uptake of the RVG peptide over a one-hour pulse experiment. This was

significant compared to untreated cells and the control transfection cell line. However, Western Blotting to confirm the decrease in protein expression was unsuccessful with these cell lines on multiple occasion. Therefore it is not possible to say with certainty that the effects observed in Figure 3.18 are due completely to knockout of the α7 nAchR or through a secondary effect of the crispr/Cas9 system.

3.4 Chapter Conclusion

The difference in the expression of the receptor panel between b.End3, PBMECs, and hCMEC/D3 cell lines are likely to be due to the difference between immortalised and primary cell-lines. The porcine cell-line expression of nAchR subunits suggests the presence of an alpha 3, beta 4 pentameric receptor (Tsunoyama and Gojobori 1998). This confirmation of the nAchR is generally seen in ganglion of the autonomic nervous system and is generally not associated with other cell types. Within the b.end3 cells the alpha 7 subunit is has the highest expression of the nAchR panel, indicating a potential for an alpha 7 exclusive pentamer (Tsunoyama and Gojobori 1998). This alpha 7 pentamer is considered a neuronal nAchR, however is seen in the peripheral nervous system and in developing muscle tissue. Additionally in endothelial cells the alpha 7 nAchR has a role in angiogenesis (Cooke and Ghebremariam 2008). Further studies into cerebral vascular nAchR expression show stimulation of the receptor with the cognate ligand triggers increased vascular permeability (Hawkins *et al.* 2005). As the full action of RVG on the acetylcholine receptors is currently unclear this effect could be a contributing factor to enhancing cerebral uptake of nanoparticles targeted with the RVG peptide. All cell lines show expression of p75 NTR, which has been shown to be a receptor for the whole virus and it is yet to be evaluated as a receptor for the RVG peptide. This is an aspect that will

be explored with later studies, looking to deplete these receptors and look at the effect on RVG peptide uptake by the cells.

The initial uptake studies of the RVG peptide demonstrate the peptide localised in punctate vesicle like structures within the cells, typically associated with endocytosed materials. This appears to be an active process as no uptake was seen at 4 ^{o}C compared with 37 ^{o}C. However, binding was not observed on the cell membrane using confocal microscopy. Alternative assay using a fluorescent plate reader or flow cytometry based assay are currently being utilised to enhance the sensitivity of detection and allow lower concentration ranges to be used in later studies. The peptide sequence was shown to be key for uptake with a scrambled sequence peptide showing undetectable uptake by confocal microscopy and present in significantly lower concentrations in plate reader based assays. Additionally, the role of the internal cysteine in the RVG sequence has been demonstrated to be necessary for cellular entry of the peptide. Studies into α-bungarotoxin binding to the nAchR show the cysteine residue in α-bungarotoxin corresponding to the cysteine within the RVG peptide interacts with an aspartic acid residue in the nAchR (Huang *et al.* 2013). Although the binding curve for the RVG peptide has yet to be established in the b.End3 cell-line, it may be that the loss of this interaction through the substitution with alanine critically reduces the ability of the peptide to bind its receptor. Further investigations into this will be undertaken in the coming months to evaluate the importance of this residue in the uptake process.

Pulse-chase studies with the RVG-[Rho] peptide demonstrated that it can undergo active efflux from both b.End3 and hCMEC/d3 cells. With the proportion retained by the cells at the conclusion of a 1 hour chase comparable to transferrin and both 8D3 antibodies in the previous chapter. This characteristic of the RVG peptide is desirable for potential targeting ligands as it show the capacity of the ligand to both be taken up and effluxed

from BMECs. Suggesting that there may be the potential to undergo transcytosis across the barrier cell-type *in vivo*.

The competition of RVG peptide uptake by α-bungarotoxin would be indicative of a receptor-mediated process, most likely involving a nAchR. These findings are concurrent with previous research using this peptide. The additional competition studies using α-bungarotoxin Alexa 647 in b.End3 cells showed the neurotoxin uptake can be inhibited by the addition of increasing concentrations of both unlabelled α-bungarotoxin and RVG peptide. This provides further evidence of the involvement of the nAchR in the RVG uptake process. Further, the uptake of the RVG peptide was inhibited by competition with unlabelled α-bungarotoxin, providing further evidence that the uptake of the RVG peptide is a receptor-mediated process, involving the α7nAchR. Additionally, due to the confounding data on the importance of the cysteine residue in the sequence structural and functional analysis of the interaction of the peptide with any putative receptors will be done to clarify the uptake process. However, overall, it possible to conclude from the bungarotoxin competition and siRNA knockdown studies, that the α7nAchR is a target for RVG peptide uptake into cells.

To progress this work further, the testing of dendrimer constructs targeted with the RVG peptide could be synthesised and used to study the effect of targeting ligand density, on the uptake and efflux of the dendrimer complexes from the BMEC cell lines. This would be of particular interest, in relation to the work with monovalent targeting antibodies, directed against the transferrin receptor (Yu *et al.* 2011; Niewoehner *et al.* 2014). Through the use of the pulse-chase assay and combination with confocal microscopy, any potential cross-linking events and alterations to trafficking efficiency could be measured with these assays.

Chapter 4: Advanced microscopy techniques for the imaging of cellular trafficking events in brain microvascular endothelial cells

4.1 Introduction

4.1.1 What is TIRF microscopy?

Total internal reflection fluorescence microscopy (TIRFM) was developed in the 1980s by Daniel Axelrod. It enables selective excitation and imaging of fluorescent artefacts, located within close proximity to the coverslip surface; such artefacts can be lost within noise when samples were imaged with alternative microscopy techniques (Axelrod 1981).

Light waves are refracted at the interface between different materials, due to the differences in the speed of light within different materials. The extent to which light will is refracted at an interface is determined by respective refractive indexes of the materials (Harrick and Beckmann, 1974; Axelrod, 1981). Other factors influencing the refraction of light include the wavelength of the light used, with longer wavelengths (far red) undergoing less refraction at a phase interface than shorter wavelengths of visible light (blue). If the angle of incidence of the light is less than the critical angle of the material it passes through, then the process of refraction will occur as standard, and the sample will receive direct illumination from the excitation source.

In the case of TIRFM, the angle of incidence from the excitation source exceeds the critical angle of the coverslip material. This causes the excitation beam to be reflected at the coverslip-sample interface and generates an electromagnetic wave, the evanescence wave, with the same wavelength as the excitation source, which propagates into the sample. The evanescence wave decays exponentially with distance above the coverslip surface, allowing for the selective excitation of fluorophores within 100-200nm above the

coverslip. The selectivity of the illumination field provides for the increased signal to noise within the evanescence field with high axial resolution, allowing for single molecule imaging above the coverslip surface (Axelrod 1981; Jaiswal and Simon 2007). To ensure the generation of the evanescence wave into the sample the objective lens, immersion oil and coverslip must have matched refractive indices.

The evanescence wave penetration depth in the sample is determined by the wavelength of the excitation light, lower wavelength, lower field depth, and the incidence angle of the reflected light, increasing the angle beyond the critical angle decreased the evanescence field depth. Lenses of high numerical aperture (NA) are therefore essential to allow for the greatest range of supercritical angles (Axelrod 1981).

Calculating the Critical Angle

Equation 4.1.

$$\theta_{critical} = sin^{-1}\left(\frac{n_1}{n_2}\right)$$

As previously stated the critical angle of a TIRFM system was determined by the difference between the refractive index of the glass (n_2) and the refractive index of the sample solvent (n_1). By knowing this angle, it is possible to calculate the illumination depth of the sample using Equation 4.2.

The depth of illumination field will vary based on the wavelength of the laser, the power of the illumination and the angle at which the laser is hitting the coverslip. However, the effect of laser power is minimal, due to the exponential decay of the evanescence field.

Equation 4.2.

$$d = \frac{\lambda}{4\pi n_2}\left(\frac{sin^2\theta}{sin^2\theta_{crit}} - 1\right)^{-\frac{1}{2}}$$

As the evanescence wave propagates from the coverslip surface, through the sample, the power decays exponentially, meaning that a fluorophore which is 1 nm from the coverslip will typically receive 5000 times the power of a fluorophore 1000 nm from the coverslip (Axelrod 1981). This change in power can be modelled using Equation 4.3, where the power (I) at a given (z) depth will be related to the initial laser power (I_o), and the depth of the evanescence field (d), calculated from Equation 4.2. A diagrammatic overview of the equations in this section as shown in Figure 4.1.

Equation 4.3.

$$I = I_0 . e^{-(\frac{z}{d})}$$

The high, localised excitation powers (100-300 nm from coverslip) allows for a high signal to noise ratio of excited fluorophores. While the z-axis resolution is typically below the diffraction limited resolution within this plane. TIRF microscopy has the advantage over other, epifluorescence microscopy, where the whole of a sample is exposed to the excitation light. This causes collection of fluorescence from both within the focal plane and out of focus light, giving a poor signal to noise ratio and axial resolution. The details of structures located in the basolateral region of cells can be lost to the fluorescence signal from other areas of the cell. Whereas in TIRF microscopy, due to the exponential decay, of the propagating evanescence wave, only structures in the basolateral compartment of the cell, that are less than ~300nm from the coverslip surface, are illuminated. The signal-to-noise with TIRF allows for axial resolutions below the diffraction limit, and tracking accuracy has improved to a resolution of within 2nm, with appropriate, post-capture analysis.

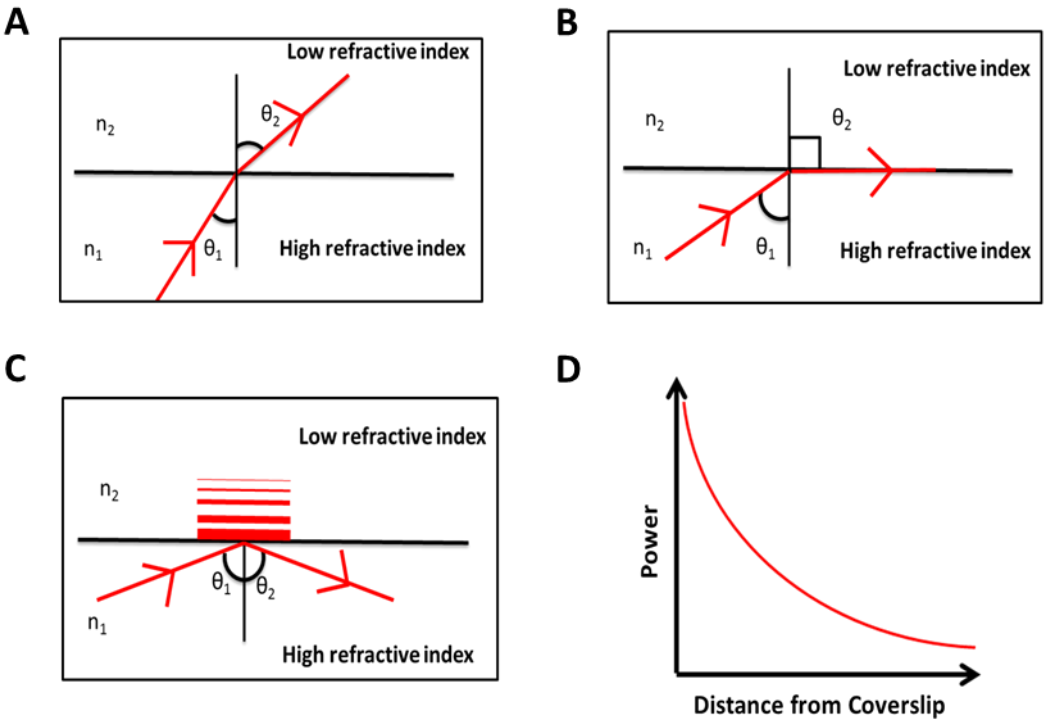

Figure 4.1: Increasing the Light Angle at an Interface Causes Total Internal Reflection
The above figure shows the effect of increasing the angle at which light passes across the interface between two materials with different refractive indexes. A represents an angle below the critical angle, so the light is refracted at the interface. In B, the light arrives at the interface at the critical angle and is refracted back along the interface. In C, the light has an angle greater than the critical angle and so is reflected at the interface and an evanescence wave propagates into the sample. The decay of this wave is exemplified in D. Adapted from Figure 2., Fish (2009)

4.1.2 Using TIRF microscopy for cell imaging

Coupling of the TIRF microscopy method with drug delivery research allows for the analysis of the basolateral membrane of cells and the real-time imaging of cellular trafficking events occurring at this site (Midorikawa and Sakaba 2015; Machado *et al.* 2015; Wennmalm and Simon 2007). A schematic diagram of the TIRF microscopy in cells is shown in Figure 4.2. By careful design of the studies and the analytical approaches taken it would be possible to track the arrival and delivery of a ligand to the basolateral membrane of the cells, that has come from an apical receptor. Cellular studies using TIRF microscopy, in the literature, have focused on the kinetics fluorescently tagged receptor

arrival within the Evanescence Field, typically, without looking at a ligand directly (Axelrod 2001; Betzig *et al.* 2013).

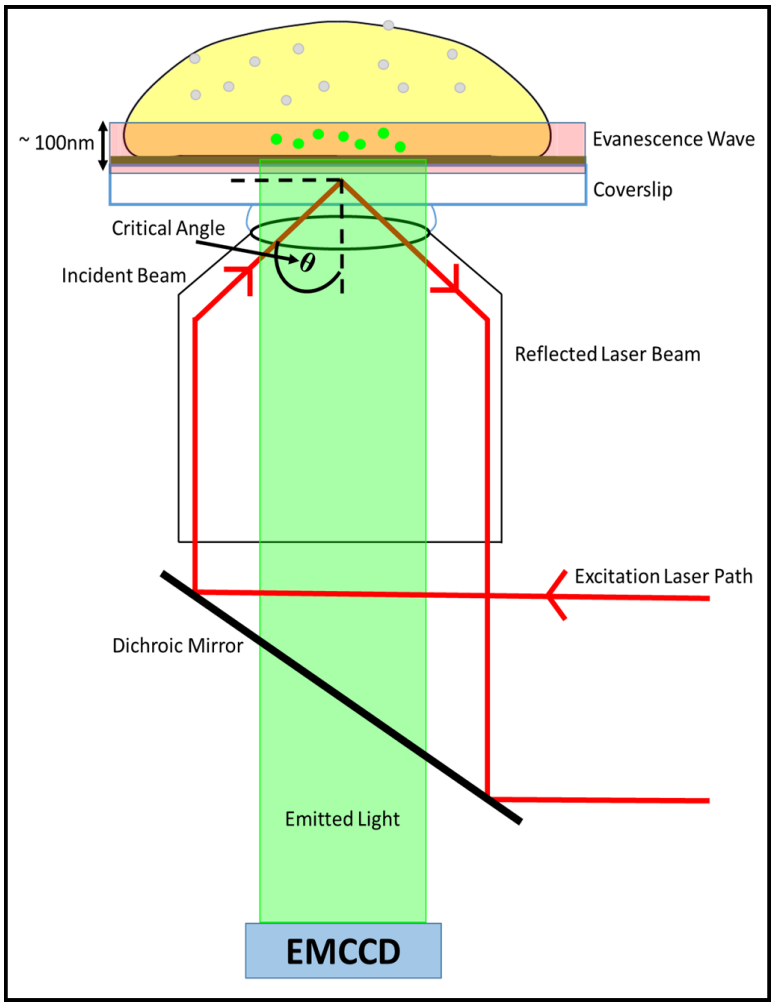

Figure 4.2: Simplified schematic of the light-path in a TIRF Microscope
The red line represents the path of the excitation laser light through the microscope. Having passed through excitation filters (not shown) it will be reflected into the objective lens of the microscope, where lenses within it ensure the light path leaves the objective at the correct angle for TIRF. The light is reflected at the coverslip-sample interface, and forms the evanescence wave (red rectangle), which propagates a short distance into the sample. Exciting fluorophores within the field (green). Fluorophores outside the evanescence wave are not excited (grey). Light emitted from the excited fluorophores (green rectangle) passes back through the microscope and into the detector (EMCCD).

TIRF microscopy has been used to study vesicle release and fusion at the basolateral membrane. However, when examining the literature, there are differences in terminology and the way events are characterised. For exocytosis characterisation, the steps would be

as follows. Firstly, a vesicle enters the evanescence field and becomes bound to the fusion site; this is an arrest of free movement of a vesicle through the cytosol and confinement of its location for an extended duration. The attachment to the cell membrane, before complete membrane fusion and content release is through the interaction of v-SNARE and t-SNARE protein complexes (Axelrod 2001). Once in place the attachment proteins "unzip" and the membranes of the vesicle and cell fuse (Vrljic *et al.* 2010).

Most protocols for examining exocytosis events will look at event duration, to ensure the vesicle is fully bound to the plasma membrane before release. Prior to the completion of vesicle fusion, the motion of the vesicle was restricted to the site of membrane binding. Some studies will then use a secondary signalling marker, such as Ca^{2+} to allow for completion of the fusion process. Due to the requirement of calcium for exocytosis to take place (Lock *et al.* 2015; Walker *et al.* 2008). Other studies use a pH-sensitive probe to confirm when the vesicles content is exposed to the extracellular environment (Shen *et al.* 2014; Bauereiss *et al.* 2015).

In "simpler" studies fluorescently tagged receptors (GFP-labelled) can be monitored at the basolateral membrane of cells to assay their exocytosis. Here studies look at the peak intensity, spot radius and total intensity to confirm vesicle release (Schmoranzer *et al.* 2000). An increase in spot diameter confirms the event as exocytosis, as the vesicle membrane "spreads" into the plasma membrane. Another study worked to characterise the types of events into arrival, loss and diffusion events at the membrane (Midorikawa and Sakaba 2015). Other studies found that some vesicles do not release their entire cargo at a single docking. Instead, several discrete fusion events were required to release the full content of the vesicle. These events have been termed as "kiss-and-run" exocytosis, or partial release events have been seen in the analysis of capture (Roman-Vendrell *et al.* 2014; Jaiswal *et al.* 2009).

Several studies have used TIRF microscopy to monitor cellular trafficking at the basolateral membrane of the cell. The group of Sally-Ward have manipulated the TIRF microscopy setup to allow for 3-dimensional tracking of vesicles, through cells, on-route to and from the basolateral membrane. The setup for this imaging is complex, involving multiple detection EMCCDs at differing locations from the microscope. Using beam splitters within the emission pathway light from a given focal plane may be deflected into the path of the detector, while allowing other light to pass through the splitter. Using this technique antibodies, and membrane receptors have been imaged at up to eight focal planes simultaneously, and the endocytosis tracked in 3D. Within the field of endothelial research, the FcRn receptor has been extensively characterised using the 3D tracking protocols (Ober *et al.* 2004).

4.1.3 Photoswitchable Proteins in Cell Imaging

For many years now the transferrin receptor (TfR) has been one of the principal targets for the study of receptor-mediated transcytosis across the brain microvascular endothelial cells (BMECs) of the blood-brain barrier (BBB). However, despite multiple investigations into the TfR, the efficiency of delivery across BMECs remains low. Indeed the precise mechanism of TfR transcytosis remains unclear. The TfR itself is known to undergo constitutive recycling within barrier cell types to facilitate the delivery of iron, bound to transferrin, within the cells.

Additional studies by both Roche and Genentech with mono- and di-valent antibody constructs as well as low and high-affinity construct showed an ability to perturb the standard trafficking. The high affinity and di-valent anti-TfR antibodies caused receptor downregulation from the surface of BMECs and increased lysosomal residence, leading to a decrease in the total TfR within BMECs. Low affinity and mono-valent antibodies

against the TfR were able to successfully deliver a protein cargo into the CNS *in-vivo* in addition to showing lower toxicity to animals in studies.

4.1.3.1 Fluorescent Protein Constructs

Fluorescent proteins have had increasing prominence in life science research since the identification of green fluorescence protein (GFP) in 1962 and its cloning in 1992 (Hughes 1998; Shimomura *et al.* 1962; Prasher *et al.* 1992). The initial studies of the GFP proteins were in association to bioluminescence in marine creatures. It was not until 1994 that GFP was used to label intracellular structures and for the study of the subcellular distribution of proteins (Chalfie *et al.* 1994). Studies of aquatic creatures including, Hydrozoa and Anthozoa revealed fluorescent proteins (FPs) with chromophore structures similar to that of GFP. Further studies along the evolutionary hierarchy of these species revealed FP both GFP-like and novel FPs such as DsRed and Kaede (Labas *et al.* 2002). Increased interest in the use of FPs in life science research has led to the discovery and cloning of FPs covering the entire range of the visible spectrum with improved fluorescent stability and intensity.

Many FPs exist in a barrel-structure with the central core forming the chromophore, comprising the internal facing amino acid side-chains (Evdokimov *et al.* 2006). Variation of these amino acid residues can tune the spectral properties, stability, catalytic activity and even generate a non-fluorescent form of the protein. The arrangement of the barrel of the FP is the process of fluorescence maturation, the process of formation of the final chromophore within the pore of the barrel. This process is considered self-catalytic with no external factors, except oxygen molecules (Evdokimov *et al.* 2006). However, beyond this little is known about the precise mechanism of the biogenesis of the chromophore

with the exact sequence of the formation being poorly understood for the even the most commonly studied, GFP.

More recent studies have found it is possible to engineer fluorescence proteins with multiple states, ie. Off or on; green or red. These FPs fall into several categories: photoactivatable (on/off), photoswitchable or photoconvertible (Zhou and Lin 2013). Changes to chromophore structure which lead to the permanent alteration of the fluorescence profile of the FP are termed photoconvertible and most deemed most useful for the studies proposed. Photoconversion requires exposure of the FP to high energy light (typically ~ 400nm) to facilitate chromophore structural alterations, shifting the excitation-emission profile of the protein. The characteristics of photoconvertible proteins can be seen in Table 4.1, below. All photoconvertible proteins require stimulation with high-energy wavelengths of light to initiate the state change (Zhou and Lin 2013). This state change often involves the breaking of peptide bonds within the structure of the chromophore, which will alter the excitation and emission profile of the protein. In some cases, these changes can be reversed by exposure to longer wavelength light and these proteins are termed as photoswitchable (Zhang *et al.* 2016). If only a single conversion is possible (i.e. green to red only), then the protein is termed as having undergone photoconversion. With these proteins, the only progression from the photoconverted state is to photobleach.

Table 4.1: Photoconvertible Fluorescent Proteins

Protein	Ex.1 (nm)	Em.1 (nm)	Conversion (nm)	Ex.2 (nm)	Em.2 (nm)
Dendra2	490	507	400±10	553	573
mEos2	508	516	400±10	571	581
mEos3.2	507	516	400±10	572	580
mEos4a	505	516	400±10	569	581
mEos4b	505	516	400±10	569	581
dEos	505	516	400±10	569	581
tdEos	505	516	400±10	569	581
mKikGR	507	517	400±10	583	593
Kaede	508	518	400±10	572	580
mGeo-M	503	514	400±10	569	581
PSmOrange	548	565	488	634	662
PSmOrange2	546	561	488	619	651

To explore this difference in trafficking of the receptor further, we have generated a TfR that is co-expressed with the photo-switchable protein PSmOrange. This protein was developed by Subach *et al.* (2012), in its standard form, PSmOrange fluoresces in the orange region of the visible spectrum (excitation 548nm, emission 565nm). However, if exposed to blue/green light sources (488nm) PSmOrange undergoes photo-oxidation and cleavage of the protein backbone to produce a chromophore with far-red fluorescence

with an excitation wavelength of 636nm and an emission wavelength of 662nm (Figure 4.3) (Pletnev *et al.* 2014). The half-life of conversion of PSmOrange is 15s so for these studies apical membrane regions were exposed for a period of 60s to ensure greater than 90% conversion within a field of view before incubation at 37^{o}C (Subach *et al.* 2011; Subach *et al.* 2012). Further, the far-red form of PSmOrange displays favourable photostability and resistance to photobleaching making it ideal for the analysis of the arrival of potentially low levels of the construct at the basolateral membrane. In combination with the electron multiplying CCD camera (EMCCD) of the TIRF microscopy imaging of single fluorescent events should be possible at the basolateral membrane.

Using this switchable PSmOrange-TfR in combination with TIRF microscopy, we will be able to selectively "switch" the fluorescence at the apical membrane to the far-red. The cells will then undergo an incubation with various ligands against the TfR at 37^{o}C for differing time courses; we will then be able to examine the basolateral cell membrane, again using TIRF microscopy to assay the arrival of an apical receptor which has undergone a transcytosis process.

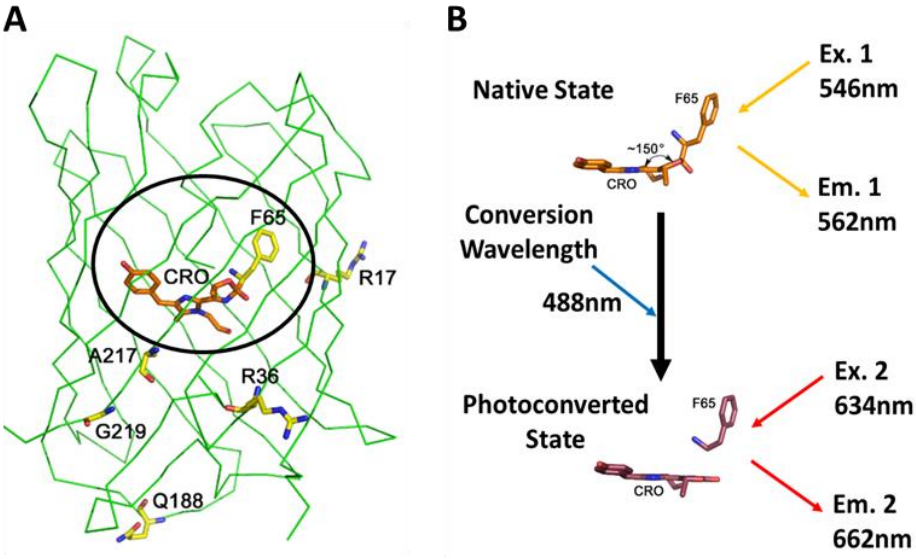

Figure 4.3: Structure of PSmOrange and Chromophore changes in photoswitching
The above shows the structure of the entire PSmOrange protein (A) with the chromophore highlighted by the black circle. The changes that occur in the chromophore structure, when exposed to photoswitching light are then shown in B, and the excitation and emission wavelengths of both states are given. Adapted from Pletnev et al (2014) Figure 3 and Figure 4.

4.1.4 Chapter Aims

The primary aim of this chapter was to assess the feasibility of using TIRF microscopy to image the basolateral cell membrane of BMECs. This was done using a fluorescently labelled ligand (transferrin) and the tagging of its receptor (TfR). To enable the characterisation of both ligand and receptor dynamics in basolateral regions of BMECs. The objectives for this chapter were as follows:

1. The characterisation of fluorescently labelled transferrin at the basolateral cell membrane, to identify putative exocytosis events.
2. The construction of photoswitchable fluorescent proteins, tagged to the TfR (PSmOrange)
3. Mathematical modelling and characterisation of PSmOrange photoswitching with BMECs using confocal and TIRF microscopy techniques.

4.2 Methods

4.2.1 Materials

EBM-2 Media was purchased from Lonza, UK. Fetal calf serum (FCS), trypsin-EDTA (0.5%) dissociation solution, Penicillin-Streptomycin (10,000U/mL), Phenol Red Free DMEM + Glutamax high glucose, Anza™ 10pk Starter Kit Restriction Enzymes, Anza™ T4 DNA Ligase Master Mix, PureLink™ Quick Gel Extraction Kit, Ethidium Bromide solution, 10x TBE buffer, Agarose, Lipofectamine™ P3000 Kit and Transferrin AlexaFluor® 647 were purchased from Life Technologies, UK. The following filters, used in the TIRF microscopy setup were purchased from SEMROCK, USA: ZET473/10x, ZET532/10, ZET635/20, FF01-676/29, FF01-593/40, NF03-633E, BLP01-473R, NF01-532U, FF640-FDi01 and DI03-r405/488/532/635. The EMCCD camera was purchased from Andor, UK. All plasmids were purchased from AddGene, USA. Plasmid Midi Prep Kit was purchased from Qiagen, UK. BSA, Hoechst and any salts not mentioned here were purchased from Sigma Aldridge, UK.

4.2.2 Cell culture

These studies were performed in hCMEC/d3 (human immortalised brain endothelial cells). These are cultured on collagen coated plastic, in media containing: 92.5% EBM-2 media supplemented with 5% FBS, 1% penicillin-streptomycin, 1% HEPES (1M stock solution) and 0.5% vitamin C. hCMEC/d3 cells were split at between 75-90% confluency by use of trypsin-EDTA solution (0.05%) and incubating the cell at 37^{o}C for ~5 minutes. The dissociated cells are then resuspended in fresh, culture media and centrifuged at 300 xg for 5 minutes, to remove trypsin-EDTA from the cells. The cell pellet is resuspended in 5 mL of media and the cells counted by haemocytometer. For maintenance, 1 million cells were seeded into a T75 flask, for assays hCMEC/d3 cells are seeded at a density of 20,000 cells/cm^2, onto collagen coated plastic ware.

4.2.3 Uptake and Pulse-Chase Study design

hCMEC/d3 cells are grown in glass-bottomed MatTek dishes (No. 1.0 coverslip) until a confluent monolayer can be observed by bright field microscopy (5-7 days post seeding). Once confluent remove the culture media from the MatTek dish and replace it with Kreb's Ringer buffer, containing 0.5% BSA (KRB). Incubate the cells with this buffer for 30 minutes at 37^{o}C to remove serum proteins from the cell surface. For the uptake and pulse-chase studies, following the starve in KRB, the cells are then incubated with the fluorescent ligand, transferrin-Alexa Fluor 647 (100pM) for 45 minutes at 37^{o}C (the uptake phase). Following this, cells are washed 5 times with PBS to remove the extracellular, unbound ligand from the imaging dish. To image at this stage cells are incubated with KRB + 2.5% BSA for the chase/imaging phase. Dishes undergoing a chase phase were incubated at 37^{o}C and 4^{o}C for up to an hour, prior to imaging. With cells being chased they are washed a second time with PBS to fluorescent ligands that are no longer cell associated following the chase.

4.2.4 TIRF microscopy design

There were multiple imaging approaches available to use with the TIRF setup available in Cardiff. The simplest form was tracking the arrival and motion of particles within the evanescence field. This can be done by recording a video of the cells, 1000 frames in duration (30ms exposure time), and post-acquisition analysis using the Fiji software. For the Alexa Fluor 647 labelled proteins, imaging setup used 634nm excitation laser, with a minimum, fibre coupled power, of 20mW, and a long-pass 660nm emission filter in place. Video acquisition was done using an EMCCD camera, with a pixel resolution of 512x512. Imaging was done through a 60X magnification lens with an additional 1.5X added within the microscope and 10X magnification at the coupling of the microscope to the camera.

4.2.4.1 Photobleaching

TIRF microscopy offers a way to track the dynamics of protein trafficking events at the basolateral membrane of cells. This can be done by live tracking of events at the membrane in long-duration videos. However, other methods exist to monitor fluorescence at the basolateral membrane and dynamics of receptor-ligand trafficking. To ensure that fluorescence arrival into the basolateral region is from the apical areas of the cells, and not merely fluorophores "flip-flopping" in and out of the evanescence field. By photobleaching fluorophores in the evanescence field, with a long exposure (30s) and then looking at the recovery of fluorescence into the field of view. This technique is known as fluorescence recovery after photobleaching (FRAP). To analyse these studies, it was proposed to study the total fluorescence recovery into the bleached region, over ten minutes, while also looking at the total number of fluorescent spots. If the trafficking of the protein is limited to purely basolateral recycling then after the photobleaching there would be limited or no return of fluorescence in the recovery. However, if the trafficking pathway of the protein is non-restrictive throughout the cell, then the recovery into the basolateral region will be more rapid.

4.2.5 Plasmid Design

To generate the PSmOrange-TfR construct, the TfR sequence was restriction cloned into the vectors pPSmOrange-N1 and pPSmOrange-C1 to produce constructs with N- and C-terminal labelling with the fluorescent protein. This was to ensure the stability and the normal functioning of the construct within cells, without interference to cognate ligand binding. The most optimal construct will be taken forward for the transcytosis studies. Two-site restriction enzyme digest of the donor and acceptor plasmids should ensure maximal incorporation of the TfR sequence within the final plasmid, before purification.

The restriction sites **EcoR1** and **Age1** have been selected, due to their flanking of the TfR sequence in the donor plasmid and their presence within multi-cloning site (MSC) of the acceptor plasmids in the desired insertion site. Also, the use of multiple restriction enzymes ensures the inserted sequence will maintain the correct orientation in the final plasmid. Thus, ensuring the expression of the sense sequence of the desired protein.

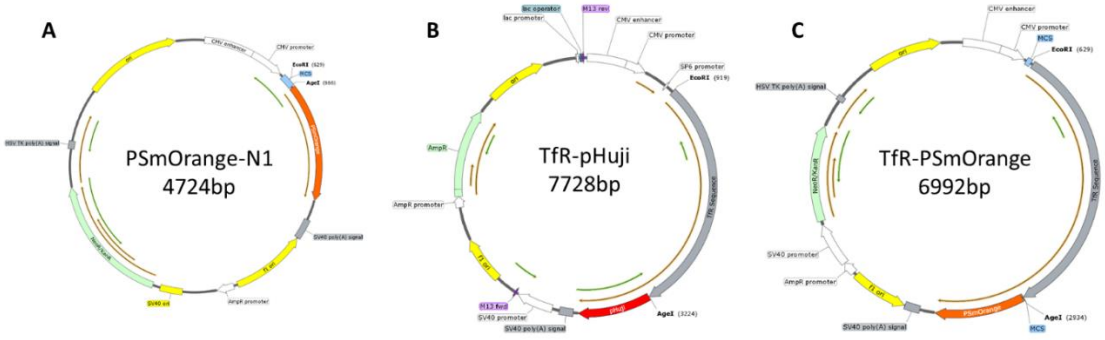

Figure 4.4: PSmOrange-TfR Plasmid Structure and Synthesis
In the above figure, the plasmids used and created are shown. Figure A shows the structure of the PSmOrange-N1 plasmid (Addgene ID = 31898). B the structure of (Addgene ID = 61505). While C is the proposed structure of the synthesized plasmid TfR-PSmOrange.

4.2.6 Restriction Digest

Restriction digests were performed as per the supplier's information. Briefly, 1µg of donor and acceptor plasmid were incubated with both restriction enzymes for 1 hour at 37ºC to ensure maximal cleavage of DNA. The cleavage products were then separated by purification along an agarose gel (0.8%) with the correct bands being collected for and the DNA extracted from the gel. The insertion fragment, containing the TfR DNA sequence, flanked by the overhanging sticky-ends, containing the complement to the restriction site, was then incubated with the cleaved, recipient plasmid and annealed using T4-ligase. Blank, insert sequence only and recipient only ligations were also performed to establish the self-annealing occurrence.

4.2.7 Bacterial Transformation

The newly created plasmids will then be transfected into DH5α *E. coli* cells by heat-shock transformation. Briefly, an aliquot of the bacterial stocks were thawed on ice and 100µL of the cells will be transferred into a chilled tube, one tube per transfection. The ligation product should be diluted 1 in 5 from the reaction and from this 1µL is added to the cells and pipetted to disperse the DNA among the cells. Cells are kept on ice for a further 30 minutes before heat-shocking the cells at 42ºC for 45s and placing the cells back on ice for 2 minutes. Cells are incubated with 900µL of S.O.C. media (room temperature) and shaken for two an hour at 37ºC. Streak the transformed bacterial cells onto LB agar plates containing selection antibiotics (ampicillin – 100µg/mL or kanamycin - 50µg/mL) and incubated overnight. The following day single colonies are picked and incubated in 5 mL LB broth and cells were incubated for 12 hours, under shaking at 37ºC, allowing for initial bacterial growth. From this 1 mL of bacterial cells are incubated in 250mL of LB broth, for 4 hours to expand bacteria for plasmid isolation.

Following isolation of plasmid from E. coli, the insert was confirmed by restriction digest of the plasmid with EcoR1 or EcoR1 plus Age1 restriction enzymes. This confirmed the molecular weight of the newly constructed plasmid and the presence of the TfR DNA within the plasmid. Additionally, the plasmid digests were extracted from the gel and sequenced to further confirm the presence of the TfR insert within the pPSmOrange-N1 plasmid.

4.2.8 Cell Transfection

To optimise the transfection protocol within hCMEC/d3 cells, three concentrations of plasmid were selected, 0.5, 1, 2 µg/well. Briefly, cells were seeded into 6-WP, MatTek imaging dishes and other plastic ware at a concentration to give 70-90% confluency 24 hours post-seeding. Plasmid transfection solutions were prepared in accordance with the

manufacturer's protocol. For example, 1 μg of plasmid was combined, in 50μL Optimem, with 2μL of P3000 reagent and 3.75μL Lipofectamine 3000 reagent and incubated at room temperature for 15 minutes before transfection. For the other concentrations of plasmid the ratios of DNA:P3000:Lipofectamine 3000 remains constant, and the volume of Optimem remains at 50μL per well. The prepared transfection solution is added to cells in culture in serum-containing media and allowed to incubate for 48 hours before analysis.

Confocal microscopy was performed to confirm the transfection and the ability of the pPSmOrange-TfR plasmid to undergo photoswitching with our microscopy setup. Cells were imaged 48 hours post-transfection with the plasmid. Before imaging the culture media was removed and replaced with imaging media (phenol red-free DMEM containing HEPES and supplemented with 0.5% BSA), to equilibrate cells for microscopy. Five minutes before imaging, cells were stained with Hoechst to ease identification and allow for visualisation of the nuclei. Cells are then washed 3 times with PBS before re-incubation with new imaging media for analysis by microscopy.

When imaging plasmid positive cells were identified by fluorescence in the orange channel (ex. 543nm, em. 560-610nm), as this is the native state of the PSmOrange. A single image was captured, by exposing cells to 543nm and 633nm lasers, this will be referred to as "Time Zero", and represents the fluorescence distribution, within to the imaging plane, before photoswitching. A time series was then taken, of the same field of view, exposing the cells to 543nm, 633nm and the switching wavelength, 488nm (at different powers). By imaging in this manner, it is possible to see the fluorescence state shift over time and establish the photoswitching kinetics for different laser powers.

Analysis of the switching kinetic series is done using Fiji software to identify regions of interest (ROIs) and quantify the mean fluorescence within these ROIs. This is done in each frame of the series and each fluorescence channels (orange and far-red). The values

are then normalised so that the fluorescence at time zero in the orange channel is equal to 1 and in the far-red channel is 0. The far-red fluorescence is then further normalised so that the maximum value for far-red fluorescence is equal to 1.

Having established the optimal switching time for the fluorescent protein, it is then possible to switch the protein without needing to simultaneously image in the orange and red channels. This allows for the performance of a modified FRAP study, where, by switching in selected regions of the cells and then imaging the entire cell it is possible to see the redistribution of the receptors within the focal plane.

4.2.9 Setting up TIRF for two colour imaging

To further optimise the TIRF microscope for photoswitching experiments, efforts were made to establish dual colour imaging with the TIRF microscopy setup, to allow simultaneous imaging of switched and native state of the protein. The optical pathway of the TIRF microscope was altered to allow for multi-excitation and image-splitting to collect two different wavelengths of emitted fluorescence simultaneously. A diagram of the light paths involved was shown below. However, in simplistically terms, excitation light from the laser sources is columnated and aligned, so that the laser spot for all three excitation sources is in the same position. This ensures maximal power output from all lasers once they were coupled into the fibre launch system. The fibre system, although reducing the laser output power at the stage, ensures uniform illumination of the sample during imaging. Free-space coupling of the excitation lasers into the microscope allows for higher excitation powers at the microscope stage. However, it also produces a Gaussian excitation profile, that is different for each excitation laser, so uniform, comparable illumination is harder to achieve.

Once the excitation light is within the microscope, it must be reflected “up” through the objective lens to the sample. To do this in multi-excitation imaging, a quad-edge dichroic

mirror was used. This dichroic mirror can reflect the excitation light from all the lasers into the objective lens, while crucially allowing the emitted light from excited fluorophores to pass back through it. The angle at which the excitation lasers hit the dichroic mirror will determine the position, relative to the centre of the objective lens, that the light will arrive at and therefore the angle at which it will leave the objective and reach the sample.

Having been totally internally reflected and exciting the fluorophores in the sample the emitted fluorescence will travel back through the objective lens. In this case, passing through the dichroic mirror and through a set of emission notch filters to "remove" any photons of light that may have come from the back reflection of the laser. The emitted light is then directed into the image splitter unit. Here there is another dichroic mirror, which will allow long wavelengths (>640nm) to pass through while reflecting wavelengths below this. The now, two paths of now pass through bandpass filters for their respective fluorescence (red = 676/29nm filter, green = 593/40nm filter). The photons that passed through the bandpass filters is then focused onto the EMCCD detector of the camera, such that half of the detector will detect "red" fluorescence and the other half "green" fluorescence.

4.2.10 Microscopy Study Preparation

For these studies, the PSmOrange-TfR plasmid was transfected into hCMEC/d3 cells, using the protocol in section 4.2.8, and cells left for 48 hours to express the fusion protein construct. After 48 hours cells were lysed, using the lysis protocol described previously and the protein concentration quantified and adjusted to 1 µg/µL with PBS. This stock of protein lysate was stored, in 10 µL aliquots at -20 ^{o}C until use. Additionally, lysates from un-transfected control cells were collected, to ensure that any observed photoswitching

was due to the predicted switch in the PSmOrange protein and not another component of the cell lysate.

4.2.11 Imaging Optimization – Channel Cross-Talk

The cell lysate (1 µL) was pipetted onto a plasma treated coverslip, at the stock concentration (1 µg/µL), and allowed to dry, so the fluorophores were in contact with the coverslip, with limited diffusion. This concentration of cell lysate allowed for the imaging of single fluorescent molecules when TIRF. Initial optimisation was done to characterise the fluorescence cross-talk between the microscope channels with the different laser configurations. These included: green laser only, red laser only, green and red lasers simultaneously, blue and green lasers simultaneously, blue and red simultaneously and all three lasers simultaneously. This cross-talk study was performed on regions of the native state (green) protein and then on regions exposed to the blue laser for a period of up to 10 minutes. This long blue exposure allows for photoswitching to take place, while not bleaching the fluorescence with the green and the red lasers.

4.2.12 Imaging Optimization – Photoswitching Procedure

The previous optimisation stage found as the number of lasers was increased the noise in the red and green imaging channels increased. This was most apparent in the far-red, as the signal to noise was much lower than in the green channel, and there was bleed-through from the brightest “spots” in the green channel. It was therefore decided to image the photoswitching process; long capture videos would be taken, 1000 frames at 30 ms exposure. With the protein exposed to the green laser only for approximately the first 50 frames, to give the locations of the fluorescent protein at the before the photoswitching. Then simultaneously exposed to the blue and red laser, for the duration of the switch (~900 frames). Before finally exposing with the green laser for the last 50 frames of the capture, these allowed the visualisation of the location of any native fluorescence at the

conclusion of the photoconversion. The total exposure time was varied by changing the number of accumulations per frame while keeping the total number of frames constant. This means, if the frame accumulation was "5", the camera would z-project five frames into one, which it saves in the video before capturing the next frame, a 1000 frame video is the length of a 5000-frame video. The number of accumulations used was: 1, 2, 3, 5 and 10; which created a series of videos from 30 seconds to 5 minutes.

4.2.13 Imaging Optimization – Image Analysis

All image analysis and quantification, unless stated otherwise was performed using Fiji and the plugins and custom macros within the software. Using two colour imaging creates a 512 x 512-pixel image, visually divided in two, based on the green (upper) and the far-red channels (lower). Before any quantification was done, the video was duplicated to produce two videos, for the green and far-red channels. These channels are then merged into a single video and assigned accordingly.

The videos were then examined to establish the frame number where the switch was made from green laser only, to blue and red lasers, back to green laser only. This was done by visual inspection and plotting the z-axis profile of the green channel to locate the "jumps" in fluorescence signal. The video is split in three at the points of laser combination change and labelled accordingly ("greenPre", "Photoswitching", "greenPost"). Z-projections of the AVERAGE INTENSITY were made for the greenPre and greenPost videos, and a SUM SLICES projection of the Photoswitching video.

To identify the events in the green channel that have disappeared during the photoswitching phase of the capture, image maths was performed as follows:

Equation 4.4

$$changeInGreen = greenPost - greenPre$$

If an event was present in the greenPre, but not the greenPost, a black spot appears in the output image. Conversely, if the spot was present in the greenPost projection, but not the greenPre a bright green spot was seen. This new image is then combined with the z-projection for the Photoswitching video and is examined to check for the co-localization of red spots with black spots. These indicate the presence of a "switched" fluorescent protein from the start of the capture. The co-localization of green spots with red spots would potentially represent a region of partial photoconversion, where several "new" native state of the fluorescent proteins arrived during the photoswitching phase. Some of these may have undergone photoswitching, into the far-red form and so fluorescence from both forms is detected at that location.

Using the built-in JACoP plugin in Fiji and the Mander's threshold co-localization test, the exact percentage of red spots that were localised with green spots could be found. This is then compared across all the frame accumulations to see the change in colocalization with increased photoswitching time.

4.2.14 Mathematical Modelling of PSmOrange Photoswitching

The mathematical modelling of the distribution of the states of the chromophore at a set time-point was done in MatLab, using the Simulink plugin. The equations were created by LaPlace Transformations based on a closed system consisting of three compartments.

4.3 Results and Discussion

TIRF microscopy allows for the detailed imaging of cellular events at the basolateral membrane of cells. As such it has a high potential for use in the understanding of cellular trafficking across brain microvascular endothelial cells.

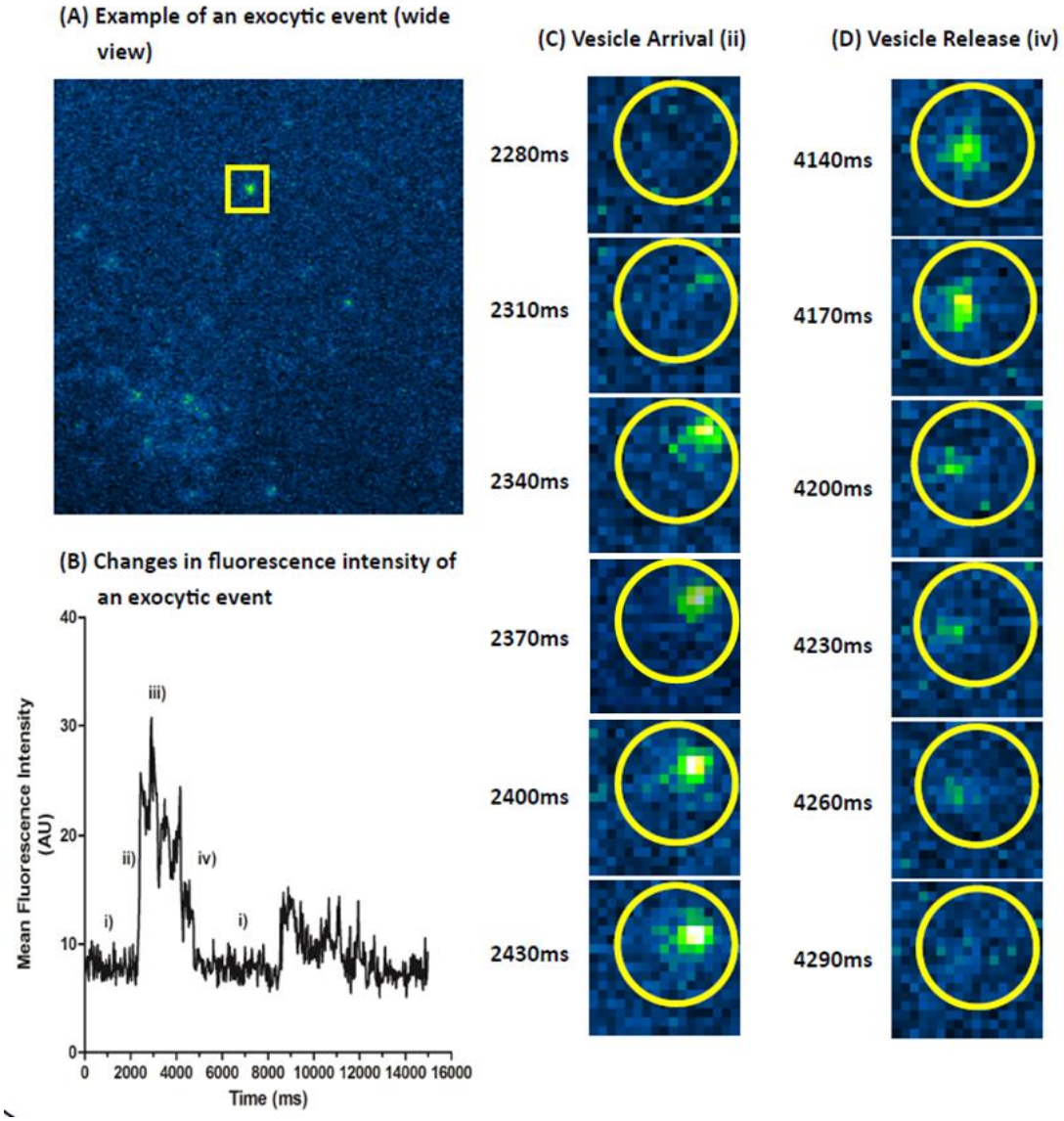

Figure 4.5: Transferrin-AlexaFluor 647 Trafficking at the Basolateral Membrane of BMECs
Figure A shows a single frame from a capture video of transferrin-AlexaFluor 647 trafficking at the basolateral membrane of hCMEC/d3 cells. The yellow square highlights a region of interest for a potential exocytic event. Graph (B) to the left shows the changes in the mean fluorescence of an ROI (yellow circle) as a vesicles arrives (ii) is fused to the membrane (iii) and is released (iv) and the fluorescence returns to background (i). The panel of images show the 17x17px area containing the ROI and illustrate vesicle arrival (C) and vesicle release events (D).

4.3.1 Transferrin TIRF Results

Initial analysis of TIRF microscopy on transferrin at the basolateral membrane of hCMEC/d3 cells was performed manually. This found several events that demonstrated a fluorescence profile that would be expected from a potential exocytic event, as demonstrated in Figure 4.5. Events arrived rapidly into the evanescence zone, in an "empty" region of the cell. The event is present in the evanescence zone for a prolonged time, and in a confined location for the entire time, it is present. Loss of fluorescence from the event occurs rapidly and returns to the background fluorescence level, following release. The second peak that was seen in Figure 4.5.B, is from a secondary event that originated outside the ROI boundaries but was partially trafficked into the ROI over the course of the capture.

Having identified characteristics indicative of potential exocytic events the process of identification was automated through criteria setting and the gating of events in the image analysis software. This process is in line with previous work on TIRF microscopy in cells. Looking at the following variable: time in evanescence field, net displacement from the arrival point, finally to ensure events of interest are arriving from within the cell, the events present in the first 100 frames were excluded from the analysis. The last characteristic was added as part of this analysis, to enhance the likelihood that the arrival event has come from within the cell, potentially by the process of transcytosis. In work by the Sally-Ward group, more complex TIRF microscopy techniques have allowed for the visualisation of cellular events approaching the membrane from further within the cell (Ober *et al.* 2004). While work with more fluorescently stable, fluorescent proteins have been able to demonstrate a spreading effect observable as vesicles reach the basolateral membrane (Schmoranzer *et al.* 2000). However, no work has been done using TIRF microscopy to observe the trafficking of fluorescently labelled targeting ligands. And

while the Alexa-dyes have a generally high photostability. The very high laser powers, decaying away from the coverslip does cause rapid photobleaching of individual fluorophores at the cell membrane. This effect is less observable in larger vesicles, containing more molecules of ligand. Any work on ligands has looked at naturally expressed proteins, labelled fluorescently to examine their release from the cells. Several studies have shown that vesicles that are undergoing directional trafficking within cells, along microtubules can have a velocity of 0.5 μm/s, and in some neuronal cells, up to 3 μm/s (Kreft et al. 2004, Grafstein and Forman 1980; Goldstein and Yang 2000).

Events following directional patterns were observed in transferrin AlexaFluor 647 capture videos. However, they appeared infrequently and were difficult to analyse using the ROI methodology described in Figure 4.5. If there were fewer events present in the evanescence field, then detection and tracking of these events would be more robust. As this was not the case an example has not been included in this chapter.

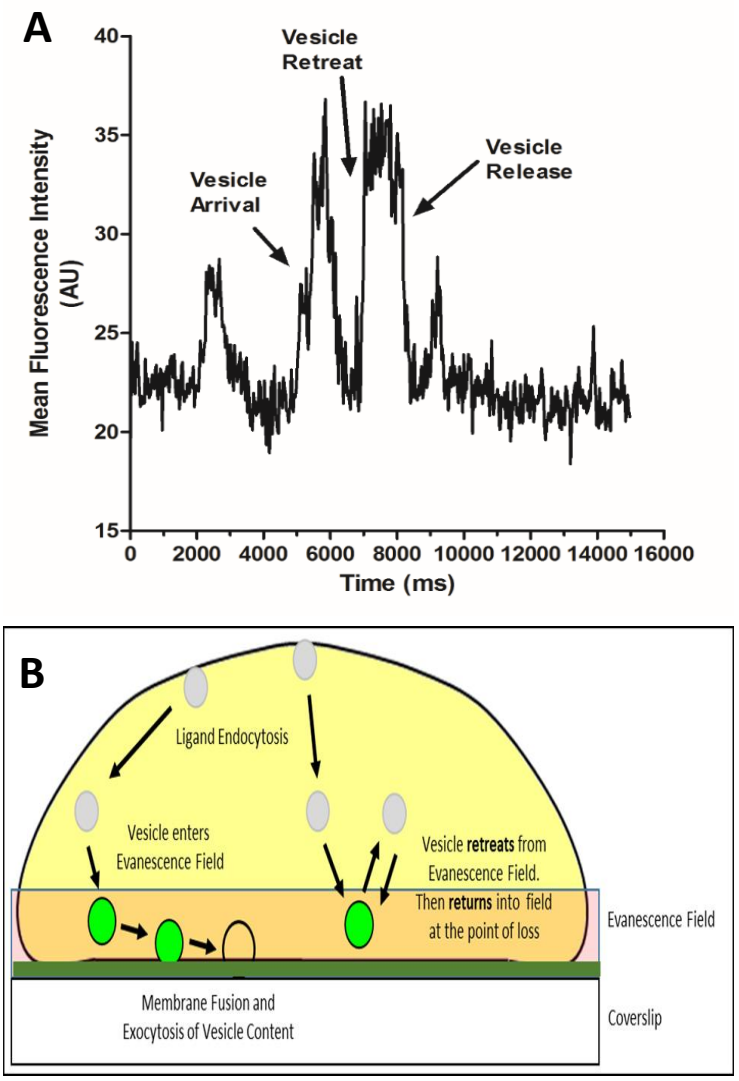

Figure 4.6: Vesicle Retreat and Return into the Evanescence Field
In some cases the vesicle can be seen to arrive into the evanescence field, retreat out of the field and then return in the exact same location within a short time frame (<1 second). Graph A shows an example of the fluorescence profile of events like this. The schematic in B shows the difference between a fusion event that stays in the same location throughout release, and the retreat and return vesicles that move in and out of the excitation field.

Other events observed in the cells mimic the kiss-and-run profiles described in previous work (Roman-Vendrell *et al.* 2014; Jaiswal *et al.* 2009). Here events appeared into the evanescence zone then retreated and returned to the same location in the field of view (Figure 4.6). With both the retreat and return characterised by rapid changes in fluorescence intensity at the location of the spot. In the event shown here the same spot appears and retreats from the same location (6 x 6-pixel area) four times within the course

of the 16-second video. Each appearance was sustained over several frames and immediately followed by a return to the background fluorescence level for that region. The potential trafficking routes of a vesicle that has arrived and departed the evanescence field were summarized in Figure 4.6 below. Events such as these may be caused by vesicles which are in fact not docking with the basolateral membrane. Instead, they are transiently entering and retreating the field of view without docking. In the example, in Figure 4.6 this may be the case, as there is no loss of fluorescence intensity between the major peaks in the graph. If full or partial docking and exocytosis had occurred before the retreat from the evanescence field. Then the second observed peak would have been at a lower intensity than the first peak. This was shown in previous work on TIRF microscopy of receptors tagged with a fluorescent protein. Here partial exocytosis was observed as a decrease in localised fluorescence, but not a complete loss from the localised region (Roman-Vendrell *et al.* 2014). This contrasts with the observations in this study, confirming the likelihood that no exocytosis occurred in this event, but that the event observed was purely intracellular vesicular movement.

To develop the detection methodology further would require an automation approach to the detection of the different types of cellular trafficking events. This would go beyond the current offerings of Fiji plugins, such as TrackMate, as it would require a classification method to link tracks that reappear in the same location as previous one. To do this effectively, a data science approach may be most efficient, to analyse the large datasets generated from each video capture. This would be an area of potential development in the future.

As a short-term method to quantify the number or percentage of total events that show the desired characteristics for potential exocytic events as sequential filtering method was developed for analysis. In this method, a field of view is loaded into Fiji and any potential

spots of fluorescence intensity are identified in the TrackMate plugin. These spots were examined, and tracks are build based on a nearest-neighbour search method within TrackMate. This produces a total number of tracks for a capture video (100 %). The total population of all the tracks was then filtered by the following: duration (number of spots in track), displacement (distance travelled) and arrival time (to ensure only "new" tracks are examined). Using these it was possible to get an estimate as to the proportion of total tracks that may be undergoing exocytosis. This method is shown in Figure 4.7, and the proportion of tracks of transferrin AlexaFluor 647 that were potential exocytic was calculated as 10.1%. These filter methods are similar to ones used in other TIRF microscopy experiments (Midorikawa and Sakaba 2015). However, it should be clarified that the findings shown in Figure 4.7 are not stating 10.1% of all tracks observed were undergoing exocytosis, instead that 10.1 % of all tracks exhibit characteristics that are expected of exocytic vesicles. To confirm whether the events truly exocytic or not a secondary label would be required, to detect if ligand and receptor are present together and attempt to visualise the dissociation of ligand from receptor on completion of the exocytic process.

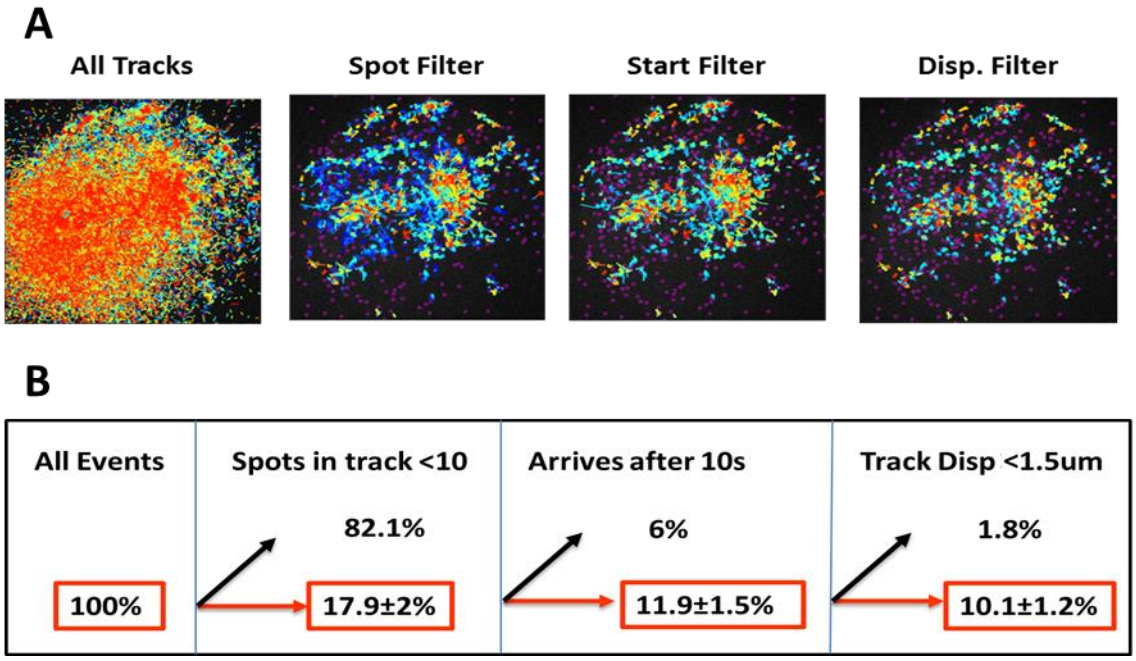

Figure 4.7 Filtering of transferrin trafficking events in TIRF microscopy
The above figure shows an example of the filtering of all detected track events in a capture video of transferrin AlexaFluro 647 (100 pM) in hCEMC/D3 cells when viewed by TIRF microscopy. The tracks shown in the images (A) are colour coded based on their start time. Any purple dots that become visible as filters are applied represent spots that were detected in that frame of capture but are no longer included in a track after filtering. The effect of the sequential filtering method on the proportion of the total number of spots is quantified in B, with the percentage of spots remaining after each filter highlighted in red and given as mean ± std (n = 10 capture videos).

4.3.2 Photoswitching

4.3.2.1 Confocal Microscopy Results

Initial tests with the PSmOrange-TfR construct in hCMEC/d3 cells confirmed the expression of the plasmid. The imaging of cells in the orange- and far-red channels before exposure to the switching wavelength confirmed that the far-red fluorescence is negligible prior to photoswitching. Cells that express the PSmOrange-TfR plasmid show strong, stable fluorescence signal in the orange channel. Exposure of PSmOrange-TfR positive cells to 543nm light allowed the calculation of the photobleaching half-life for the PSmOrange protein. The was calculated to be 316.8 seconds and a rate constant of $2.19 \times 10^{-3}\ s^{-1}$ when exposing the PSmOrange-TfR positive cells to the 543nm laser at 0.09 mW power (Figure 4.8). The rate of photobleaching is related to the exposure power

of the laser. However, for the photoswitching studies the power of the 543nm laser was kept constant at this power.

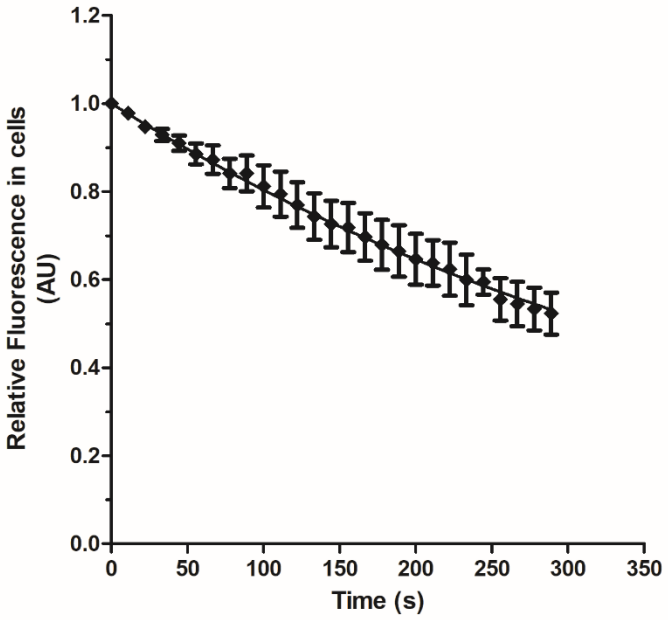

Figure 4.8: Photobleaching of the orange form of PSmOrange
The graph shows how exposure of the native state PSmOrange to only "orange" excitation light bleaches the fluorophore. The half-life of photobleaching, at a laser power of 0.09mW was calculated as 316.8 seconds. N = 3 in triplicate, mean ± std

Initial studies, exposing PSmOrange positive cells, to the switching wavelength (488nm) triggers a rapid shift from the orange to far-red fluorescence states, Figure 4.9 below. The rate of switching was calculated by the "arrival" of far-red fluorescence into the field of view and was confirmed by comparing it to the loss of orange-fluorescence from the image. With imaging in this manner, we see the far-red fluorescence increase rapidly in the early frames, but as the amount of protein to be switched decreases the far-red fluorescence begins to plateau and even decreased in later frames. This decrease was likely due to the bleaching of the far-red form and movement of the PSmOrange-TfR from the plane of view.

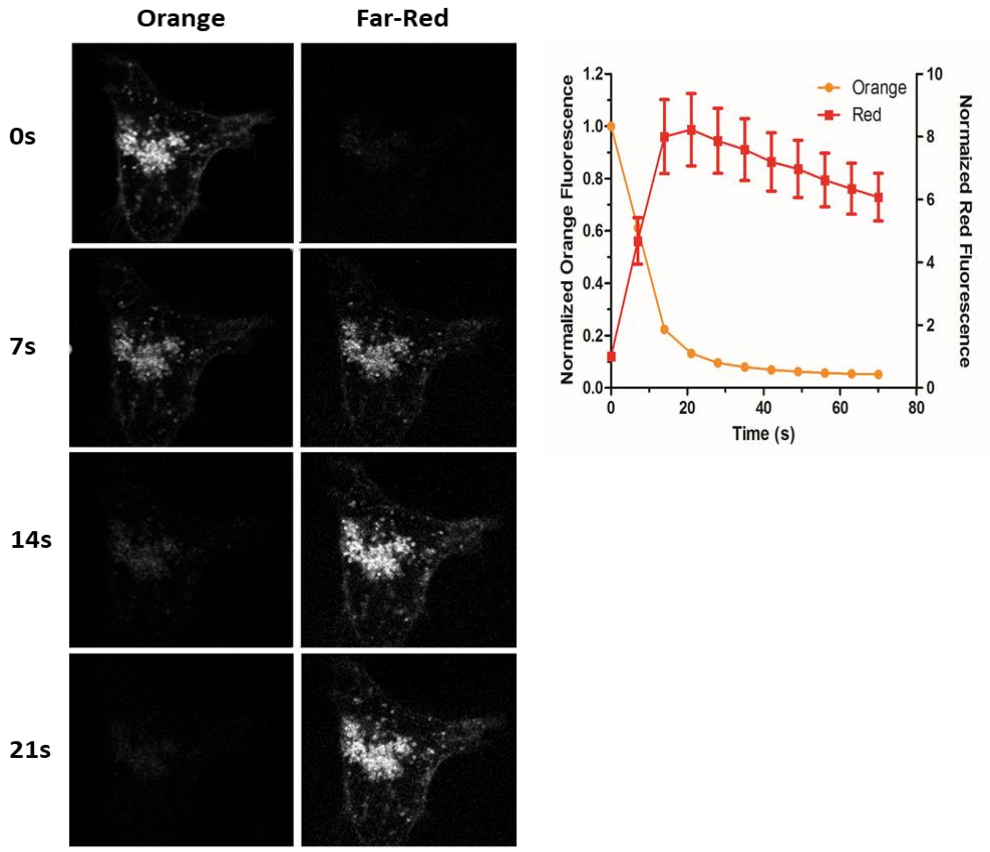

Figure 4.9: TfR-PSmOrange switching by confocal microscopy
The above images in A show the effect of exposing the PSmOrange fluorophore to 488nm switching light. The decrease in signal in the orange channel (left) is accompanied by the rapid rise in signal in the far-red channel (right). The quantification of the fluorescence in orange and far-red channels is shown in B, with all values expressed relative to the fluorescence in first frame of switch exposure. n = 3 in triplicate, mean ± std.

Having confirmed that the PSmOrange-TfR construct can undergo photoswitching when exposed to high laser powers, the next stage was to explore the dynamics of the photoswitching with varied 488nm laser power. Throughout these studies, the power of the 543 nm and 633 nm laser power was kept constant. In this way, the rate of photoswitching was shown to be modulated by the power of the 488nm laser. As the 488nm laser power was increased the photoconversion rate also increased. To calculate the rate of photoswitching from the loss of orange fluorescence the following equations were applied.

Equation 4.5

$$\boldsymbol{Orange(t)} = e^{-(K_{total})t}$$

In Eqn 1., the combined rate of loss of orange fluorescence, from both photobleaching and photoswitching is represented by K_{total}. The K_{total} value will be equal to the sum of the photoswitching rate (K_{switch}) and photobleaching rate (K_{off1}), as shown in Equation 4.6

Equation 4.6

$$\boldsymbol{K_{total} = K_{switch} + K_{off1}}$$

From this analysis, it was possible to observe the relationship between the laser power and the photoswitching rate. With a linear relationship between the $\log_{10}$(Laser Power) and $\log_{10}(K_{switch})$. This is shown in the graph below (Figure 4.10) and relationship was shown mathematically as seen in Equation 4.7.

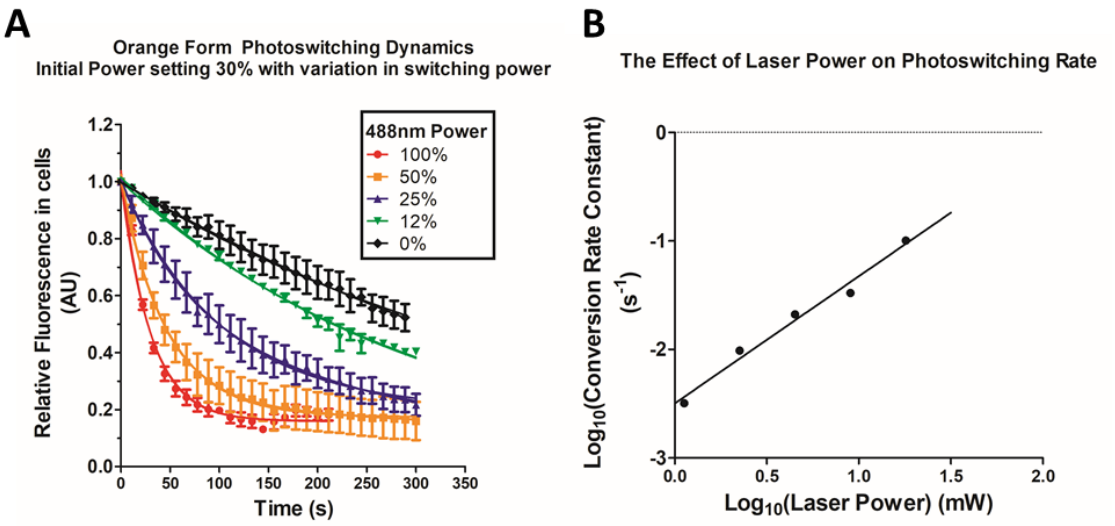

Figure 4.10: The effect of changing photoswitching power on PSmOrnage-TfR.
The graphs show the effect that switching power has on the orange form of PSmOrange. As the power of 488nm is increased to maximum power, the rate of switching (K_{switch}) increases. Graph A shows the quantification of the orange fluorescence during the switch exposure. While graph B plots the estimates K_{switch} values against the laser power. Figure A has n = 3 in triplicate, mean ± std, Figure B uses the calculated K_{switch} from the replicates in Figure A as the data points.

Equation 4.7

$$K_{switch} = 10^{(1.524 \times \log_{10}(Laser\ Power) - 2.069)}$$

Quantification of the fluorescence within the far-red channel while exposing the PSmOrange-TfR cells to the switching laser, confirms the more rapid loss of fluorescence in the orange channel is matched by an increase in the fluorescence in the far-red channel.

4.3.2.2 Modelling the Fluorophore State Transitions

Understanding the behaviour of the fluorophore and its distribution between the fluorescence states is key for predicting and defining the optimal switching conditions. In the following section, we will derive the equations to summarise the distribution of fluorescence between the orange, far red and bleached states. The relationships between the fluorescence states of PSmOrange is summarised below, the model assumes a closed system, with all fluorescence existing in the orange state (X_1). Fluorescence can be lost from the orange state by either photobleaching (exposure to 543nm laser) or photoswitched (exposure to 488nm laser). The far-red state (X_2) will accumulate fluorescence from the orange state with the rate of K_{switch}; this rate could be controlled by the power of the 488nm laser. Further, the far-red state will lose fluorescence by photobleaching (exposure to 633nm laser). The bleached state (X_3) will be an accumulating compartment, receiving fluorophores from both the orange state (rate = K_{off1}) and the far-red state (rate = K_{off2}). A diagrammatic representation of the fluorescent states of PSmOrange is shown below in Figure 4.11.

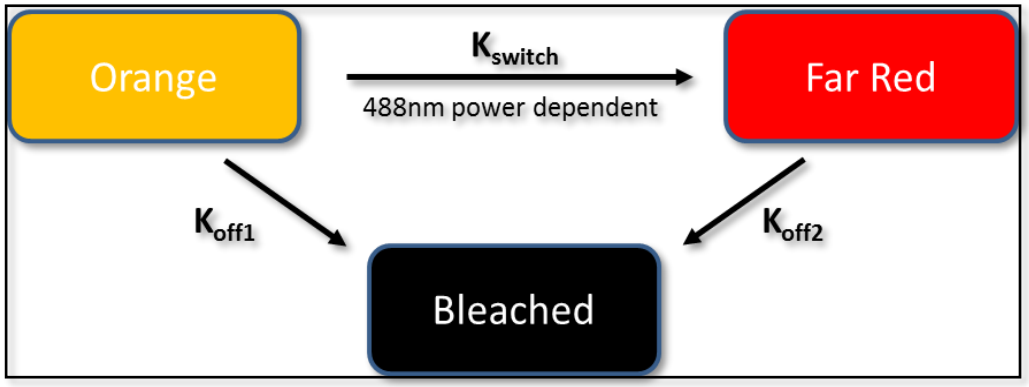

Figure 4.11: States of PSmOrange for mathematical modelling of conversion rates

Using the rate constants described above it is possible to form the following three differential equations (Equations 4.7-4.9), describing the change within each compartment.

Equation 4.7:

$$\frac{dX_1}{dt} = -K_{switch}X_1 - K_{off1}X_1$$

Equation 4.8:

$$\frac{dX_2}{dt} = K_{switch}X_1 - K_{off2}X_2$$

Equation 4.9:

$$\frac{dX_3}{dt} = K_{off1}X_1 + K_{off2}X_2$$

Integrations of Equations 4.7-4.9 and the use of Laplace transformations will allow for the derivation of formulae for the proportion of fluorophores within a given state at any given time. The assumed starting for the compartments at time zero are as follows: $X_1^0 = 1$, $X_2^0 = 0$ and $X_3^0 = 0$, these values will be substituted into the proof at the required stages.

Equation 4.10:

$$s\bar{X}_1 - X_1^0 = -K_{switch}\bar{X}_1 - K_{off1}\bar{X}_1$$

Equation 4.11:

$$s\bar{X}_2 - X_2^0 = K_{switch}\bar{X}_1 - K_{off2}\bar{X}_2$$

Equation 4.12:

$$s\bar{X}_3 - X_3^0 = -K_{off1}\bar{X}_1 - K_{off2}\bar{X}_2$$

Substitution of $X_1^0 = 1$ into Equation 4.10 and rearrangement to make X_1 the subject of the equation results in the following (Equation 4.13).

Equation 4.13:

$$X_1 = \frac{1}{s + K_{switch} + K_{off1}}$$

As $K_{switch} + K_{off1}$ are both constants, the sum of K_{switch} and K_{off1} will therefore also be a constant, termed 'a'. The formula is suitable to be used with the Laplace transformation (Equation 4.14) to produce the equation to solve for X_1 with respect to time (Equation 4.15).

Equation 4.14:

$$\frac{1}{(s+a)} = e^{-at}$$

Equation 4.15:

$$Orange(t) = e^{-(K_{switch} + K_{off1})t}$$

Having found the equation to calculate the fraction of fluorophores within the orange state at any given time, it is possible to substitute the equation for X_1 (Equation 4.13) into the integration for the far-red compartment (Equation 4.11). Further, as X_2^0 will be equal to zero, this component is removed from the equation.

Equation 4.16:

$$s\bar{X}_2 = \frac{K_{switch}}{\left(s + K_{switch} + K_{off1}\right)} - K_{off2}\bar{X}_2$$

The equation is then rearranged to solve for X_2.

Equation 4.17:

$$\bar{X}_2(s + K_{off2}) = \frac{K_{switch}}{\left(s + K_{switch} + K_{off1}\right)}$$

Equation 4.18:

$$\bar{X}_2 = \frac{K_{switch}}{(s + K_{switch} + K_{off1})(s + K_{off2})}$$

Equation 4.18 is now in the correct format to undergo the Laplace transformation (Equation 4.19 and give the equation for the far-red component at any given time.

Equation 4.19:

$$\frac{1}{(s + a)(s + b)} = \frac{1}{(b - a)}(e^{-at} - e^{-bt})$$

Equation 4.20:

$$Far\ Red(t) = \frac{K_{switch}}{K_{off2} - \left(K_{switch} + K_{off1}\right)}(e^{-(K_{switch}+K_{off1})t} - e^{-K_{off2}t})$$

Now having rearranged the integration formulae for X_1 (Equation 4.13) and X_2 (Equation 4.18) it is possible to substitute these into Equation 4.12. The equation can then be rearranged to make X_3 the subject of the formula.

Equation 4.21:

$$\bar{X}_3 = \frac{K_{off1}}{s\left(s + K_{switch} + K_{off1}\right)} + \frac{K_{off2}K_{switch}}{s(s + K_{switch} + K_{off1})(s + K_{off2})}$$

Both sections of Equation 4.21 are Laplace transforms and represent the bleached components coming from the orange and far-red forms of PSmOrange respectively.

Equation 4.22:

$$\frac{1}{s(s+a)} = \frac{1}{a}(1 - e^{-at})$$

Equation 4.23:

$$\frac{1}{s(s+a)(s+b)} = \frac{1}{ab}\left[1 + \frac{1}{(a-b)}(be^{-at} - ae^{-bt})\right]$$

Equation 4.24:

$$Bleached(t) = \frac{K_{off1}}{\left(K_{switch} + K_{off1}\right)}\left(1 - e^{-\left(K_{switch}+K_{off1}\right)t}\right) + \left\{\frac{K_{switch}K_{off2}}{K_{off2}\left(K_{switch} + K_{off1}\right)}\left[1 + \frac{1}{\left(\left(K_{switch} + K_{off1}\right) - K_{off2}\right)}\left(K_{off2}e^{-\left(K_{switch}+K_{off1}\right)t} - \left(K_{switch} + K_{off1}\right)e^{-K_{off2}t}\right)\right]\right\}$$

For the three equations (Equation 4.15, 4.20 and 4.24) to be valid, at any given time point the sum of the orange, far-red and bleached states must equal one. This is due to the closed nature of the system.

Having established the equations for the distribution of fluorophores between states, these were tested using values for K_{switch}, K_{off1} and K_{off2} that had been measured in preliminary microscopy experiments. For these studies, the power of the 543nm and 633nm lasers were kept constant, while the power of the switching laser was varied between 0-60% of maximum power. Values for K_{off1} and K_{off2} were calculated by exposure of the PSmOrange-TfR expressing cells to just the bleaching wavelengths, 543nm and 633nm respectively. From these graphs rates of photobleaching can be found. As the 543nm and 633nm laser powers are not altered throughout the experiment, these values were viewed as constant.

By knowing the values of K_{off1} and K_{off2} in standard, non-converting conditions, it is possible to simulate a range of K_{switch} values to assess the minimal requirements for

efficient photoswitching. This is shown in Figure 4.12, where the maximal values for Far-Red state are plotted vs. K_{switch}.

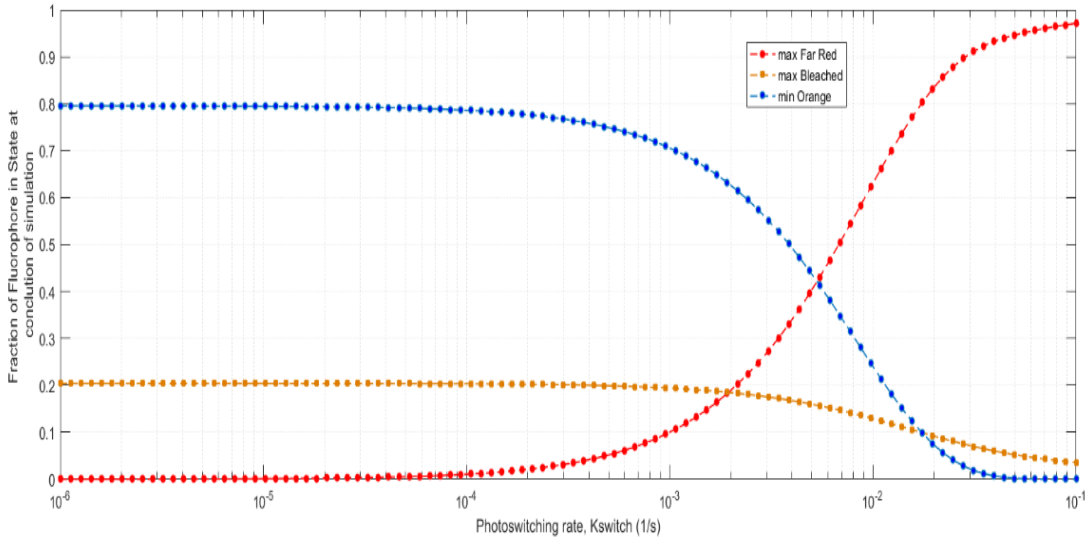

Figure 4.12: The effect of varying the K_{switch} on the distribution of PSmOrange's fluorescence states after 100 second switch exposure
The above shows the simulated model of PSmOrange states based on the equations derived previously. The simulation was done with constant K_{off1} and K_{off2} rates with only K_{switch} values between 10^{-6} and 10^{-1} s^{-1}. Blue = orange fluorescence, Red = far-red fluorescence, orange = bleached chromophore.

4.3.2.3 Photoswitching with TIRF microscopy

With TIRF microscopy, only a limited region of the sample, in close proximity to the coverslip, is excited at any given time. As such the signal to noise ratio in this technique is greater than that of confocal microscopy. However, the excitation field in TIRF decays exponentially with distance from the coverslip surface. This means that the switching power will decrease as the distance from the coverslip increases, causing the overall switching time to increase. To demonstrate this, hCMEC/d3 cells transfected with the PSmOrange-TfR plasmid were imaged by TIRF microscopy to establish the rate of photo-conversion at the basolateral membrane. In contrast to photoswitching by confocal microscopy, where the conversion half-life was in the seconds range. TIRF microscopy

photoswitching appears to take several minutes for an effective switch to occur, as shown in the Figure 4.13 below.

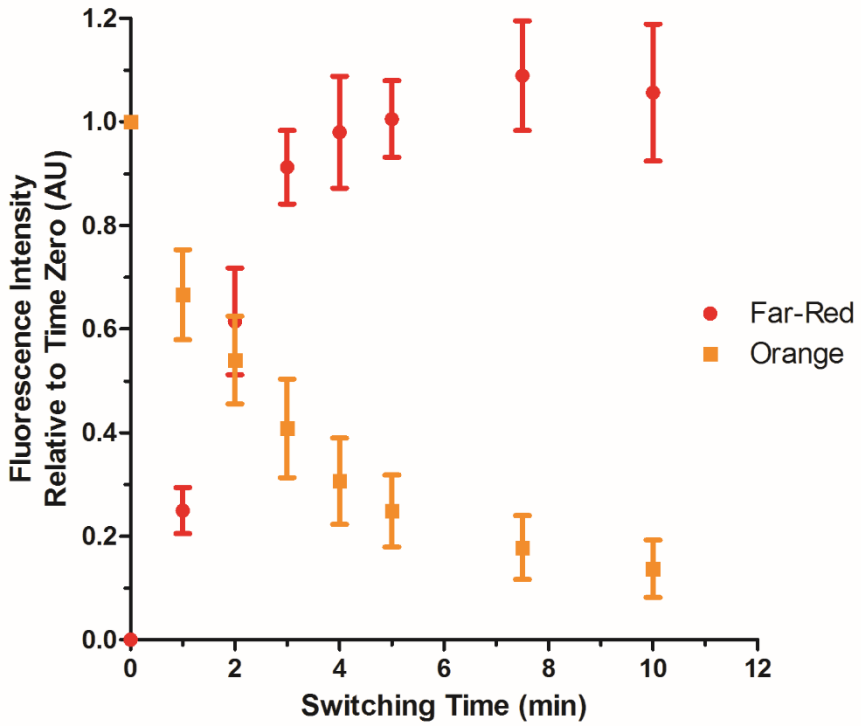

Figure 4.13: PSmOrange-TfR photoswitching by TIRF microscopy
This graph shows the quantification of both the orange and far-red fluorescence states of PSmOrange, while exposed to the switching laser in TIRF illumination. N = 3 in triplicate, mean ± std.

To explain this "slow" switching fully, the decay of excitation power across the evanescence field must be studied (Figure 4.13). Using the standard TIRF equations listed earlier in the chapter, more specifically Equation 4.2. This allows a graphical visualization of the field decay when modelled with a defined power, in this example 25mW of the blue laser at the microscope stage (Figure 4.14). By using the switching data from the confocal microscopy, the photo-conversion rate at a given power could be modelled. Now, knowing the decay of the laser power and relationship between photo-conversion and laser power the change in switching rate across the evanescence can be estimated. This modelling shows that although the photoswitching rate is greatest at the coverslip surface, 50 nm into the sample the photoswitching rate has decreased by 10-fold. By

looking at electron micrographs of BMECs grown on a collagen matrix it was estimated that the depth of collagen, between the coverslip and the cell basolateral membrane, is ~40nm. The phospholipid bilayer depth must also be accounted for (~10nm). Therefore, there is approximately 60 nm between the coverslip and the PSmOrange fluorophore fused to the TfR. This will decrease the laser power by over 80 % and so greatly reduce the photoswitching rate.

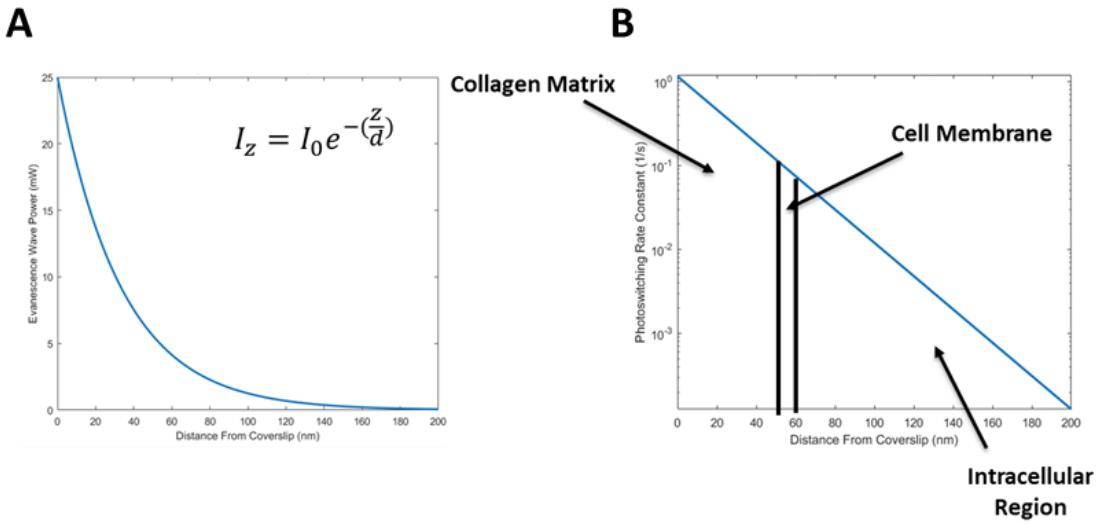

Figure 4.14: Change of the photoswitching rate at different depths in the evanescence field
Graph A shows how the laser power decays as the depth from the coverslip increases, based on a laser power out of the microscope of 25 mW. Graph B converts the laser powers in graph A to an estimate of K_{switch} using Equation 4.7. This is then plotted against depth from coverslip surface. Marked onto this graph is the depth of collagen and cell membrane to show the power of the that is reaching the intracellular compartment and the fluorophore.

This depth, before the fluorophore can be excited, is likely to be the main reason why photoswitching of PSmOrange-TfR is lower using TIRF microscopy compared to confocal microscopy.

4.3.2.4 Imaging Optimization – Channel Cross-Talk

As was predicted, the highest signal to noise was observed in the images where only a single excitation laser was used. This was true both pre- and post-photoswitching with

the red and the green lasers. When imaging, if a second excitation laser was added, mid video, there was seen to be a “jump” in the average fluorescence intensity in both the green and red channels. This “jump” in fluorescence intensity was seen again when a third laser was added to the imaging, mid-capture.

These changes in fluorescence are likely due to inefficiencies in the emission filter sets used. As all emission filters are not perfect restrictors of fluorescence transmission and have oscillating profiles at the maximum (99.8-100%) and minimum (0-0.2%) transmission points. With the high laser powers used in these studies, even small inefficiencies, such as these, are likely to allow enough of the lasers’ back-reflection through to cause the number of photons at the detector to increase. This appears as an increase in the fluorescence signal in the imaging channel.

Due to this increase in signal, with the addition of more excitation lasers, it was decided that for photoswitching studies, a maximum of two lasers should be used at any given stage of the capture. To maximise the fluorophores able to undergo photoconversion that the exposure to the green laser should be minimal (at the start and conclusion of capture), while the exposure to the red laser should be in parallel to blue laser exposure. Thus, ensuring that any converted state, far-red fluorescence is recorded in the conversion time.

4.3.2.5 Photoswitching Procedure Optimization

Having established the optimal laser setup for the photoconversion studies the next stage was for the live capture of the switching and validation that the far-red fluorescence generated by the switch has come from the orange form of the protein. The macro used for analysis allows for the change in fluorescence in the green (orange) channel to be visualised and compared to all red (far-red) events for co-localization analysis.

In this way, it was observed that ~5% of "new" red spots, appearing over the course of the photoswitching time, colocalised with green spots that were no longer present at the conclusion of the switch. This low colocalization value following the switch may result from several factors. Firstly, the green capture at the start of the video does not account for the arrival of any new green events that may occur during the switch. These new events, if converted to the far-red form would not appear in the green-channel despite being present in the red maximum projection for the time course. The laser power from the blue laser (488 nm) was sub-optimal for photoswitching, with an output from the fibre launch of 3-4 mW. This is compared to green and red laser powers both more than 20 mW. As modelled earlier in the chapter, the photoswitching efficiency is related to the laser power output reaching the sample and the depth above the coverslip of the fluorophore. If the laser power is less than a fifth of the anticipated laser power, then the photoswitching efficiency will be reduced. For the use of PSmOrange to measure exocytosis this means that the fluorophore takes longer to switch between states than initially predicted. Therefore, if measuring the turnover of receptors at the basolateral membrane, based on the proportion of unswitched (newly arrived) to switched (already present) receptors will be difficult as complete conversion of receptors is less likely to have taken place if the conversion time is longer. Meaning the ability to accurately measure the arrival of receptors from the apical membrane is not possible. To overcome this, an alternative photoswitchable protein may be used, such as Dendra2 or dEOS, as these have a higher rate of photoconversion than PSmOrange. And so, despite lower laser powers at the cell membrane, would be able to undergo a more efficient switch that PSmOrange. However the conversion wavelengths for Dendra2 and dEOS (405nm) are not currently supported by the TIRF setup, and so were not selected as fluorophores for these studies (Chudakov *et al.* 2007).

4.4 Conclusions and Future Developments

While, using TIRF it was possible to visualise, transferrin molecules at the basolateral membrane of hCMEC/d3 cells and to identify potential events of interest. It was not possible to distinguish between an endocytic or exocytic event at the basolateral membrane. However, this was to be expected, as the majority of studies with TIRF have so far been concerned with the trafficking of fluorescently labelled receptors, or calcium signalling events associated to release and not targeting ligands (Mattheyses *et al.* 2010; Roman-Vendrell *et al.* 2014; Walker *et al.* 2008). The photostability of the AlexaFluor® 647 fluorophore, relative to fluorescent proteins, means that long capture videos lead to photobleaching of most fluorophores within the excitation field, making tracking over time periods greater than 10s challenging. As well as obscuring, potentially exocytic events with bleaching of the fluorophore rather than the release of a vesicle. To overcome this the use of alternatively labelled ligands, with quantum dots, resistant to photobleaching could be used, as done by Roche in their work with TfR antibodies (Niewoehner *et al.* 2014).

To optimise the photoswitching protocol with PSmOrange, the selection of a more rapidly converted photoswitchable protein would ideally lead to an improved sensitivity of the assay and a reduction in the time required to expose cells to switching laser. This would allow for more sensitive measures of the dynamics of receptor trafficking at the basolateral membrane of cells. However, was not attempted initially due to machine setup constraints and laser configurations.

The end goal would be to photoconvert the fluorophore at the basolateral cell membrane and examine the replenishment with native state fluorophores. If this replenishment was not present, then it could be inferred that within the switch all receptors at the basolateral

cell membrane are trafficked in an independent pathway to the apical transferrin receptors. A ligand undergoing transcytosis must release the receptor within the endosomal compartment and find an alternate route to the basolateral membrane. If, however, the native fluorescence is replenished within the basolateral evanescence zone, the receptors from apical compartments are likely to be able to be trafficked to the basolateral compartment. Giving them the potential to undergo transcytosis across the cell.

To further confirm that a receptor from the apical membrane was capable of trafficking a ligand to the basolateral membrane, combining the photoswitching assay (described in Figure 4.15) with a fluorescent ligand would be required. If a receptor arrived in the basolateral region in the native state (following the switch), with a ligand colocalised to it. Then it could be inferred that both the receptor and ligand had come from the apical region of the cell and been trafficked together across the cell. However, without these feasibility studies, then it is unclear if this technique could be used to characterise receptor and ligand transcytosis.

Limitations of the microscope setups meant the fastest photoconverting fluorophores could not be used. To improve the sensitivity and feasibility of the assay further, a more fluorophore that undergoes more rapid photoswitching would be more suitable.

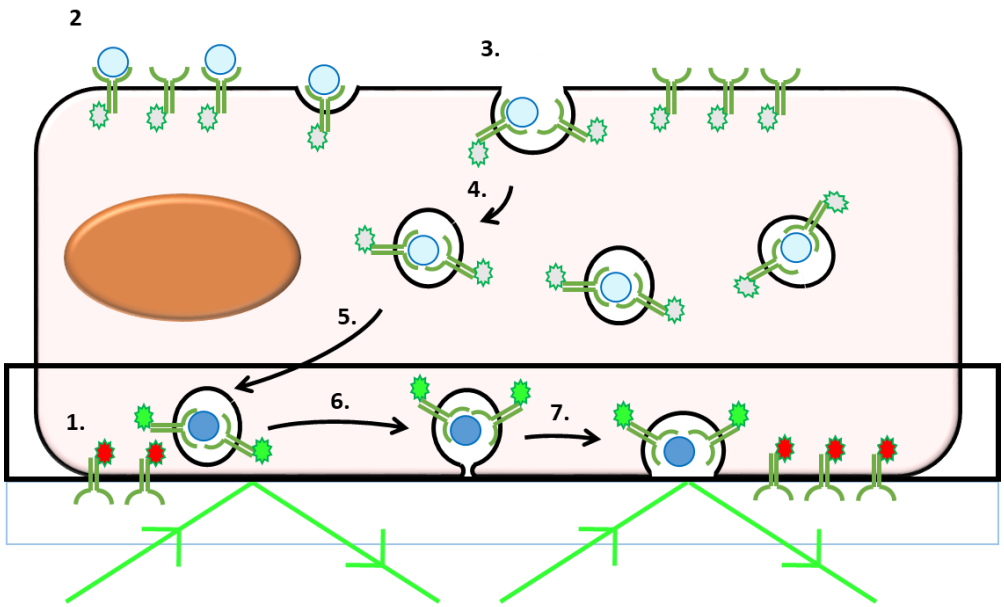

Figure 4.15: Future Development of the Photoswitching TIRF assay

1. **Photoswitching of receptors in the basolateral field –** Done by exposing the fluorescent protein to the switching wavelength of light for an extended duration to ensure maximal photoconversion, prior to the start of the assay. And providing a differentiator to determine if a ligand is bound to an apical TfR that has arrived in the Evanescence field or been internalized by a basolateral receptor.
2. **Ligand Binding** – The transferrin (blue circle) binds to TfR at the apical membrane. There is no fluorescence signal here from either the transferrin or the receptor as they are outside the evanescence field (black rectangle)
3. **Receptor-Ligand endocytosis** – This will occur constitutively with the transferrin receptor, without the presence of a ligand. The clathrin scaffold and associated proteins, will form around the pit to facilitate the internalisation
4. **Association to the Early Endosome** – once the vesicle is cleaved away from the plasma membrane it will be trafficked to the early endosome for initial sorting. From here it is possible for the receptor to undergo recycling back to the apical membrane of the cells.
5. **Trafficking of vesicle into Evanescence field** – Now, if the receptor and the ligand, internalized at the apical membrane are trafficked into the evanescence field together. New, native state, photoswitchable protein will be present at the membrane. The pre-switching at the basolateral membrane allowing the differentiation of the two states. The ligand would then appear co-localized with the receptor.
6. **Docking of vesicle to basolateral membrane** – The vesicle is now bound to the basolateral membrane and begins to "open" out to the extracellular microenvironment.
7. **Complete vesicle fusion and opening** – The vesicle is now completely integrated into the basolateral membrane and the ligand can be released from the cell. Due to the proximity of the cell membrane to the coverslip this may not be seen as a loss of ligand fluorescence, but the remaining signal from the apical (green fluorescence state) will remain in this location. Confirming that the ligand must have come from a more apical compartment of the cell to be released at the basolateral membrane and potentially having undergone transcytosis.

Chapter 5: General Conclusion and Future Work

Due to complexity, restrictive nature and extensiveness of the BBB *in vivo* will remain the main bottle-neck for the delivery of therapeutics to the CNS for the treatment of neurological pathologies. Methods that can overcome the BBB and improve delivery standards will remain a research goal, with the identification of novel, efficient targeting ligands being essential. The methods used *in vitro* must go beyond "simple" permeability assays across BMEC monolayers and look at the intracellular trafficking of targeting ligands and DDSs within endothelial cells. Full characterisation of targeting ligands and DDSs *in vitro* before *in vivo* testing will improve pre-clinical and clinical outcomes. The studies in this thesis aimed to bring forward this, through the pulse-chase assay and combination with subcellular microscopy imaging techniques.

The use of immortalised cell lines to test BBB ligands is limited, by the loss of the restrictive phenotype as cells are cultured. However, immortalised cell lines have the benefit of overcoming the inconsistencies between isolations, which is associated with primary BMEC cells. Chapter 2 highlighted the limitations of using permeability assays with immortalised cell lines, demonstrating the benefits of the pulse-chase assay. Pulse-chase methodologies allowed for confirmation, in static conditions, that a targeting ligand or DDS could be internalised by the BMECs. It was shown to be able to differentiate between probes with receptor-driven, cellular trafficking pathways (transferrin, 8D3) and those without (dextran). Further, the pulse-chase methodology could distinguish between the saturated and unsaturated ligand uptake and trafficking. In the case of saturation of the receptor-mediated uptake mechanism, excess ligand, at the cell surface was seen to be trapped within the cells throughout the chase phase. This was observed with all targeted probes used within the assay (transferrin, 8D3, 8D3-4). Coupling of the pulse-chase assay with microscopy techniques to examine the subcellular distribution of remain

ligand allows a further layer of detail to the assay. Allowing for the visualisation of "trapped" excess ligand within lysosomal compartments, and unable to undergo further cellular trafficking. The impact of the receptor saturation was seen when using the assay to characterise the 8D3 antibody variants. With the low-affinity, 8D3-4 showed a greater ability to be effluxed by cells at high concentrations, compared to the native 8D3 antibody (high affinity). The main conclusion of this chapter was the benefits of using multiple techniques when attempting to characterise BMEC targeting strategies.

In Chapter 3 the focus was the characterisation of the uptake of the RVG peptide into BMECs and the confirmation of the target receptor for the peptide. The uptake of the RVG peptide was compared to a scrambled sequence peptide and a peptide with the internal cysteine mutated for an alanine. These uptake studies confirmed the sequence of the RVG peptide and the internal cysteine of the RVG peptide were required for cellular uptake of the peptide. The uptake of the RVG peptide was shown to be self-competitive, and the pulse-chase profile of this targeting ligand suggested a defined trafficking pathway within BMECs. Finally, in this chapter, studies to confirm the target receptor of the RVG peptide demonstrated the role of α7nAchR as a receptor for uptake of RVG into BMECs. Competition with α-bungarotoxin, siRNA knockdown of the receptor decreasing the uptake of RVG into cells. PCR tests for α7nAchR confirmed the receptor was expressed in b.End3 and hCMEC/d3 cell-lines, making this a viable target for the ligand in BMECs. Through the use of pulse-chase assays, as described in Chapter 2, the internalisation and efflux of RVG was characterised. This showed that RVG can undergo active efflux from BMECs, confirming its suitability as a targeting strategy for CNS delivery.

To expand on the assays described previously and enhance the understanding of cellular trafficking at the basolateral membrane of cells, TIRF microscopy was used to look at

ligand localisation to the basolateral compartment of BMECs (Chapter 4). The technique confirmed that the transferrin ligand, if applied to the apical surface of cells, can be visualised at the basolateral membrane. However, due to the inherent "leakiness" of immortalised BMEC cell-lines, this may be due to ligand passing between cells and entering the cell from the basolateral membrane. An inability to identify if the events visualised were exocytic or endocytic, with single colour imaging, was a key issue with this technique. But, it was possible to identify individual events within the capture videos that may be of interest. To improve the assay and add to the potential for exocytic readouts, the use of photoswitchable proteins expressed with a receptor of interest was suggested, and PSmOrange selected for use in the studies. The distribution of the fluorescent states of PSmOrange was modelled mathematically, to demonstrate the effect of varying the switching rate on the distribution of the chromophore states. The PSmOrange-TfR plasmid was synthesised and expressed in hCMEC/d3 cells for characterisation. Confocal microscopy confirmed expression of the photoswitchable receptors and the ability to convert rapidly between the states when exposed to the switching. However, when used in TIRF microscopy studies, the decreased depth of the excitation field, coupled with its decay with distance from the coverslip surface meant that the switching powers the sample was exposed to were far less than those used in confocal imaging. As such the rate of photoswitching using TIRF microscopy was seen to be significantly lower than confocal. And will require further development to take the assay forward and this will be covered in the future work section below.

Future Work and Development

RVG Peptide

Having characterised the RVG peptide, concerning uptake and loss and the receptor target, the next step with this would be to look at the effect of ligand valency on the ability

of the RVG peptide to deliver a sample cargo in BMECs. This could be done using dendrimer, with a fluorescent cargo, to allow for the assessment of cellular localisation of the constructs. In this way, the valency of the constructs could be altered, and the sub-cellular distribution assess. Through the pulse-chase assay developed here, it would be possible to assess the impact of ligand density on the potential to be taken up by BMECs and the ability of internalised constructs to undergo further trafficking within the endothelial cells. Optimization of ligand density *in vitro* would then allow for favourable constructs to be taken forward for use *in vivo*, to test the capability of them reaching the brain parenchyma.

TIRF microscopy

The work with TIRF microscopy, to develop an exocytosis assay for delivery of cargo across the cell requires several studies to progress it further. The critical step will be the combination of the photoswitchable receptor with a fluorescently labelled targeting ligand. Imaging in this manner will allow for the visualisation of the receptor and ligand co-localized together at the basolateral membrane, in the first instance. Moving this further, by then periodically switching the switchable fluorophores within the basolateral region of the cells, it would be possible to detect whether the ligand-receptor complex was residing purely in a basolateral trafficking loop. For instance, if this were the case, then you would reach a point where only the switched form of the receptor was present in the evanescence field. Due to an inability of the "new" apical receptors to enter this pathway. However, if there is not a localised trafficking pathway within the basolateral region of the cell, and receptors may come from the apical compartment. Then there would be the presence of both fluorescent states of the receptor in the field at any given time. If this occurred and a ligand was co-localized with the un-switched fluorophore that had arrived in the evanescence field, then this must have come from a more apical

receptor within the cell and potentially undergone transcytosis to reach the basolateral region of the cell. Progression of the assay to this stage, with the transferrin receptor and ligands, would be required before this could be used with other BBB targeting ligands.

Bibliography

Abbruscato, T.J., Lopez, S.P., Mark, K.S., Hawkins, B.T. and Davis, T.P. (2002). Nicotine and cotinine modulate cerebral microvascular permeability and protein expression of ZO-1 through nicotinic acetylcholine receptors expressed on brain endothelial cells. *Journal of pharmaceutical sciences* **91**:2525–38.

Akache, B., Grimm, D., Pandey, K., Yant, S.R., Xu, H. and Kay, M.A. (2006). The 37/67-kilodalton laminin receptor is a receptor for adeno-associated virus serotypes 8, 2, 3, and 9. *Journal of virology* **80**:9831–9836.

Aktaş, Y., Yemisci, M., Andrieux, K., Gürsoy, R.N., Alonso, M.J., Fernandez-Megia, E., Novoa-Carballal, R., *et al.* (2005). Development and brain delivery of chitosan-PEG nanoparticles functionalized with the monoclonal antibody OX26. *Bioconjugate Chemistry* **16**:1503–1511.

Albertini, A. a V, Baquero, E., Ferlin, A. and Gaudin, Y. (2012). Molecular and cellular aspects of rhabdovirus entry. *Viruses* **4**:117–139.

Alpuche-Aranda, C.M., Racoosin, E.L., Swanson, J.A. and Miller, S.I. (1994). Salmonella stimulate macrophage macropinocytosis and persist within spacious phagosomes. *Journal of Experimental Medicine* **179**:601.

Alvarez-Erviti, L., Seow, Y., Yin, H., Betts, C., Lakhal, S. and Wood, M.J. a (2011). Delivery of siRNA to the mouse brain by systemic injection of targeted exosomes. *Nature biotechnology* **29**:341–345.

Amerongen, H., Weltzin, R., Farnet, C., Michetti, P., Haseltine, W. and Neutra, M. (1991). Transepithelial Transport of HIV-1 by Intestinal M Cells: A Mechanism for Transmission of AIDS. *Journal of Acquired Immune Deficiency Syndromes* **4**:760–765.

Attwell, D., Buchan, A.M., Charpak, S., Lauritzen, M., Macvicar, B.A. and Newman, E.A. (2010). Glial and neuronal control of brain blood flow. *Nature* **468**:232–243.

Axelrod, D. (1981). Cell-substrate contacts illuminated by total internal reflection fluorescence. *Journal of Cell Biology* **89**:141.

Axelrod, D. (2001). Total internal reflection fluorescence microscopy in cell biology. *Traffic* **2**:764–774.

Balda, M.S., Anderson, J.M. and Matter, K. (1996). The SH3 domain of the tight junction protein ZO-1 binds to a serine protein kinase that phosphorylates a region C-terminal to this domain. *FEBS Letters* **399**:326–332.

Bauereiss, A., Welzel, O., Jung, J., Grosse-Holz, S., Lelental, N., Lewczuk, P., Wenzel, E.M., *et al.* (2015). Surface Trafficking of APP and BACE in Live Cells. *Traffic* **16**:655.

Betzig, E., Betzig, E., Patterson, G.H., Sougrat, R., Lindwasser, O.W., Olenych, S., Bonifacino, J.S., *et al.* (2013). Imaging Intracellular Fluorescent Proteins at Nanometer Resolution. *Sc* **1642**:1642–1646.

Bickel, U., Kang, Y.S., Yoshikawa, T. and Pardridge, W.M. (1994). In vivo demonstration of subcellular localization of anti-transferrin receptor monoclonal antibody-colloidal gold conjugate in brain capillary endothelium. *Journal of Histochemistry & Cytochemistry* **42**:1493–1497.

Bien-Ly, N., Yu, Y.J., Bumbaca, D., Elstrott, J., Boswell, C.A., Zhang, Y., Luk, W., *et al.* (2014). Transferrin receptor (TfR) trafficking determines brain uptake of TfR antibody affinity variants. *The Journal of experimental medicine* **211**:233–44.

Binder, D.K., Yao, X., Zador, Z., Sick, T.J. and S., V.A. (2006). Increased seizure duration and slowed potassium kinetics in mice lacking aquaporin-4 water channels. *Glia* **53**:631–636.

Van der Bliek, A., Redelmeier, T., Damke, H., Tisdale, E., Meyerowitz, E. and Schmid, S. (1993). Mutations in human dynamin block an intermediate stage in coated vesicleformation. *Journal of Cell Biology* **122**:553–563.

Boado, R.J., Hui, E.K., Lu, J.Z. and Pardridge, W.M. (2010). Drug targeting of erythropoietin across the primate blood-brain barrier with an IgG molecular Trojan horse. *Journal of Pharmacology and Experimental Therapeutics* **333**:961–969.

Boado, R.J., Hui, E.K., Lu, J.Z., Zhou, Q.H. and Pardridge, W.M. (2010). Selective targeting of a TNFR decoy receptor pharmaceutical to the primate brain as a receptor-specific IgG fusion protein. *Journal of biotechnology* **146**:84–91.

Boado, R.J. and Pardridge, W.M. (2011). The Trojan Horse Liposome Technology for Nonviral Gene Transfer across the Blood-Brain Barrier. *Journal of drug delivery* **2011**:296151.

Boado, R.J., Zhang, Y. and Pardridge, W.M. (2009). Engineering and Expression of a Chimeric Transferrin Receptor Monoclonal Antibody for Blood-Brain Barrier Delivery in Mouse. *Biotechnology Bioengineering* **102**:1251–1258.

Boado, R.J., Zhang, Y., Zhang, Y., C.F. Xia, Y., Wang and Pardridge, W.M. (2008). Genetic engineering of a lysosomal enzyme fusion protein for targeted delivery across the human blood-brain barrier. *Biotechnol. Bioeng* **99**:475–484.

Boado, R.J., Zhang, Y., Zhang, Y. and W.M. Pardridge (2007). Humanization of anti-human insulin receptor antibody for drug targeting across the human blood-brain barrier. *Biotechnol. Bioeng* **96**:381–391.

Bobo, R.H., Laske, D.W., Akbasak, A., Morrison, P.F., Dedrick, R.L. and E.H. Oldfield (1994). Convection-enhanced delivery of macromolecules in the brain. *Proc. Natl. Acad. Sci* **91**:2076–2080.

Bomsel, M. (1997). Transcytosis of infectious human immunodeficiency virus across a tight human epithelial cell line barrier. *Nature medicine* **3**:42–47.

Booth, R. and Kim, H. (2012). Characterization of a microfluidic in vitro model of the blood-brain barrier (μBBB). *Lab on a Chip* **12**:1784.

Booth, R. and Kim, H. (2014). Permeability Analysis of Neuroactive Drugs Through a Dynamic Microfluidic In Vitro Blood Brain Barrier Model. *Annals of Biomedical Engineering* **42**:2379–2391.

Bowman, P., Ennis, S., Rarey, K., Betz, A. and Goldstein, G. (1983). Brain microvessel endothelial cells in tissue culture: a model for study of blood-brain barrier permeability. *Annals of Neurology* **14**:396–402.

Cabezon, I., Manich, G., Martin-Venegas, R., Camins, A., Pelegri, C. and Vilaplana, J. (2015). Trafficking of Gold Nanoparticles Coated with the 8D3 Anti-Transferrin Receptor Antibody at the Mouse Blood-Brain Barrier. *Molecular Pharmaceutics* **12**:4137–4145.

Chalfie, M., Tu, Y., Euskirchen, G., Ward, W. and Prasher, D. (1994). Green fluorescent protein as a marker for gene expression. *Science* **263**:802–805.

Cho, H., Seo, J.H., Wong, K.H.K., Terasaki, Y., Park, J., Bong, K., Arai, K., *et al.* (2015). Three-Dimensional Blood-Brain Barrier Model for in vitro Studies of Neurovascular Pathology. *Scientific reports* **5**:15222.

Chrone, C. and Olesen, S. (1982). Electrical resistance of brain microvascular endothelium. *Brain research* **241**:49–55.

Chudakov, D.M., Lukyanov, S. and Lukyanov, K.A. (2007). Tracking intracellular protein movements using photoswitchable fluorescent proteins PS-CFP2 and Dendra2. *Nature Protocols* **2**:2024–2032.

Cooke, J.P. and Ghebremariam, Y.T. (2008). Endothelial Nicotinic Acetylcholine Receptors and Angiogenesis. *Trends Cardiovasc Med* **18**:247–253.

Cooray, H.C., Blackmore, C.G., Maskell, L. and Barrand, M.A. (2002). Localisation of breast cancer resistance protein in microvessel endothelium of human brain. *Neuroreport* **13**:2059–2063.

CORDENONSI, M., D'ATRI, F., HAMMAR, E., PARRY, D.A., KENDRICK-JONES, J., SHORE, D. and CITI, S. (1999). Cingulin contains globular and coiled-coil domains and interacts with ZO-1, ZO-2, ZO-3, and myosin. *Journal of Cell Biology* **147**:1569–1582.

Couch, J. a, Yu, Y.J., Zhang, Y., Tarrant, J.M., Fuji, R.N., Meilandt, W.J., Solanoy, H., *et al.* (2013). Addressing safety liabilities of TfR bispecific antibodies that cross the blood-brain barrier. *Science translational medicine* **5**:183ra57, 1–12.

Coyne, C., Gambling, T., Boucher, R., Carson, J. and Johnson, L. (2003). Role of claudin interactions in airway tight junctional permeability. *American journal of physiology. Lung Cell Molecular Physiology* **285**:1166–1178.

Crone, C. and Christensen, O. (1981). Electrical resistance of a capillary endothelium. *Journal of General Physiology* **77**:349–371.

Cucina, A., Sterpetti, A. V, Pupelis, G., Fragale, A., Lepidi, S., Cavallaro, A., Giustiniani, Q., *et al.* (1995). Shear Stress Induces Changes in the Morphology and Cytoskeleton Organisation of Arterial Endothelial Cells. *Eur J Vasc Endovasc Surg* **9**:86–92.

Cucullo, L., Hallene, K., Dini, G., Dal Toso, R. and Janigro, D. (2004). Glycerophosphoinositol and dexamethasone improve transendothelial electrical resistance in an in vitro study of the blood-brain barrier. *Brain research* **997**:147–151.

Cucullo, L., Marchi, N., Hossain, M. and Janigro, D. (2010). A dynamic in vitro BBB model for the study of immune cell trafficking into the central nervous system. *Journal of Cerebral Blood Flow & Metabolism* **31**:767–777.

Culot, M., Lundquist, S., Vanuxeem, D., Nion, S., Landry, C., Delplace, Y., Dehouck, M.P., *et al.* (2008). An in vitro blood-brain barrier model for high throughput (HTS) toxicological screening. *Toxicology in Vitro* **22**:799–811.

Dalkara, T., Gursoy-Ozdemir, Y. and Yemisci, M. (2011). Brain microvascular pericytes in health and disease. *Acta Neuropathologica* **122**:1–9.

Daniels, B.P., Cruz-Orengo, L., Pasieka, T.J., Couraud, P.-O., Romero, I. a., Weksler, B., Cooper, J. a., *et al.* (2013). Immortalized human cerebral microvascular endothelial cells maintain the properties of primary cells in an in vitro model of immune migration across the blood brain barrier. *Journal of Neuroscience Methods* **212**:173–179.

Dauchy, S., Miller, F., Couraud, P.O., Weaver, R.J., Weksler, B., Romero, I.A., Scherrmann, J.M., *et al.* (2009). Expression and transcriptional regulation of ABC transporters and cytochromes P450 in hCMEC/D3 human cerebral microvascular endothelial cells. *Biochemical Pharmacology* **77**:897–909.

Dautry-Varsat, A., Ciechanover, A. and Lodish, H.F. (1983). pH and the recycling of transferrin during receptor-mediated endocytosis. *Proceedings of the National Academy of Sciences of the United States of America* **80**:2258–2262.

Deinhardt, K., Reversi, A., Berninghausen, O., Hopkins, C.R. and Schiavo, G. (2007). Neurotrophins redirect p75NTR from a clathrin-independent to a clathrin-dependent endocytic pathway coupled to axonal transport. *Traffic* **8**:1736–1749.

Dejana, E. (2004). Endothelial cell-cell junctions: happy together. *Nature reviews. Molecular Cell Biology* **5**:261–270.

Dejana, E., Orsenigo, F. and Lampugnani, M. (2008). The role of adherens junctions and VE-cadherin in the control of vascular permeability. *Journal of Cell Science* **121**:2115–2122.

Deli, M., Abrahám, C., Kataoka, Y. and Niwa, M. (2005). Permeability studies on in vitro blood-brain barrier models: physiology, pathology, and pharmacology. *Cellular and Molecular Neurobiology* **25**:59–127.

Demeule, M., Poirier, J., Jodoin, J., Bertrand, Y., Desrosiers, R.R., Dagenais, C., Nguyen, T., *et al.* (2002). High transcytosis of melanotransferrin (P97) across the blood-brain barrier. *Journal of Neurochemistry* **83**:924–933.

Dewey, C., Gimbrone, M., Davies, P. and Bussolari, S. (1981). The dynamic response of vascular endothelial cells to fluid shear stress. *Journal of Biochemical Engineering* **103**:177–185.

Dietzschold, B., Wiktor, T.J., Trojanowski, J.Q., Macfarlan, R.I., Wunner, W.H., Torres-Anjel, M.J. and Koprowski, H. (1985). Differences in cell-to-cell spread of pathogenic and apathogenic rabies virus in vivo and in vitro. *Journal of virology* **56**:12–18.

Ebnet, K., Schulz, C.U., Meyer Zu Brickwedde, M.K., Pendl, G.G. and Vestweber, D. (2000). Junctional adhesion molecule interacts with the PDZ domain-containing proteins AF-6 and ZO-1. *The Journal of biological chemistry* **275**:27979–88.

Ebnet, K., Suzuki, A., Ohno, S. and Vestweber, D. (2004). Junctional adhesion molecules (JAMs): more molecules with dual functions. *Journal of Cell Science* **117**:19–29.

Escudero-Esparza, A., Jiang, W. and Martin, T. (2012). Claudin-5 participates in the regulation of endothelial cell motility. *Molecular and Cellular Biochemisty* **362**:71–85.

Evdokimov, A., Pokross, M., Egorov, N., Zaraisky, A., Yampolsky, I., Merzlyak, E., Shkoporov, A., *et al.* (2006). Structural basis for the fast maturation of Arthropoda green fluorescent protein. *EMBO* **7**:1006–1012.

Fang, F., Zou, D., Wang, W., Yin, Y., Yin, T., Hao, S., Wang, B., *et al.* (2017). Non-invasive approaches for drug delivery to the brain based on the receptor mediated transport. *Materials Science and Engineering C* **76**:1316–1327.

Fassshauer, D. and Margittai, M. (2004). Transient N-terminal interaction of SNAP-25 and syntaxin nucleates SNARE assembly. *Journal of Biological Chemistry* **279**:7613–7621.

Fenster, C.P., Whitworth, T.L., Sheffield, E.B., Quick, M.W. and Lester, R.A. (1999). Upregulation of surface alpha4beta2 nicotinic receptors is initiated by receptor desensitization after chronic exposure to nicotine. *The Journal of neuroscience : the official journal of the Society for Neuroscience*.

Ferlin, A., Raux, H., Baquero, E., Lepault, J. and Gaudin, Y. (2014). Characterization of pH-Sensitive Molecular Switches That Trigger the Structural Transition of Vesicular Stomatitis Virus Glycoprotein from the Postfusion State toward the Prefusion State. *Journal of Virology* **88**:13396–13409.

Finke, S., Brzózka, K., Brzo, K. and Conzelmann, K. (2004). Tracking Fluorescence-Labeled Rabies Virus : Enhanced Green Fluorescent Protein-Tagged Phosphoprotein P Supports Virus Gene Expression and Formation of Infectious Particles Tracking Fluorescence-Labeled Rabies Virus : Enhanced Green Fluorescent Protein-Ta. *Journal of Virology* **78**:12333–12343.

Fish, K.N. (2009). Total Internal Reflection Fluorescence (TIRF) Microscopy. *Current Protocols in Cytometry* **Oct**:8.

Fishman, J.B., Rubin, J.B., Handrahan, J. V, Connor, J.R. and Fine, R.E. (1987). Receptor-Mediated Transcytosis of Transferrin Across the Blood-Brain Barrier. **304**:299–304.

Frame, M. and Sarelius, I. (2000). Flow-Induced Cytoskeletal Changes in Endothelial Cells Growing on Curved Surfaces. *Microcirculation* **7**:419–427.

Franke, H., Galla, H.J. and Beuckmann, C.T. (1999). An improved low-permeability in vitro-model of the blood-brain barrier: Transport studies on retinoids, sucrose, haloperidol, caffeine and mannitol. *Brain Research* **818**:65–71.

Fukuda, A.M. and Badaut, J. (2012). Aquaporin 4: a player in cerebral edema and neuroinflammation. *Journal of Neuroinflammation* **9**:279.

Furgason, M.L.M., MacDonald, C., Shanks, S.G., Ryder, S.P., Bryant, N.J. and Munson, M. (2009). The N-terminal peptide of the syntaxin Tlg2p modulates binding of its closed conformation to Vps45p. *Proceedings of the National Academy of Sciences of the United States of America* **106**:14303–8.

Gaillard, P.J., Brink, A. and de Boer, A.G. (2005). Diphtheria toxin receptor-targeted brain drug delivery. *International Congress Series* **1277**:185–198.

Gaillard, P.J., Voorwinden, L.H., Nielsen, J.L., Ivanov, a, Atsumi, R., Engman, H., Ringbom, C., *et al.* (2001). Establishment and functional characterization of an in vitro model of the blood-brain barrier, comprising a co-culture of brain capillary endothelial cells and astrocytes. *European journal of pharmaceutical sciences : official journal of the European Federation for Pharmaceutical Sciences* **12**:215–22.

Gao, H.L., Pang, Z.Q., Fan, L., Hu, K.L., Wu, B.X. and Jiang, X.G. (2010). Effect of lactoferrin- and transferrin-conjugated polymersomes in brain targeting: in vitro and in vivo evaluations. *Acta Pharmacolica Sinica* **31**:237–243.

Gaudin Y, RW, R., C, T., M, K. and A., F. (1992). Rabies virus glycoprotein is a trimer. *Virology* **182**:627–632.

Gaudin, Y., Ruigrok, R.O.B.W.H., Knossow, M. and Flamand, A. (1993). Low-pH Conformational Changes of Rabies Virus Glycoprotein and Their Role in Membrane Fusion. *Journal of Virology* **67**.

Georgieva, J. V, Kalicharan, D., Couraud, P.-O., Romero, I. a, Weksler, B., Hoekstra, D. and Zuhorn, I.S. (2011). Surface characteristics of nanoparticles determine their intracellular fate in and processing by human blood-brain barrier endothelial cells in vitro. *Molecular Therapy* **19**:318–325.

Gluska, S., Zahavi, E., Chein, M., Gradus, T., Bauer, A., Finke, S. and Perlson, E. (2014). Rabies Virus Hijacks and Accelerates the p75NTR Retrograde Axonal Transport Machinery. *PloS Pathogens* **10**.

Glyn, M.C.P. and Ward, B.J. (2000). Contraction in cardiac endothelial cells contributes to changes in capillary dimensions following ischaemia and reperfusion. *Cardiovascular Research* **48**:346–356.

Gordon, G.R., Mulligan, S.J. and MacVicar, B.A. (2007). Astrocyte control of the cerebrovasculature. *Glia* **55**:1214–1221.

Gumbiner, B. and Simons, K. (1986). A functional assay for proteins involved in establishing an epithelial occluding barrier: identification of a uvomorulin-like polypeptide. *Journal of Cell Biology* **102**:457–468.

Gumbleton, M. and Audus, K.L. (2001). Progress and limitations in the use of in vitro cell cultures to serve as a permeability screen for the blood-brain barrier. *Journal of Pharmaceutical Science* **90**:1681 – 1698.

Haley, T. and McCormick (1957). Pharmacological effects produced by intracerebral injection of drugs in the conscious mouse. *British Journal of Pharmacology and Chemotherapy* **12**:12–15.

Hannan, S., Mortensen, M. and Smart, T.G. (2015). Snake neurotoxin α-bungarotoxin is an antagonist at native GABAA receptors. *Neuropharmacology* **93**:28–40.

Harrick, N.J. and Beckmann, K.H. (1974). Internal Reflection Spectroscopy. In: Kane, P. F. and Larrabee, G. B. (eds.) *Characterization of Solid Surfaces*. Boston, MA: Springer US, pp. 215–245.

Hatherell, K., Couraud, P.O., Romero, I. a., Weksler, B. and Pilkington, G.J. (2011). Development of a three-dimensional, all-human in vitro model of the blood-brain barrier using mono-, co-, and tri-cultivation Transwell models. *Journal of Neuroscience Methods* **199**:223–229.

Hawkins, B.T. and Davis, T.P. (2005). The Blood-Brain Barrier/Neurovascular Unit in Health and Disease. *Pharmacology Reviews* **57**:173–185.

Hawkins, B.T., Egleton, R.D. and Davis, T.P. (2005). Modulation of cerebral microvascular permeability by endothelial nicotinic acetylcholine receptors. *American journal of physiology. Heart and circulatory physiology* **289**:H212–H219.

Heimark, R., Degner, M. and Schwartz, S. (1990). Identification of a Ca2(+)-dependent cell-cell adhesion molecule in endothelial cells. *Journal of Cell Biology* **110**:1745–56.

Henne, W., Boucrot, E., Meinecke, M., Evergren, E., Vallis, Y., Mittal, R. and McMahon, H. (2010). FCHo proteins are nucleators of clathrin-mediated endocytosis. *Science* **328**:1281–1284.

Hersom, M., Helms, H.C., Pretzer, N., Goldemann, C., Jensen, A.I., Severin, G., Neilsen, M., *et al.* (2017). Transferrin receptor expression and role in transendothelial transport of transferrin in cultured brain endothelial monolayers. *Molecular and Cellular Neuroscience* **76**:59–67.

Hervé, F., Ghinea, N. and J.-M. Scherrmann (2008). CNS delivery via adsorptive transcytosis. *AAPS J* **10**:455–472.

Hoheisel, D., Nitz, T., Franke, H., Wegener, J., Hakvoort, A., Tilling, T. and Galla, H. (1998). Hydrocortisone reinforces the blood-brain properties in a serum free cell culture system. *Biochemical and Biophysical Research Communications* **247**:312–315.

Huang, R., Ke, W., Han, L., Liu, Y., Shao, K., Ye, L., Lou, J., *et al.* (2009). Brain-targeting mechanisms of lactoferrin-modified DNA-loaded nanoparticles. *Journal of Cerebral Blood Flow & Metabolism* **29**:1914–1923.

Huang, R.B. and Eniola-Adefeso, O. (2012). Shear stress modulation of IL-1-induced E-selectin expression in human endothelial cells. *PLoS ONE* **7**:1–9.

Huang, S., Li, S.-X., Bren, N., Cheng, K., Gomoto, R., Chen, L. and Sine, S.M. (2013). Complex between α-bungarotoxin and an α7 nicotinic receptor ligand-binding domain chimaera. *The Biochemical journal* **454**:303–10.

Huber, J., Egleton, R. and Davis, T. (2001). Molecular physiology and pathophysiology of tight junctions in the blood-brain barrier. *Trends in Neuroscience* **24**:719–725.

Huebers, H.A. and Finch, C.A. (1987). The physiology of transferrin and transferrin receptors. *Physiological Reviews* **67**:520–582.

Hughes, H. (1998). The Green Fluorescent Protein. *Annual Review of Biochemistry* **67**:509–544.

Humphries, W.H., Szymanski, C.J. and Payne, C.K. (2011). Endo-lysosomal vesicles positive for Rab7 and LAMP1 are terminal vesicles for the transport of dextran. *PLoS One* **6**:e26626.

Huwyler, J., Froidevaux, S., Roux, F. and Eberle, A.M. (1999). Characterization of Transferrin Receptor in an Immortalized Cell Line of Rat Brain Endothelial Cells, RBE4. *Journal of Receptors and Signal Transduction* **19**:729–739.

Huwyler, J. and Pardridge, W.M. (1998). Examination of Blood — Brain Barrier Transferrin Receptor by Confocal Fluorescent Microscopy of Unfixed Isolated Rat Brain Capillaries. :883–886.

Iadecola, C. and Nedergaard, M. (2007). Glial regulation of the cerebral microvasculature. *Nature Neuroscience* **10**:1369–1376.

Van Itallie, C.M., Fanning, A.S., Bridges, A. and Anderson, J.M. (2009). ZO-1 Stabilizes the Tight Junction Solute Barrier through Coupling to the Perijunctional Cytoskeleton. *Molecular Biology of the Cell* **20**:3930–3940.

Jaiswal, J.K., Rivera, V.M. and Simon, S.M. (2009). Exocytosis of Post-Golgi Vesicles Is Regulated by Components of the Endocytic Machinery. *Cell* **137**:1308–1319.

Jaiswal, J.K. and Simon, S.M. (2007). Imaging single events at the cell membrane. *Nature Chemical Biology* **3**:92–98.

Ji, B., Maeda, J., Higuchi, M., Inoue, K., Akita, H., Harashima, H. and Suhara, T. (2006). Pharmacokinetics and brain uptake of lactoferrin in rats. *Life Science* **78**:851–855.

Kamiya, A., Bukhari, R. and Togawa, T. (1987). Adaptive regulation of wall shear stress optimizing vascular tree function. *Bulletin of Mathematical Biology* **46**:127–137.

Karkan, D., Pfeifer, C., Vitalis, T.Z., Arthur, G., Ujiie, M., Chen, Q., Tsai, S., *et al.* (2008). A unique carrier for delivery of therapeutic compounds beyond the blood-brain barrier. *Plos One* **3**:e2469.

Kasheverov, I.E., Utkin, Y.N. and Tsetlin, V.I. (2009). Naturally Occurring and Synthetic Peptides Acting on Nicotinic Acetylcholine Receptors. *Current Pharmaceutical Design* **15**:2430–2452.

Kerr, M., Lindsay, M., Luetterforst, R., Hamilton, N., Simpson, F., Parton, R., Gleeson, P., *et al.* (2006). Visualisation of macropinosome maturation by the recruitment of sorting nexins. *Journal of Cell Science* **119**:3967–3980.

Khan, O. and Sefton, M. (2011). Endothelial cell behaviour within a microfluidic mimic of the flow channels of a modular tissue engineered construct. *Biomedical Microdevices* **13**:69–87.

Kim, J.A., Kim, H.N., Im, S.K., Chung, S., Kang, J.Y. and Choi, N. (2015). Collagen-based brain microvasculature model in vitro using three-dimensional printed template. *Biomicrofluidics* **9**.

Kim, R.B., Fromm, M.F., Wandel, C., Leake, B., Wood, A.J., Roden, D.M. and Wilkinson, G.R. (1998). The drug transporter P-glycoprotein limits oral absorption and brain entry of HIV-1 protease inhibitors. *Journal of Clinical Investigation* **101**:289–294.

Kissel, K., Hamm, S., Schulz, M., Vecchi, A., Garlanda, C. and Engelhardt, B. (1998). Immunohistochemical localization of the murine transferrin receptor (TfR) on blood-tissue barriers using a novel anti-TfR monoclonal antibody. *Histochemistry and Cell Biology* **110**:63–72.

Kittler, J.T., Delmas, P., Jovanovic, J.N., Brown, D. a, Smart, T.G. and Moss, S.J. (2000). Constitutive endocytosis of GABAA receptors by an association with the adaptin AP2 complex modulates inhibitory synaptic currents in hippocampal neurons. *The Journal of neuroscience : the official journal of the Society for Neuroscience* **20**:7972–7977.

Koepsell, H. and Endou, H. (2004). The SLC22 drug transporter family. *Pflugers Arch.* **447**:666–676.

Kohn, J.C., Zhou, D.W., Bordeleau, F., Zhou, A.L., Mason, B.N., Mitchell, M.J., King, M.R., *et al.* (2015). Cooperative effects of matrix stiffness and fluid shear stress on endothelial cell behavior. *Biophysical Journal* **108**:471–478.

Kumar, P., Wu, H., McBride, J.L., Jung, K.-E., Kim, M.H., Davidson, B.L., Lee, S.K., *et al.* (2007). Transvascular delivery of small interfering RNA to the central nervous system. *Nature* **448**:39–43.

Kuo, Y.C. and Chung, C.Y. (2012). Transcytosis of CRM197-grafted polybutylcyanoacrylate nanoparticles for delivering zidovudine across human brain-microvascular endothelial cells. *Colloids and Surfaces B: Biointerfaces* **91**:242–249.

Kuo, Y.C. and Chung, C.Y. (2012). Transcytosis of CRM197-grafted polybutylcyanoacrylate nanoparticles for delivering zidovudine across human brain-microvascular endothelial cells. *Colloids Surf. B: Biointerfaces* **91**:242–249.

Kuo, Y.C. and Ko, H.F. (2013). Targeting delivery of saquinavir to the brain using 83-14 monoclonal antibody-grafted solid lipid nanoparticles. *Biomaterials* **32**:4818–4830.

Kuo, Y.C. and Liu, Y.C. (2014). Cardiolipin-incorporated liposomes with surface CRM197 for enhancing neuronal survival against neurotoxicity. *International Journal of Pharmaceutics* **473**:334–344.

Kuo, Y.C. and Wang, I.H. (2015). Enhanced delivery of etoposide across the blood–brain barrier to restrain brain tumor growth using melanotransferrin antibody- and tamoxifen-conjugated solid lipid nanoparticles. *Journal of Drug Targeting*.

Labas, Y. a, Gurskaya, N.G., Yanushevich, Y.G., Fradkov, a F., Lukyanov, K. a, Lukyanov, S. a and Matz, M. V (2002). Diversity and evolution of the green fluorescent protein family. *Proceedings of the National Academy of Sciences of the United States of America* **99**:4256–61.

Laduron, P. and Leysen, J. (1979). Domperidone, a specific in vitro dopamine antagonist, devoid of in vivo central dopaminergic activity. *Biochemical Pharmacology* **28**:2161–2165.

Lafon, M. (2005). Rabies Virus Receptors. *Journal of Neurovirology* **11**:82–87.

Langevin, C. and Tuffereau, C. (2002). Mutations conferring resistance to neutralization by a soluble form of the neurotrophin receptor (p75NTR) map outside of the known antigenic sites of the rabies virus glycoprotein. *Journal of virology* **76**:10756–10765.

Lee, H., Zhang, Y., Zhu, C., Duff, K. and Pardridge, W. (2002). Imaging brain amyloid of Alzheimer disease in vivo in transgenic mice with an Abeta peptide radiopharmaceutical. *Journal of Cerebral Blood Flow and Metabolism* **22**:223–231.

Lee, H.J., Engelhardt, B., Lesley, J., Bickel, U. and Pardridge, W.M. (2000). Targeting rat anti-mouse transferrin receptor monoclonal antibodies through blood-brain barrier in mouse. *The Journal of pharmacology and experimental therapeutics* **292**:1048–1052.

Lee, H.W.A.J., Engelhardt, B., Lesley, J., Bickel, U., Pardridge, W.M., Angeles, L., California, H.J.L., *et al.* (2000). Targeting Rat Anti-Mouse Transferrin Receptor Monoclonal Antibodies through Blood-Brain Barrier in Mouse 1. **292**:1048–1052.

Lejeune, J.T. and Hancock, D.D. (2001). Raw Meat Diets To Dogs. *JAVMA* **219**:1222–1225.

Lencer, W., Weyer, P., Verkman, A., Ausiello, D. and Brown, D. (1990). FITC-dextran as a probe for endosome function and localization in kidney. *American journal of physiology.* **258**:309–317.

Lentz, T., Hawrot, E. and Wilson, P. (1987). Synthetic peptides corresponding to sequences of snake venom neurotoxins and rabies virus glycoprotein bind to the nicotinic acetylcholine receptor. *Proteins* **2**:298–307.

Lentz, T.L. (1982). Is the Acetylcholine Receptor a Rabies Virus Receptor ? *Science* **215**:182–184.

Lentz, T.L. (1985). Rabies virus recepto. *TINS* **3**:360–364.

Lentz, T.L., Benson, R.J., Klimowicz, D., Wilson, P.T. and Hawrot, E. (1986). Binding of rabies virus to purified Torpedo acetylcholine receptor. *Brain research* **387**:211–219.

Lentz TL (1990). Rabies virus binding to an acetylcholine receptor alpha-subunit peptide. *J Mol Recognit.* **3**:82–88.

Lewis, P., Fu, Y. and Lentz, T.L. (2000). Rabies virus entry at the neuromuscular junction in nerve-muscle cocultures. *Muscle & nerve* **23**:720–30.

Li, G., Simon, M.J., Cancel, L.M., Shi, Z.-D., Ji, X., Tarbell, J.M., Morrison, B., *et al.* (2010). Permeability of endothelial and astrocyte cocultures: in vitro blood-brain barrier models for drug delivery studies. *Annals of biomedical engineering* **38**:2499–511.

Lim, J.P. and Gleeson, P.A. (2011). Macropinocytosis: an endocytic pathway for internalising large gulps. *Immunology and Cell Biology* **89**:836–843.

Lim, R.G., Quan, C., Reyes-Ortiz, A.M., Lutz, S.E., Kedaigle, A.J., Gipson, T. a., Wu, J., *et al.* (2017). Huntington's Disease iPSC-Derived Brain Microvascular Endothelial Cells Reveal WNT-Mediated Angiogenic and Blood-Brain Barrier Deficits. *Cell Reports* **19**:1365–1377.

Lippmann, E.S., Al-Ahmad, A., Azarin, S.M., Palecek, S.P. and Shusta, E. V. (2015). A retinoic acid-enhanced, multicellular human blood-brain barrier model derived from stem cell sources. *Scientific Reports* **4**:4160.

Lippmann, E.S., Azarin, S.M., Kay, J.E., Nessler, R. a, Wilson, H.K., Al-Ahmad, A., Palecek, S.P., *et al.* (2012). Derivation of blood-brain barrier endothelial cells from human pluripotent stem cells. *Nature Biotechnology* **30**:783–791.

Liu, J.K., Teng, Q., Garrity-Moses, M., Federici, T., Tanase, D., Imperiale, M.J. and Boulis, N.M. (2005). A novel peptide defined through phage display for therapeutic protein and vector neuronal targeting. *Neurobiology of Disease* **19**:407–418.

Liu, Y., Huang, R., Han, L., Ke, W., Shao, K., Ye, L., Lou, J., *et al.* (2009). Brain-targeting gene delivery and cellular internalization mechanisms for modified rabies virus glycoprotein RVG29 nanoparticles. *Biomaterials* **30**:4195–202.

Lock, J., Ellesen, K., Settle, B., Parker, I. and Smith, I. (2015). Imaging Local Ca2+ Signals in Cultured Mammalian Cells. *Journal of Visualized Experiments* **97**:52516.

Loufrani, L. and Henrion, D. (2008). Role of the cytoskeleton in flow (shear stress)-induced dilation and remodeling in resistance arteries. *Med Biol Eng Comput.* **46**:451–460.

Machado, E., White-Gilbertson, S., van de Vlekkert, D., Janke, L., Moshiach, S., Campos, Y., Finkelstein, D., *et al.* (2015). Regulated lysosomal exocytosis mediates cancer progression. *Science Advances* **1**:e1500603–e1500603.

Macklin, K.D., Maus, a D., Pereira, E.F., Albuquerque, E.X. and Conti-Fine, B.M. (1998). Human vascular endothelial cells express functional nicotinic acetylcholine receptors. *The Journal of pharmacology and experimental therapeutics* **287**:435–9.

Manders, E.M.M., Verbeek, F.J. and Aten, J.A. (1993). Measurement of co-localization of objects in dual-colour confocal images. *Journal of Microscopy* **169**:375–382.

Mark, K.S. and Davis, T.P. (2002). Cerebral microvascular changes in permeability and tight junctions induced by hypoxia-reoxygenation. *American journal of physiology. Heart and circulatory physiology* **282**:H1485–94.

Mathers, C.D. and Loncar, D. (2006). Projections of Global Mortality and Burden of Disease from 2002 to 2030. *PLOS Medicine* **3**:2011–2030.

Matthews, D., Rudenski, A., Burnett, M., Darling, P. and Turner, R. (1985). The half-life of endogenous insulin and C-peptide in man assessed by somatostatin suppression. *Clinical Endocrinology* **23**:71–79.

Mattheyses, A., Simon, S. and Rappoport, J. (2010). Imaging with total internal reflection fluorescence microscopy for the cell biologist. *Journal of cell science* **123**:3621–8.

McCann, C.M., Bracamontes, J., Steinbach, J.H. and Sanes, J.R. (2006). The cholinergic antagonist alpha-bungarotoxin also binds and blocks a subset of GABA receptors. *Proceedings of the National Academy of Sciences of the United States of America* **103**:5149–5154.

Mercer, J. and Helenius, A. (2008). Vaccinia virus uses macropinocytosis and apoptotic mimicry to enter host cells. *Science* **320**:531–535.

Midorikawa, M. and Sakaba, T. (2015). Imaging Exocytosis of Single Synaptic Vesicles at a Fast CNS Presynaptic Terminal. *Neuron* **88**:492–498.

Mishra, V., Mahor, S., Rawat, A., Gupta, P., Bubey, P., Khatri, K. and Vyas, S. (2006). Targeted brain delivery of AZT via transferrin anchored pegylated albumin nanoparticles. *Journal of Drug Targeting*:45–53.

Moody, P.R., Sayers, E.J., Magnusson, J.P., Alexander, C., Borri, P., Watson, P. and Jones, A.T. (2015). Receptor Crosslinking: A General Method to Trigger Internalization and Lysosomal Targeting of Therapeutic Receptor:Ligand Complexes. *Molecular Therapy* **23**:1888–1898.

Moos, T. and Morgan, E.H. (1998). Evidence for low molecular weight, non-transferrin-bound iron in rat brain and cerebrospinal fluid. *Journal of Neuroscience Research* **54**:486–494.

Mori, S., Takanaga, H., Ohtsuki, S., Deguchi, T., Kang, Y.S., Hosoya, K. and Terasaki, T. (2003). Rat organic anion transporter 3 (rOAT3) is responsible for brain-to-blood efflux of homovanillic acid at the abluminal membrane of brain capillary endothelial cells. *Blood Flow Metabolism* **23**:432–440.

Morigi, M., Angioletti, S., Imberti, B., Donadelli, R., Micheletti, G., Figliuzzi, M., Remuzzi, A., *et al.* (1998). Leukocyte-endothelial interaction is augmented by high glucose concentrations and hyperglycemia in a NF-kB-dependent fashion. *Journal of Clinical Investigation* **101**:1905–1915.

Morigi, M., Zoja, C., Figliuzzi, M., Foppolo, M., Micheletti, G., Bontempelli, M., Saronni, M., *et al.* (1995). Fluid shear stress modulates surface expression of adhesion molecules by endothelial cells. *Blood* **85**:1696–703.

Morita, K., Sasaki, H., Furuse, M. and Tsukita, S. (1999). Endothelialclaudin: claudin-5/TMVCF constitutes tight junction strands in endothelialcells. *Journal of Cell Biology* **147**:185–194.

Murakami, T., Felinski, E. a. and Antonetti, D. a. (2009). Occludin phosphorylation and ubiquitination regulate tight junction trafficking and vascular endothelial growth factor-induced permeability. *Journal of Biological Chemistry* **284**:21036–21046.

Nabi, I.R. (2009). Cavin fever: regulating caveolae. *Nature Cell Biology* **11**:789–791.

Nagafuchi, A. (2001). Molecular architecture of adherens junctions. *Current Opinions in Cell Biology* **13**:600–603.

Neri, P., Bracci, L., Rustici, M. and Santucci, A. (1990). Sequence homology between HIV gp120, Rabies virus glycoprotein and snake venom neurotoxins. Is the nicotinic acetylcholine receptor an HIV receptor? *Virology* **114**:265–269.

Neuhaus, W., Gaiser, F., Mahringer, A., Franz, J., RiethmÃ¼ller, C. and FÃ¶rster, C. (2014). The pivotal role of astrocytes in an in vitro stroke model of the blood-brain barrier. *Frontiers in Cellular Neuroscience* **8**:352.

Ng, P.P., Cruz, J.S. Dela, Sorour, D.N., Stinebaugh, J.M., Shin, S., Shin, D.S., Morrison, S.L., *et al.* (2002). An anti-transferrin receptor-avidin fusion protein exhibits both strong proapoptotic activity and the ability to deliver various molecules into cancer cells.

Niewoehner, J., Bohrmann, B., Collin, L., Urich, E., Sade, H., Maier, P., Rueger, P., *et al.* (2014). Increased brain penetration and potency of a therapeutic antibody using a monovalent molecular shuttle. *Neuron* **81**:49–60.

Nitz, T., Eisenblätter, T., Psathaki, K. and Galla, H. (2003). Serum-derived factors weaken the barrier properties of cultured porcine brain capillary endothelial cells in vitro. *Brain research* **981**:30–40.

Ober, R.J., Martinez, C., Lai, X., Zhou, J. and E. Sally Ward (2004). Exocytosis of IgG as mediated by the receptor, FcRn: An analysis at the single-molecule level. *Proceedings of the National Academy of Sciences of the United States of America* **101**:11076–11081.

Oh, P., Borgstrom, P., Witkiewicz, H., Y. Li, B.J.B., Chrastina, A., Iwata, K., Zinn, K.R., *et al.* (2007). Live dynamic imaging of caveolae pumping targeted antibody rapidly and specifically across endothelium in the lung. *Nature Biotechnology* **25**:327–337.

Olesen, J., Gustavsson, A., Svensson, M., Wittchen, H.-U. and Jonsson, B. (2012). The economic cost of brain disorders in Europe. *European Journal of Neurology* **19**:155–162.

Omidi, Y., Campbell, L., Barar, J., Connell, D., Akhtar, S. and Gumbleton, M. (2003). Evaluation of the immortalised mouse brain capillary endothelial cell line, b.End3, as an in vitro blood-brain barrier model for drug uptake and transport studies. *Brain Research* **990**:95–112.

ONS (2015). *What Are the Top Causes of Death by Age and Gender?* [Online]. Available at: http://visual.ons.gov.uk/what-are-the-top-causes-of-death-by-age-and-gender/ [Accessed: 15 June 2017].

Ozaki, H., Ishii, K., Arai, H., Horiuchi, H., Kawamoto, T., H., S. and Kita, T. (2000). Junctional adhesion molecule (JAM) is phosphorylated by protein kinase C upon platelet activation. *Biochemical and Biophysical Research Communications* **276**:873–878.

Pardridge, W.M., Eisenberg, J. and Yang, J. (1985). Human blood-brain barrier insulin receptor. *Journal of Neurochemistry* **44**:1771–1778.

Pardridge, W.M., Kang, Y.S., Buciak, J.L. and J. Yang (1995). Human insulin-receptor monoclonal-antibody undergoes high-affinity binding to human brain capillaries in-vitro and rapid transcytosis through the blood-brain-barrier in-vivo in the primate. *Pharmaceutical research* **12**:807–816.

Paris-Robidas, S., Emond, V., Tremblay, C. and Soulet, D. (2011). In Vivo Labeling of Brain Capillary Endothelial Cells after Intravenous Injection of Monoclonal Antibodies Targeting the Transferrin Receptor □. *Molecular Pharmacology* **80**:32–39.

Patabendige, A., Skinner, R. a., Morgan, L. and Joan Abbott, N. (2013). A detailed method for preparation of a functional and flexible blood-brain barrier model using porcine brain endothelial cells. *Brain Research* **1521**:16–30.

Patel, R., Page, S. and Al-Ahmad, A.J. (2017). Isogenic blood-brain barrier models based on patient-derived stem cells display inter-individual differences in cell maturation and functionality. *Journal of Neurochemistry* **142**:74–88.

Perel, P., Roberts, I., Sena, E., Wheble, P., Briscoe, C., Sandercock, P., Maceod, M., *et al.* (2007). Comparison of treatment effects between animal experiments and clinical trials. *BMJ*:197.

Piccinotti, S., Kirchhausen, T. and Whelan, S.P.J. (2013). Uptake of rabies virus into epithelial cells by clathrin-mediated endocytosis depends upon actin. *Journal of virology* **87**:11637–47.

Piontek, J., Winkler, L., Wolburg, H., Muller, S., Zuleger, N., Piehl, C., Wiesner, B., *et al.* (2008). Formation of tight junction: determinants of homophilic interaction between classic claudins. *FASEB* **22**:146–158.

Pletnev, S., Shcherbakova, D.M., Subach, O.M., Pletneva, N. V., Malashkevich, V.N., Almo, S.C., Dauter, Z., *et al.* (2014). Orange fluorescent proteins: Structural studies of LSSmOrange, PSmOrange and PSmOrange2. *PLoS ONE* **9**:1–12.

Poduslo, J.F., Curran, G.L. and Berg, C.T. (1994). Macromolecular permeability across the blood-nerve and blood–brain barriers. *Proc. Natl. Acad. Sci* **91**:5705–5709.

Prabhakarpandian, B., Shen, M.C., Nichols, J.B., Garson, C.J., Mills, I.R., Matar, M.M., Fewell, J.G., *et al.* (2015). Synthetic tumor networks for screening drug delivery systems. *Journal of Controlled Release* **201**:49–55.

Prabhakarpandian, B., Shen, M.-C., Nichols, J.B., Mills, I.R., Sidoryk-Wegrzynowicz, M., Aschner, M. and Pant, K. (2013). SyM-BBB: a microfluidic blood brain barrier model. *Lab on a Chip* **13**:1093–1101.

Prasher, D., Eckenrode, V., Ward, W., Prendergast, F. and Cormier, M. (1992). Primary structure of the Aequorea victoria green-fluorescent protein. *Gene* **111**:229–233.

Qian, Z., Li, H., Sun, H. and Ho, K. (2002). Targerted drug delivery via the transferrin receptor-mediated endocytosis pathway. *Pharmacology Reviews*:561–587.

Racoonsin, E.L. and Swanson, J.A. (1993). Macropinosome maturation and fusion with tubular lysosomes in macrophages. *Journal of Cell Biology* **121**:1011–1020.

Ran, F.A., Hsu, P.D., Wright, J., Agarwala, V., Scott, D.A. and Zhang, F. (2013). Genome engineering using the CRISPR-Cas9 system. *Nature Protocols* **8**:2281–2308.

Rapoport, S.I., Ohno, K., Fredericks, W.R. and Pettigrew, K.D. (1978). Regional cerebrovascular permeability to [14C]sucrose after osmotic opening of the blood-brain barrier. *Brain research* **150**:653–657.

Raub, T.J. and Newton, C.R. (1991). Recycling Kinetics and Transcytosis of Transferrin in Primary Cultures of Bovine Brain Microvessel Endothelial Cells. *Journal of Celluar Physiology* **149**:141–151.

Reagan, K.J. and Wunner, W.H. (1985). Rabies Virus Interaction with Various Cell Lines Is Independent of the Acetylcholine Receptor. *Archives of Virology* **282**:277–282.

Rizzo, V., Morton, C., DePaola, N., Schnitzer, J.E. and Davies, P.F. (2003). Recruitment of endothelial caveolae into mechanotransduction pathways by flow conditioning in vitro. *American journal of physiology. Heart and circulatory physiology* **285**:H1720–H1729.

Roberts, R.L., Fine, R.E. and Sandra, A. (1993). Receptor-mediated endocytosis of transferrin at the blood-brain barrier. **532**:521–532.

Roman-Vendrell, C., Chevalier, M., Acevedo-Canabal, A.M. a. M., Delgado-Peraza, F., Flores-Otero, J. and Yudowski, G. a. G. a. (2014). Imaging of kiss-and-run exocytosis of surface receptors in neuronal cultures. *Frontiers in Cellular Neuroscience* **8**:1–10.

Sade, H., Baumgartner, C., Hugenmatter, A., Moessner, E., Freskg??rd, P.O. and Niewoehner, J. (2014). A human blood-brain barrier transcytosis assay reveals antibody transcytosis influenced by pH-dependent receptor binding. *PLoS ONE* **9**.

Saffarian, S., Cocucci, E. and Kirchhausen, T. (2009). Distinct dynamics of endocytic clathrin-coated pits and coated plaques. *PloS Biology* **7**:e1000191.

Sagare, A.P., Bell, R.D., Zhao, Z., Ma, Q., Winkler, E.A., Ramanathan, A. and Zlokovic, B.V. (2013). Pericyte loss influences Alzheimer-like neurodegeneration in mice. *Nature communications* **4**:2932.

Salvalaio, M., Rigon, L., Belletti, D., D'Avanzo, F., Pederzoli, F., Ruozi, B., Marin, O., *et al.* (2016). Targeted polymeric nanoparticles for brain delivery of high molecular weight molecules in lysosomal storage disorders. *PLoS ONE* **11**:1–17.

Santra, S., Yang, H., Stanley, J.T., Holloway, P.H., Moudgil, B.M., Walterd, G. and Mericle, R.A. (2005). Rapid and effective labeling of brain tissue using TAT-conjugated CdS:Mn/ZnS quantum dots. *Chemical Communications*:3144–3146.

Sato, K., Ernstrom, G.G., Watanabe, S., Weimer, R.M., Chen, C.-H., Sato, M., Siddiqui, A., *et al.* (2009). Differential requirements for clathrin in receptor-mediated endocytosis and maintenance of synaptic vesicle pools. *Proceedings of the National Academy of Sciences of the United States of America* **106**:1139–1144.

SATOH, H., ZHONG, Y., ISOMURA, H., SAITOH, M., ENOMOTO, K., SAWADA, N. and MORI, M. (1996). Localization of 7H6 tight junction-associated antigen along the cell border of vascular endothelial cells correlates with paracellular barrier function against ions, large molecules, and cancer cells. *Experimental cell research* **222**:269–274.

Schlachetzki, F., Zhu, C. and William M. Pardridge (2002). Expression of the neonatal Fc receptor (FcRn)at the blood–brain barrier. *Journal of Neurochemistry* **81**:203–206.

Schlageter, K.E., Molnar, P., Lapin, G.D. and Groothuis, D.R. (1999). Microvessel organization and structure in experimental brain tumors: microvessel populations with distinctive structural and functional properties. *Microvascular Research* **58**:312–328.

Schmoranzer, J., Goulian, M., Axelrod, D. and Simon, S.M. (2000). Imaging constitutive exocytosis with total internal reflection fluorescence microscopy. *Journal of Cell Biology* **149**:23–31.

Schnell, M.J., McGettigan, J.P., Wirblich, C. and Papaneri, A. (2010). The cell biology of rabies virus: using stealth to reach the brain. *Nature reviews. Microbiology* **8**:51–61.

Schrade, A., Sade, H., Couraud, P., Romero, I., Weksler, B.B. and Niewoehner, J. (2012). Expression and localization of claudins-3 and -12 in transformed human brain endothelium. *Fluids and Barriers of the CNS* **9**.

Schwarze, S.R., Ho, A., Vocero-Akbani, A. and Dowdy, S.F. (1999). In Vivo Protein Transduction: Delivery of a Biologically Active Protein into the Mouse. *Science* **285**:1569–1572.

Shankar, V., Dietzschold, B. and Koprowski, H. (1991). Direct entry of rabies virus into the central nervous system without prior local replication. *Journal of virology* **65**:2736–2738.

Shao, K., Wu, J., Chen, Z., Huang, S., Li, J., Ye, L., Lou, J., *et al.* (2012). A brain-vectored angiopep-2 based polymeric micelles for the treatment of intracranial fungal infection. *Biomaterials* **33**:6898–6907.

Shapiro, R.E., Specht, C.D., Collins, B.E., Woods, A.S., Cotter, R.J. and Schnaar, R.L. (1997). Identification of a ganglioside recognition domain of tetanus toxin using a novel ganglioside photoaffinity ligand. *Journal of Biological Chemistry* **272**:30380–30386.

Sheikov, N., McDannold, N., Jolesz, F., Zhang, Y.-Z., Tam, K. and Hynynen, K. (2006). Brain arterioles show more active vesicular transport of blood-borne tracer molecules than capillaries and venules after focused ultrasound-evoked opening of the blood-brain barrier. *Ultrasound Med. Biol* **32**:1399–1409.

Shen, J., Tareste, D.C., Paumet, F., Rothman, J.E. and Melia, T.J. (2007). Selective activation of cognate SNAREpins by Sec1/Munc18 proteins. *Cell* **128**:183–195.

Shen, Y., Rosendale, M., Campbell, R. and Perrais, D. (2014). pHuji, a pH-sensitive red fluorescent protein for imaging of exo- and endocytosis. *Journal of Cell Biology* **207**:419–432.

Shimomura, O., Johnson, F. and Saiga, Y. (1962). Extraction, purification and properties of aequorin, a bioluminescent protein from the luminous hydromedusan, Aequorea. *Journal of Cellular and Comparative Physiology* **59**:223–239.

Shin, S., Friden, P., Moran, M., Olson, T., Kang, Y., Pardridge, W. and Morrison, S. (1995). Transferrin-antibody fusion proteins are effective in brain targeting. *PNAS*:2820–2824.

Siegal, T., Rubinstein, R., Bokstein, F., Schwartz, A., Lossos, A., Shalom, E., Chisin, R., *et al.* (2000). In vivo assessment of the window of barrier opening after osmotic blood-brain barrier disruption in humans. *Journal of Neurosurgery* **92**:599–605.

Sioka, C. and Kyritsis, A.P. (2009). Central and peripheral nervous system toxicity of common chemotherapeutic agents. *Cancer Chemotherapy and Pharmacology* **63**:761–7.

Sissoëff, L., Mousli, M., England, P. and Tuffereau, C. (2005). Stable trimerization of recombinant rabies virus glycoprotein ectodomain is required for interaction with the p75NTR receptor. *Journal of General Virology* **86**:2543–2552.

Smith, M., Omidi, Y. and Gumbleton, M. (2007). Primary porcine brain microvascular endothelial cells: Biochemical and functional characterisation as a model for drug transport and targeting. *Journal of Drug Targeting* **15**:253–268.

Smith, M.W. and Gumbleton, M. (2006). Endocytosis at the blood–brain barrier: From basic understanding to drug delivery strategies. *Journal of Drug Targeting* **14**:191–214.

Sobue, K., Yamamoto, N., Yoneda, K., Hodgson, M., Yamashiro, K., Tsuruoka, N., Tsuda, T., *et al.* (1999). Induction of blood-brain barrier properties in immortalized bovine brain endothelial cells by astrocytic factors. *Neuroscience Research* **35**:155–164.

Sodeik, B. (2000). Mechanisms of viral transport in the cytoplasm. *Trends in microbiology* **8**:465–72.

Soma, T., Chiba, H., Kato-Mori, Y., Wada, T., Yamashita, T., Kojima, T. and Sawada, N. (2004). Thr(207) of claudin-5 is involved in size-selective loosening of the endothelial barrier by cyclic AMP. *Experimental cell research* **300**:202–212.

Somani, S., Blatchford, D.R., Millington, O., Stevenson, M.L. and Dufes, C. (2014). Transferrin-bearing polypropylenimine dendrimer for targeted gene delivery to the brain. *Journal of Controlled Release* **188**:78–86.

Stimpson, H.E., Toret, C.P., Cheng, A.T., Pauly, B.S. and Drubin, D.G. (2009). Early-arriving Syp1p and Ede1p function in endocytic site placement and formation in budding yeast. *Molecular biology of the cell* **20**:4640–4651.

Subach, O.M., Entenberg, D., Condeelis, J.S. and Verkhusha, V. V. (2012). A FRET-facilitated photoswitching using an orange fluorescent protein with the fast photoconversion kinetics. *Journal of the American Chemical Society* **134**:14789–14799.

Subach, O.M., Patterson, G.H., Ting, L.-M., Wang, Y., Condeelis, J.S. and Verkhusha, V. V (2011). A photoswitchable orange-to-far-red fluorescent protein, PSmOrange. *Nature methods* **8**:771–7.

Sudhof, T.C. and Rothman, J.E. (2009). Membrane fusion: grappling with SNARE and SM proteins. *Science* **323**:474–477.

Taylor, M.J., Perrais, D. and Merrifield, C.J. (2011). A highprecision survey of the molecular dynamics of mammalian clathrin-mediated endocytosis. *PloS Biology* **9**:e1000604.

Thomas, F.C., Taskar, K., Rudraraju, V., Goda, S., Thorsheim, H.R., Gaasch, J.A., Mittapalli, R.K., *et al.* (2009). Uptake of ANG1005, a novel paclitaxel derivative, through the blood-brain barrier into brain and experimental brain metastases of breast cancer. *Pharmaceutical research* **26**:2486–2494.

Thorne, R.G., Pronk, G.J., Padmanabhan, V. and Frey, W.H. (2004). Delivery of insulin-like growth factor-I to the rat brain and spinal cord along olfactory and trigeminal pathways following intranasal administration. *Neuroscience* **127**:481–496.

Thoulouze, M.I., Lafage, M., Schachner, M., Hartmann, U., Cremer, H. and Lafon, M. (1998). The neural cell adhesion molecule is a receptor for rabies virus. *Journal of virology* **72**:7181–90.

Tosi, G., Bortot, B., Ruozi, B., Dolcetta, D., Vandelli, M., Forni, F. and Severini, G. (2013). Potential use of polymeric nanoparticles for drug delivery across the blood-brain barrier. *Current Medicinal Chemistry* **20**:2212–2225.

Tosi, G., Fano, R., Bondioli, L., Badiali, L., Benassi, R., Rivasi, F., Ruozi, B., *et al.* (2011). Investigation on mechanisms of glycopeptide nanoparticles for drug delivery across the blood-brain barrier. *Nanomedicine* **6**:423–436.

Tripothi, R.C., Kolli, S.P., Borisurh, N.C. and Triporhi, B.J. (1992). Identification and Quantification of Transferrin Receptors on Trabecular Cells. *Investigative Ophthalmology & Visual Science* **33**:3449–3453.

Tsunoyama, K. and Gojobori, T. (1998). Evolution of nicotinic acetylcholine receptor subunits. *Molecular biology and evolution* **15**:518–527.

Tuma, P.L. and Hubbard, A.L. (2003). Transcytosis: crossing cellular barriers. *Physiological reviews* **83**:871–932.

Ulbrich, K., Hekmatara, T., Herbert, E. and Kreuter, J. (2009). Transferrin- and transferrin-receptor-antibody-modified nanoparticles enable drug delivery across the blood-brain barrier (BBB). *European journal of Biopharmaceuticals* **71**:251–256.

Ulbrich, K., Knobloch, T. and Kreuter, J. (2011). Targeting the insulin receptor: nanoparticles for drug delivery across the blood-brain barrier (BBB). *Journal of Drug Targeting* **19**:125–132.

Urquhart, B.L. and Kim, R.B. (2009). Blood−brain barrier transporters and response to CNS-active drugs. *European Journal of Clinical Pharmacology* **65**:1063.

Vilella, A., Tosi, G., Grabrucker, A.M., Ruozi, B., Belletti, D., Vandelli, M.A., Boeckers, T.M., *et al.* (2014). Insight on the fate of CNS-targeted nanoparticles. Part I: Rab5-dependent cell-specific uptake and distribution. *Journal of Controlled Release* **174**:195–201.

De Vries, N.A., Zhao, J., Kroon, E., Buckle, T., Beijnen, J.H. and van Tellingen, O. (2007). P-glycoprotein and breast cancer resistance protein: two dominant transporters working together in limiting the brain penetration of topotecan. *Clinical Cancer Research* **13**:6440–6449.

Vrljic, M., Strop, P., Ernst, J.A., Sutton, B., Chu, S. and Brunger, A.T. (2010). Molecular mechanism of the synaptotagmin–SNARE interaction in Ca2+-triggered vesicle fusion. *NATURE STRUCTURAL & MOLECULAR BIOLOGY* **17**:325–331.

Walker, S., Cunniffe, N., Bootman, M. and Roderick, H. (2008). Dynamic imaging of calcium and STIM1 in the same cell using wide-field and TIRF microscopy. *Biotechniques* **45**:347–348.

Walus, L.R., Pardridge, W.M., Starzyk, R.M. and Friden, P.M. (1996). Enhanced uptake of rsCD4 across the rodent and primate blood-brain barrier after conjugation to anti-transferrin receptor antibodies. *Journal of Pharmacology and Experimental Therapeutics* **277** :1067–1075.

Wang, P., Xue, Y., Shang, X. and Liu, Y. (2010). Diphtheria toxin mutant CRM197-mediated transcytosis across blood-brain barrier in vitro. *Cellular and Molecular Neurobiology* **30**:717–725.

Warrell, M.J. and Warrell, D. a (2004). Rabies and other lyssavirus diseases. *Lancet* **363**:959–69.

Weksler, B.B., Subileau, E.A., Perrière, N., Charneau, P., Holloway, K., Leveque, M., Tricoire-Leignel, H., *et al.* (2005). Blood-brain barrier-specific properties of a human adult brain endothelial cell line. *The FASEB Journal* **26**:1–26.

Wennmalm, S. and Simon, S.M. (2007). Studying Individual Events in Biology. *Annual Review of Biochemistry* **76**:419–446.

Wiley, D.T., Webster, P., Gale, A. and Davis, M.E. (2013). Transcytosis and brain uptake of transferrin-containing nanoparticles by tuning avidity to transferrin receptor.

Proceedings of the National Academy of Sciences of the United States of America **110**:8662–7.

Williams, R.L., Risau, W., Zerwes, H.G., Drexler, H., Aguzzi, A. and Wagner, E.F. (1989). Endothelioma cells expressing the polyoma middle T oncogene induce hemangiomas by host cell recruitment. *Cell* **57**:1053–1063.

Wolff, A., Antfolk, M., Brodin, B. and Tenje, M. (2015). In Vitro Blood-Brain Barrier Models - An Overview of Established Models and New Microfluidic Approaches. *Journal of Pharmaceutical Sciences* **104**:2727–2746.

Wong, V. (1997). Phosphorylation of occludin correlates with occludin localization and function at the tight junction. *The American journal of physiology* **273**:C1859–67.

Xin, H., Jiang, X., Gu, J., Sha, X., Chen, L., Law, K., Chen, Y., *et al.* (2011). Angiopep-conjugated poly(ethylene glycol)-co-poly(ε-caprolactone) nanoparticles as dual-targeting drug delivery system for brain glioma. *Biomaterials* **32**:4293–4305.

Xu, Y., Su, L. and Rizo, J. (2010). Binding of Munc18–1 to synaptobrevin and to the SNARE four-helix bundle. *Biochemistry* **49**:1568–1576.

Xue, Y.Q., Ma, B.F., Zhao, L.R., Tatom, J.B., Li, B., Jiang, L.X., Klein, R.L., *et al.* (2010). AAV9-mediated erythropoietin gene delivery into the brain protects nigral dopaminergic neurons in a rat model of Parkinson's disease. *Gene Therapy* **17**:83–94.

Yaffe, Y., Shepshelovitch, J., Nevo-Yassaf, I., Yeheskel, A., Shmerling, H., Kwiatek, J., Gaus, K., *et al.* (2012). The MARVEL transmembrane motif of occludin mediates oligomerization and targeting to the basolateral surface in epithelia. *Journal of Cell Science*:3545–3556.

Yamagata, K., Tagami, M., Nara, Y., Mitani, M., Kubota, A., Fujino, H., Numano, F., *et al.* (1997). Astrocyte-conditioned medium induces blood-brain barrier properties in endothelial cells. *Clincial and Experimental Pharmacology and Physiology*:710–713.

Yemisci, M., Gursoy-Ozdemir, Y., Vural, A., Can, A., Topalkara, K. and Dalkara, T. (2009). Pericyte contraction induced by oxidative-nitrative stress impairs capillary refl ow despite successful opening of an occluded cerebral artery. *Nature medicine* **15**:1031–1037.

Yu, Y.J., Atwal, J.K., Zhang, Y., Tong, R.K., Wildsmith, K.R., Tan, C., Bien-Ly, N., *et al.* (2014). Therapeutic bispecific antibodies cross the blood-brain barrier in nonhuman primates. *Science Translational Medicine* **6**:261ra154–261ra154.

Yu, Y.J., Zhang, Y., Kenrick, M., Hoyte, K., Luk, W., Lu, Y., Atwal, J., *et al.* (2011). Boosting brain uptake of a therapeutic antibody by reducing its affinity for a transcytosis target. *Science translational medicine* **3**:84ra44.

Yue, P.J., He, L., Qiu, S.W., Li, Y., Liao, Y.J., Li, X.P., Xie, D., *et al.* (2014). OX26/CTX-conjugated PEGylated liposome as a dual-targeting gene delivery system for brain glioma. *Molecular Cancer* **13**:191.

Zhang, X., Zhang, M., Li, D., He, W., Peng, J., Betzig, E. and Xu, P. (2016). Highly photostable, reversibly photoswitchable fluorescent protein with high contrast ratio for live-cell superresolution microscopy. *Proceedings of the National Academy of Sciences*:201611038.

Zhou, Q.H., Boado, R.J., LU, J.Z., Hui, E.K. and William M. Pardridge (2010). Re-engineering erythropoietin as an IgG fusion protein that penetrates the blood-brain barrier in the mouse. *Molecular Pharmaceutics* **7**:2148–2155.

Zhou, X. and Lin, M. (2013). Photoswitchable fluorescent proteins: ten years of colorful chemistry and exciting applications. *Current Opinions in Chemical Biology* **17**:682–690.

Appendices

Appendix 1 – PBS buffer composition

Table 2.1.1 – Composition of PBS buffer		
Chemical	**Concentration (g/L)**	**Source**
Sodium Chloride	8.00	Fisher scientific
Potassium Chloride	0.20	Fisher scientific
Disodium Hydrogen Phosphate	1.44	Fisher scientific
Potassium Dihydrogen Phosphate	0.24	Fisher scientific

Appendix 2 – Krebs-Ringer Buffer composition

Table 2.1.2 – Composition of Krebs-Ringer Buffer		
Chemical	**Concentration (g/L)**	**Source**
Magnesium Chloride	0.047	Fisher scientific
Potassium Chloride	0.340	Fisher scientific
Sodium Chloride	7.000	Fisher scientific
Calcium Chloride	0.277	Fisher scientific
Disodium Hydrogen Phosphate	0.100	Fisher scientific
Sodium Dihydrogen Phosphate	0.180	Fisher scientific
Sodium Bicarbonate	1.260	Fisher scientific
D-Glucose	1.800	Fisher scientific
Bovine Serum Albumin	1.000	Sigma Aldridge

Appendix 3 – Collagen Coating of Plastic

Table 2.2.1 - Collagen Coating volumes for plastic cell culture surfaces

Culture Surface	Surface Area (cm2)	Mass of collagen (µg)	Volume of collagen (µL)	PBS volume (µL)	Total volume (µL)
24 Well Insert	0.33	1.65	0.7	59	59.7
24 Well Plate	1.9	9.5	4.1	195	199.1
6 Well Insert	4.67	23.35	10.2	490	500.2
6 Well Plate	9.5	47.5	20.7	480	500.7
Imaging dish	9.5	47.5	20.7	480	500.7
T 25 Flask	25	125	54.3	345	399.3
T 75 Flask	75	375	163.0	837	1000.0

Appendix 4: Isolation of Porcine Brain Microvascular Endothelial Cells

The isolation of PBMECs is performed using four pigs heads obtained on the day from a local abattoir.

Brain removal

1) A mid-line incision is made from the top of the snout to the back of the head and the skin removed to expose the skull.
2) The exposed skull is cut in three places to give a loose wedge of bone that can be removed to expose the brain, within the meninges beneath.
3) An incision along the length of the meninges exposes the brain.
4) The brain can now be pulled free from the skull and placed in ice-cold PBS

Cell Isolation

1) After the brains have been removed from the skulls they are transferred to a Category 2 cell culture hood for the following steps of the isolation.
2) The large, surface vessels and the white matter are removed from the brain using forceps and the remainder of the brain stored in PBS until further use.
3) The brains are minced into a fine paste and divided into four equal volumes in 250 mL centrifuge bottles.
4) To each bottle 40mL of porcine preparation medium (M199 + penicillin - 100units/mL, streptomycin 100 µg/mL) containing, 1g of dispase, is added and the bottles incubated at 37 ^{o}C on a roller shaker for two hours (Digestion 1).
5) The bottles are placed on ice to inhibit the action of the dispase and the bottles filled with 30% percoll solution, prior to centrifuging at 6000 xg for 10 minutes at 4 ^{o}C. This step allows the separation of fats from other components of the brain.

6) The fats will be floating at the surface of the centrifuge bottles and should be removed by stripette. At this stage red streaks of vessels will begin to be visible at the base of the centrifuge bottles and care must be taken not to disturb these while removing fats from the tube.
7) The remaining solution in the bottles is then re-centrifuged at 1700 xg for 10 minutes at 4 ^{o}C to pellet the remaining vessels in the solution.
8) The remaining supernatant is carefully removed to ensure the red streaks remain at the base of the bottle.
9) The streaks are re-suspended in 7 mL of porcine culture media, PCM (90% M199, 10% horse serum, penicillin 100 units/mL, streptomycin 100µg/mL) and the mixtures collected into one tube.
10) To this tube is added collagenase/dispase to give a concentration of 1 mg/mL. The tube is placed at 37 ^{o}C for 1-1.5 hours and monitored throughout this time to see if a single cell suspension could be observed (Digestion 2).
11) Following the conclusion of Digestion 2 the tube was placed at 4 ^{o}C to stop the enzymatic digest.
12) The cell suspension is passed through 180µm and 20µm meshes to prevent any larger vessels being present in the final collection. Care must be taken in this step to avoid rupturing the membranes.
13) The volumes remaining are split evenly between two centrifuge tubes and pelleted by centrifugation at 185 xg for 10 minutes at 4 ^{o}C. The resulting pellets were then re-suspended in 10mL of PCM.
14) While the tubes are centrifuging the discontinuous percoll gradients were prepared. This was done by adding 10mL of Heavy Percoll (density = 1.07g/mL) beneath 10mL of Light Percoll (density = 1.03g/mL), ensuring a sharp interface

between the densities. To the gradients is added 5mL of the re-suspended cell solution, again ensuring a sharp interface between the Light Percoll and the cell solution.

15) The gradients are centrifuged at 1300 xg for 13 minutes at 4ºC with slow acceleration and no deceleration to ensure the interfaces between the different densities remains.
16) The endothelial cells are located at the interface between the heavy and light percoll gradients (density of 1.05-1.052 g/mL). The excess upper solution is discarded and the cells at the interface collected into a new centrifuge tube.
17) Fresh PCM is added to the cells and the tubes are centrifuges at 1300 xg for 10 minutes to pellet the endothelial cells and remove the percoll from the solution.
18) Cells are re-suspended in 40mL Porcine Freezing Medium (70% M199, 25% horse serum, 5% DMSO) and divided into 1mL aliquots for long term storage at -140 ºC.

Appendix 5 – PBMEC cell growth

The porcine microvascular endothelial cells isolated in laboratory were grown on plastic with daily imaging to assess the growth and morphology of the cells in the culture. Small islands of cells were visualised on the plastic from day 3 onwards and have been seen to expand day by day until a complete monolayer could be observed, day 6-7.

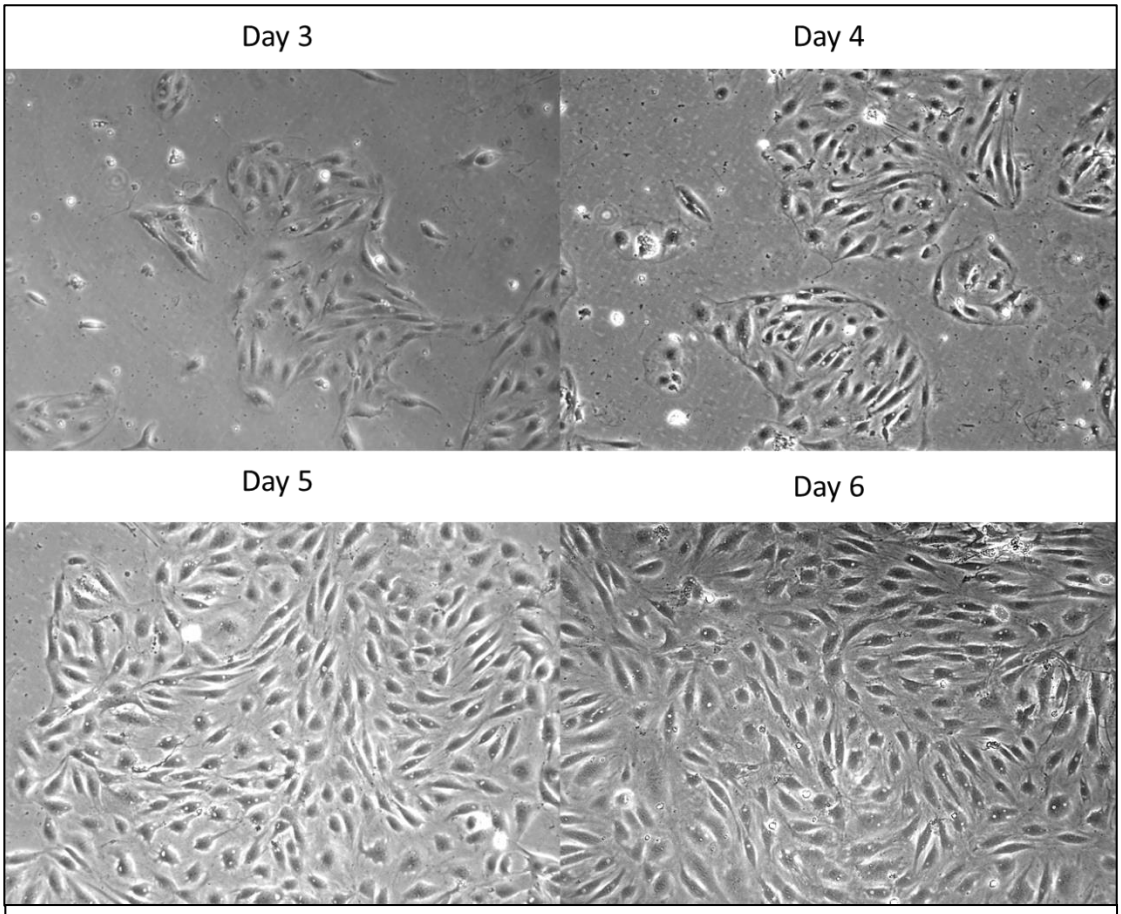

Imaging of primary porcine brain microvascular endothelial cell growth

Cells have been seeded onto collagen coated plastic cell culture dishes and inspected using phase-contrast microscopy daily until a confluent monolayer of cells was observed across the plate.

When a monolayer is observed cells have a "spindle" morphology, typical of endothelial cells can be seen by light microscopy. Trials into collagen coating density confirmed that 5µg/cm^2 coating density was optimal for cell growth and was continued with for all studies presented here unless otherwise mentioned.